

AD-A107 199

AIR FORCE INST OF TECH WRIGHT-PATTERSON AFB OH

F/G 4/2

TOPOGRAPHICALLY INDUCED DIURNAL BOUNDARY LAYER OSCILLATIONS: YW--ETC(U)

DEC 79 D W MCLAWHORN

NSF-ATM77-26094

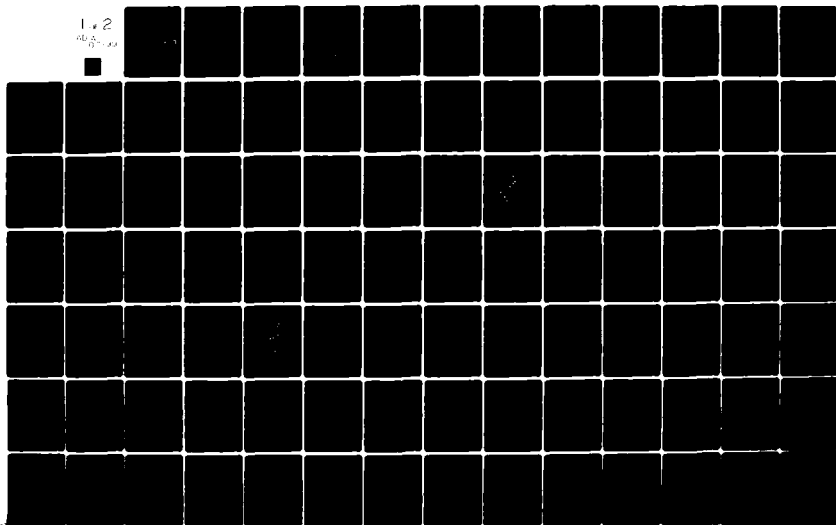
NL

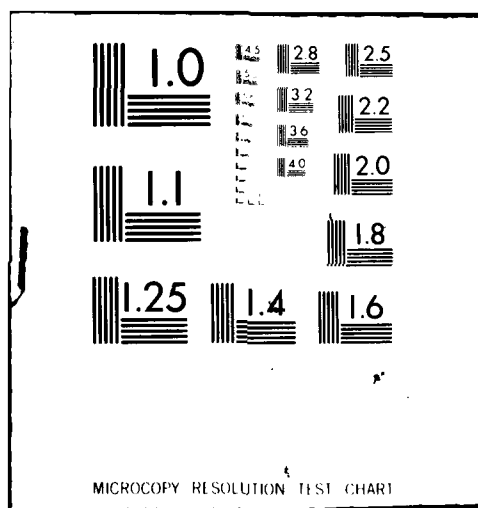
UNCLASSIFIED

AFIT-CI-79-2690

1 of 2

AD-A107 199





UNCLASS

SECURITY CLASSIFICATION OF THIS PAGE (When Data Entered)

AD A107199

DTIC FILE COPY

REPORT DOCUMENTATION PAGE		READ INSTRUCTIONS BEFORE COMPLETING FORM
1. REPORT NUMBER 79-269D	2. GOVT ACCESSION NO. ADA107199	3. RECIPIENT'S CATALOG NUMBER
4. TITLE (and Subtitle) Topographically Induced Diurnal Boundary Layer Oscillations: Two Dimensional Synoptic Scale Modeling		5. TYPE OF REPORT & PERIOD COVERED THESIS/DISSERTATION
7. AUTHOR(s) David W. McLawhorn		6. PERFORMING ORG. REPORT NUMBER
9. PERFORMING ORGANIZATION NAME AND ADDRESS AFIT STUDENT AT: The University of Utah		8. CONTRACT OR GRANT NUMBER(s)
11. CONTROLLING OFFICE NAME AND ADDRESS AFIT/NR WPAFB OH 45433		10. PROGRAM ELEMENT, PROJECT, TASK AREA & WORK UNIT NUMBERS 15 NSF-ATM77-26074
14. MONITORING AGENCY NAME & ADDRESS (if different from Controlling Office) LEVEL II		12. REPORT DATE 11 Dec 1979
		13. NUMBER OF PAGES 154 12 187
		15. SECURITY CLASS. (of this report) UNCLASS
16. DISTRIBUTION STATEMENT (of this Report) APPROVED FOR PUBLIC RELEASE; DISTRIBUTION UNLIMITED 14 AFIT-91-2-12		15a. DECLASSIFICATION DOWNGRADING SCHEDULE
17. DISTRIBUTION STATEMENT (of the abstract entered in Block 20, if different from Report) DTIC FILE COPY		
18. SUPPLEMENTARY NOTES APPROVED FOR PUBLIC RELEASE: IAW AFR 190-17 FREDRIC C. LYNCH, Major, USAF Director of Public Affairs Air Force Institute of Technology (ATC) Wright Patterson AFB, OH 45433		
19. KEY WORDS (Continue on reverse side if necessary and identify by block number)		
20. ABSTRACT (Continue on reverse side if necessary and identify by block number) ATTACHED		

81 10 26 147

DD FORM 1473

EDITION OF 1 NOV 65 IS OBSOLETE

SECURITY CL.

UNCLASS

SECURITY CLASSIFICATION OF THIS PAGE (When Data Entered)

012204

Knee

ABSTRACT

A two dimensional boundary layer model is developed for the study of diurnal cycles in boundary layer convergence over synoptic scale sloping terrain and thermally inhomogeneous surfaces. To properly resolve the terrain configuration, a local terrain following coordinate system is developed. The local coordinate system has characteristics which are superior to the terrain following coordinate systems commonly used. Truncation errors are significantly reduced in the local system so variations in the flow field due to physical forcing are easily discernable from those due to truncation error. Also, it appears that the local system can resolve coarser terrain configurations under numerically stable conditions.

The model exhibits a sensitivity to latitude. The phase of the maximum vertical velocities forecast by the model occurs six hours later at 22°N. vs. 38°N. The boundary layer model is apparently not very sensitive to radiative flux divergence calculations but did show a marked reaction to soil type. Both the amplitude and phase of the maximum vertical velocities are modified by changes in soil type.

Accession For	
NTIS GRA&I	<input checked="" type="checkbox"/>
DTIC TAB	<input type="checkbox"/>
Unannounced	<input type="checkbox"/>
Justification	
By	
Distribution/	
Availability Codes	
Avail and/or	
Dist	Special
A	

81 10 26 147

100-25-40

TOPOGRAPHICALLY INDUCED DIURNAL BOUNDARY LAYER OSCILLATIONS:
TWO DIMENSIONAL SYNOPTIC SCALE MODELING

by

David W. McLawhorn

A dissertation submitted to the faculty of The
University of Utah in partial fulfillment of the requirements
for the degree of

Doctor of Philosophy

Department of Meteorology

The University of Utah

December 1979

THE UNIVERSITY OF UTAH GRADUATE SCHOOL

SUPERVISORY COMMITTEE APPROVAL

of a dissertation submitted by

David W. McLawhorn

I have read this dissertation and have found it to be of satisfactory quality for a doctoral degree.

June 18, 1979
Date

Jan Paegle
Jan Paegle
Chairman, Supervisory Committee

I have read this dissertation and have found it to be of satisfactory quality for a doctoral degree.

June 18, 1979
Date

S. K. Kao
S. K. Kao
Member, Supervisory Committee

I have read this dissertation and have found it to be of satisfactory quality for a doctoral degree.

June 18, 1979
Date

Kuo-Nan Liou
Kuo-Nan Liou
Member, Supervisory Committee

I have read this dissertation and have found it to be of satisfactory quality for a doctoral degree.

June 18, 1979
Date

An-Ching Lin
An-Ching Lin
Member, Supervisory Committee

I have read this dissertation and have found it to be of satisfactory quality for a doctoral degree.

June 18, 1979
Date

Julia N. Paegle
Julia N. Paegle
Member, Supervisory Committee

THE UNIVERSITY OF UTAH GRADUATE SCHOOL

FINAL READING APPROVAL

To the Graduate Council of The University of Utah:

I have read the dissertation of David W. McLawhorn in its final form and have found that (1) its format, citations, and bibliographic style are consistent and acceptable; (2) its illustrative materials including figures, tables, and charts are in place; and (3) the final manuscript is satisfactory to the Supervisory Committee and is ready for submission to the Graduate School.

Nov. 16, 1979
Date

Jan Paegle
Jan Paegle
Member, Supervisory Committee

Approved for the Major Department

S. K. Kao
S. K. Kao
Chairman/Dean

Approved for the Graduate Council

James L. Clayton
James L. Clayton
Dean of The Graduate School

ABSTRACT

A two dimensional boundary layer model is developed for the study of diurnal cycles in boundary layer convergence over synoptic scale sloping terrain and thermally inhomogeneous surfaces. To properly resolve the terrain configuration, a local terrain following coordinate system is developed. The local coordinate system has characteristics which are superior to the terrain following coordinate systems commonly used. Truncation errors are significantly reduced in the local system so variations in the flow field due to physical forcing are easily discernable from those due to truncation error. Also, it appears that the local system can resolve coarser terrain configurations under numerically stable conditions.

The model exhibits a sensitivity to latitude. The phase of the maximum vertical velocities forecast by the model occurs six hours later at 22°N . vs. 38°N . The boundary layer model is apparently not very sensitive to radiative flux divergence calculations but did show a marked reaction to soil type. Both the amplitude and phase of the maximum vertical velocities are modified by changes in soil type.

TABLE OF CONTENTS

	<u>Page</u>
ABSTRACT	iv
LIST OF ILLUSTRATIONS	vii
ACKNOWLEDGMENTS	xviii
CHAPTER	
1. INTRODUCTION	1
2. EQUATIONS	7
2.1 System of Equations	7
2.2 Meteorological and Mathematical Symbols	8
2.3 Application	9
3. COORDINATE SYSTEM	10
3.1 Terrain Following Coordinate System	10
3.2 Linearized Pressure Gradient Force	11
3.3 Transformation of Vertical Coordinates	11
4. NUMERICAL ASPECTS	13
4.1 Horizontal and Vertical Grids	13
4.2 Differencing Schemes	13
4.3 Boundary and Interface Conditions	20
4.4 Moisture Constraint	21
5. EXCHANGE COEFFICIENT	22
5.1 KEYPS Formulation	22
5.2 Length Scale	24
5.3 Exchange Coefficient for Heat	24
6. RADIATION	26
6.1 Radiative Effects	26
6.2 Global Radiation	26
6.3 Flux Divergence	28
6.4 Solar Zenith Angle	32
6.5 Numerical Considerations	34

TABLE OF CONTENTS (Continued)

	<u>Page</u>
CHAPTER (Continued)	
7. SENSITIVITY TESTS	35
7.1 Coordinate System	35
7.2 Latitude	71
7.3 Radiation	94
7.4 Soil Type	118
8. CONCLUSIONS	144
Appendices	
A. DERVIATION OF TERRAIN FOLLOWING COORDINATE SYSTEM . . .	148
B. CALCULATING SPECIFIC HUMIDITY FROM DEW POINT TEMPERATURE	160
REFERENCES	162
VITA	166

LIST OF ILLUSTRATIONS

Tables

<u>Number</u>		<u>Page</u>
1.	Atmospheric and soil computational levels (meters) . .	16
2.	Mid-latitude summer climatology data used in radiational model	29
3.	Terrain slopes for grid points used in the coordinate system tests	40
4.	A coordinate system comparison of averages of $ U_{max} $ from selected grid points	69
5.	A coordinate system comparison of averages of $ W_{max} $ from selected grid points	70
6.	Comparisons of parameter values computed from radiational models of different depths and vertical grid spacings (McClatchey mid-latitude summer data was used for the calculations)	95
7.	Parameters for the three soils tested	119
8.	Effects of altering soil type on amplitude and phase of boundary layer vertical velocity fields	119
9.	Table of cosines	148
10.	Table of cosines	152

Figures

1.	Relationship between the horizontal grid and state boundaries. (1) California, (2) Nevada, (3) Utah, (4) Colorado, (5) Kansas, (6) Missouri, (7) Illinois, (8) Kentucky, (9) West Virginia, and (10) Virginia . .	14
2.	Relationship between the horizontal grid and certain geographical features. (1) Sierra Nevada Mts., (2) Great Basin, (3) San Juan Mts. (4) High Plains, (5) Ozark Plateau, (6) Mississippi River Valley, and (7) Appalachian Highlands and Mts.	15

<u>Number</u>		<u>Page</u>
3.	Vertical variation of the water vapor pathlength, U, and its relation to Z	30
4.	Comparison of observed and calculated cooling rates in a clear tropical atmosphere from (1) Roewe and Liou, (2) observations, (3) Rodgers and Walshaw, and (4) present study	33
5.	The temperature inversion portion of Condition A used to test the local and standard terrain following coordinate systems	37
6.	The temperature inversion portion of Condition B used to test the local and standard terrain following coordinate systems	38
7.	Selected grid points for a comparison test of the terrain following coordinate systems	39
8.	Variation of the maximum U component with time above grid point 5 for the local (.) and standard (x) terrain following coordinate systems. Left, Condi- tion A and right, Condition B	41
9.	Variation of the maximum U component with time above grid point 5 for the local (.) and standard (x) terrain following coordinate systems. Condition C . .	42
10.	Variation of the maximum U component with time above grid point 14 for the local (.) and standard (x) terrain following coordinate systems. Left, Condi- tion A and right, Condition B	43
11.	Variation of the maximum U component with time above grid point 14 for the local (.) and standard (x) terrain following coordinate systems. Condition C . .	44
12.	Variation of the maximum U component with time above grid point 15 for the local (.) and standard (x) terrain following coordinate systems. Left, Condi- tion A and right, Condition B	45
13.	Variation of the maximum U component with time above grid point 15 for the local (.) and standard (x) terrain following coordinate systems. Condition C . .	46
14.	Variation of the maximum U component with time above grid point 18 for the local (.) and standard (x) terrain following coordinate systems. Left, Condi- tion A and right, Condition B	47

<u>Number</u>		<u>Page</u>
15.	Variation of the maximum U component with time above grid point 18 for the local (.) and standard (x) terrain following coordinate systems. Condition C . .	48
16.	Variation of the maximum U component with time above grid point 25 for the local (.) and standard (x) terrain following coordinate systems. Left, Condition A and right, Condition B	49
17.	Variation of the maximum U component with time above grid point 25 for the local (.) and standard (x) terrain following coordinate systems. Condition C . .	50
18.	Variation of the maximum U component with time above grid point 27 for the local (.) and standard (x) terrain following coordinate systems. Left, Condition A and right, Condition B	51
19.	Variation of the maximum U component with time above grid point 27 for the local (.) and standard (x) terrain following coordinate systems. Condition C . .	52
20.	Variation of the vertical velocity at the top of the model with time above grid point 5 for the local terrain following coordinate system (.), left, and for the standard terrain following system (x), right. Condition A	53
21.	Variation of the vertical velocity at the top of the model with time above grid point 5 for the local terrain following coordinate system (.), left, and for the standard terrain following coordinate system (x), right. Condition B	54
22.	Variation of the vertical velocity at the top of the model with time above grid point 5 for the local terrain following coordinate system (.), left, and or the standard terrain following coordinate system (x), right. Condition C	55
23.	Variation of the vertical velocity at the top of the model with time above grid point 14 for the local terrain following coordinate system (.), left, and for the standard terrain following coordinate system (x), right. Condition A	56
24.	Variation of the vertical velocity at the top of the model with time above grid point 14 for the local terrain following coordinate system (.), left, and for the standard terrain following coordinate system (x), right. Condition B	57

<u>Number</u>		<u>Page</u>
25.	Variation of the standard vertical velocity at the top of the model with time above grid point 14 for the local terrain following coordinate system (.), left, and for the standard terrain following coordinate system (x), right. Condition C	58
26.	Variation of the vertical velocity at the top of the model with time above grid point 15 for the local terrain following coordinate system (.), left, and for the standard terrain following coordinate system (x), right. Condition A	59
27.	Variation of the vertical velocity at the top of the model with time above grid point 15 for the local terrain following coordinate system (.), left and for the standard terrain following coordinate system (x), right. Condition B	60
28.	Variation of the vertical velocity at the top of the model with time above grid point 15 for the local terrain following coordinate system (.), left, and for the standard terrain following coordinate system (x), right. Condition C	61
29.	Variation of the vertical velocity at the top of the model with time above grid point 18 for the local (.) and standard (x) terrain following coordinate system. Condition A, left, and Condition B, right	62
30.	Variation of the vertical velocity at the top of the model with time above grid point 18 for the local (.) and standard (x) terrain following coordinate system. Condition C	63
31.	Variation of the vertical velocity at the top of the model with time above grid point 25 for the local (.) and standard (x) terrain following coordinate systems. Condition A, left, and conditions B, right	64
32.	Variation of the vertical velocity at the top of the model with time above grid point 25 for the local terrain following coordinate system (.), left, and for the standard terrain following coordinate system (x) right. Condition C	65

<u>Number</u>		<u>Page</u>
33.	Variation of the vertical velocity at the top of the model with time above grid point 27 for the local terrain following coordinate system (.), left, and the standard terrain following coordinate system (x), right. Condition A	66
34.	Variation of the vertical velocity at the top of the model with time above grid point 27 for the local (.) and standard (x) terrain following coordinate systems. Condition B	67
35.	Variation of the vertical velocity at the top of the model with time above grid point 27 for the local terrain following coordinate system (.), left, and for the standard terrain following coordinate system (x), right. Condition C	68
36.	Vertical velocity at the top of the model after eight hours with the local terrain following coordinate system, Condition A. The plotting convention is as follows: ↑ represents rising motion, ↓ represents sinking motion, ⚡ = 1mm/sec, ⚡ = 5mm/sec, ⚡ = 10mm/sec, and ⚡ = 85mm/sec (too large to plot)	72
37.	Vertical velocity at the top of the model after eight hours with the standard terrain following coordinate system, Condition A. See Figure 36 for plotting convention	73
38.	Vertical velocity at the top of the model after 18 hours with the local terrain following coordinate system, Condition A. See Figure 36 for plotting convention	74
39.	Vertical velocity at the top of the model after 18 hours with the standard terrain following coordinate system, Condition A. See Figure 36 for plotting convention	75
40.	Vertical velocity at the top of the model after eight hours with the local terrain following coordinate system, Condition B. See Figure 36 for plotting convention	76
41.	Vertical velocity at the top of the model after eight hours with the standard terrain following coordinate system, Condition B. See Figure 36 for plotting convention	77

<u>Number</u>		<u>Page</u>
42.	Vertical velocity at the top of the model after 18 hours with the local terrain following coordinate system, Condition B. See Figure 36 for plotting convention	78
43.	Vertical velocity at the top of the model after 18 hours with the standard terrain following coordinate system, Condition B. See Figure 36 for plotting convention	79
44.	Vertical velocity at the top of the model after eight hours with the local terrain following coordinate system, Condition C. See Figure 36 for plotting convention	80
45.	Vertical velocity at the top of the model after eight hours with the standard terrain following coordinate system, Condition C. See Figure 36 for plotting convention	81
46.	Vertical velocity at the top of the model after 18 hours with the local terrain following coordinate system, Condition C. See Figure 36 for plotting convention	82
47.	Vertical velocity at the top of the model after 18 hours with the standard terrain following coordinate system, Condition C. See Figure 36 for plotting convention	83
48.	Amplitude and phase of the maximum vertical velocity forecast for 38° latitude. The plotting convention is as follows: A vector directed from the north denotes a midnight maximum, while one directed from the east denotes a 6 A.M.(local time) maximum, etc. \uparrow = 1mm/sec and \uparrow = 5mm/sec	86
49.	Amplitude and phase of the maximum vertical velocity forecast for 30° latitude. See Figure 48 for plotting convention	87
50.	Amplitude and phase of the maximum vertical velocity forecast for 22° latitude. See Figure 48 for plotting convention	88
51.	Amplitude and phase of the maximum vertical velocity forecast at grid point 16 for 22°, 30°, and 38° latitude. The position of the latitude around the dial denotes the time of the max W for that latitude while the distance from the center of the dial denotes the amplitude in mm/sec	89

<u>Number</u>		<u>Page</u>
52.	Amplitude and phase of the maximum vertical velocity forecast at grid point 18 for 22°, 30° and 38° latitude. See Figure 51 for plotting convention . . .	90
53.	Amplitude and phase of the maximum vertical velocity forecast at grid point 20 for 22°, 30°, and 38° latitude. See Figure 51 for plotting convention . . .	91
54.	Amplitude and phase of the maximum vertical velocity forecast at grid point 22 for 22°, 30°, and 38° latitude. See Figure 51 for plotting convention . . .	92
55.	Amplitude and phase of the maximum vertical velocity forecast at grid point 25 for 22°, 30°, and 38° latitude. See Figure 51 for plotting convention . . .	93
56.	Amplitude and phase of the maximum vertical velocity with radiation fields updated every two hours. See Figure 48 for plotting convention	97
57.	Amplitude and phase of the maximum vertical velocity with radiation fields updated every three hours. See Figure 48 for plotting convention	98
58.	Amplitude and phase of the maximum vertical velocity with radiation fields updated every four hours. See Figure 48 for plotting convention	99
59.	Amplitude and phase of the maximum vertical velocity with infrared radiation a constant. See Figure 48 for plotting convention	100
60.	Amplitude and phase of the maximum subsidence with radiational fields updated every two hours. See Figure 48 for plotting convention	101
61.	Amplitude and phase of the maximum subsidence with radiational fields updated every three hours. See Figure 48 for plotting convention	102
62.	Amplitude and phase of the maximum subsidence with radiational fields updated every four hours. See Figure 48 for plotting convention	103
63.	Amplitude and phase of the maximum subsidence with infrared radiation a constant. See Figure 48 for plotting convention	104
64.	Grid points selected for a study of the radiational effects on the thermal structure	105

<u>Number</u>		<u>Page</u>
65.	Diurnal temperature curves from grid point 15. Height is .01m. + = radiation update at two hour intervals, 0 = radiation update at three hour intervals, and Δ = radiation update at four hour intervals	106
66.	Diurnal temperature curves from grid point 15. Height is 49m. See Figure 65 for plotting convention	107
67.	Diurnal temperature curves from grid point 15. Height is 133m. See Figure 65 for plotting convention	108
68.	Diurnal temperature curves from grid point 15. Height is 480m. See Figure 65 for plotting convention	109
69.	Diurnal temperature curves from grid point 18. Height is .01m. See Figure 65 for plotting convention	110
70.	Diurnal temperature curves from grid point 18. Height is 49m. See Figure 65 for plotting convention	111
71.	Diurnal temperature curves from grid point 18. Height is 133m. See Figure 65 for plotting convention	112
72.	Diurnal temperature curves from grid point 18. Height is 480m. See Figure 65 for plotting convention	113
73.	Diurnal temperature curves from grid point 22. Height is .01m. See Figure 65 for plotting convention	114
74.	Diurnal temperature curves from grid point 22. Height is 49m. See Figure 65 for plotting convention	115
75.	Diurnal temperature curves from grid point 22. Height is 133m. See Figure 65 for plotting convention	116
76.	Diurnal temperature curves from grid point 22. Height is 480m. See Figure 65 for plotting convention	117

<u>Number</u>		<u>Page</u>
77.	Amplitude and phase of maximum vertical velocity with dry sand soil (conductive capacity = 108). See Figure 48 for plotting convention	120
78.	Amplitude and phase of maximum vertical velocity with clayland pasture (conductive capacity = 194). See Figure 48 for plotting convention	121
79.	Amplitude and phase of maximum vertical velocity with sandy clay (conductive capacity = 357). See Figure 48 for plotting convention	122
80.	Amplitude and phase of maximum vertical velocity for sandy clay (X), clayland pasture (P), and dry sand (S) for grid point 4. See Figure 51 for plotting convention	123
81.	Amplitude and phase of maximum vertical velocity for sandy clay (X), clayland pasture (P), and dry sand (S) for grid point 8. See Figure 51 for plotting convention	124
82.	Amplitude and phase of maximum vertical velocity for sandy clay (X), clayland pasture (P), and dry sand (S) for grid point 15. See Figure 51 for plotting convention	125
83.	Amplitude and phase of maximum vertical velocity for sandy clay (X), clayland pasture (P), and dry sand (S) for grid point 18. See Figure 51 for plotting convention	126
84.	Amplitude and phase of maximum vertical velocity for sandy clay (X), clayland pasture (P), and dry sand (S) for grid point 20. See Figure 51 for plotting convention	127
85.	Amplitude and phase of maximum vertical velocity for sandy clay (X), clayland pasture (P), and dry sand (S) for grid point 22. See Figure 51 for plotting convention	128
86.	Amplitude and phase of maximum vertical velocity for sandy clay (X), clayland pasture (P), and dry sand (S) for grid point 24. See Figure 51 for plotting convention	129
87.	Amplitude and phase of maximum vertical velocity for sandy clay (X), clayland pasture (P), and dry sand (S) for grid point 28. See Figure 51 for plotting convention	130

<u>Number</u>		<u>Page</u>
88.	Diurnal temperature curves for grid point 15. Height is Z_0 . See Figure 65 for plotting convention	132
89.	Diurnal temperature curves for grid point 15. Height is 49m. See Figure 65 for plotting convention	133
90.	Diurnal temperature curves for grid point 15. Height is 133m. See Figure 65 for plotting convention	134
91.	Diurnal temperature curves for grid point 15. Height is 480m. See Figure 65 for plotting convention	135
92.	Diurnal temperature curves for grid point 18. Height is Z_0 . See Figure 65 for plotting convention	136
93.	Diurnal temperature curves for grid point 18. Height is 49m. See Figure 65 for plotting convention	137
94.	Diurnal temperature curves for grid point 18. Height is 133m. See Figure 65 for plotting convention	138
95.	Diurnal temperature curves for grid point 18. Height is 480m. See Figure 65 for plotting convention	139
96.	Diurnal temperature curves for grid point 22. Height is Z_0 . See Figure 65 for plotting convention	140
97.	Diurnal temperature curves for grid point 22. Height is 49m. See Figure 65 for plotting convention	141
98.	Diurnal temperature curves for grid point 22. Height is 133m. See Figure 65 for plotting convention	142
99.	Diurnal temperature curves for grid point 22. Height is 480m. See Figure 65 for plotting convention	143
100.	Coordinate systems O-XYZ- $\alpha\beta\gamma$ (top) and O- $X_1Y_1Z_1$ - $\alpha_1\beta_1\gamma_1$ (bottom)	149

<u>Number</u>		<u>Page</u>
101.	Closed broken line which goes from O to P using the system $O-XYZ$ and returns from P to O by way of system $O-X_1Y_1Z_1$	151
102.	Orthogonal system $O-X_1Y_1Z_1-\alpha\beta\gamma$ (top) and terrain following system $O-X_1Y_1Z_1-\alpha_1\beta_1\gamma_1$ (bottom)	153
103.	Graphical representation of angles $\epsilon, \phi, \lambda, \mu,$ $\epsilon,$ and γ	154

ACKNOWLEDGEMENTS

I wish to express my sincere appreciation to Dr. Jan Paegle for his guidance, encouragement, and support during the course of my research. I consider it an honor and a privilege to have known and worked for this individual. Through the many months of my research he gave unselfishly and willingly many hours of his personal time to inspire and encourage me toward the successful completion of my dissertation. For this I am indeed grateful.

I would like to thank the members of my supervisory committee for their helpful comments and suggestions and for serving on my committee. A special thank you also goes to Mrs. Deanna Plumhof, my typist.

To my family, Rena and Tamie, I can say that we finally made it. Truly, this was a family effort. Without their emotional support and understanding, none of this would have been possible. My wife, Rena, also lended technical support by drafting many of the figures in this dissertation. Thanks also to my fellow Air Force officers, Major Ed Tomlinson, Captain Fred Lewis, and Captain Grant Aufderhaar, for helping me in ways that only friends can.

I would like to extend a special thank you to the United States Air Force for the privilege of returning to school and pursuing my doctorate degree. The research was supported by the National Science Foundation under NSF Grant ATM 77-26094.

CHAPTER 1

INTRODUCTION

The diurnal variability of precipitation over the United States was first documented by Kincer (1916) who used summer rainfall data from 175 stations. He noted that at many stations in the central and north central United States more rain fell at night than during the day. Wallace (1975) conducted a comprehensive study of the amplitude and phase of the diurnal cycle of precipitation over the United States. He also noted that over the central part of the United States in summer thunderstorms have a maximum frequency of occurrence around midnight with most other forms of precipitation occurring later in the night. This is interesting since, in general, thunderstorms not associated with frontal activity have a tendency for maximum occurrence in the afternoon hours when lapse rates may be steep due to surface heating.

Hewson (1937) proposed that radiative cooling from cloud tops could explain the nocturnal thunderstorm maximum over the central United States in summer. Means (1944) attributed the nocturnal maximum to low level warm advection. Although both processes may act to destabilize the atmosphere at night, it has not been shown that these processes are strong enough to counter the stabilizing influence at night of sensible heat flux from the ground.

It has been recognized that over much of the central portion of the United States during summer the atmosphere is convectively unstable 24 hours a day. Bleeker and André (1951) suggested that under unstable

conditions even a small diurnal cycle in the boundary layer convergence and the accompanying rising motion at the top of the boundary layer may be sufficient to control the timing of convection.

Many investigators have related the diurnal cycle in boundary layer convergence in the central United States to the occurrence of a low level jet in the southern Great Plains. Bonner (1968) determined the maximum frequency of occurrence of the southerly low level jet to be in western Oklahoma with the axis of maximum frequency oriented northeastward into northeastern Kansas and northwestern Iowa. A statistical study by Pitchford and London (1962) revealed a correspondence between the mean axis of the low level jet on 127 summer days and the line of maximum nocturnal thunderstorm occurrence.

Bonner et al (1968) used kinematically computed vertical velocities for 10 southerly low level jets and found ascending air of a synoptic scale in the downstream portion of the jets. Bonner concluded that the downstream portion of the jet should be a preferred region for the formation of nocturnal thunderstorms. Means (1952), Curtis and Panofsky (1958), and others have presented arguments linking the low level jet and its associated vertical velocity field with the occurrence of convective activity.

Many theories have been advanced as to the cause of the low level jet in the Great Plains. Blackadar (1957) attempted to show that the low level jet arose from an inertial oscillation of the ageostrophic wind vector as the air near the top of the friction layer was decoupled from the air below by the formation of a nocturnal inversion. Wexler (1961) proposed that the jet formed as a result of the northward deflection by the Rocky Mountains of a shallow layer of air flowing

westward across the Gulf of Mexico. Bonner (1968) found that the diurnal oscillation of the wind in the boundary layer was important in producing a southerly low level jet. He also found that the synoptic conditions which favored large scale jet formation were those which contribute to a strong pressure gradient across the Great Plains with a smooth, uninterrupted flow of air northward from the Gulf of Mexico. These synoptic conditions are common over the southern Great Plains during summer.

Several models of the boundary layer have been developed in order to gain further understanding of the diurnal oscillation of the boundary layer wind and the related low level jet. The effect of varying eddy viscosity in a constant geostrophic field was modeled by Buajitti and Blackadar (1957) and Ooyama (1957). Holton (1967) developed a model which included the effect of a diurnal temperature cycle over sloping terrain with constant eddy viscosity. Bonner and Paegle (1970) developed a model which included both effects. None of these models, however, were capable of predicting supergeostrophic flows as strong as those observed by Bonner et al (1968).

All of the models mentioned above assumed horizontally uniform flow which is a valid assumption for flows where the Rossby number is much less than one. Bonner et al (1968) found that for the 10 southerly low level jets examined, the average horizontal wind speed gradient approached $f/2$ to the right of the jet core ($R_0=1/2$) and f to the left of the jet core ($R_0=1$). Therefore it is apparent that a numerical model of the boundary layer should allow horizontally non-uniform flow in order to better predict the strong supergeostrophic flows that are observed.

In 1972 Paegle developed a numerical model of the boundary layer which incorporated the effects of horizontally non-uniform flow and diurnal oscillations of the eddy stresses and geostrophic wind field. Paegle and Rasch (1973) conducted exhaustive tests of this model for idealized flows. Their solutions above the terrain slopes of the Great Plains differed significantly from the steady, linear, Ekman solutions. The model was capable of producing strong low level southerly jets in the western portions of moderate anticyclones over very slight terrain slopes. The areas just downstream of the jets were characterized by boundary layer convergence and rising motion. It appeared that the greatest single contributing factor to the nocturnal jet and boundary layer convergence pattern was the Great Plains topography with the eddy stress oscillation of lesser importance.

Paegle and McLawhorn (1973) used the model to investigate the relationship between nocturnal thunderstorm activity and boundary layer convergence. An analysis was made of 11 Great Plains nocturnal thunderstorm occurrences that had no obvious synoptic scale support. The time and space phasing of the vertically integrated boundary layer convergence forecast by the model was compared with the time and space phasing of the 11 thunderstorm occurrences. The results of the investigation were very promising and seemed to corroborate the hypothesis that nocturnal thunderstorms might often have their birth in boundary layer processes. There were several weaknesses in the model, however. The formulation of eddy stresses was rather arbitrary, second horizontal derivatives of the flow field were neglected, and there was an implicit assumption of neutral stratification.

Paegle (1978) relaxed certain assumptions inherent in the model

used by Paegle and Rasch (1973) and Paegle and McLawhorn (1973) by permitting the model pressure field to be modified by the convergence field. The resulting system contained gravity wave modes which were excluded in the earlier model. He used the new gravity inertia wave model to examine slope induced diurnal gravity wave convergence fields over the United States. He found that the magnitude of these fields may be sufficiently large to completely compensate low level divergence fields induced by free tropospheric effects. Sensitivity tests conducted with this model indicated that the topographically induced boundary layer convergence fields over the United States were sensitive to dissipation, to boundary layer heating and its vertical extent, as well as to the ambient circulation.

It has become apparent that in order to further an understanding of the physical processes and simulation requirements of those boundary layer motions that are determined by the diurnal cycle and which play an important role in convective weather a particular type of boundary layer model is needed. The preliminary studies of Paegle and Rasch (1973), Paegle and McLawhorn (1973), and Paegle (1978) have suggested that the diurnal cycle of boundary layer convergence over the central United States is highly dependent upon:

- (1) The previous history of about one to two days of the boundary layer flow and low level forcings.
- (2) The ambient large-scale circulation.
- (3) The evolution and vertical structure of the boundary layer thermal wave.

General circulation models have only a few, if any, explicit forecast levels in the boundary layer; therefore, these large scale models

generally lack the vertical resolution and physics to account for items (1) and (3). Many new mesoscale models have recently been developed, (e.g. Anthes et al. (1977), Pielke and Mahrer (1977), Perkey (1977) and others). These models have more explicit resolution of the boundary layer. On a smaller scale, Deardorff (1974), Orlanski et al. (1974), Welch et al. (1977), Yamada and Mellor (1974) and others have performed detailed boundary layer forecasts in models with 30 or more computational levels within the boundary layer, but ignore, or minimize troposphere interaction. These mesoscale models can usually be run out to only one day or less because of expense and boundary contamination. Therefore it is not likely that item (1) can be satisfied.

It is likely that the above mentioned models do simulate boundary layer convergence fields adequately for the particular phenomena that have been studied. However, the adequacy of their approaches remains to be demonstrated for the diurnally oscillating case over synoptic scale sloping terrain where boundary layer convergence fields may often dominate large scale processes. This is especially true for the nocturnal convection over the central United States that is characterized by sharp, strongly supergeostrophic nocturnal jets in the lowest kilometer.

The intent of the present research has been to develop a boundary layer model with sufficient resolution and physics to define the interacting thermal and momentum boundary layers on diurnal time scales above synoptic scale sloping terrain and thermally inhomogeneous surfaces.

CHAPTER 2

EQUATIONS

2.1 System of Equations

The formulation of the governing system of equations is based upon the following approximations: (1) Boussinesq, (2) hydrostatic, and (3) two-dimensional (no variation of the meteorological parameters or terrain in the north-south direction). The resulting boundary layer model equations in a terrain following coordinate system are:

2.1.1 The east-west momentum equation

$$\frac{\partial u}{\partial t} + u \frac{\partial u}{\partial x} + w \frac{\partial u}{\partial z} - f v = - \frac{1}{\rho} \frac{\partial p'}{\partial x} - g \frac{\rho'}{\rho} \sin \theta + \frac{\partial}{\partial z} (K_M \frac{\partial u}{\partial z}) \quad (1)$$

2.1.2 The north-south momentum equation

$$\frac{\partial v}{\partial t} + u \frac{\partial v}{\partial x} + w \frac{\partial v}{\partial z} + f u = \frac{\partial}{\partial z} (K_M \frac{\partial v}{\partial z}) \quad (2)$$

2.1.3 The moisture equation

$$\frac{\partial q}{\partial t} + u \frac{\partial q}{\partial x} + w \frac{\partial q}{\partial z} = \frac{\partial}{\partial z} (K_\theta \frac{\partial q}{\partial z}) \quad (3)$$

2.1.4 The thermodynamic equation

$$\frac{\partial \theta}{\partial t} + u \frac{\partial \theta}{\partial x} + w \frac{\partial \theta}{\partial z} = Q + \frac{\partial}{\partial z} (K_\theta \frac{\partial \theta}{\partial z}) \quad (4)$$

2.1.5 The soil heat conduction equation

$$\frac{\partial T_s}{\partial t} = \frac{\partial}{\partial z} (K_s \frac{\partial T_s}{\partial z}) \quad (5)$$

2.1.6 The hydrostatic equation

$$\frac{\partial P'}{\partial z} = -\rho'g = -\left(\frac{P' - \bar{\rho}RT'_v}{\bar{T}R}\right)g \quad (6)$$

2.1.7 The continuity equation

$$\frac{\partial w}{\partial z} = -\frac{\partial u}{\partial x} \quad (7)$$

2.1.8 The equation of state

$$P = \rho RT_v \quad \bar{P} = \bar{\rho} \bar{R} \bar{T} \quad P' = \rho' \bar{R} \bar{T} + \bar{\rho} R T'_v \quad (8)$$

2.1.9 The potential temperature equation

$$\theta = T \left(\frac{P_0}{P}\right)^{R/C_p} \quad \theta' = T' \left(\frac{P_0}{P}\right)^{R/C_p} \quad (9)$$

2.1.10 The virtual temperature equation

$$T_v = T(1+.61q) \quad T'_v = T + .61q \bar{T} - \bar{T} \quad (10)$$

2.2 Meteorological and Mathematical Symbols

The meteorological and mathematical symbols are defined as follows:

2.2.1 ($\bar{\quad}$) represents a standard atmospheric value.

2.2.2 (\quad') represents a deviation from the standard atmospheric value.

2.2.3 u is the west-east velocity component of the wind which is parallel to the west-east slope of the terrain.

2.2.4 v is the south-north velocity component of the wind which is parallel to the south-north slope of the terrain.

2.2.5 w is the vertical velocity component of the wind which is perpendicular to the X-Y plane.

2.2.6 θ is the west to east slope of the terrain.

2.2.7 K_M , K_θ , K_S are the momentum, thermal and soil exchange coefficients.

2.2.8 Q represents heating.

2.2.9 P and ρ are atmospheric pressure and density.

2.2.10 T and T_S are atmospheric and soil temperatures.

2.2.11 T_V and θ are virtual and potential temperatures.

2.2.12 R and C_p are gas constants for dry air.

2.2.13 q represents specific humidity.

2.2.14 f is the Coriolis parameter.

2.2.15 g is gravitational acceleration.

2.3 Application

The equations may be applied in vertical-horizontal coordinates or in a non-orthogonal sigma coordinate system such as Gerrity (1967). They also have an interesting interpretation in an orthogonal terrain following coordinate system (Appendix A).

CHAPTER 3

COORDINATE SYSTEM

3.1 Terrain Following Coordinate System

The important relationship between terrain configuration and boundary layer convergence was established in Chapter 1. It is apparent that one of the main requirements for proper simulation of boundary layer convergence is a terrain following coordinate system that can properly relate the terrain configuration to the governing system of equations. To satisfy this requirement a new terrain following coordinate system was established. A complete derivation of this system is contained in Appendix A.

The u component of the momentum equation written in the local terrain following coordinates is listed as an example.

$$\begin{aligned} \frac{\partial u}{\partial t} + \left[\frac{\cos^2 \theta}{1 - \sin^2 \theta \sin^2 \phi} \right] u \frac{\partial u}{\partial x} + \left[\frac{1}{\tan^2 \theta + \sec^2 \phi} \right] w \frac{\partial u}{\partial z} - \frac{\cos \phi}{\cos \theta} f_v = \\ - \left[\frac{1}{1 - \sin^2 \theta \sin^2 \phi} \right] \frac{1}{\rho} \frac{\partial p'}{\partial x} - \left[\frac{\sin \theta}{\cos^2 \theta \tan^2 \phi + 1} \right] \frac{\rho'}{\rho} g + \frac{1}{\cos \theta} \frac{\partial}{\partial z} \left(K_M \frac{\partial u}{\partial z} \right) \end{aligned} \quad (11)$$

where ϕ is the south-north slope of the terrain. The terrain slopes encountered during this research are sufficiently small (the maximum slope is about $.4853 \times 10^{-2}$ radians) to simplify the coordinate system. The u component of the momentum equation written in the simplified coordinates is :

$$\frac{\partial u}{\partial t} + u \frac{\partial u}{\partial x} + w \frac{\partial u}{\partial z} - fv = - \frac{1}{\rho} \frac{\partial P'}{\partial x} - \frac{\rho'}{\rho} g \sin \theta + \frac{\partial}{\partial z} (K_M \frac{\partial u}{\partial z}) \quad (12)$$

The governing equations were integrated out to 28 hours using two boundary layer models which are identical except for the coordinate systems. One model used the local terrain following coordinates while the other model used the simplified version. There was no perceptible difference in the forecast fields at any time during the 28 hour forecast period. Based upon the results of this test, the simplified terrain following coordinate system was adopted for the boundary layer model. The governing equations of Chapter 2 were written in terms of the simplified coordinate system.

3.2 Linearized Pressure Gradient Force

The pressure gradient force term in the u component of the momentum equation is linearized to separate out the hydrostatic vertical portion. Therefore, the horizontal pressure gradient force is no longer formulated as a small balance of large terms over sloping terrain. This avoids major numerical truncation errors in the vicinity of mountains that are common for most types of terrain following coordinates such as the frequently used sigma coordinates.

3.3 Transformation of Vertical Coordinates

Another important requirement for the proper modeling of boundary layer convergence is the correct simulation of the evolution and vertical structure of the low level thermal field. This simulation requires a very fine vertical grid spacing in the air and soil near the air-soil interface. To provide this vertical grid spacing while retaining some

degree of economy the following logarithmic height transformation is used for the atmosphere.

$$Z = Z_0 e^{\xi/L} \quad \xi = L \ln(Z/Z_0) \quad (13)$$

where Z = old height coordinate

ξ = new height coordinate

Z_0 = roughness height

L = 1 meter

In the transformed coordinate (ξ), logarithmic variations in Z become linear in ξ , thereby substantially increasing the accuracy of the numerical model in the surface layer. The u component of the momentum equation written in the transformed height coordinate becomes:

$$\begin{aligned} \frac{\partial u}{\partial t} + u \frac{\partial u}{\partial x} + \left(\frac{L}{Z}\right) w \frac{\partial u}{\partial \xi} - fv = - \frac{1}{\rho} \frac{\partial P'}{\partial x} - \frac{\rho'}{\rho} g \sin \theta \\ + \left[\left(\frac{L}{Z}\right)^2 \frac{\partial K_M}{\partial \xi} - \left(\frac{L}{Z^2}\right) K_M\right] \frac{\partial u}{\partial \xi} + K_M \left(\frac{L}{Z}\right)^2 \frac{\partial^2 u}{\partial \xi^2} \end{aligned} \quad (14)$$

Analogous forms hold for equations (2) - (4).

A quadratic height transformation was used for the soil.

$$Z = -L_s \xi_s^2 + Z_0 \quad \xi_s = \left(\frac{-Z+Z_0}{L_s}\right)^{1/2} \quad (15)$$

where Z = old depth coordinate

ξ_s = new depth coordinate

L_s = .005 meters

The soil heat conduction equation written in the transformed height coordinate becomes

$$\frac{\partial T_s}{\partial t} = \frac{-K_s}{4L_s^2} \left(\frac{L_s}{-Z+Z_0}\right)^{3/2} \frac{\partial T_s}{\partial \xi_s} + \frac{K_s}{4L_s^2} \left(\frac{L_s}{-Z+Z_0}\right) \frac{\partial^2 T_s}{\partial \xi_s^2} \quad (16)$$

CHAPTER 4

NUMERICAL ASPECTS

4.1 Horizontal and Vertical Grids

The horizontal grid for the boundary layer model consists of 31 grid points which extend across the United States from 130°W to 70°W at 38°N latitude. The relationship between the grid, state boundaries and certain geographical features is depicted in Figures 1 and 2.

Horizontal grid spacing is 2° longitude or 175,246 meters. Actual terrain data from the Air Force Aeronautical Chart and Information Center (ACIC) was used. This data was properly smoothed by multiple applications of a single nine-point operator as described by Shuman (1957) to insure that all variations in the smoothed terrain could be resolved on the 2° horizontal grid. Terrain slopes were computed by centered space differencing.

The vertical grid consists of the roughness height at .01 meters plus 14 computational levels in the soil. The atmosphere comprises 20 computational levels in the transformed grid plus 15 equally spaced levels up to a height of 1520 meters. Computational levels for the boundary layer model are depicted in Table 1.

4.2 Differencing Schemes

Implicit differencing with respect to the diffusive terms provides stable solutions with time steps of 300 seconds. $\alpha=.75$, $\beta=.25$ were used in a modified form of the Crank-Nicholson scheme as discussed in

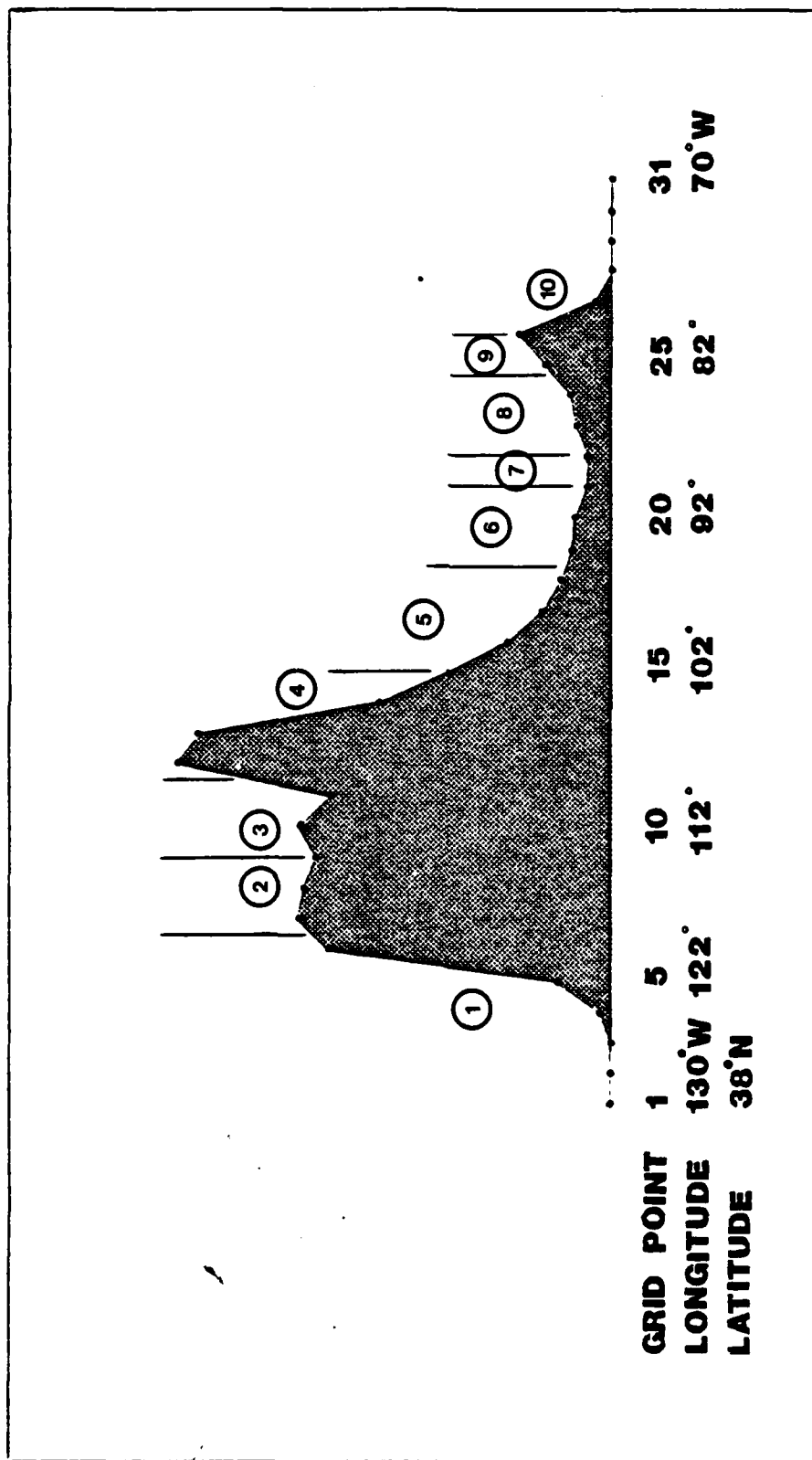


Figure 1. Relationship between the horizontal grid and state boundaries.
 (1) California, (2) Nevada, (3) Utah, (4) Colorado, (5) Kansas,
 (6) Missouri, (7) Illinois, (8) Kentucky, (9) West Virginia,
 and (10) Virginia.

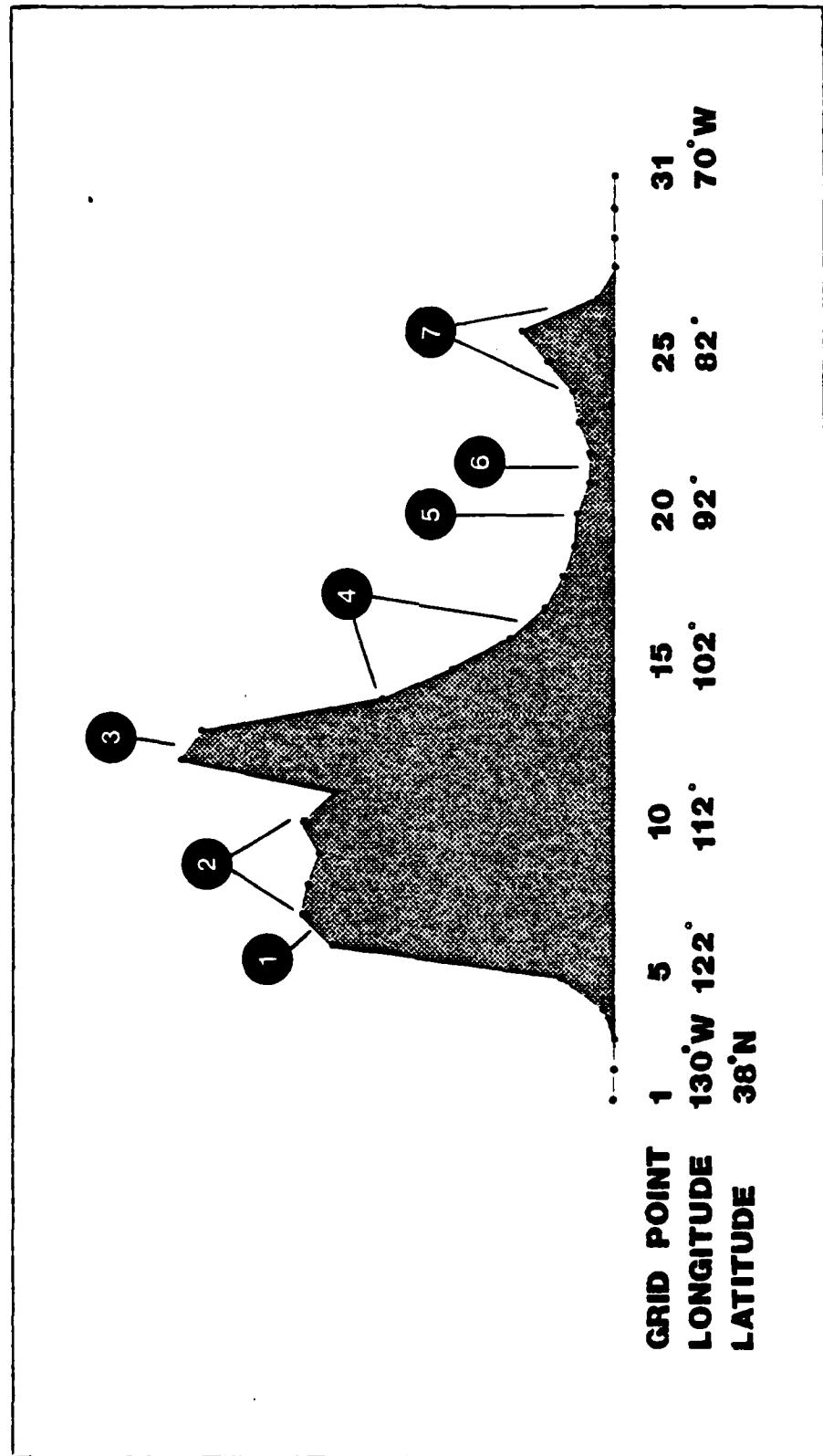


Figure 2. Relationship between the horizontal grid and certain geographical features. (1) Sierra Nevada Mts., (2) Great Basin, (3) San Juan Mts., (4) High Plains, (5) Ozark Plateau, (6) Mississippi River Valley, and (7) Appalachian Highlands and Mts.

Table 1. Atmospheric and Soil Computational Levels (Meters)

Soil	Atmosphere
Quadratic Transformation	Logarithmic Transformation
.010 - Roughness Height - .0100	
.005	.0165
-.010	.0272
-.035	.0448
-.070	.0739
-.110	.1218
-.170	.2009
-.235	.3312
-.310	.5460
-.390	.9002
-.490	1.4841
-.595	2.4469
-.710	4.0343
-.835	6.6514
-.970	10.9663
	18.0804
	29.8096
	49.1477
	81.0308
	133.5970
	220.2650
	Constant $\Delta Z = 86.668$
	306.932
	393.599
	480.267
	566.934
	653.602
	740.269
	826.936
	913.604
	1000.270
	1086.938
	1173.606
	1260.274
	1346.942
	1433.610
	1520.278

Paegle et al. (1976). The strong physical forcing and damping in the model allows use of centered second order space differencing approximations for the advective terms without incurring non-linear instabilities. The finite difference form of the governing system of equations written in the simplified terrain following coordinates and transformed height coordinates follows with $A=1.5$ and $B=.5$:

4.2.1 The east-west momentum equation

$$\begin{aligned}
 & -\left(\frac{u_{i,K}^{n+1} - u_{i,K}^{n-1}}{2\Delta t}\right) + C \frac{A}{2} \left(\frac{u_{i,K+1}^{n+1} - u_{i,K-1}^{n+1}}{2\Delta \xi}\right) + D \frac{A}{2} \left(\frac{u_{i,K+1}^{n+1} + u_{i,K-1}^{n+1} - 2u_{i,K}^{n+1}}{\Delta \xi^2}\right) = \\
 & -C \frac{B}{2} \left(\frac{u_{i,K+1}^{n-1} - u_{i,K-1}^{n-1}}{2\Delta \xi}\right) - D \frac{B}{2} \left(\frac{u_{i,K+1}^{n-1} + u_{i,K-1}^{n-1} - 2u_{i,K}^{n-1}}{\Delta \xi^2}\right) \\
 & + u_{i,K}^n \left(\frac{u_{i+1,K}^n - u_{i-1,K}^n}{2\Delta x}\right) + w_{i,K}^n \left(\frac{L}{Z_K}\right) \left(\frac{u_{i,K+1}^n - u_{i,K-1}^n}{2\Delta \xi}\right) - f v_{i,K}^n \\
 & + \frac{1}{\rho_{i,K}^n} \left(\frac{p_{i+1,K}^n - p_{i-1,K}^n}{2\Delta x}\right) + \frac{\rho_{i,K}^n}{\rho_{i,K}^n} g \sin \theta_i \quad (17)
 \end{aligned}$$

4.2.2 The north-south momentum equation

$$\begin{aligned}
 & -\left(\frac{v_{i,K}^{n+1} - v_{i,K}^{n-1}}{2\Delta t}\right) + C \frac{A}{2} \left(\frac{v_{i,K+1}^{n+1} - v_{i,K-1}^{n+1}}{2\Delta \xi}\right) + D \frac{A}{2} \left(\frac{v_{i,K+1}^{n+1} + v_{i,K-1}^{n+1} - 2v_{i,K}^{n+1}}{\Delta \xi^2}\right) = \\
 & -C \frac{B}{2} \left(\frac{v_{i,K+1}^{n-1} - v_{i,K-1}^{n-1}}{2\Delta \xi}\right) - D \frac{B}{2} \left(\frac{v_{i,K+1}^{n-1} + v_{i,K-1}^{n-1} - 2v_{i,K}^{n-1}}{\Delta \xi^2}\right) \\
 & + u_{i,K}^n \left(\frac{v_{i+1,K}^n - v_{i-1,K}^n}{2\Delta x}\right) + w_{i,K}^n \left(\frac{L}{Z_K}\right) \left(\frac{v_{i,K+1}^n - v_{i,K-1}^n}{2\Delta \xi}\right) + f u_{i,K}^n \quad (18)
 \end{aligned}$$

In the north-south and east-west momentum equations

$$C = \left(\frac{L}{Z_K}\right)^2 \left(\frac{K_M^n u_{i,K+1} - K_M^n u_{i,K-1}}{2\Delta \xi}\right) - K_M^n u_{i,K} \left(\frac{L}{Z_K}\right) \quad (19)$$

and

$$D = K_M^n u_{i,K} \left(\frac{L}{Z_K}\right)^2 \quad (20)$$

4.2.3 The moisture equation

$$\begin{aligned}
& -\left(\frac{q_{i,K}^{n+1} - q_{i,K}^{n-1}}{2\Delta t}\right) + C \frac{A}{2} \left(\frac{q_{i,K+1}^{n+1} - q_{i,K-1}^{n+1}}{2\Delta \xi}\right) + D \frac{A}{2} \left(\frac{q_{i,K+1}^{n+1} + q_{i,K-1}^{n+1} - 2q_{i,K}^{n+1}}{\Delta \xi^2}\right) = \\
& -C \frac{B}{2} \left(\frac{q_{i,K+1}^{n-1} - q_{i,K-1}^{n-1}}{2\Delta \xi}\right) - D \frac{B}{2} \left(\frac{q_{i,K+1}^{n-1} + q_{i,K-1}^{n-1} - 2q_{i,K}^{n-1}}{\Delta \xi^2}\right) \\
& + u_{i,K}^n \left(\frac{q_{i+1,K}^n - q_{i-1,K}^n}{2\Delta x}\right) + w_{i,K}^n \left(\frac{L}{Z_K}\right) \left(\frac{q_{i,K+1}^n - q_{i,K-1}^n}{2\Delta \xi}\right) \quad (21)
\end{aligned}$$

4.2.4 The thermodynamic equation

$$\begin{aligned}
& -\left(\frac{\theta_{i,K}^{n+1} - \theta_{i,K}^{n-1}}{2\Delta t}\right) + C \frac{A}{2} \left(\frac{\theta_{i,K+1}^{n+1} - \theta_{i,K-1}^{n+1}}{2\Delta \xi}\right) + D \frac{A}{2} \left(\frac{\theta_{i,K+1}^{n+1} + \theta_{i,K-1}^{n+1} - 2\theta_{i,K}^{n+1}}{\Delta \xi^2}\right) = \\
& -C \frac{B}{2} \left(\frac{\theta_{i,K+1}^{n-1} - \theta_{i,K-1}^{n-1}}{2\Delta \xi}\right) - D \frac{B}{2} \left(\frac{\theta_{i,K+1}^{n-1} + \theta_{i,K-1}^{n-1} - 2\theta_{i,K}^{n-1}}{\Delta \xi^2}\right) \\
& + u_{i,K}^n \left(\frac{\theta_{i+1,K}^n - \theta_{i-1,K}^n}{2\Delta x}\right) + w_{i,K}^n \left(\frac{L}{Z_K}\right) \left(\frac{\theta_{i,K+1}^n - \theta_{i,K-1}^n}{2\Delta \xi}\right) - Q_{i,K}^n \quad (22)
\end{aligned}$$

In the thermodynamic and moisture equations

$$C = \left(\frac{L}{Z_K}\right)^2 \left(\frac{K_{\theta i,K+1}^n - K_{\theta i,K-1}^n}{2\Delta \xi}\right) - K_{\theta i,K}^n \left(\frac{L}{Z_K^2}\right) \quad (23)$$

and

$$D = K_{\theta i,K}^n \left(\frac{L}{Z_K}\right)^2 \quad (24)$$

4.2.5 The soil heat conduction equation

$$\begin{aligned}
& -\left(\frac{T_{s,i,K}^{n+1} - T_{s,i,K}^{n-1}}{2\Delta t}\right) + C \frac{A}{2} \left(\frac{T_{s,i,K+1}^{n+1} - T_{s,i,K-1}^{n+1}}{2\Delta \xi}\right) + D \frac{A}{2} \left(\frac{T_{s,i,K+1}^{n+1} + T_{s,i,K-1}^{n+1} - 2T_{s,i,K}^{n+1}}{\Delta \xi^2}\right) \\
& = -C \frac{B}{2} \left(\frac{T_{s,i,K+1}^{n-1} - T_{s,i,K-1}^{n-1}}{2\Delta \xi}\right) - D \frac{B}{2} \left(\frac{T_{s,i,K+1}^{n-1} + T_{s,i,K-1}^{n-1} - 2T_{s,i,K}^{n-1}}{\Delta \xi^2}\right)
\end{aligned} \quad (25)$$

where

$$C = \frac{-K_{s,i,K}^n}{4L_s^2} \left(\frac{L_s}{-Z+Z_0}\right)^{3/2} + \left(\frac{1}{4L_s(-Z+Z_0)}\right) \left(\frac{K_{s,i,K+1}^n - K_{s,i,K-1}^n}{2\Delta \xi_s}\right) \quad (26)$$

and

$$D = \frac{K_{s,i,K}^n}{4L_s(-Z+Z_0)} \quad (27)$$

4.2.6 The hydrostatic equation

$$P_{i,K}^n = P_{i,K+1}^n + (P_{i,K+1}^n - R_{\rho,i,K} T_{v,i,K}^n) \left(\frac{-g}{T_{i,K}^n}\right) \left(\frac{Z_K + Z_{K+1}}{2L}\right) \Delta \xi \quad (28)$$

4.2.7 The continuity equation

$$W_{i,K}^n = W_{i,K-1}^n - \Delta \xi \left(\frac{Z_K + Z_{K-1}}{2L}\right) \left(\frac{u_{i+1,K}^n - u_{i-1,K}^n}{2\Delta x}\right) \quad (29)$$

In the above finite difference equations, the subscripts i and K denote horizontal and vertical grid positions, respectively. The superscript n denotes the time step. All other variables and mathematical symbols were defined in Chapter 2 with the exception of Z which denotes height above the terrain surface.

The coefficient matrix for each system of finite difference equations is written in tridiagonal form and solved by an efficient form of Gauss elimination (Lindzen and Kuo, 1969). The complete boundary layer model requires approximately 3,100 seconds of Univac 1108 CPU time for a 60 hour forecast or approximately four seconds per five minute time step.

4.3 Boundary and Interface Conditions

Values for forecast variables u , v and q are specified at the roughness height ($Z=Z_0$) and at the top of the model ($Z=1520$ meters).

At $Z=Z_0$

$$u=v=w=0$$

$$q=q_0$$

At $Z=1520$ meters

u and v are specified

$$q=q_0$$

$$\theta=\theta_0$$

P' is specified

where $()_0$ = initial value. Lateral boundary conditions specify a closed domain: $\frac{\partial}{\partial x}(u,v,q,\theta,P') = 0$, i.e. total reflection.

The temperature field required special treatment. The soil and atmospheric temperature fields are linked through conditions of heat balance and continuity of temperature at the roughness height. The surface heat balance equation is

$$G - F + \rho C_p K_\theta \frac{\partial \theta}{\partial Z} + \rho_s C_s K_s \frac{\partial T_s}{\partial Z} = 0 \text{ at } Z = Z_0 \quad (30)$$

where G = global radiation

F = net longwave radiative flux

ρ_s, c_s = soil density and conductivity

The temperature continuity equation is

$$T_{\text{air}} = T_s \text{ at } Z=Z_0 \quad (31)$$

In finite difference form the surface heat balance equation becomes:

$$G = F + \rho_{i,0}^n C_p K_{\theta} \left(\frac{\theta_{i,1} - \theta_{i,0}}{Z_1 - Z_0} \right) - \rho_s C_s K_s \left(\frac{\left(\frac{P_{i,1}}{1013} \right) \theta_{i,0}^n - T_{s,i,-1}^n}{Z_0 - Z_{-1}} \right) \quad (32)$$

Because of the low conductivity of the soil, the soil temperature at a depth of approximately one meter is assumed to undergo no diurnal variation over the forecast periods of the model; therefore, the lower boundary condition for temperature was $T_s = T_{s_0}$ at $Z = -.97$ meters.

4.4 Moisture Constraint

The moisture field forecast by the model is constrained to prevent supersaturation. At each time step, the newly forecast moisture field is converted to a dew point field. The dew point field is compared to the newly computed temperature field. Any dew point value larger than its corresponding temperature value is set equal to the temperature value. The moisture field is then recovered from the corrected dew point field. The expression which relates the moisture field (q) and the dew point field (T_D) follows:

$$q = 0.622 \left\{ \frac{6.11}{p} * \exp \left[\frac{597 - 0.285(T_D - 273)}{0.11} \left(\frac{1}{273} - \frac{1}{T_D} \right) \right] \right\} \quad (33)$$

where T_D = dew point. A derivation of the above expression is contained in Appendix B.

CHAPTER 5

EXCHANGE COEFFICIENT

5.1 KEYPS Formulation

A search for the appropriate formulation of exchange coefficient included the investigation of a turbulent energy closure scheme (Morin and Yaglom, 1970), the Blackadar formulation for a neutral atmosphere modified for non-neutral conditions (Yu, 1977), and the KEYPS formulation. Numerical instabilities were encountered when the turbulent energy closure scheme and Blackadar's formulation were structured for the boundary layer model vertical grid. The KEYPS formulation functioned well in the model environment and was adopted for the boundary layer model.

Assumptions inherent in the KEYPS formulation are best shown by a brief derivation of the KEYPS expression. The turbulent energy equation is written in the following form:

$$\frac{db}{dt} + \nabla \cdot \mathbf{v}'b = -u'w' \frac{\partial \bar{u}}{\partial z} - v'w' \frac{\partial \bar{v}}{\partial z} + \frac{g}{T} w'\theta' - \epsilon \quad (34)$$

where $(\bar{\quad})$ denotes horizontal averages. The terms on the left side of the equation are neglected and the following approximations are made:

$$u'w' = -K_M \frac{\partial \bar{u}}{\partial z} \quad v'w' = -K_M \frac{\partial \bar{v}}{\partial z} \quad w'\theta' = -K_\theta \frac{\partial \bar{\theta}}{\partial z} \quad (35)$$

Multiplying by K_M , equation (34) becomes

$$K_M^2 \left[\left(\frac{\partial \bar{u}}{\partial z} \right)^2 + \left(\frac{\partial \bar{v}}{\partial z} \right)^2 \right] - \frac{g}{T} K_\theta K_M \frac{\partial \bar{\theta}}{\partial z} - K_M \epsilon = 0 \quad (36)$$

Let $\gamma = \frac{K_M \theta}{K_M \theta}$ and through the usual dimensional considerations (e.g. Plate, 1971) let

$$\epsilon = \frac{K_M^3}{(C\ell)^4}$$

where $C = \text{constant}$

$\ell = \text{length scale}$

Equation (36) now becomes

$$K_M^2 \left[\left(\frac{\partial \bar{u}}{\partial z} \right)^2 + \left(\frac{\partial \bar{v}}{\partial z} \right)^2 \right] - \frac{g}{\theta} \gamma K_M^2 \frac{\partial \bar{\theta}}{\partial z} - \frac{K_M^4}{(C\ell)^4} = 0 \quad (37)$$

Note that

$$U^* = \sqrt{K_M \frac{\partial |\mathbf{v}|}{\partial z}} \quad \left| \begin{array}{l} \text{surface layer} \end{array} \right.$$

where

$$|\mathbf{v}| = \sqrt{u^2 + v^2}$$

and U^* is friction velocity. Making these substitutions equation (37) becomes

$$U_*^4 - \frac{g}{\theta} \gamma K_M^2 \frac{\partial \bar{\theta}}{\partial z} - \frac{K_M^4}{(C\ell)^4} = 0 \quad (38)$$

Although strictly valid only in the surface layer, equation (38) is used for the entire boundary layer. Solving equation (38) for K_M gives our final result.

$$K_M = \frac{C\ell}{\sqrt{2}} \left\{ \left(-(C\ell)^2 \gamma \frac{g}{\theta} \frac{\partial \bar{\theta}}{\partial z} \right) + \left([(C\ell)^2 \gamma \frac{g}{\theta} \frac{\partial \bar{\theta}}{\partial z}]^2 + 4U_*^4 \right)^{1/2} \right\}^{1/2} \quad (39)$$

Values of the constants are $\gamma = 14$ (Lumley and Panofsky, 1964) and $C=1$ which insured well behaved and realistic values for K_M . Selection of $C=1$ also insures that the KEYPS formulation for K_M matches similarity theory under neutral stratification in the surface boundary layer, i.e. $K_M = U^*kz$ where k is von Karmon's constant.

The KEYPS formulation projected a great sensitivity to the vertical profile of the potential temperature and tended to produce larger than normal values of K_M in the upper portion of the boundary layer. To offset the latter tendency, K_M was allowed to attain a maximum value below a specified level and then its value was exponentially decreased with height to the top of the boundary layer.

5.2 Length Scale

The length scale used in conjunction with the KEYPS formulation was defined by Djolov (1973) as

$$z = \frac{kZ}{\frac{kZ}{\lambda} + \phi_M\left(\frac{Z}{L}\right)} \quad (40)$$

where $\lambda = 0.00027 \frac{G}{F}$ (Blackadar, 1962), $\phi_M\left(\frac{Z}{L}\right)$ is the Obukhov profile function for momentum, L is the Monin-Obukhov length, and G is the geostrophic wind.

5.3 Exchange Coefficient for Heat

The KEYPS formulation provides an expression for the exchange coefficient of momentum. In order to calculate the exchange coefficient for heat, the following relationship from similarity theory is used:

$$K_\theta = K_M \frac{\phi_M}{\phi_\theta} \quad (41)$$

The functional forms of ϕ_M and ϕ_θ are adopted from Carl et al. (1973) and Webb (1970) and applied as in Zdunkowski et al. (1976). The simplifying assumption that $\phi_\theta = \phi_q$ was made. The KEYPS formulation assumes that the ratio of K_θ to K_M is constant with height; therefore there is the implied assumption that the ratio of ϕ_θ to ϕ_M is constant with height. In keeping with this basic assumption of the KEYPS formulation, the ratio of ϕ_θ to ϕ_M was calculated in the surface boundary layer and held constant with height. This procedure was also followed by Yu (1977) with favorable results.

CHAPTER 6

RADIATION

6.1 Radiative Effects

Radiation appears explicitly in the model as the heating term in the thermodynamic equation and as global and terrestrial radiation in the statement of heat balance at the roughness height. The radiative effects vary throughout the boundary layer as these three terms act and react to other influences simulated by the model.

6.2 Global Radiation

Global radiation is calculated as in Zdunkowski et al. (1975). A semi-empirical formula from Phillips (1962) is used which combines the effects of diffuse and direct solar radiation. The formula expresses the global radiation in terms of Linke's turbidity factor, τ_L .

$$G = J (.755 - .054 \tau_L) \cos \theta_Z \quad (42)$$

where J = solar constant

θ_Z = solar zenith angle

Equation (42) assumes an average ground reflectivity of 20%. The Linke Turbidity factor is defined as

$$\tau_L = (\beta_R + \beta_W) / \beta_R \quad (43)$$

where β_R = complex Rayleigh scattering coefficient

β_W = complex water vapor absorption coefficient

From Feussner and Dubois (1930)

$$\beta_R = - \ln(.907 m^{.018}) \quad (44)$$

where m = air mass.

The air mass is normally approximated by $\sec \theta_0$. A more precise expression from Paltridge and Platt (1976) was used in the model. The expression follows:

$$m = \{ [(\frac{rg\rho}{P}) \cos\theta_z]^2 + 2(\frac{rg\rho}{P}) + 1 \}^{1/2} - (\frac{rg\rho}{P}) \cos\theta_z \quad (45)$$

where r = earth's radius

ρ, P = Atmospheric density and pressure at Z_0 .

g = gravity

McDonald (1960) provided an approximation for β_W where

$$\beta_W = (\frac{-1}{m}) \ln (1 - .077u^{.30}) \quad (46)$$

$$u = U_1 * m \quad (47)$$

U_1 is the total water vapor pathlength of the atmosphere. It was calculated using

$$U_1 = \int_0^{\infty} q\rho \frac{P}{P_0} dz \quad \text{where } P_0 = 1013 \text{ mb.} \quad (48)$$

Infinity, as the upper limit of integration, was actually the top of the model; therefore, in order to obtain more realistic values for the water vapor pathlength, the top of the model was extended five kilometers with a constant vertical grid separation of approximately 86 meters. The resulting radiational model is 6.52 KM deep with 94 computational levels. An average mid-latitude summer atmosphere

(McClatchey et al., 1971) was incorporated in the upper five kilometers of the radiational model (see Table 2).

6.3 Flux Divergence

The heating term in the thermodynamic equation is expressed in terms of the flux divergence.

$$Q = \frac{-1}{\rho C_p} \left(\frac{P_0}{P} \right)^{R/C_p} \frac{\partial F}{\partial z} \quad (49)$$

where F = infrared flux

$$P_0 = 1013 \text{ mb}$$

The infrared flux divergence $\left(\frac{\partial F}{\partial z} \right)$ was calculated in accordance with Liou (1979). Flux up ($F_{\uparrow}(U)$) and flux down ($F_{\downarrow}(U)$) are calculated at each level of the radiational model. $F(U)$ is defined as

$$F(U) = F_{\uparrow}(U) - F_{\downarrow}(U) \quad (50)$$

The flux divergence is the difference in $F(U)$ between layers of the model.

The flux equations for the radiational model are written in terms of U . Since the model atmosphere is considered to contain only water vapor, U is the optical pathlength of water vapor and is calculated from the following expression:

$$U(z) = \int_0^z q(z) \rho(z) \left(\frac{P(z)}{P_0} \right) dz \quad (51)$$

where $P_0 = 1013 \text{ mb}$

The value of U increases from zero at the roughness height to a maximum value at the top of the radiational model as depicted in Figure 3. The flux equations are:

Table 2. Mid-latitude summer climatology data used in radiational model.

Height(KM)	Pressure(mb)	Temperature(°K)	Density(g/m ³)	Water vapor(g/m ³)
0	1013	294	1.191E+03	1.4E+01
1	902	290	1.080E+03	9.3E+00
2	802	285	9.757E+02	5.9E+00
3	710	279	8.846E+02	3.3E+00
4	628	273	7.998E+02	1.9E+00
5	554	267	7.211E+02	1.0E+00
6	487	261	6.487E+02	6.1E-01
7	426	255	5.830E+02	3.7E-01
8	372	248	5.225E+02	2.1E-01
9	324	242	4.669E+02	1.2E-01
10	281	235	4.159E+02	6.4E-02

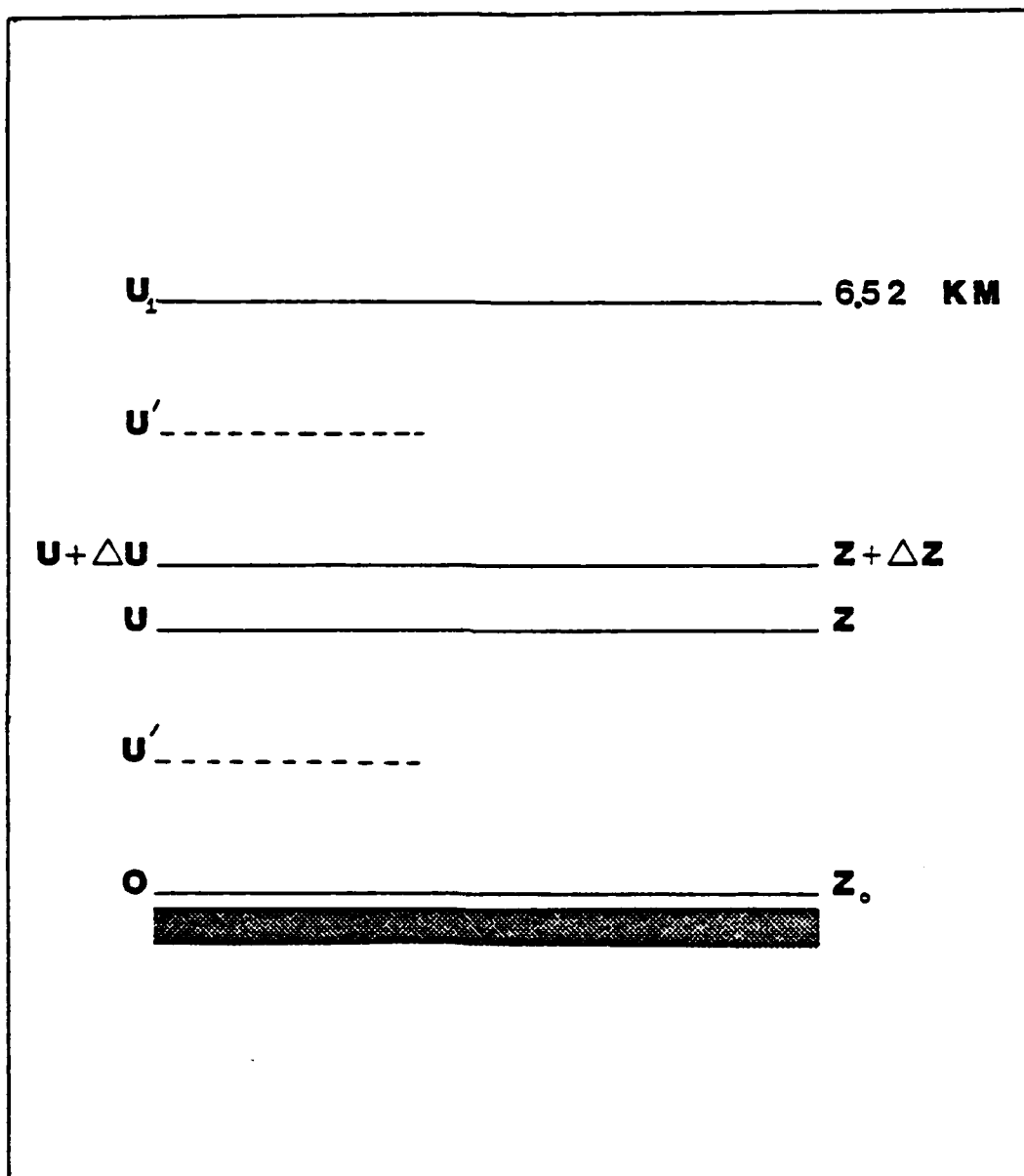


Figure 3. Vertical variation of the water vapor pathlength, U , and its relation to Z .

$$F_{\uparrow}(U) = \sigma T^4(U) - 4\sigma \int_0^U t^F(U-U') T^3(U') \frac{dT(U')}{dU'} dU' \quad (52)$$

$$F_{\uparrow}(U) = \sigma T^4(U) - \sigma T^4(U_1) t^F(U_1-U) - 4\sigma \int_{U_1}^U t^F(U'-U) T^3(U') \frac{dT(U')}{dU'} dU' \quad (53)$$

where σ = Stefan-Boltzman constant

t^F = broad-band flux transmissivity

U_1 = U at the top of the radiational model

U' = U at an intermediary computational level

The temperature of the surface and the air immediately overlying the surface are assumed to be the same in expression (52)

The broad-band flux transmissivity is calculated in terms of the broad-band flux emissivity where

$$t^F = 1 - \epsilon^F \quad (54)$$

ϵ^F is assumed to be a function of U only (there is a slight variation of ϵ^F with temperature). Broad-band flux emissivity values were obtained from Stanley and Jarica (1970). These values include the rotational band, window, and 6.3 μ band for water vapor. Functions were developed to express emissivity values in terms of $u(u = \log_{10} U)$ for use in the model. The functions are:

$$\begin{array}{ll} u \leq -3 & \epsilon^F = .0276u^2 + .282u + .7436 \\ -3 < u \leq -1 & \epsilon^F = .0045u^2 + .1535u + .566 \\ -1 < u \leq 1 & \epsilon^F = .0515u^2 + .2395u + .605 \\ 1 < u & \epsilon^F = -.13u^2 + .4823u + .5437 \end{array} \quad (55)$$

Infrared cooling rates calculated by the radiational model were compared with cooling rates from Roewe and Liou (1970) for a clear tropical atmosphere (McClatchey et al., 1971). The results are depicted in Figure 4. The low cooling rates in the lower troposphere are mainly due to the failure of the emissivity values to fully account for the water dimer effect which is largely responsible for water vapor absorption in the lower troposphere (Roewe and Liou, 1978).

6.4 Solar Zenith Angle

The solar zenith angle is calculated by the following well known expression (Paltridge and Platt, 1976):

$$\cos \theta_z = \sin \delta \sin \phi + \cos \delta \cos \phi \cos t_h \quad (56)$$

where θ_z = solar zenith angle

δ = declination

ϕ = latitude

t_h = hour angle

The maximum change in δ in 24 hours is less than 5° so a single value of δ was used for each day. The expression is (Spencer, 1971):

$$\begin{aligned} \delta = & .006918 - .399912 \cos \theta_D + .070257 \sin \theta_D \\ & - .006758 \cos 2\theta_D + .000907 \sin 2\theta_D \\ & - .002697 \cos 3\theta_D + .001480 \sin 3\theta_D \end{aligned} \quad (57)$$

θ_D , in radians, is defined in terms of the day number, d_n , which ranges from 0 on 1 January to 364 on 31 December.

$$\theta_D = \frac{2\pi d_n}{365} \quad (58)$$

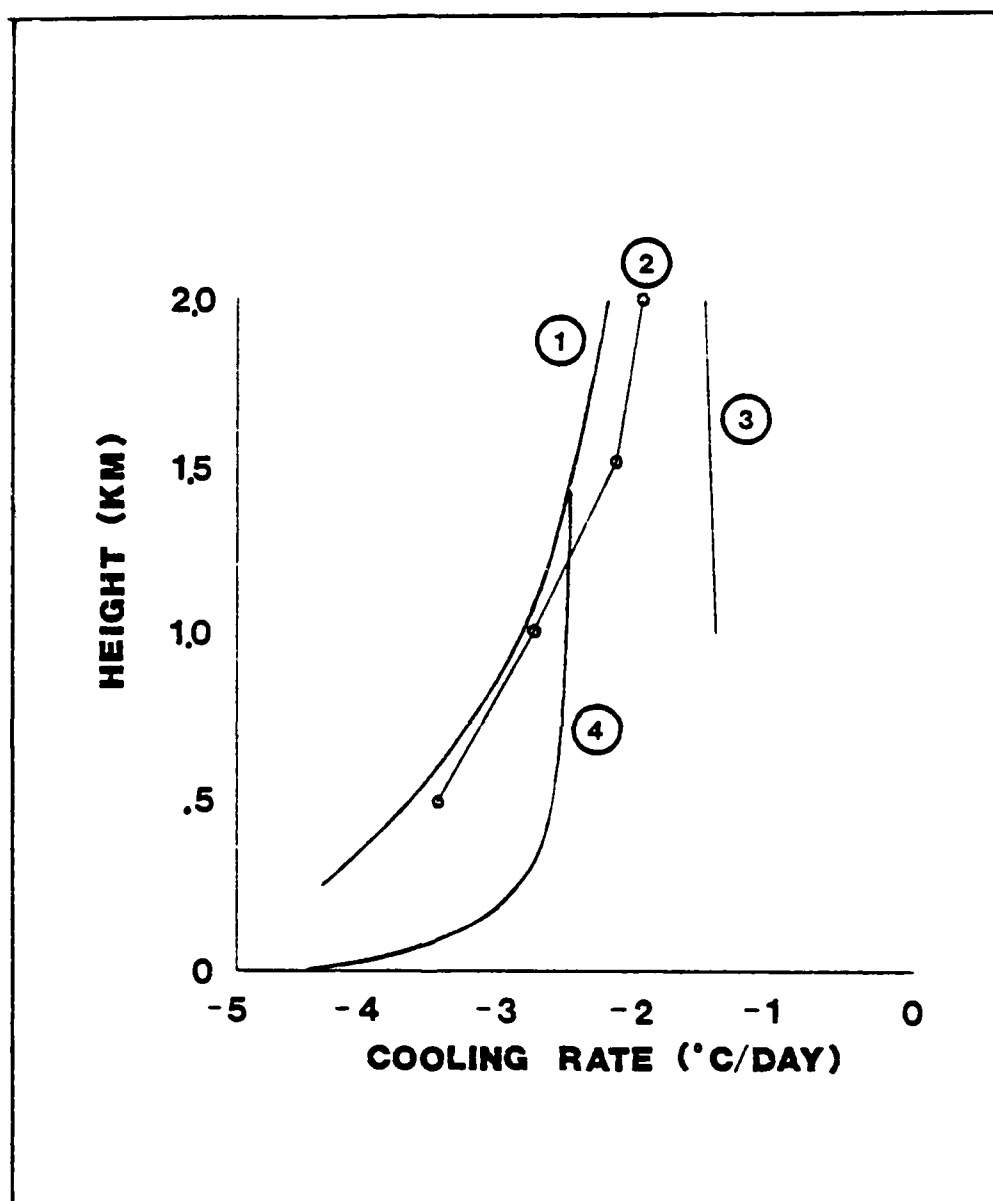


Figure 4. Comparison of observed and calculated cooling rates in a clear tropical atmosphere from (1) Roewe and Liou, (2) observations, (3) Rodgers and Walshaw, and (4) present study.

The sun's hour angle, t_h , is measured from the midday position and changes 360° per day or 15° per hour. The radiational model contains two internal clocks which up-date the day number and local time at each grid point.

6.5 Numerical Considerations

The number of mathematical operations required for the radiational computations was at least an order of magnitude larger than the number of operations required for the remainder of the boundary layer model; therefore, the radiational computations were completed every 23 time steps. More details about radiation are given in Chapter 7.

CHAPTER 7

SENSITIVITY TESTS

7.1 Coordinate System

7.1.1 Purpose

The purpose of this test is to give some indication of the relative merits of the local terrain following coordinate system used in the boundary layer model as compared to a standard terrain following coordinate system (as in Gerrity, 1967).

7.1.2 Test Description

The local terrain following coordinate system and the coordinate system used by Gerrity (1967) differ only in the manner in which the pressure gradient force is expressed. In the local coordinate system, the pressure gradient force is written in terms of the pressure and density deviations from standard; whereas, in the coordinate system employed by Gerrity, it is expressed in the normal manner. Since pressure and density deviations from standard may be of concern, the coordinate systems were tested under various degrees of stratification. Care was taken for two of the cases to initialize the model in such a way that little or no flow would be generated; therefore, the amount of flow that was generated would be a measure of the truncation error inherent in the numerical computation of horizontal pressure derivatives over sloping terrain in terrain following coordinate systems.

The tests were categorized by initial atmosphere as follows: (1) Condition A, (2) Condition B, and (3) Condition C. Conditions A and B

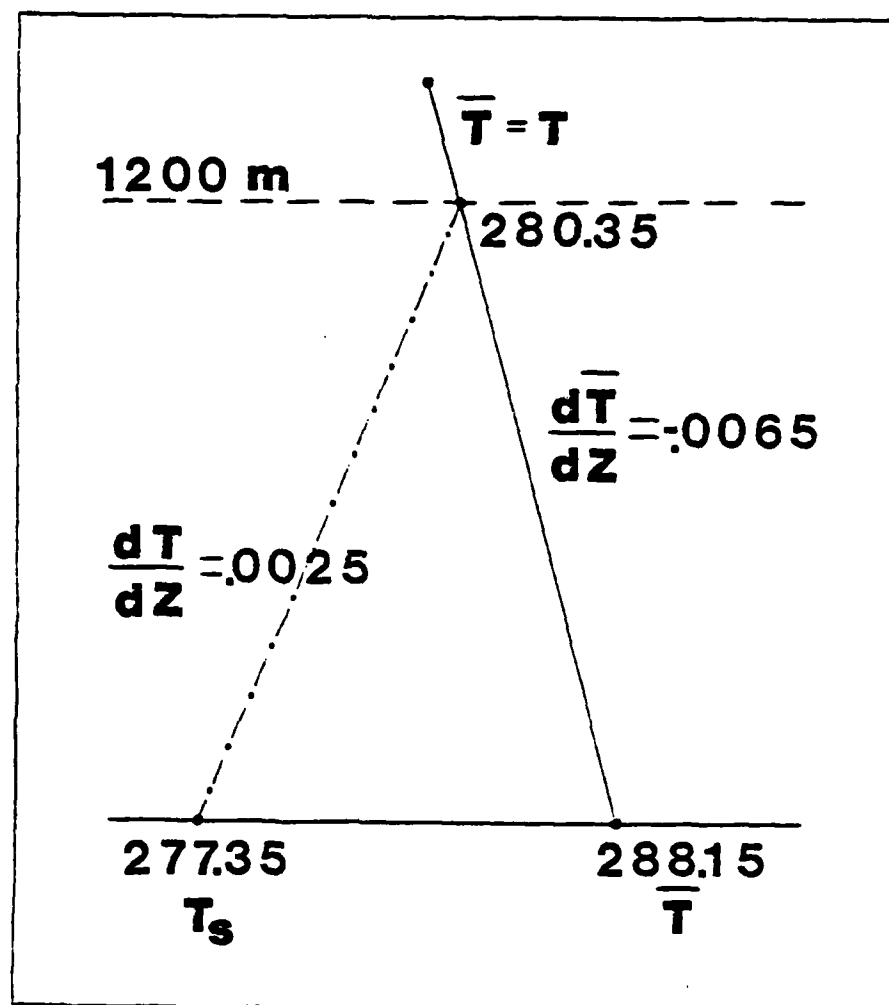
had the same initial atmosphere except for the type and strength of temperature inversion (see Figures 5 and 6). The model atmosphere was considered dry and in hydrostatic balance with the U, V, and W components of the wind field equal to zero. Global radiation and radiative flux divergence were omitted. Friction was considered constant with K_M and K_0 equal to one meter square per second. The model atmosphere for Condition C was more realistic with moisture, global radiation, and friction retained. A southerly geostrophic wind of 10 m/sec existed with the U component of the wind field still equal to zero. The V component of the initial wind field increased logarithmically from zero at the roughness height to 10 m/sec at 50m and was then constant with height to the top of the model.

The boundary layer model was executed using each coordinate system with the three initial atmospheres for a 48 hour forecast period.

7.1.3 Results

A detailed analysis of six grid points, shown in Figure 7, is presented. The grid points were carefully selected to insure that the absolute value of the terrain slopes associated with these grid points were representative of the range of slope values found on the grid (Table 3). The generation of the flow field during each test is represented by graphs of the maximum U component vs time as well as graphs of the integrated vertical velocity at the top of the model vs time for each of the selected grid points. These graphs are depicted in Figures 8 through 35. Averages compiled from these figures are contained in Tables 4 and 5.

Data contained in the figures and tables reveals an apparent superiority of the local terrain following coordinate system over the



CONDITION A

Figure 5. The temperature inversion portion of Condition A used to test the local and standard terrain following coordinate systems.

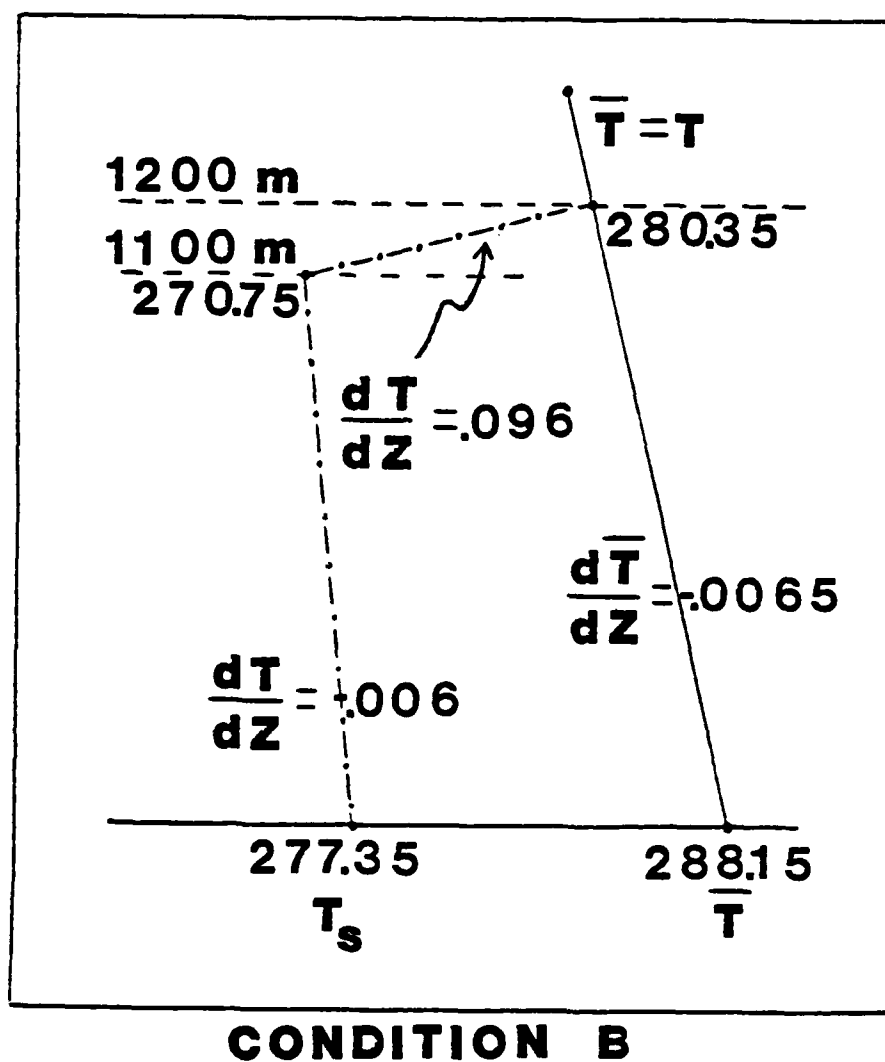


Figure 6. The temperature inversion portion of Condition B used to test the local and standard terrain following coordinate systems.

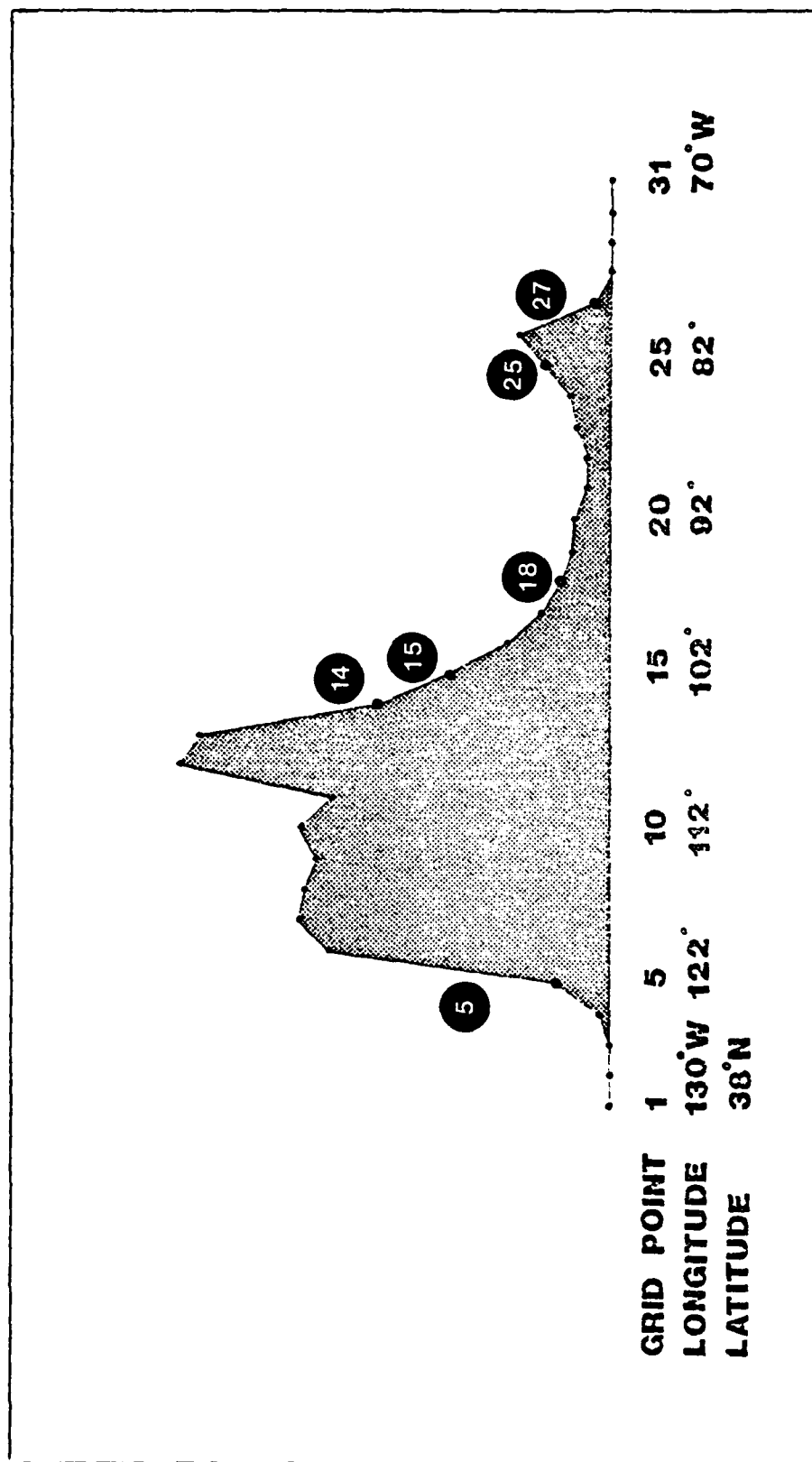


Figure 7. Selected grid points for a comparison test of the terrain following coordinate systems.

Table 3. Terrain slopes for grid points used in the coordinate system tests.

Grid Point	Slope
5	.004853
14	.004508
15	.002322
27	.001746
25	.000993
18	.000485

standard system. In most cases examined, the amount of flow generated ($|U_{\max}|$) in the standard terrain following coordinate system increased as the terrain slope increased; whereas in the local coordinate system, the flow generally increased from Condition A to Condition B. These statements also apply to the generation of the vertical velocity fields in the standard coordinate system but only for the larger terrain slopes when the local system is considered.

Under more realistic conditions (Condition C) the flow is generated by physical forcing as well as truncation error. The amount of flow generated under this condition with the standard terrain following coordinate system is not appreciably different (with the exception of grid point 5) from the amount generated solely by truncation error (Conditions A and B). Therefore, under realistic conditions it may be difficult to determine variations in the flow field due solely to physical forcing. This is not the case with the local terrain following system. It appears that the truncation error has been reduced to such a degree (with the exception of grid point 5) that variations in the flow field due solely to physical forcing clearly dominate any

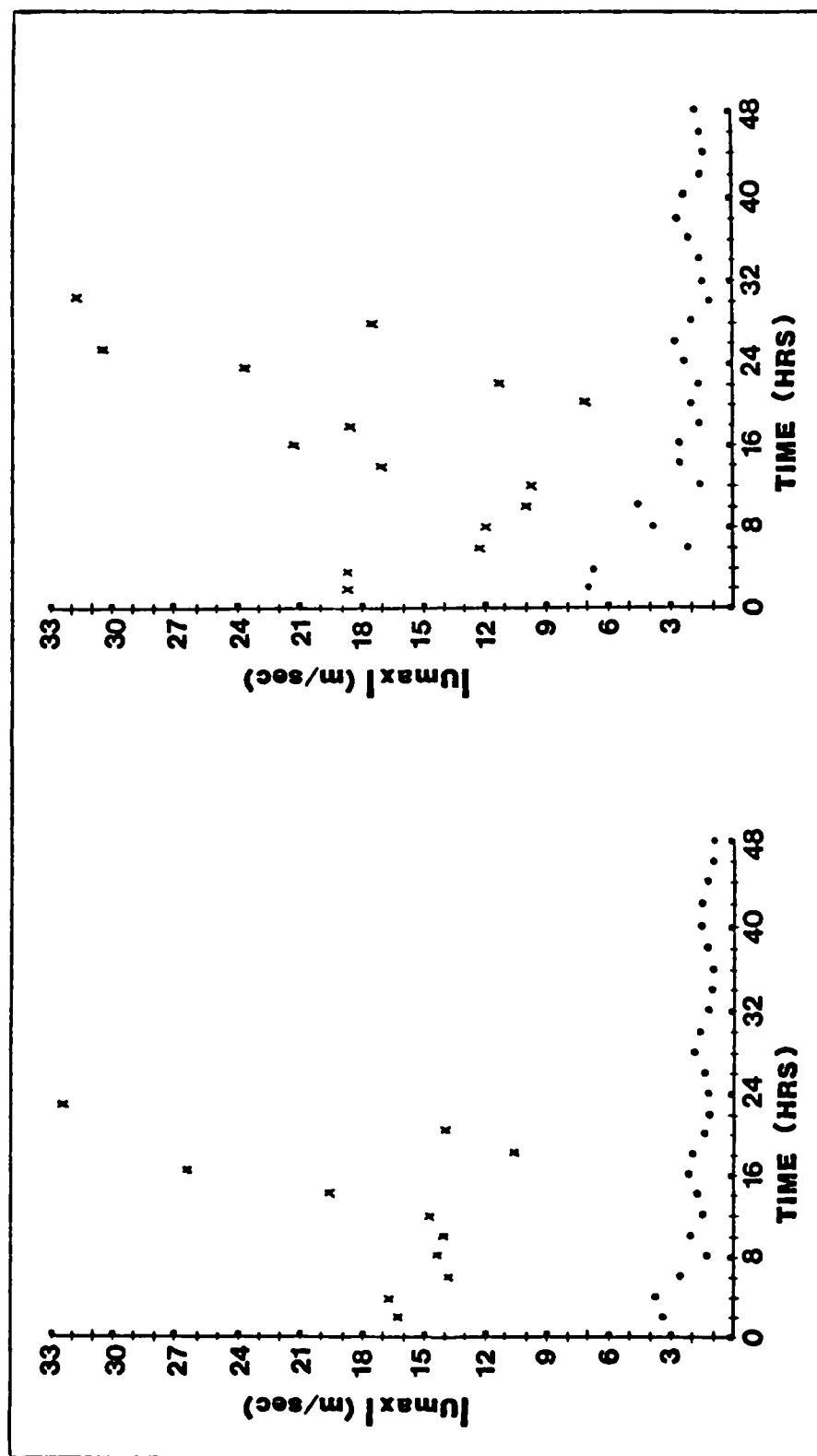


Figure 8. Variation of the maximum U component with time above grid point 5 for the local (x) and standard (.) terrain following coordinate systems. Left, Condition A and right, Condition B.

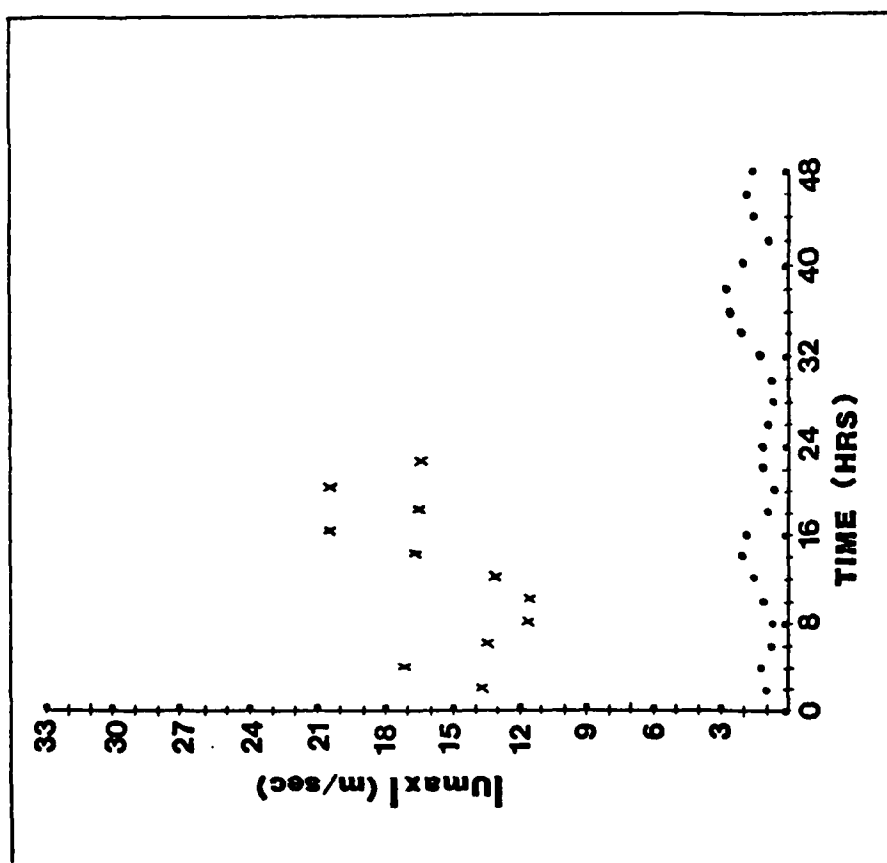


Figure 9. Variation of the maximum U component with time above grid point 5 for the local (.) and standard (x) terrain following coordinate systems. Condition C.

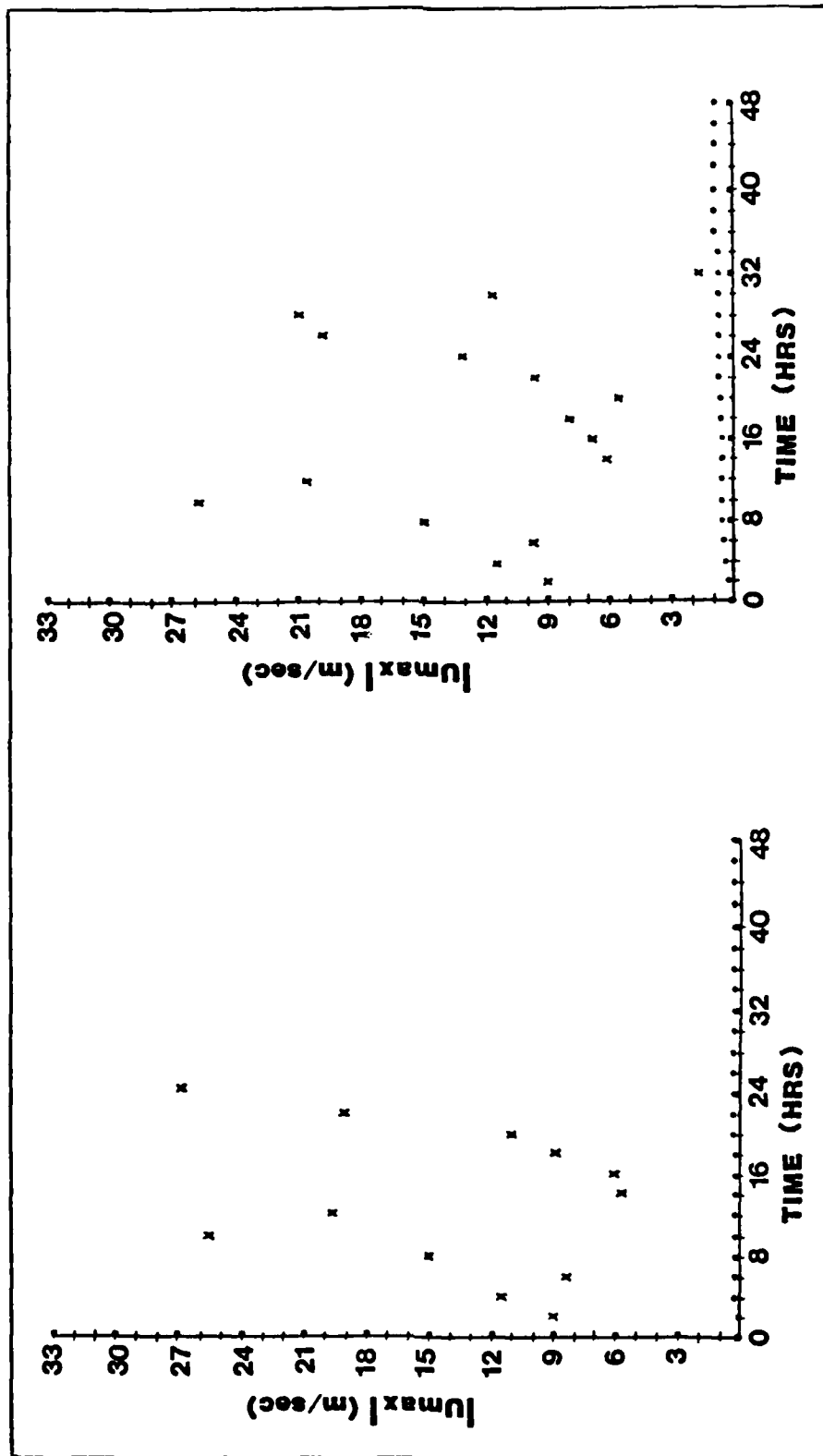


Figure 10. Variation of the maximum U component with time above grid point 14 for the local (.) and standard (x) terrain following coordinate systems. Left, Condition A and right, Condition B.

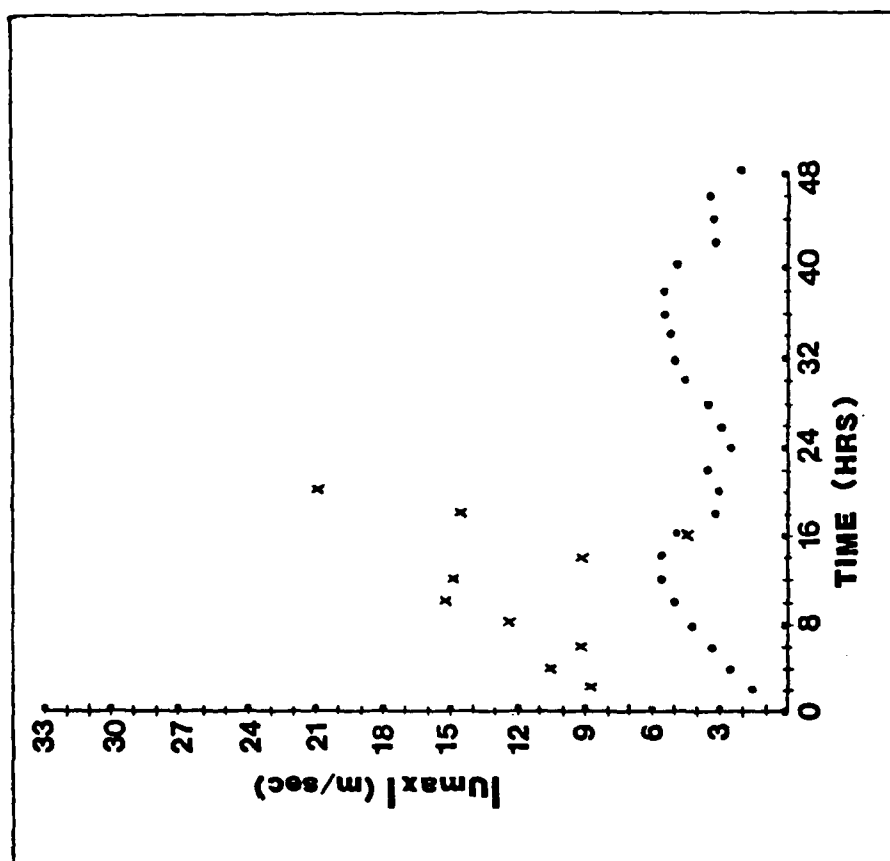


Figure 11. Variation of the maximum U component with time above grid point 14 for the local (.) and standard (x) terrain following coordinate systems. Condition C.

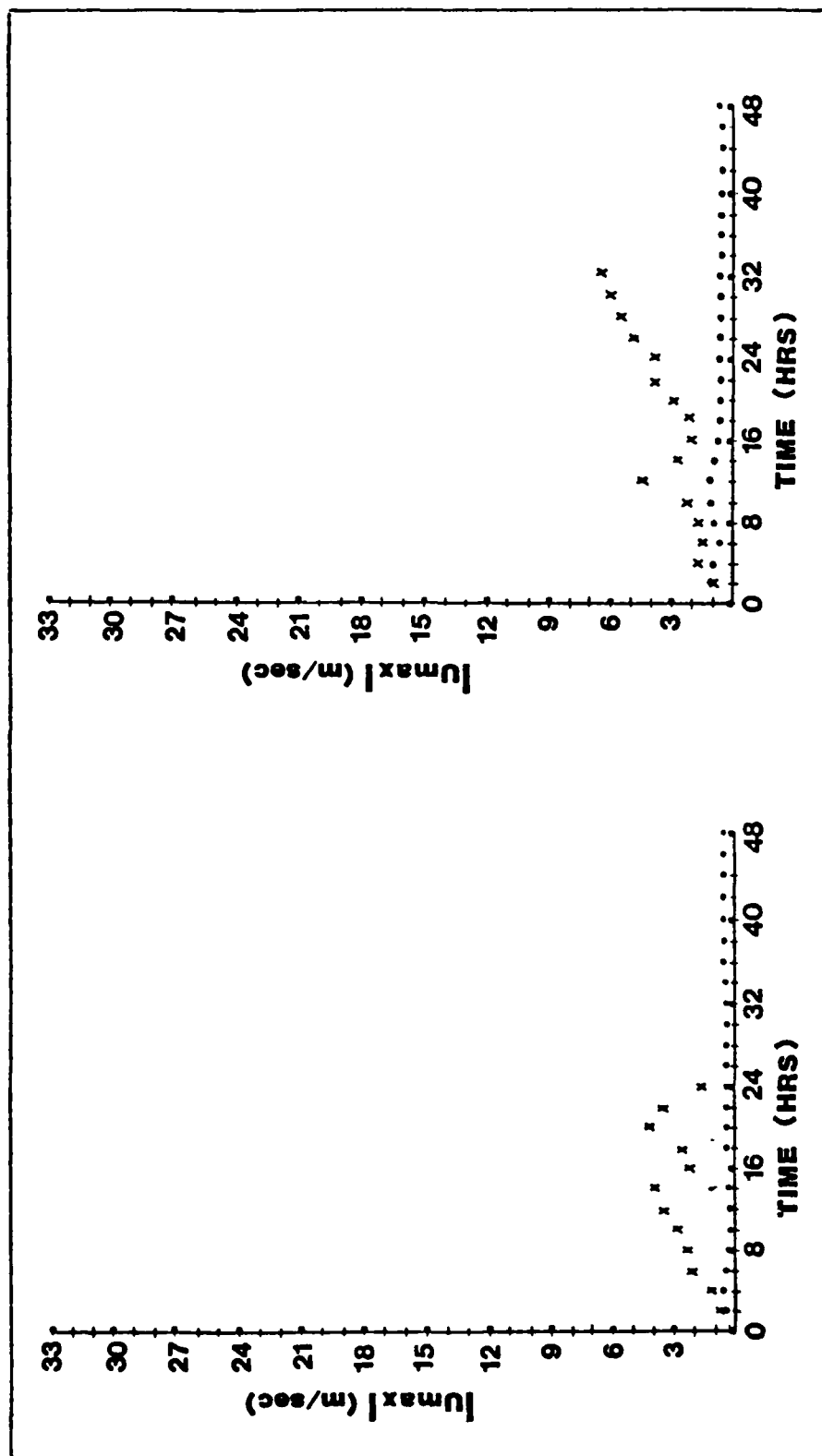


Figure 12. Variation of the maximum U component with time above grid point 15 for the local (.) and standard (x) terrain following coordinate systems. Left, Condition A and right, Condition B.

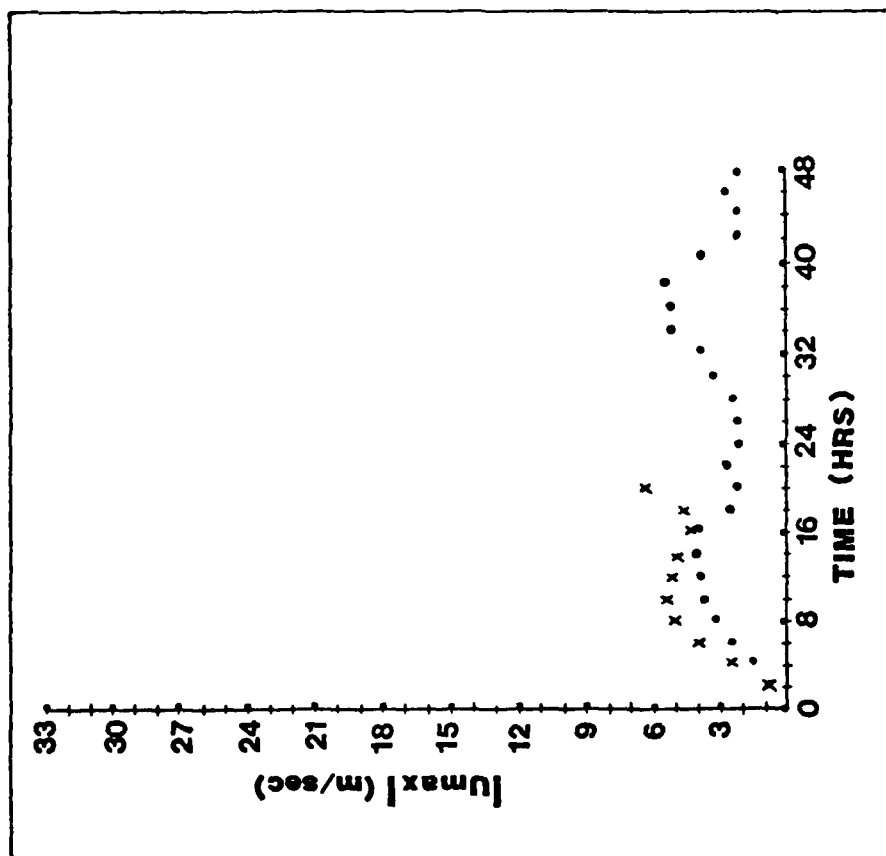


Figure 13. Variation of the maximum U component with time above grid point 15 for the local (.) and standard (x) terrain following coordinate systems. Condition C.

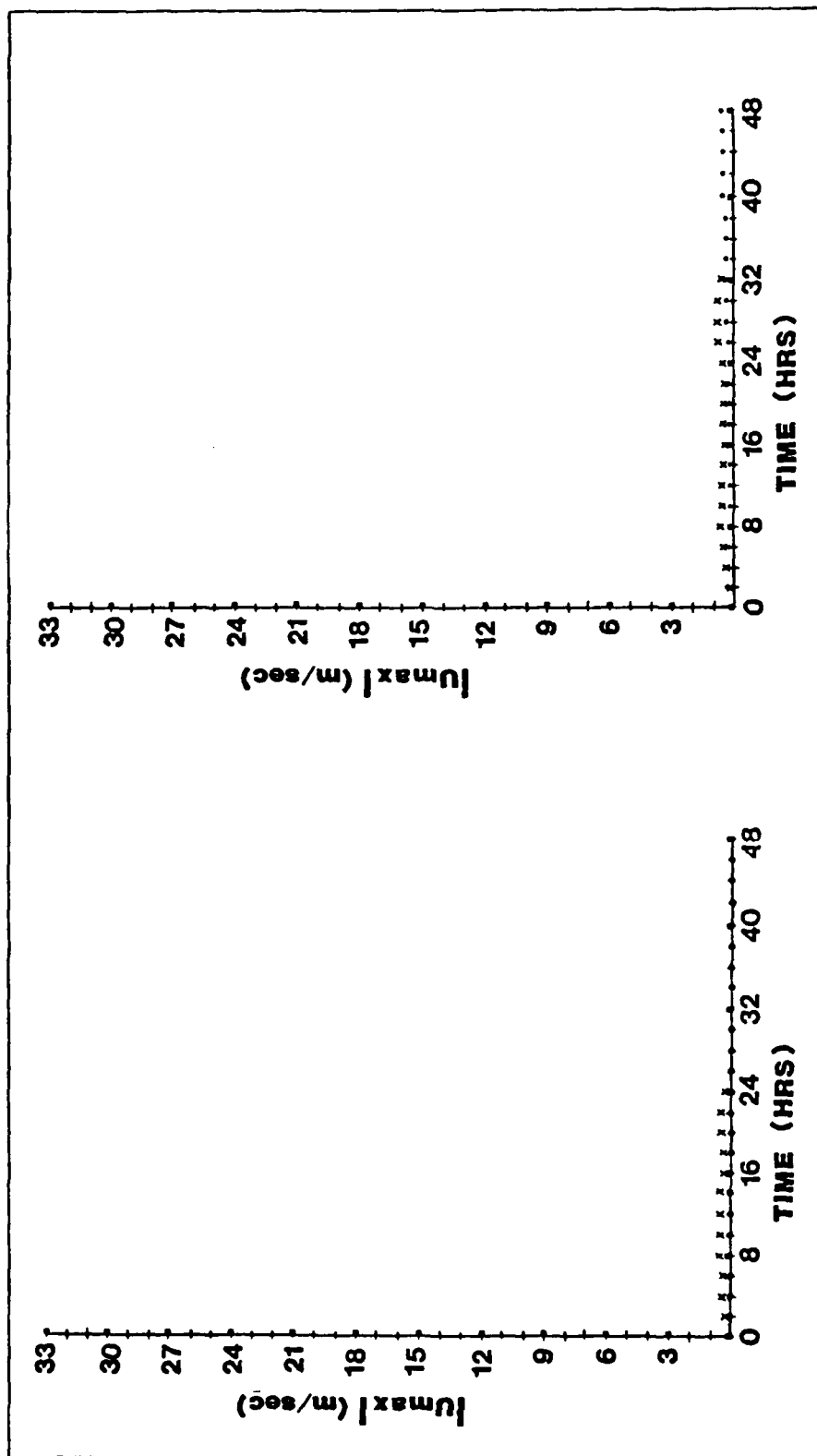


Figure 14. Variation of the maximum U component with time above grid point 18 for the local (.) and standard (x) terrain following coordinate systems. Left, Condition A and right, Condition B.

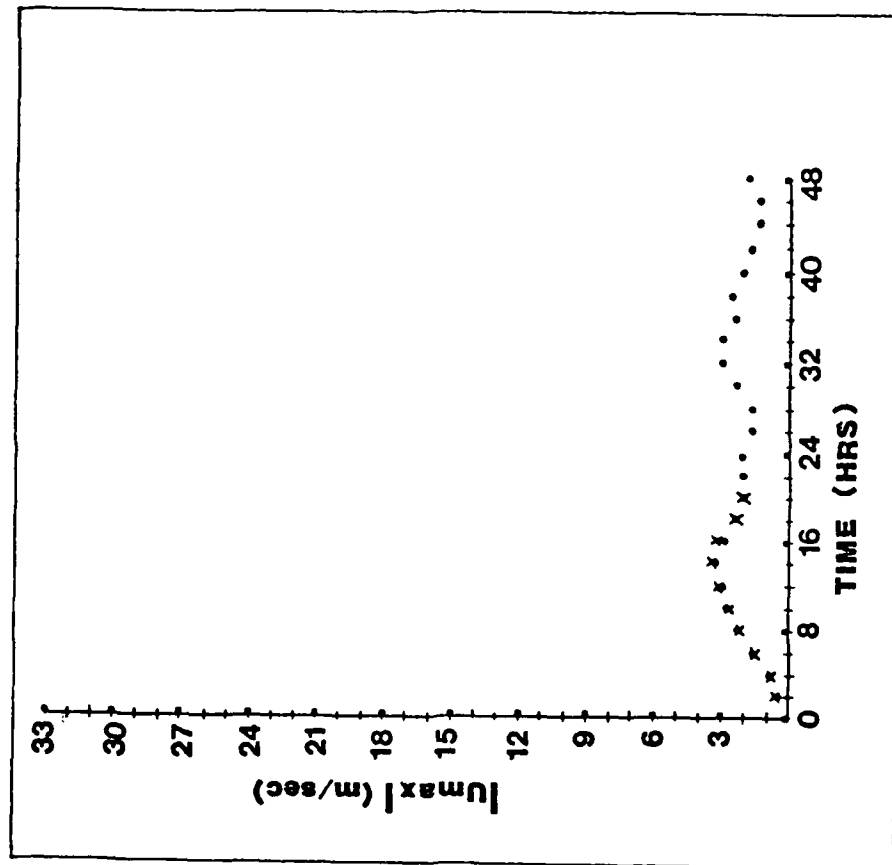


Figure 15. Variation of the maximum U component with time above grid point 18 for the local (.) and standard (x) terrain following coordinate systems. Condition C.

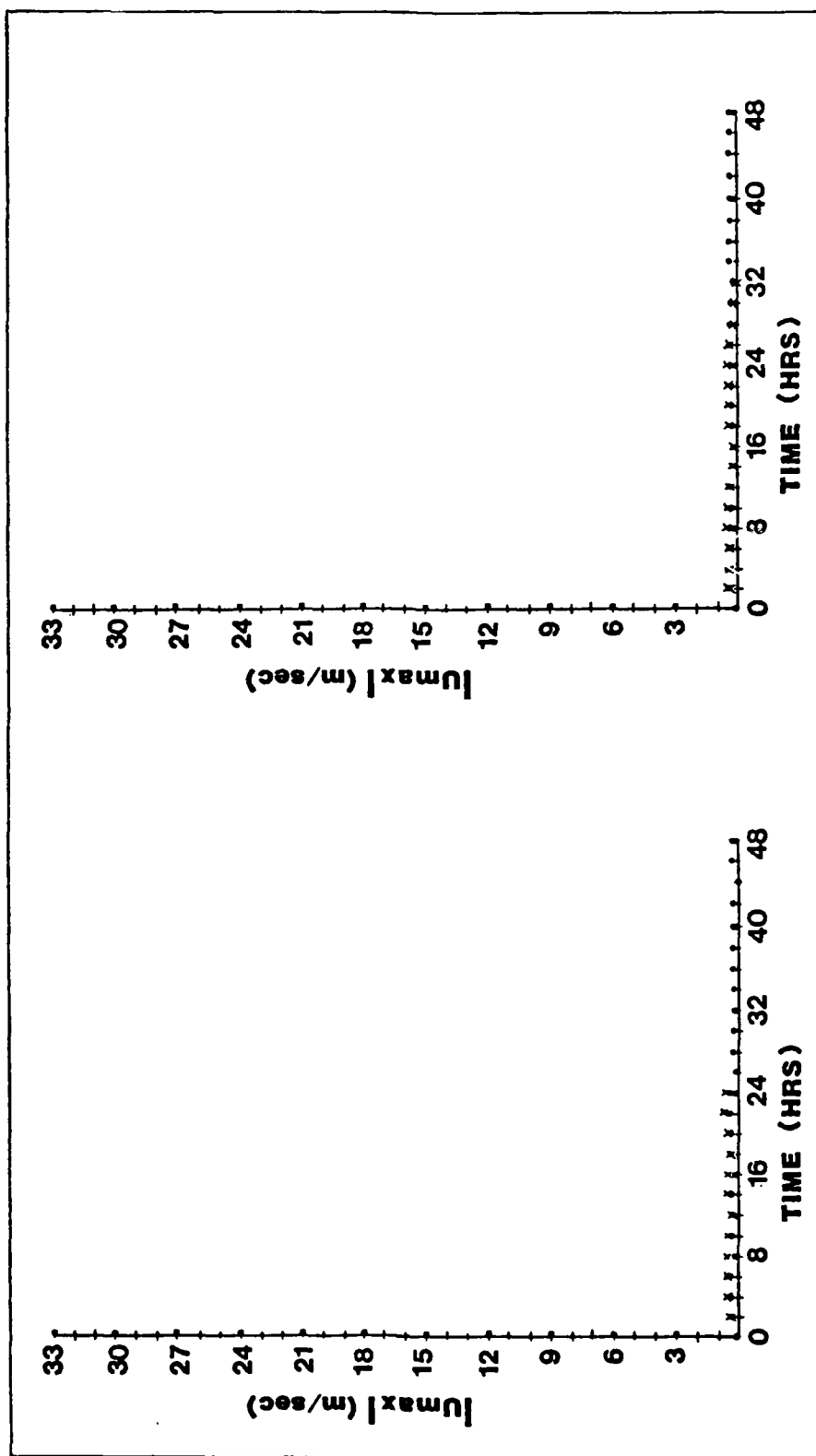


Figure 16. Variation of the maximum U component with time above grid point 25 for the local (.) and standard (x) terrain following coordinate systems. Left, Condition A and right, Condition B.

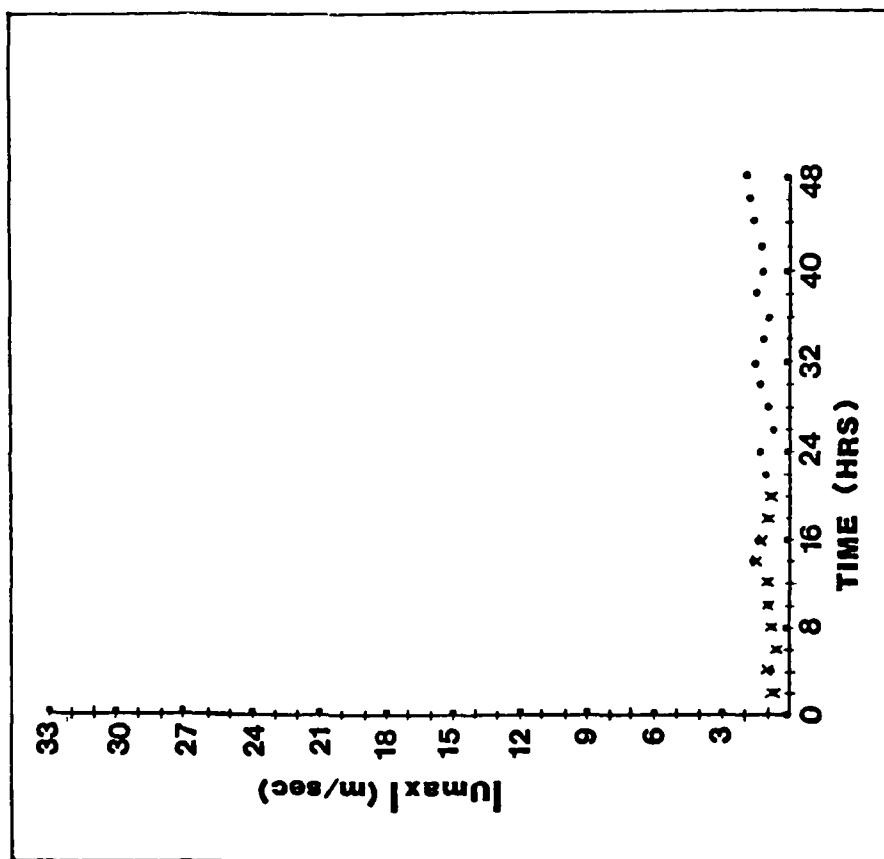


Figure 17. Variation of the maximum U component with time above grid point 25 for the local (.) and standard (x) terrain following coordinate systems. Condition C.

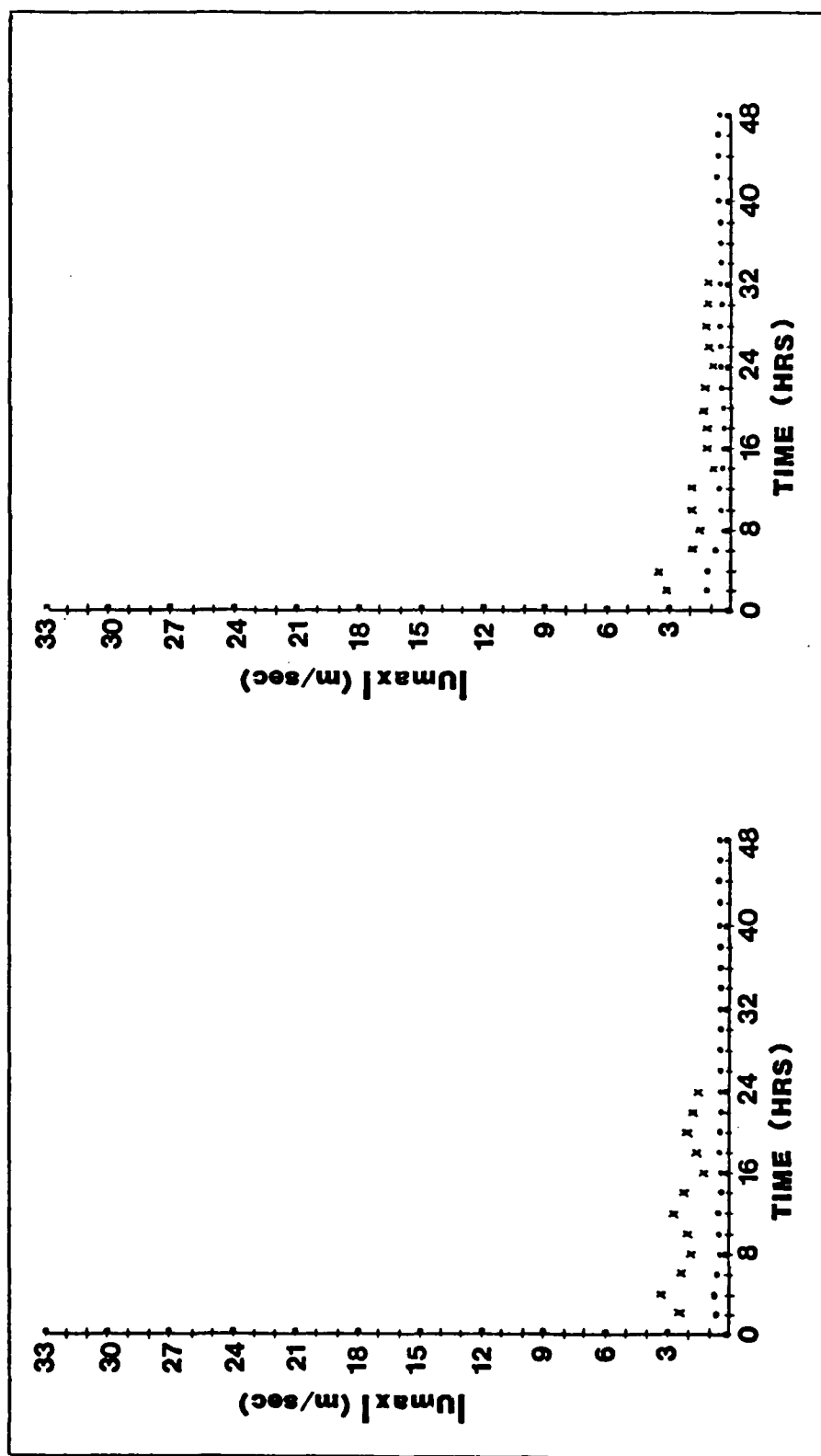


Figure 18. Variation of the maximum U component with time above grid point 27 for the local (.) and standard (x) terrain following coordinate systems. Left, Condition A and right, Condition B.

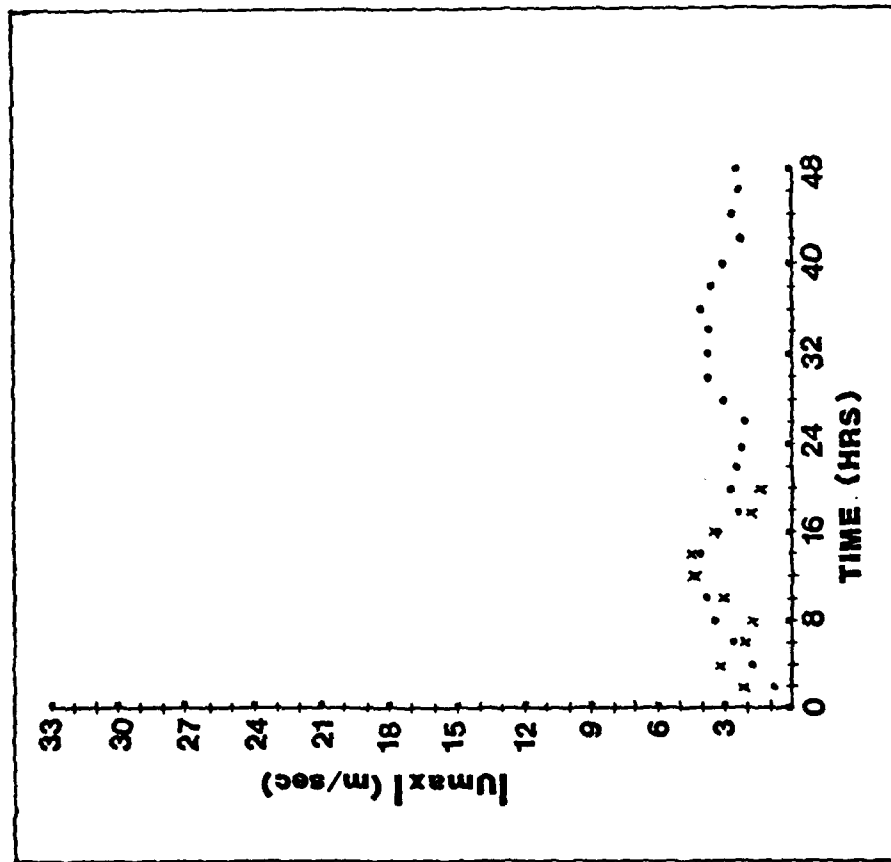


Figure 19. Variation of the maximum U component with time above grid point 27 for the local (.) and standard (x) terrain following coordinate systems. Condition C.

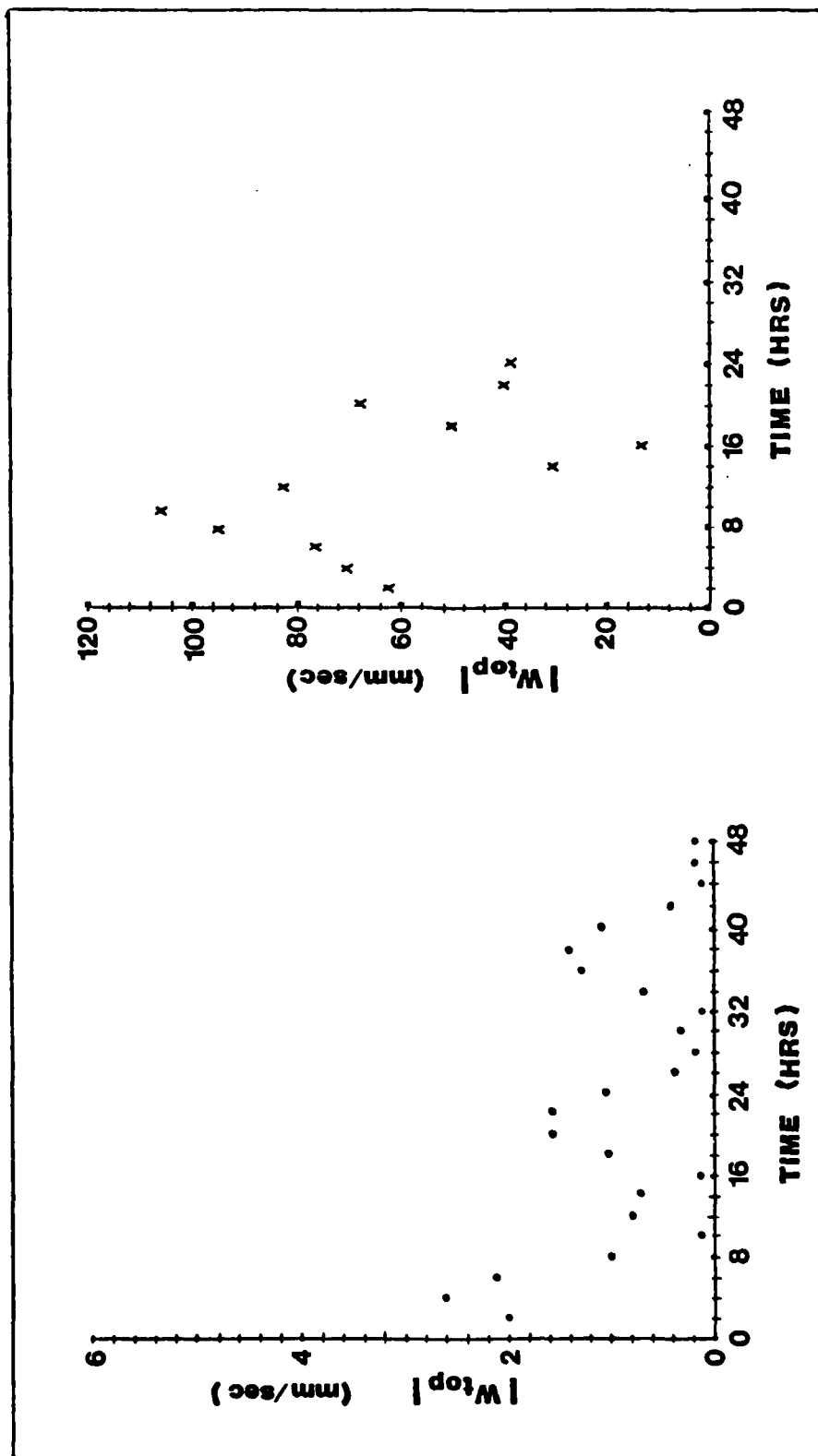


Figure 20. Variation of the vertical velocity at the top of the model with time above grid point 5 for the local terrain following coordinate system (.), left, and for the standard terrain following coordinate system (x), right. Condition A.

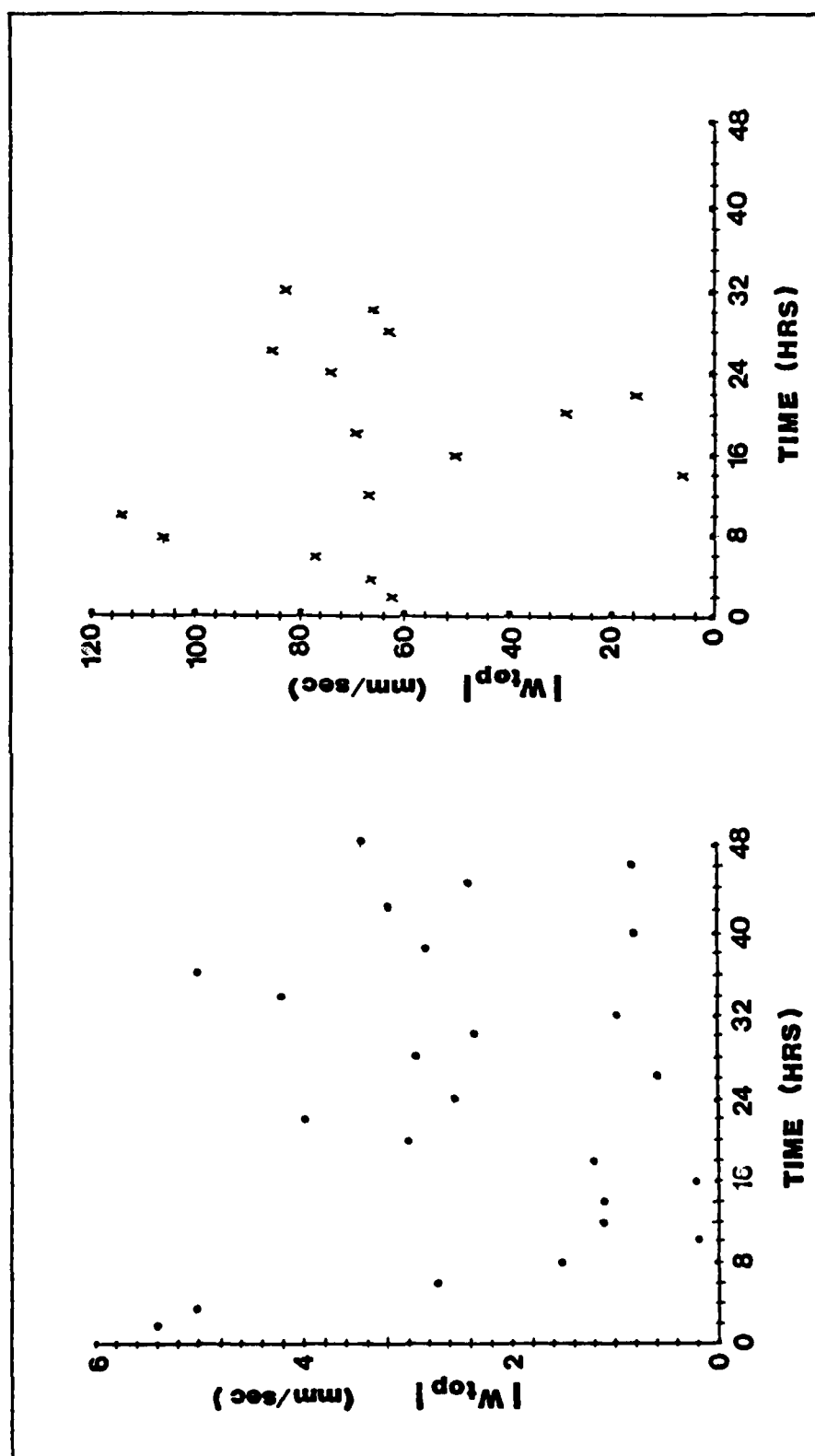


Figure 21. Variation of the vertical velocity at the top of the model with time above grid point 5 for the local terrain following coordinate system (.), left, and for the standard terrain following coordinate system (x), right. Condition B.

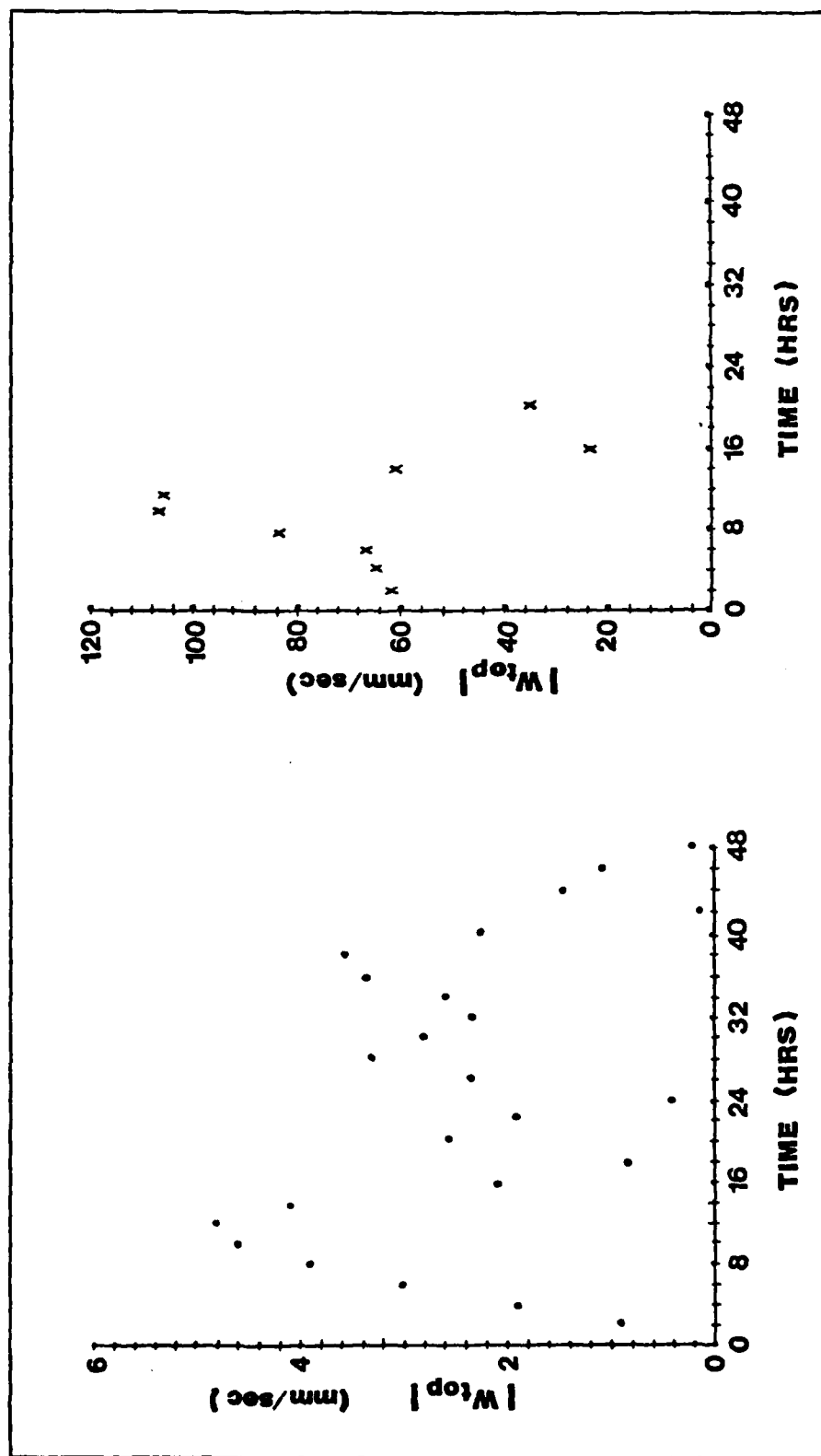


Figure 22. Variation of the vertical velocity at the top of the model with time above grid point 5 for the local terrain following coordinate system (.), left, and for the standard terrain following coordinate system (x), right. Condition C.

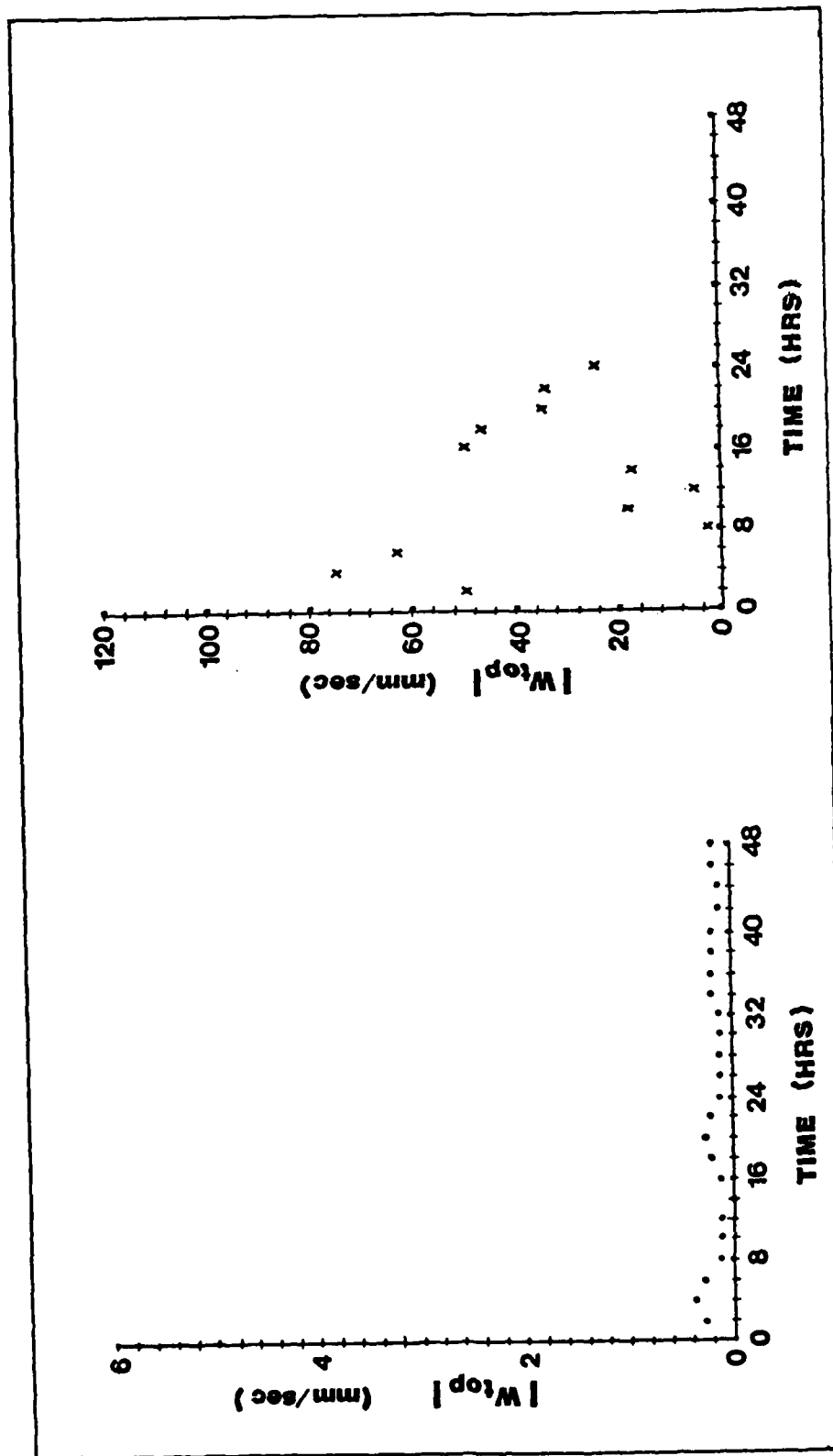


Figure 23. Variation of the vertical velocity at the top of the model with time above grid point 14 for the local terrain following coordinate system (.), left, and for the standard terrain following coordinate system (x), right. Condition A.

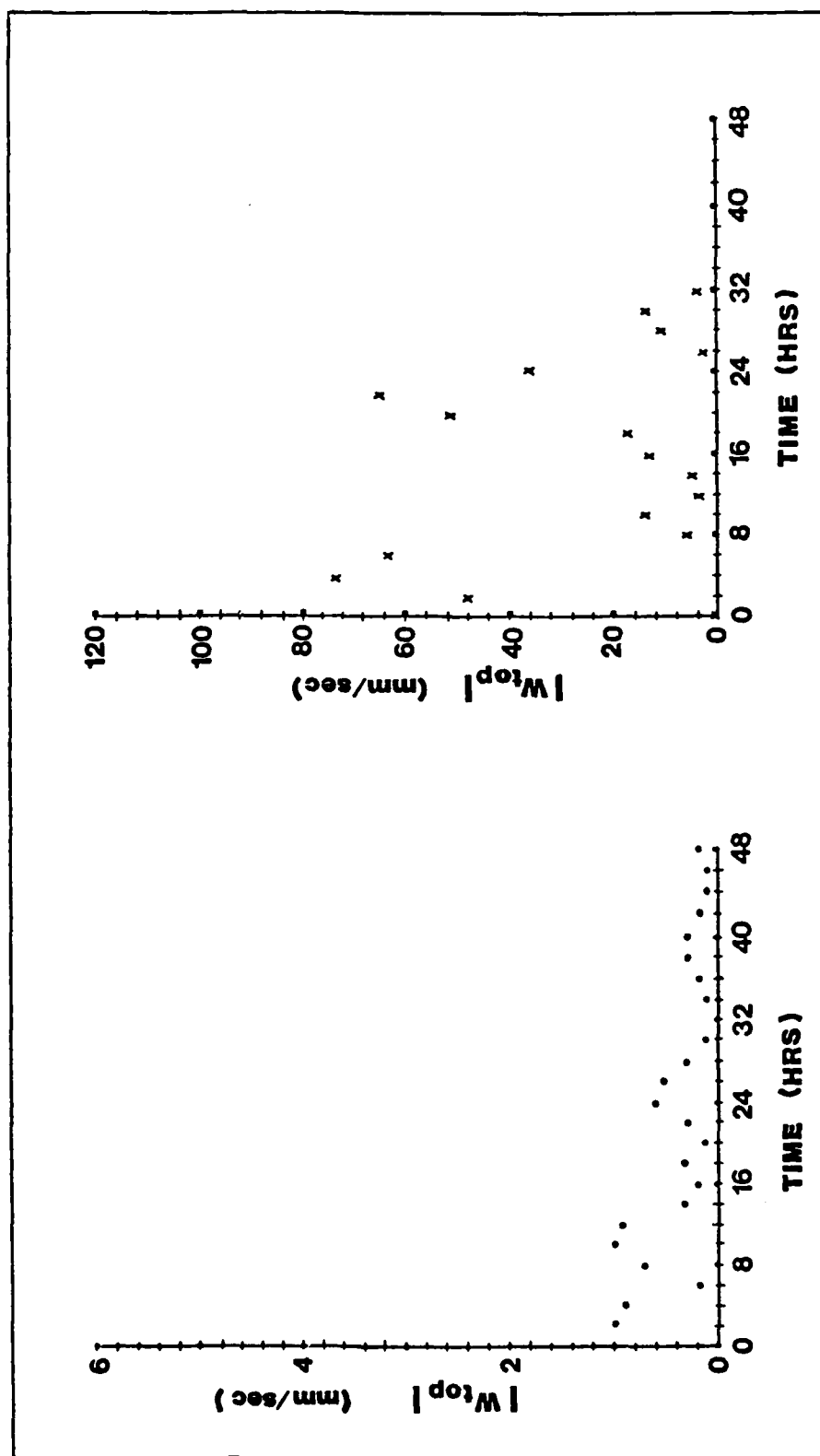


Figure 24. Variation of the vertical velocity at the top of the model with time above grid point 14 for the local terrain following coordinate system (•), left, and for the standard terrain following coordinate system (x), right. Condition B.

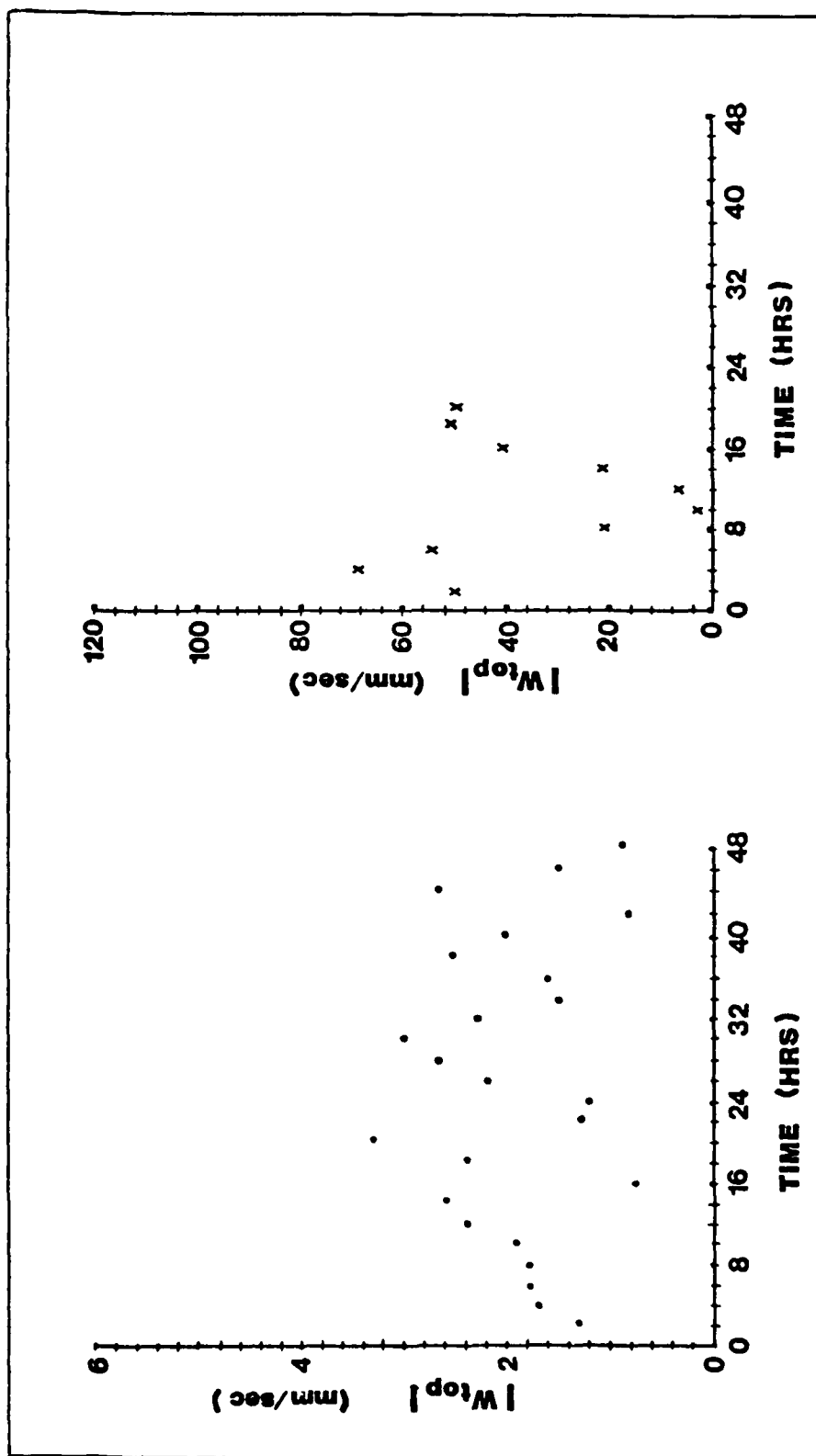


Figure 25. Variation of the vertical velocity at the top of the model with time above grid point 14 for the local terrain following coordinate system (.), left, and for the standard terrain following coordinate system (x), right. Condition C.

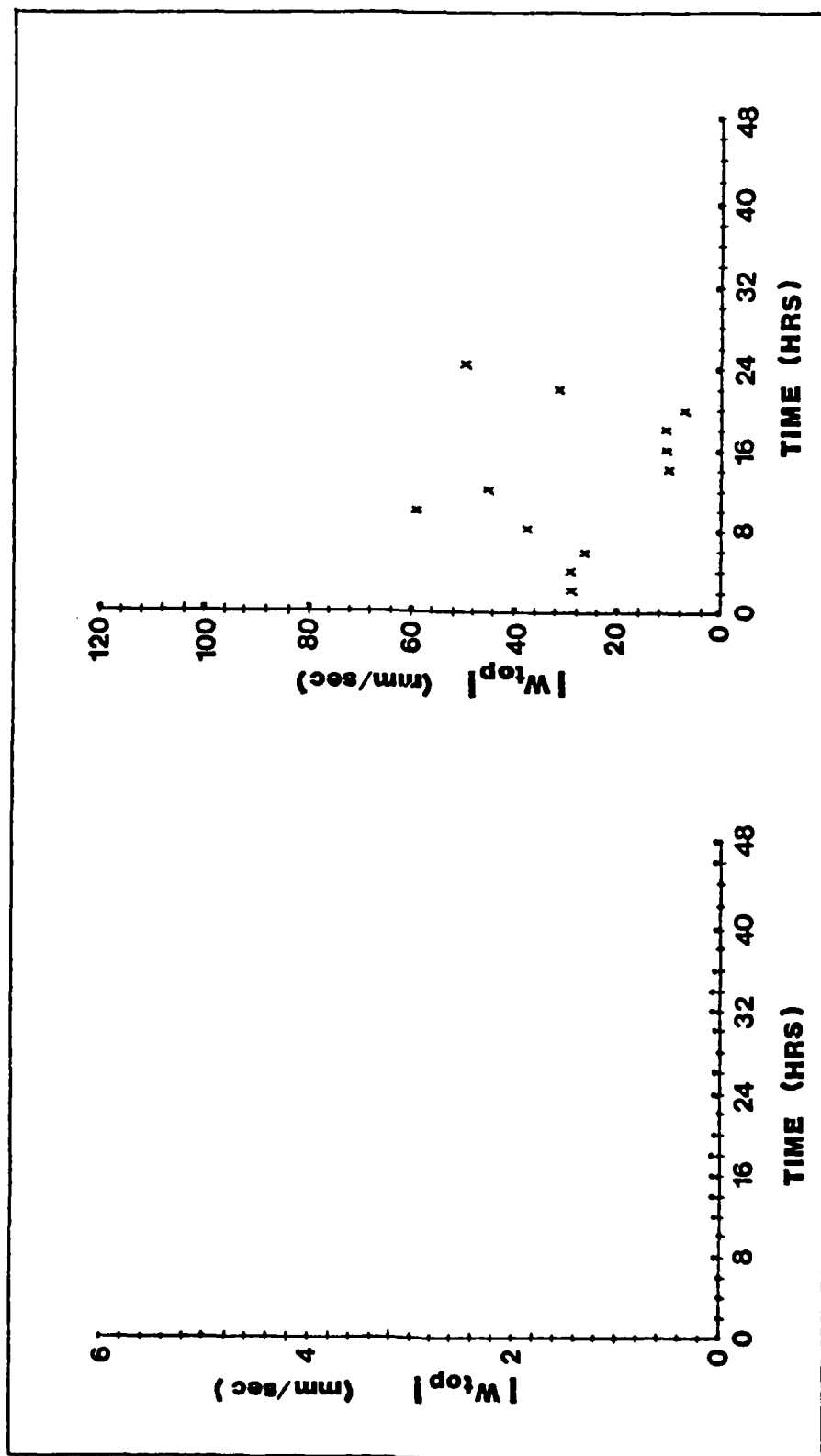


Figure 26. Variation of the vertical velocity at the top of the model with time above grid point 15 for the local terrain following coordinate system (.), left, and for the standard terrain following coordinate system (x), right. Condition A.

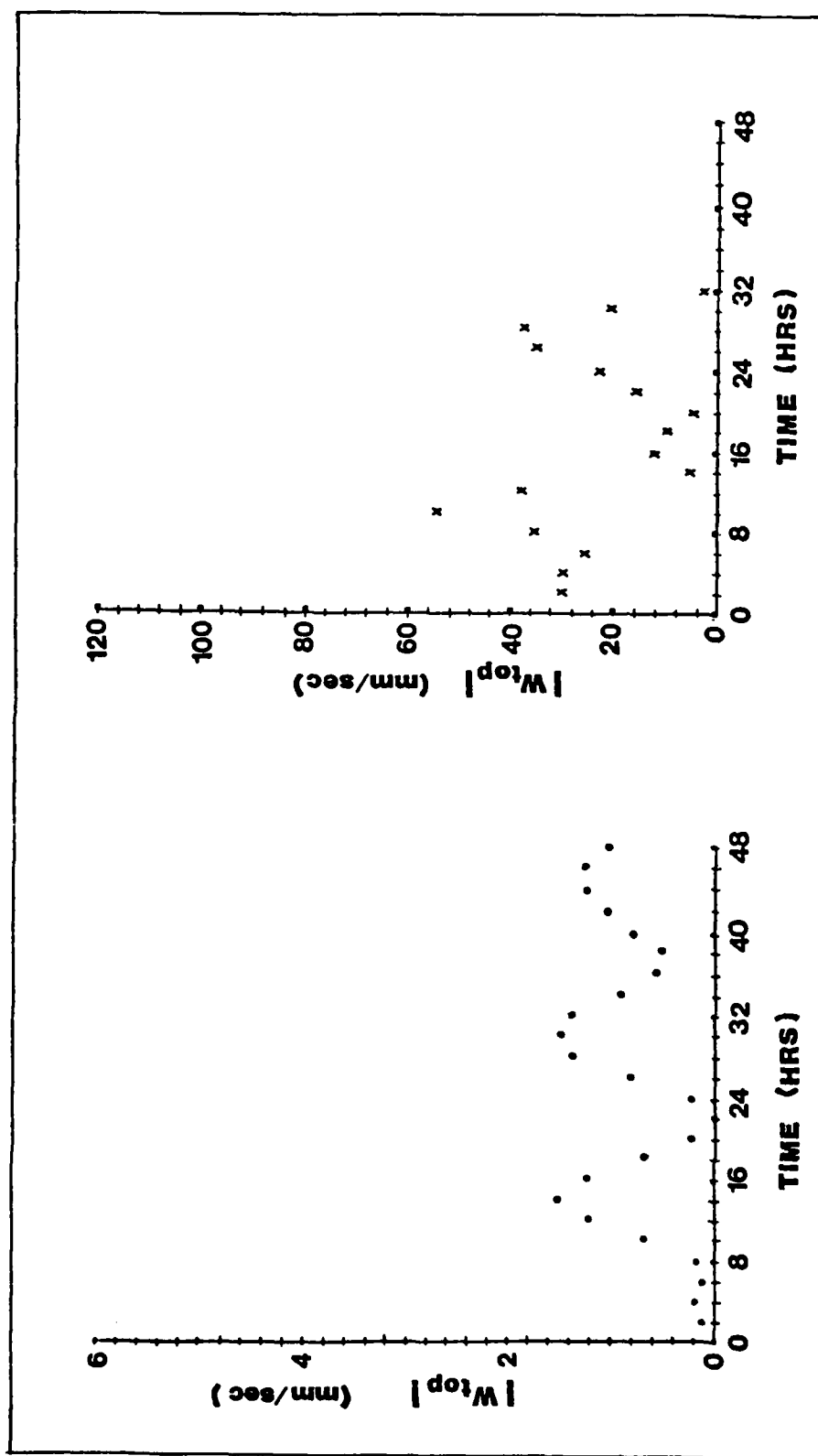


Figure 27. Variation of the vertical velocity at the top of the model with time above grid point 15 for the local terrain following coordinate system (.), left, and for the standard terrain following coordinate system (x), right. Condition B.

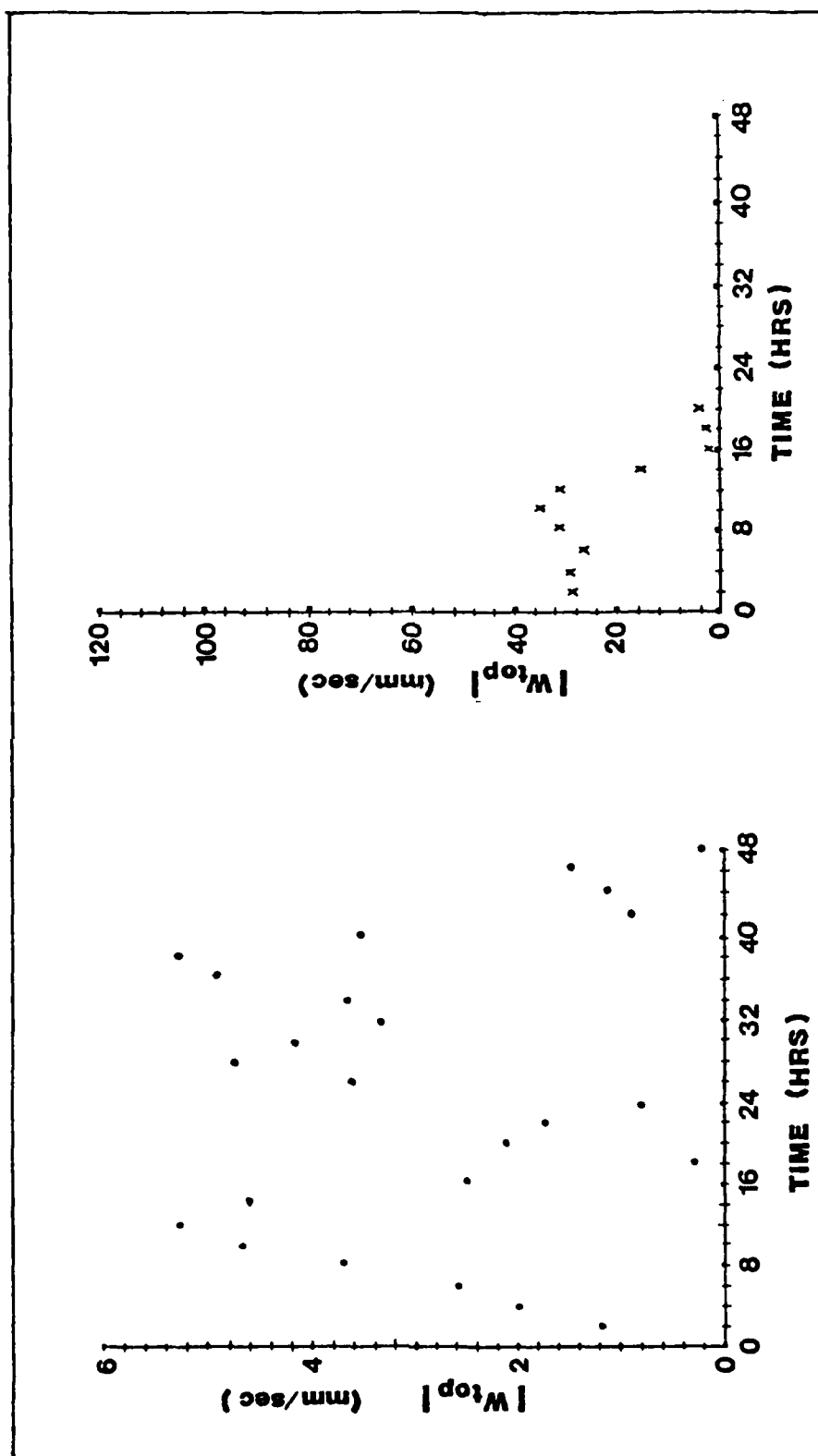


Figure 28. Variation of the vertical velocity at the top of the model with time above grid point 15 for the local terrain following coordinate system (.), left, and for the standard terrain following coordinate system (x), right. Condition C.

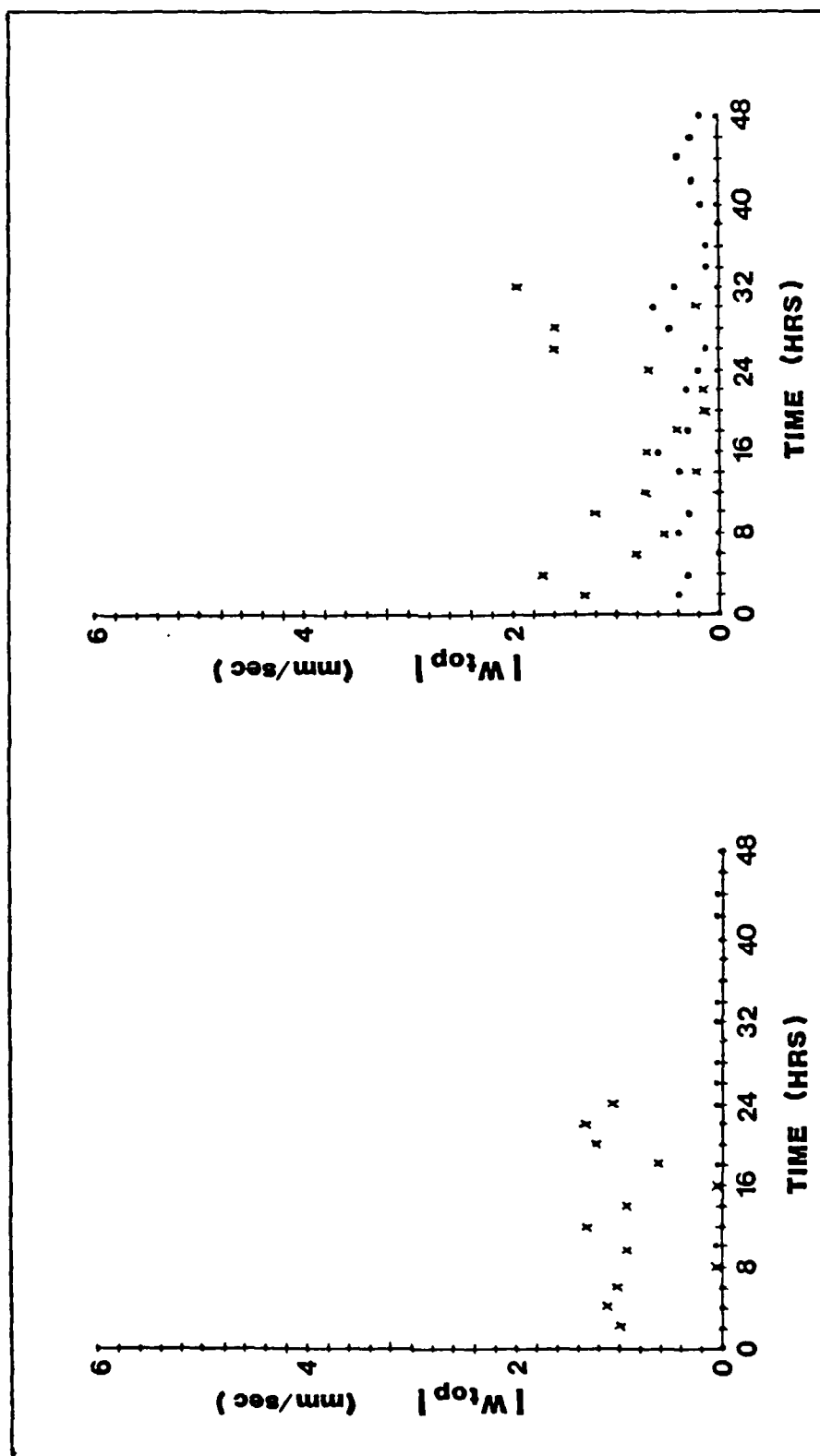


Figure 29. Variation of the vertical velocity at the top of the model with time above grid point 18 for the local (.) and standard (x) terrain following coordinate systems. Condition A, left, and Condition B, right.

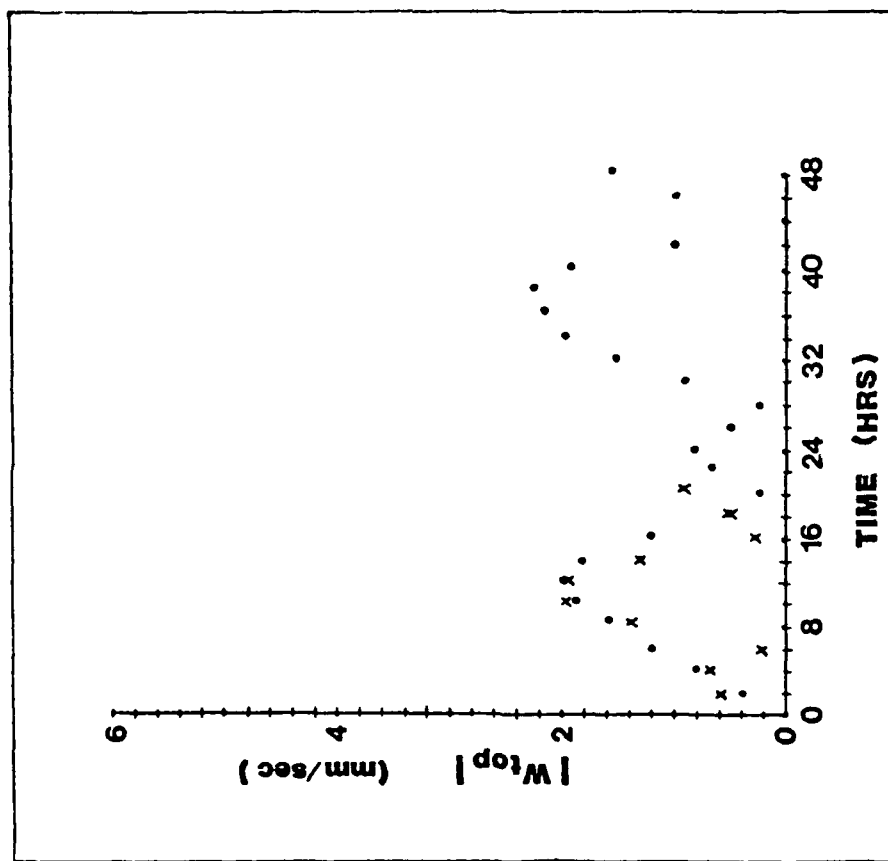


Figure 30. Variation of the vertical velocity at the top of the model with time above grid point 18 for the local (.) and standard (x) terrain following coordinate systems. Condition C.

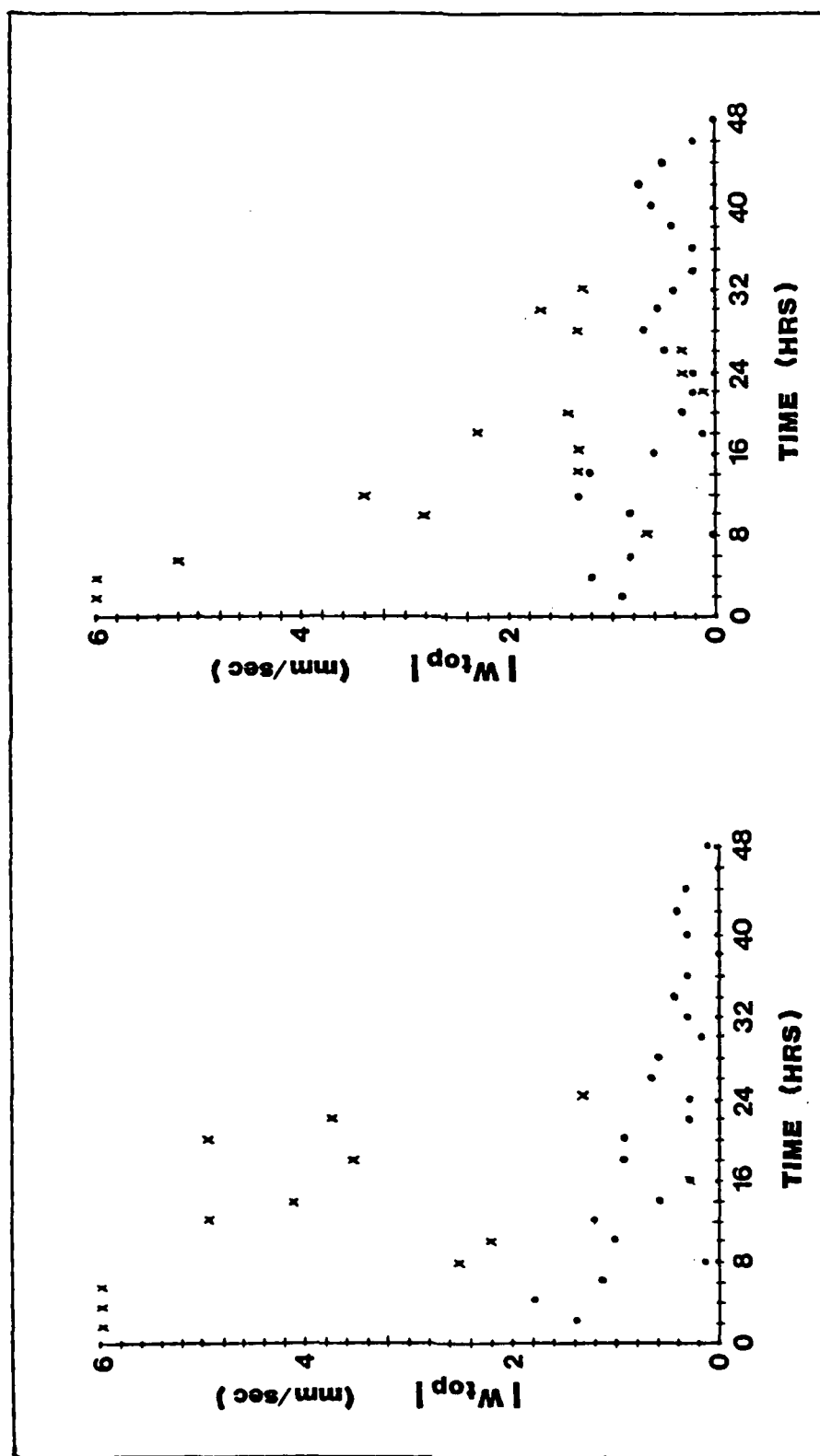


Figure 31. Variation of the vertical velocity at the top of the model with time above grid point 25 for the local (.) and standard (x) terrain following coordinate systems. Condition A, left, and Condition B, right.

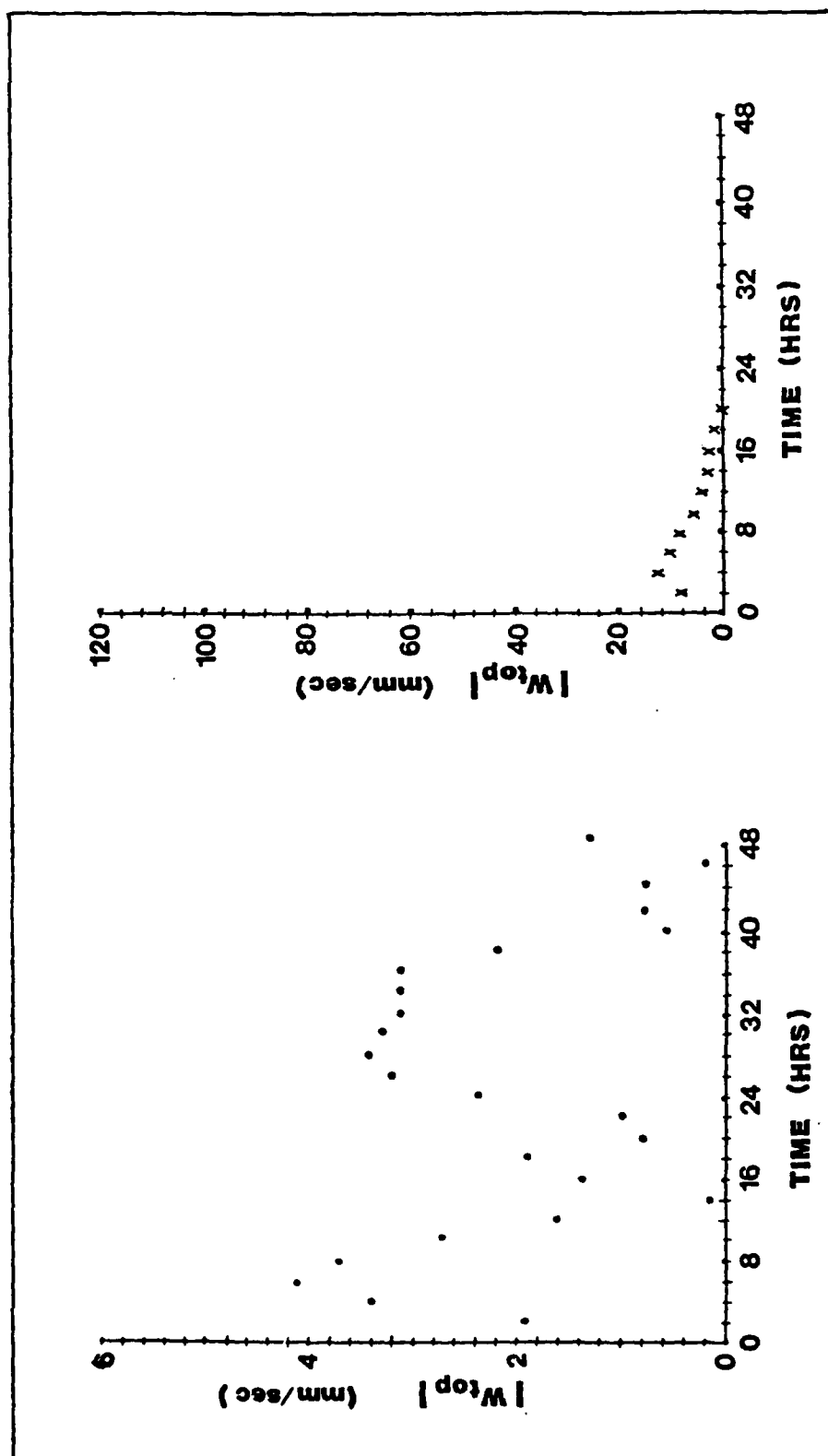


Figure 32. Variation of the vertical velocity at the top of the model with time above grid point 25 for the local terrain following coordinate system (.), left, and for the standard terrain following coordinate system (x), right. Condition C.

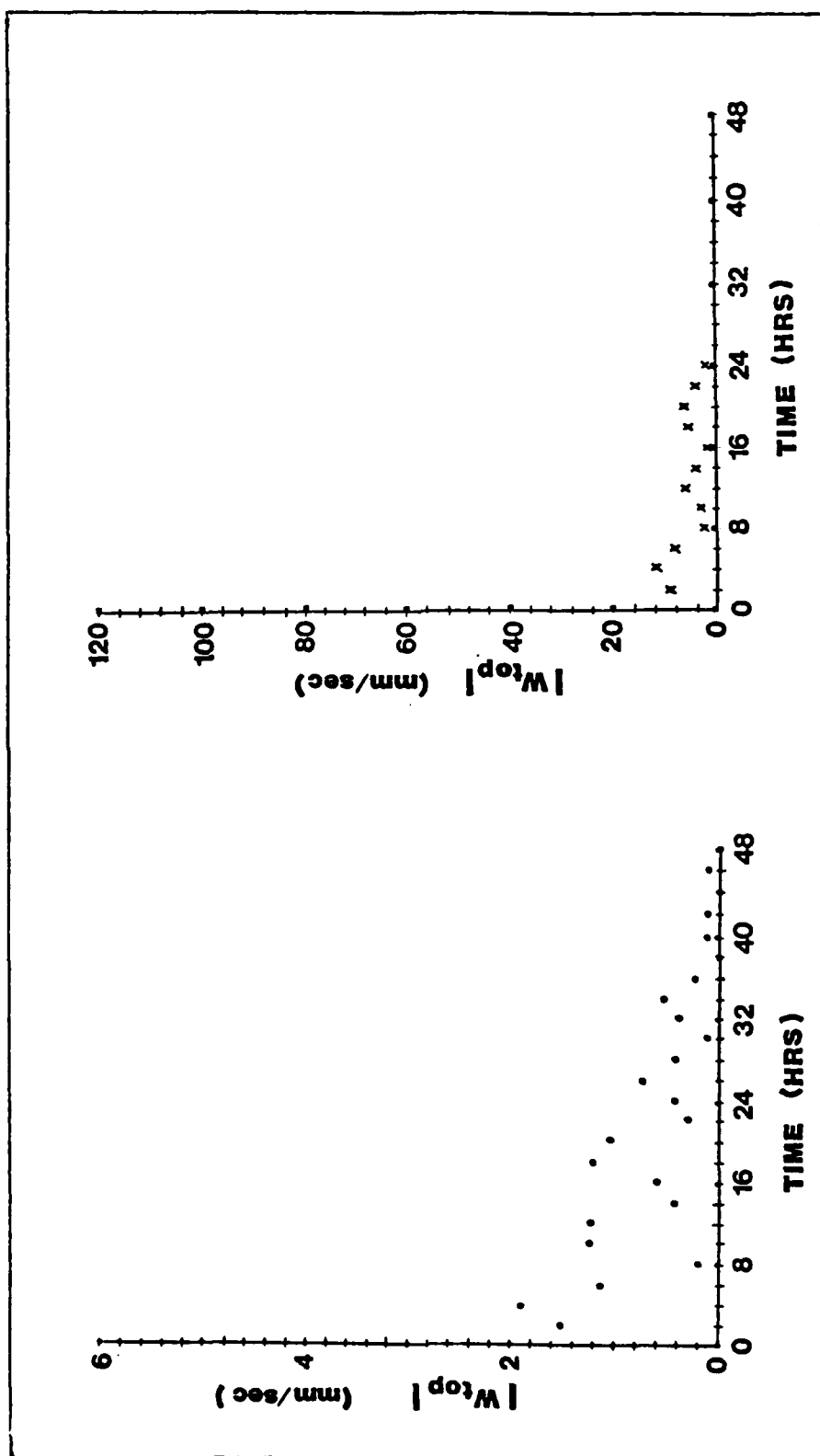


Figure 33. Variation of the vertical velocity at the top of the model with time above grid point 27 for the local terrain following coordinate system (.), left, and the standard terrain following coordinate system (x), right. Condition A.

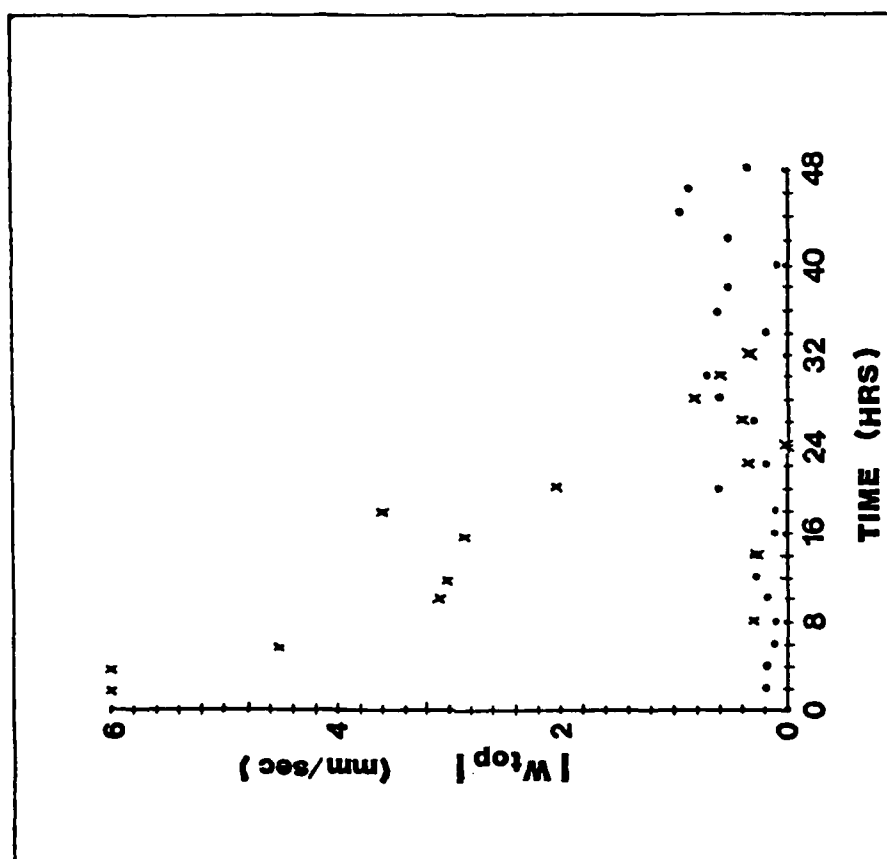


Figure 34. Variation of the vertical velocity at the top of the model with time above grid point 27 for the local (.) and standard (x) terrain following coordinate systems. Condition B.

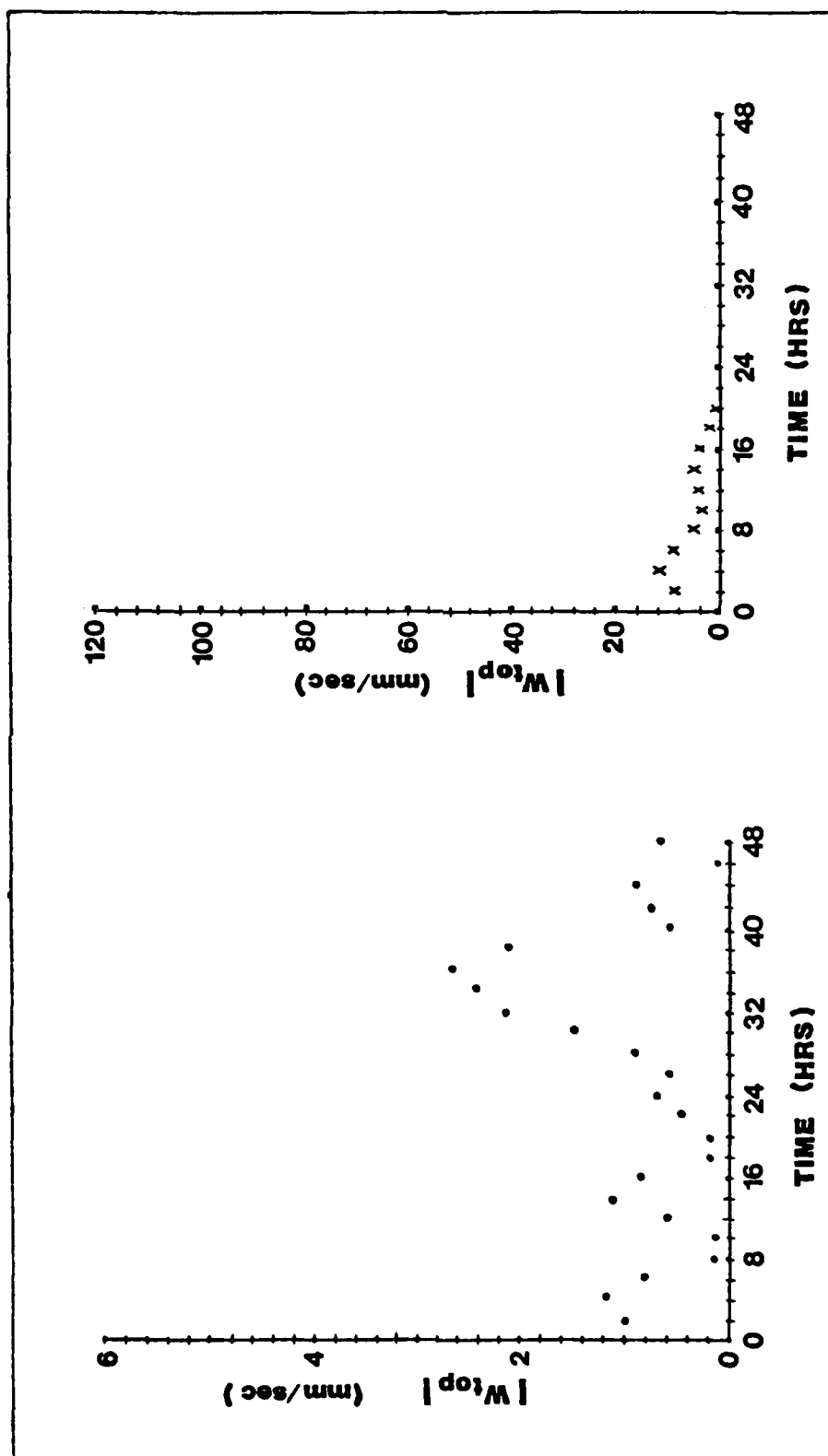


Figure 35. Variation of the vertical velocity at the top of the model with time above grid point 27 for the local terrain following coordinate system (.), left, and for the standard terrain following coordinate system (x), right. Condition C.

Table 4. A coordinate system comparison of averages of $|U_{\max}|$ from selected grid points.

Grid Point		Average $ U_{\max} $ (m/sec)	
		Local Terrain Following Coordinate System	Standard Terrain Following Coordinate System
CONDITION A	5	1.6	16.0
	14	0.2	12.9
	15	0.3	2.3
	27	0.4	1.9
	25	0.1	0.2
	18	0.0	0.2
CONDITION B	5	2.4	17.0
	14	0.8	11.4
	15	0.8	3.1
	27	0.5	1.5
	25	0.2	0.2
	18	0.2	0.4
CONDITION C	5	1.4	13.4
	14	3.7	11.0
	15	2.8	3.9
	27	3.7	2.6
	25	1.2	1.0
	18	2.6	0.4

Table 5. A coordinate system comparison of averages of $|W_{top}|$ from selected grid points.

Grid Point		Average $ W_{top} $ (mm/sec)	
		Local Terrain Following Coordinate System	Standard Terrain Following Coordinate System
CONDITION A	5	0.8	56.2
	14	0.2	31.8
	15	0.1	26.7
	27	0.5	9.6
	25	0.5	4.1
	18	0.4	0.8
CONDITION B	5	2.3	60.9
	14	0.4	25.1
	15	0.7	22.4
	27	0.3	2.3
	25	0.5	2.3
	18	0.3	0.9
CONDITION C	5	2.3	55.9
	14	1.8	33.5
	15	2.8	18.6
	27	0.9	5.2
	25	2.0	5.0
	18	1.1	0.9

flow associated with truncation error.

A numerical instability was apparently caused when the standard terrain following coordinate system was employed. The presence of this instability may indicate that the present terrain configuration cannot be resolved by the standard system without additional smoothing. If this is indeed the case, the local system enjoys an additional advantage over the standard system. That advantage is the ability to resolve a coarser terrain configuration and still present stable solutions.

Figures 36 through 47 present an opportunity to examine the horizontal variation of the truncation error produced by the two coordinate systems. These figures show the integrated vertical velocity field at the top of the model for each case tested after integrations of eight and eighteen hours. If the air was rising the barb points up; if the air was sinking, the barb points down. The plotting convention is as follows: \uparrow = 1mm/sec, \uparrow = 55mm/sec, \uparrow = 10mm/sec, and \downarrow = 85mm/sec (too large to plot).

7.2 Latitude

7.2.1 Purpose

The purpose of this test is to determine the sensitivity of the forecast vertical motion field to latitude.

7.2.2 Test Description

As discussed in Chapter 1, the phenomena believed responsible for boundary layer convergence are the diurnal oscillation of eddy stresses and buoyancy forces above sloping terrain. Closely associated with these diurnal forcings is the inertial oscillation of the ageostrophic component of the wind. This oscillation is linked to the formation of

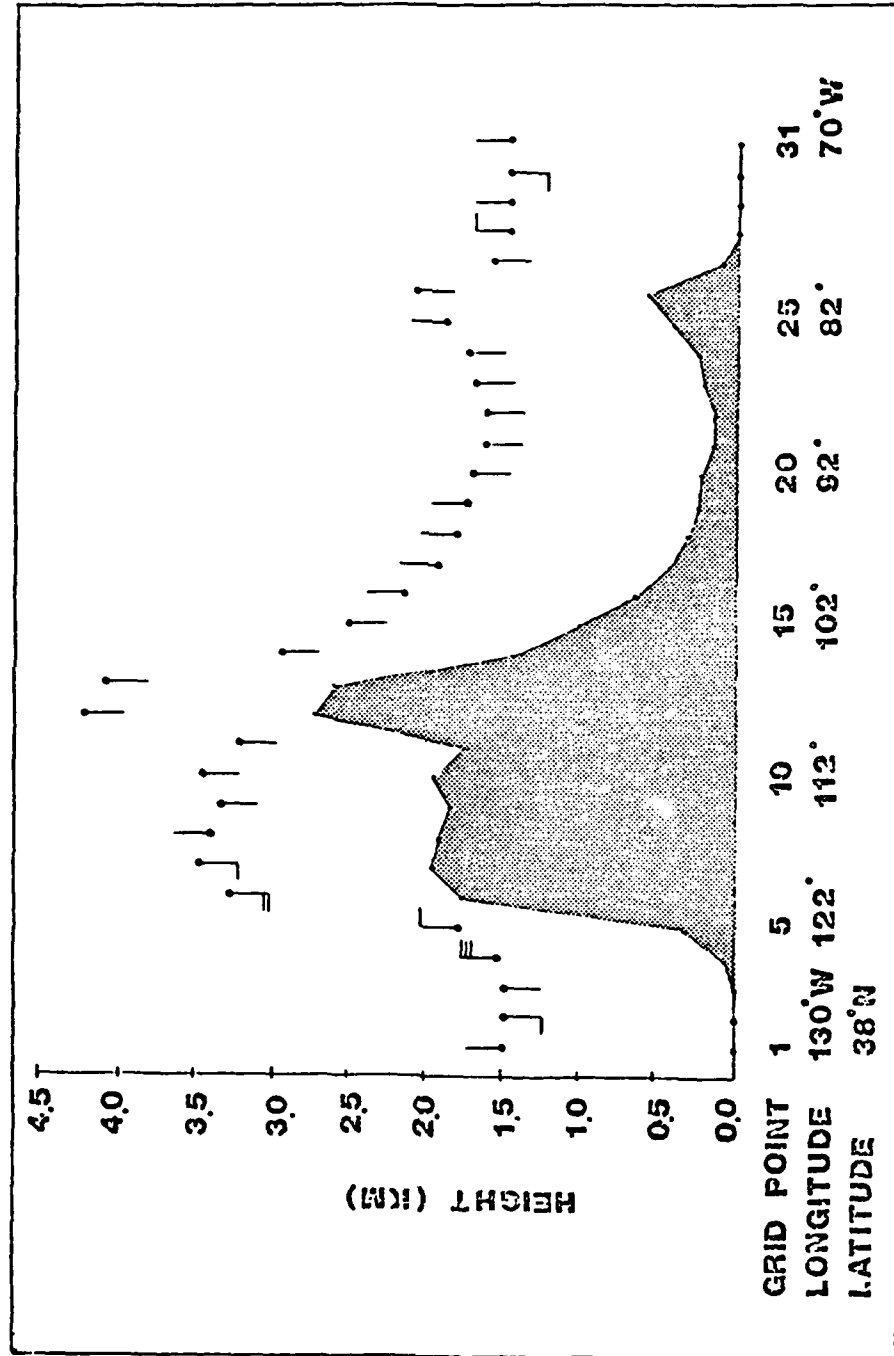


Figure 36. Vertical velocity at the top of the model after eight hours with the local terrain following coordinate system, Condition A. The plotting convention is as follows: ↑ represents rising motion, ↓ represents sinking motion, ↑ = 1mm/sec, ↓ = 5mm/sec, ↑ = 10mm/sec, and ↓ = 85mm/sec (too large to plot).

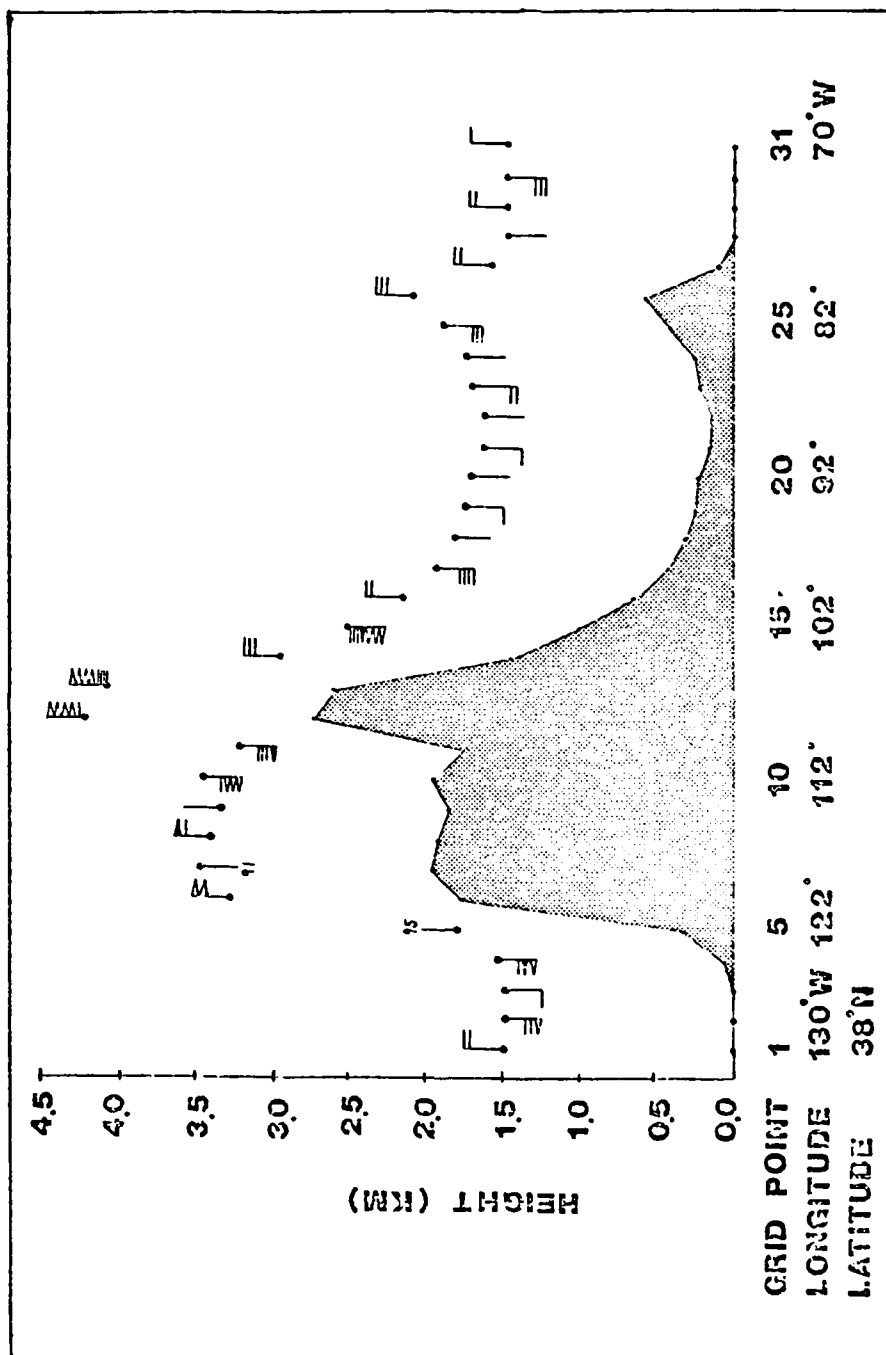


Figure 37. Vertical velocity at the top of the model after eight hours with the standard terrain following coordinate system, Condition A. See Figure 36 for plotting convention.

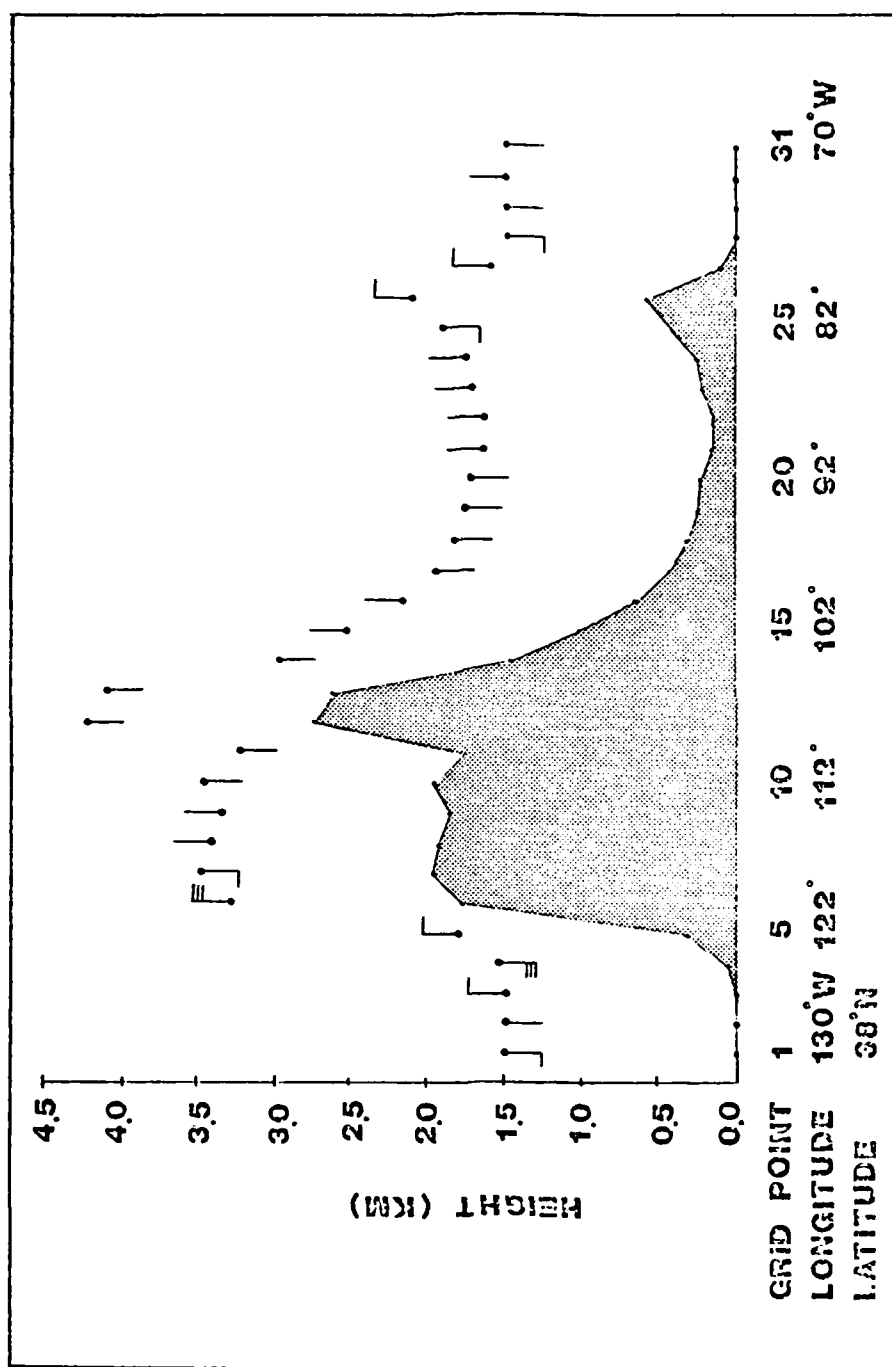


Figure 38. Vertical velocity at the top of the model after 18 hours with the local terrain following coordinate system, Condition A. See Figure 36 for plotting convention.

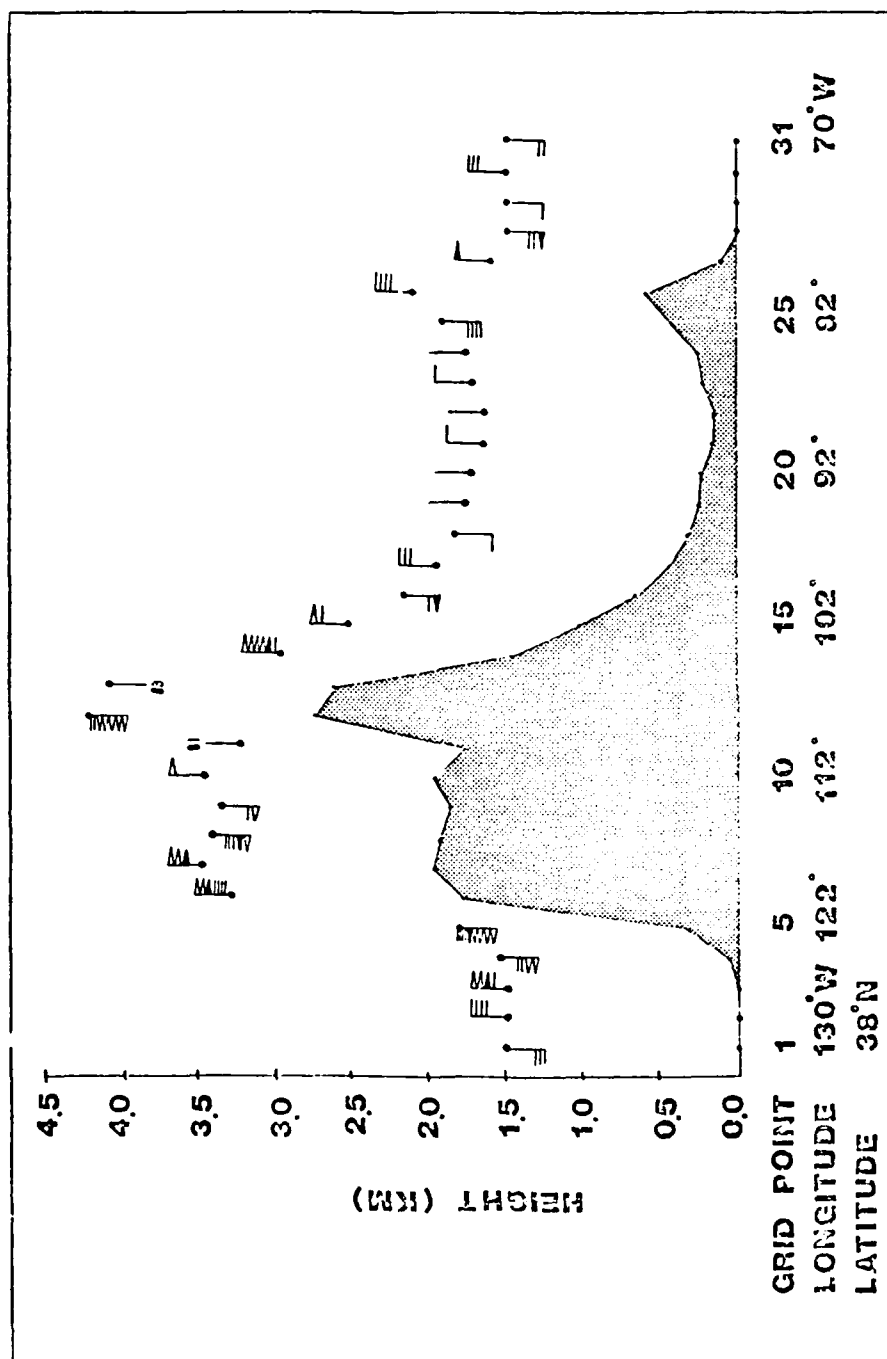


Figure 39. Vertical velocity at the top of the model after 18 hours with the standard terrain following coordinate system, Condition A. See Figure 36 for plotting convention.

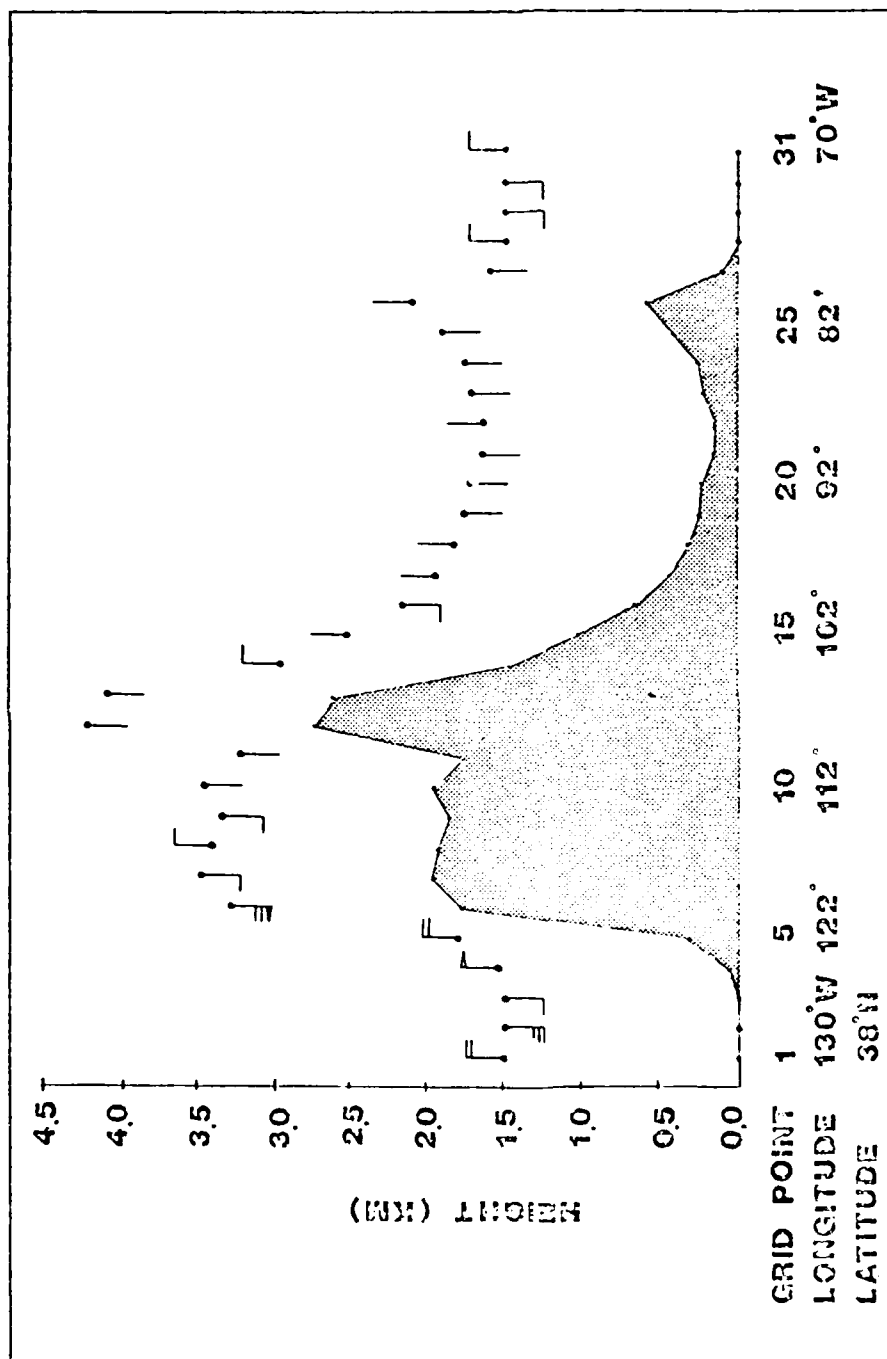


Figure 40. Vertical velocity at the top of the model after eight hours with the local terrain following coordinate system, Condition B. See Figure 36 for plotting convention.

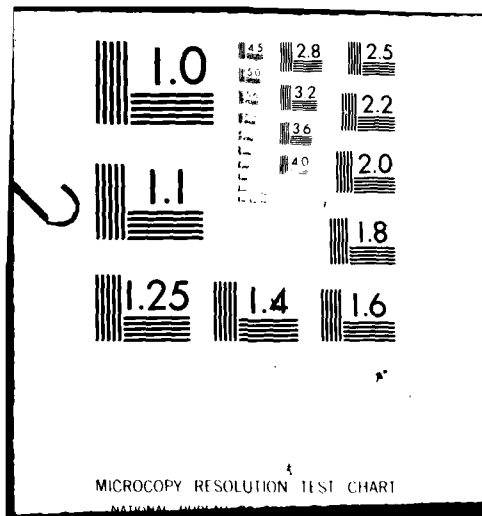
UNCLASSIFIED

AIR FORCE INST OF TECH WRIGHT-PATTERSON AFB OH F/6 4/2
TOPOGRAPHICALLY INDUCED DIURNAL BOUNDARY LAYER OSCILLATIONS: TW--ETC(U)
DEC 79 D W MCLAWHORN NSF-ATM77-26094
AFIT-CI-79-269D NL

2.2

Q. 102

END
DATE
FILMED
2-8
DTIC



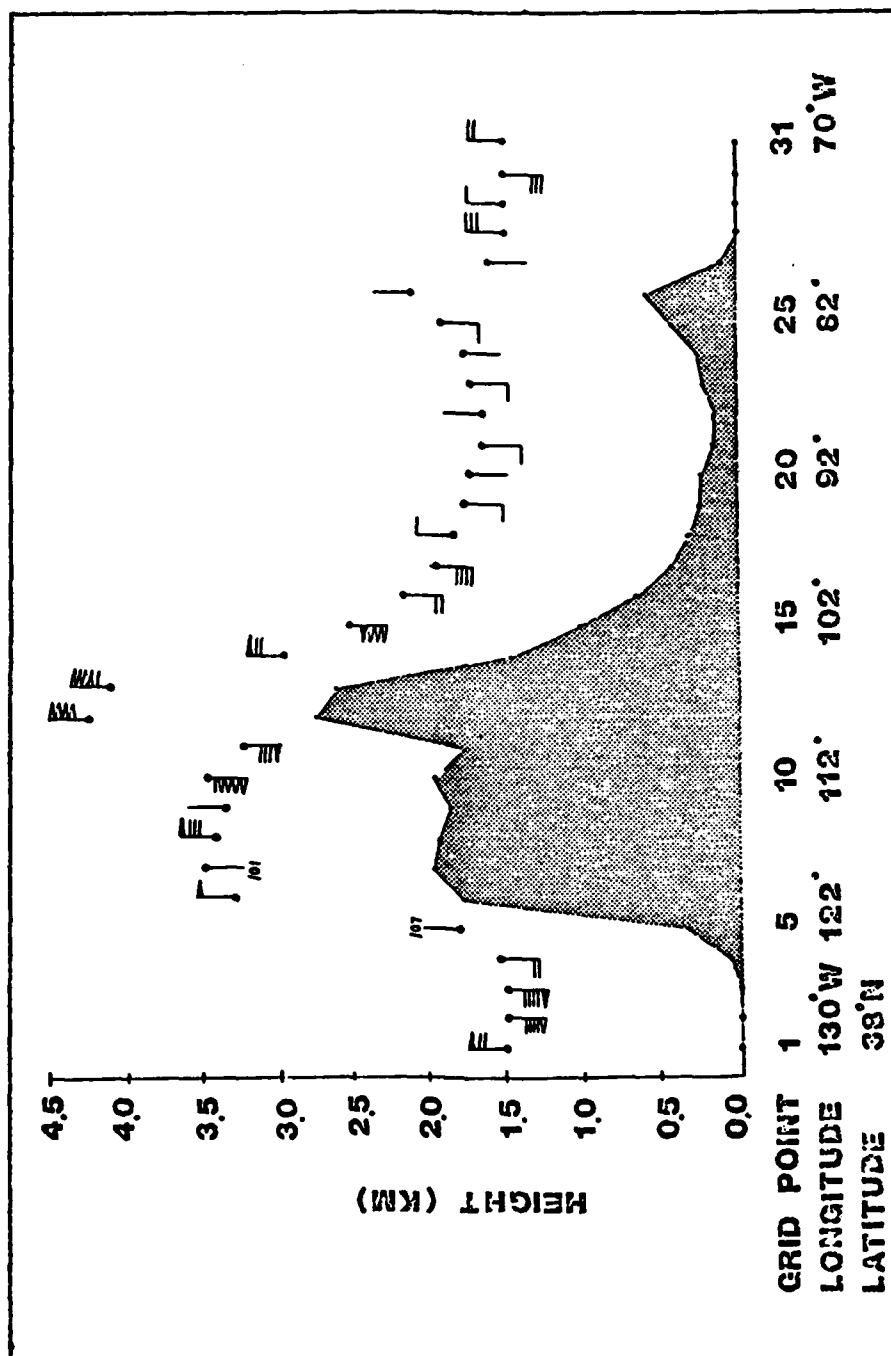


Figure 41. Vertical velocity at the top of the model after eight hours with the standard terrain following coordinate system, Condition B. See Figure 36 for plotting convention.

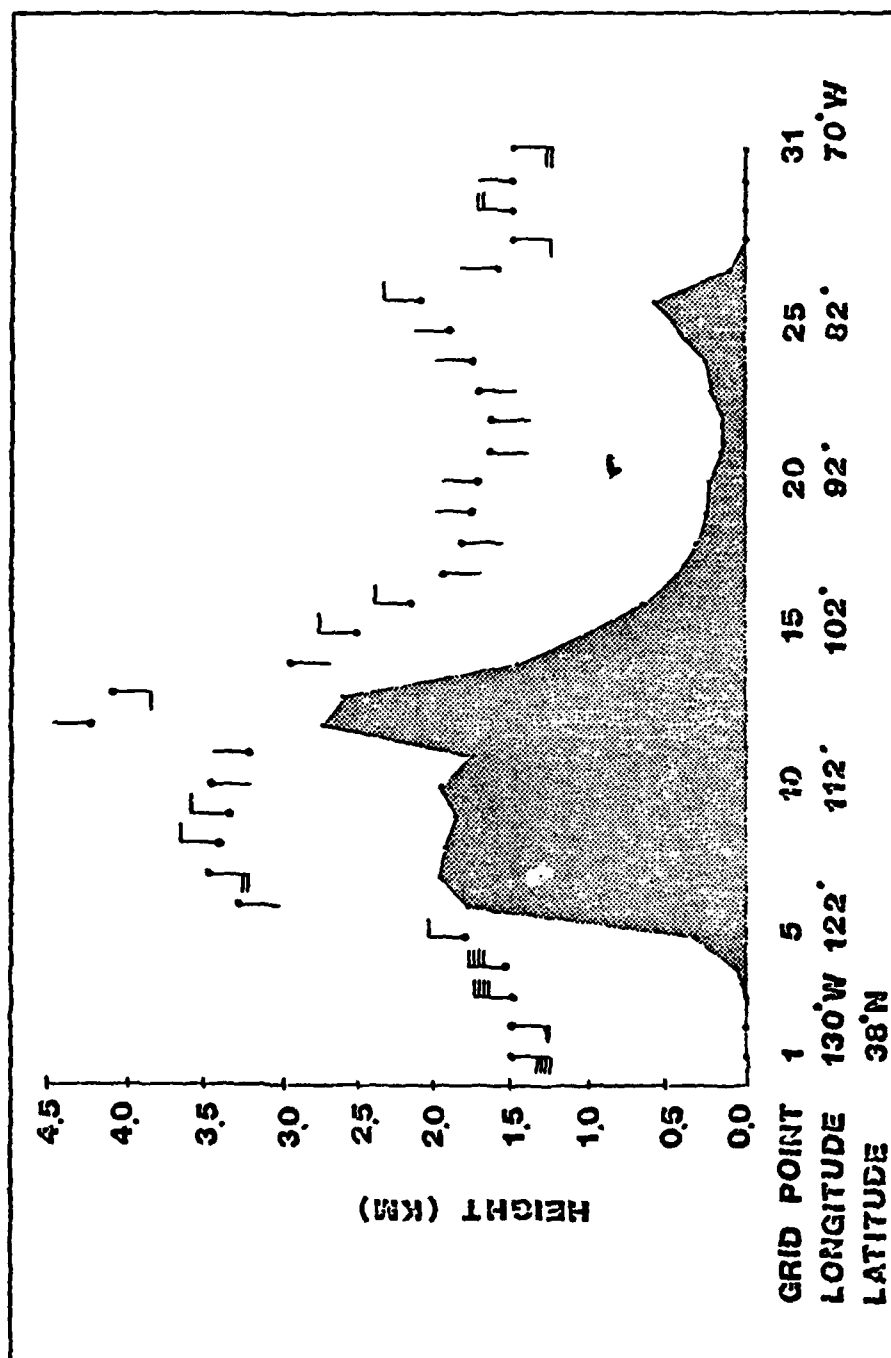


Figure 42. Vertical velocity at the top of the model after 18 hours with the local terrain following coordinate system, Condition B. See Figure 36 for plotting convention.

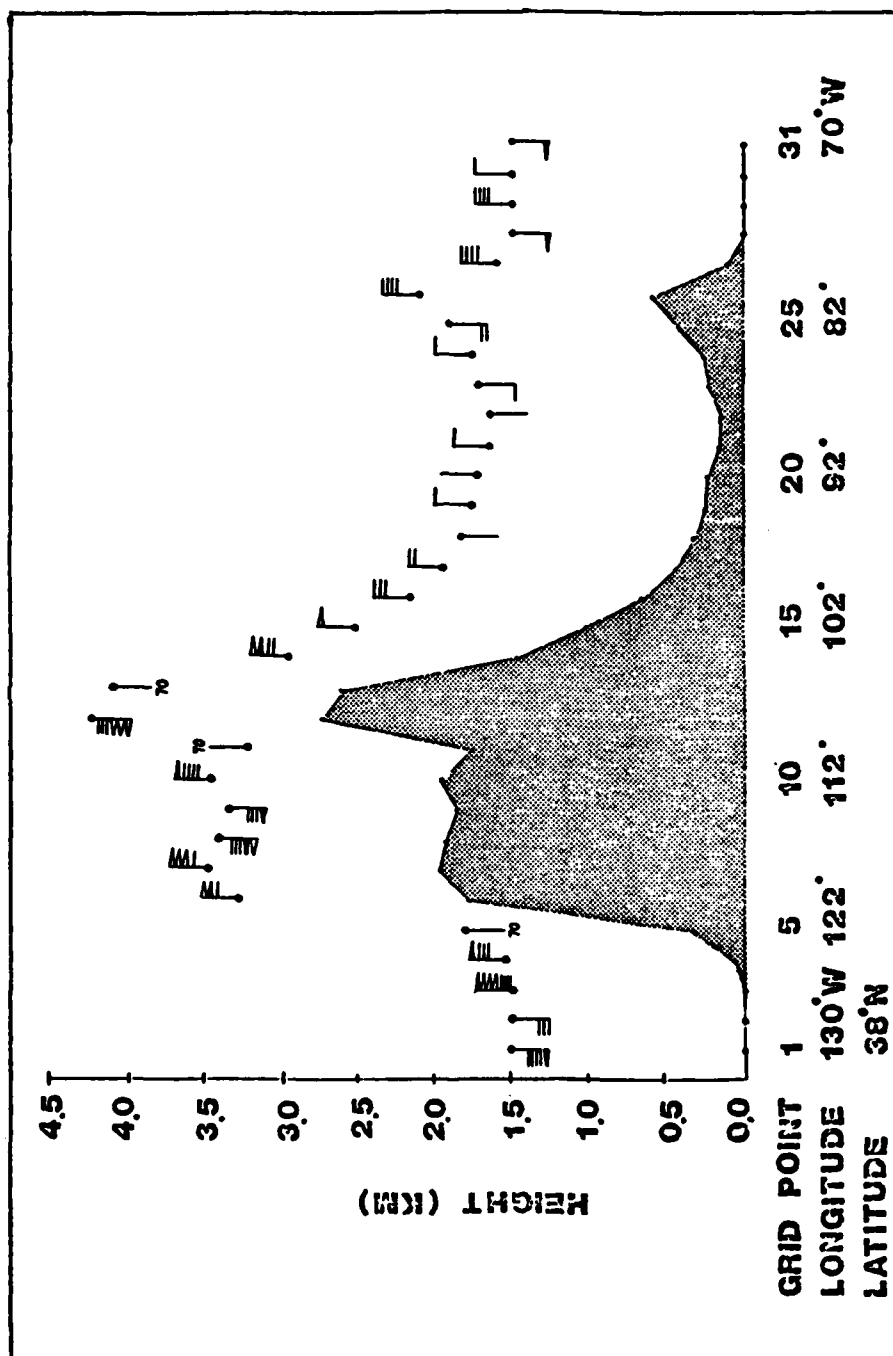


Figure 43. Vertical velocity at the top of the model after 18 hours with the standard terrain following coordinate systems, Condition B. See Figure 36 for plotting convention.

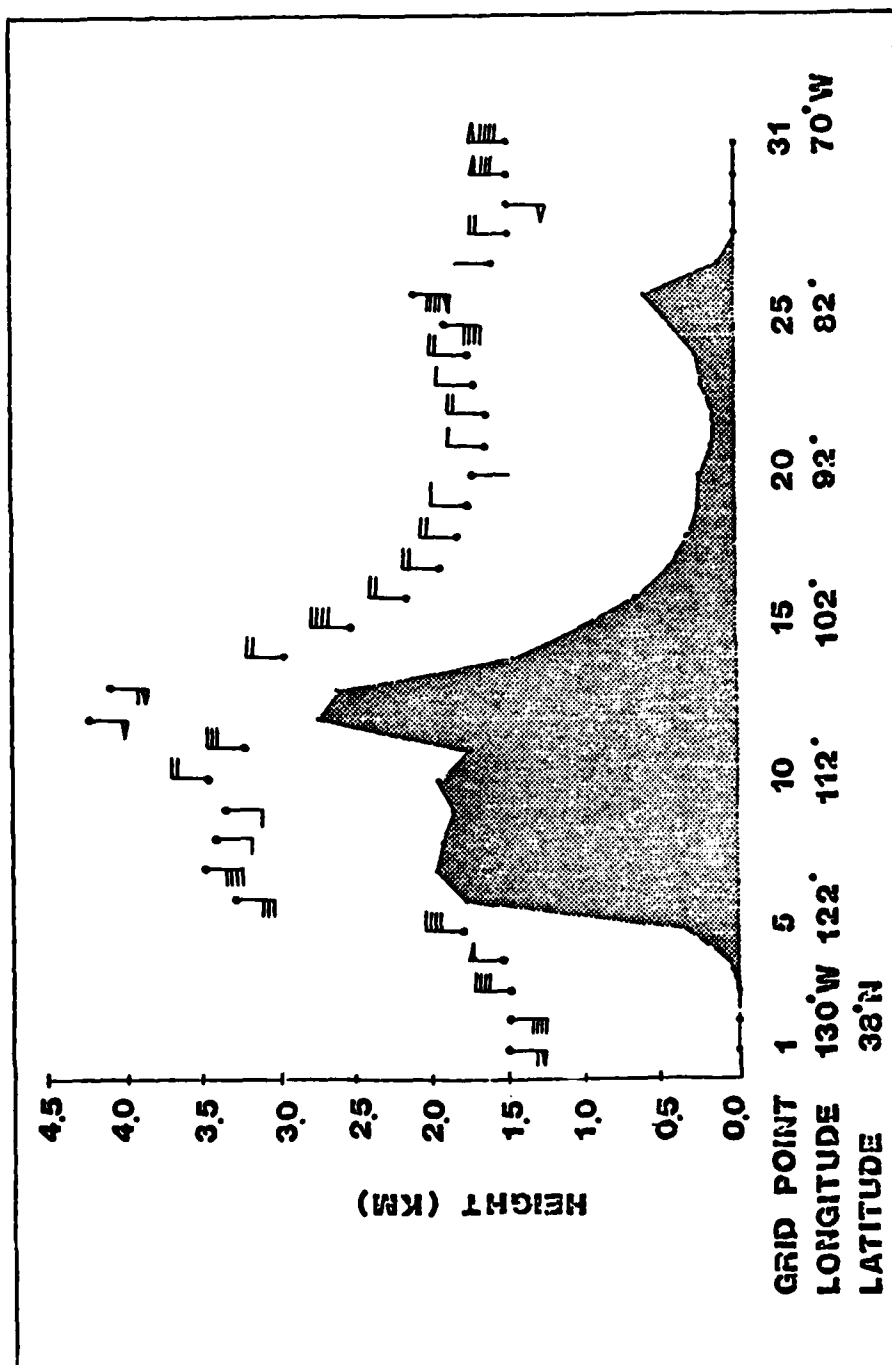


Figure 44. Vertical velocity at the top of the model after eight hours with the local terrain following coordinate system, Condition C. See Figure 36 for plotting convention.

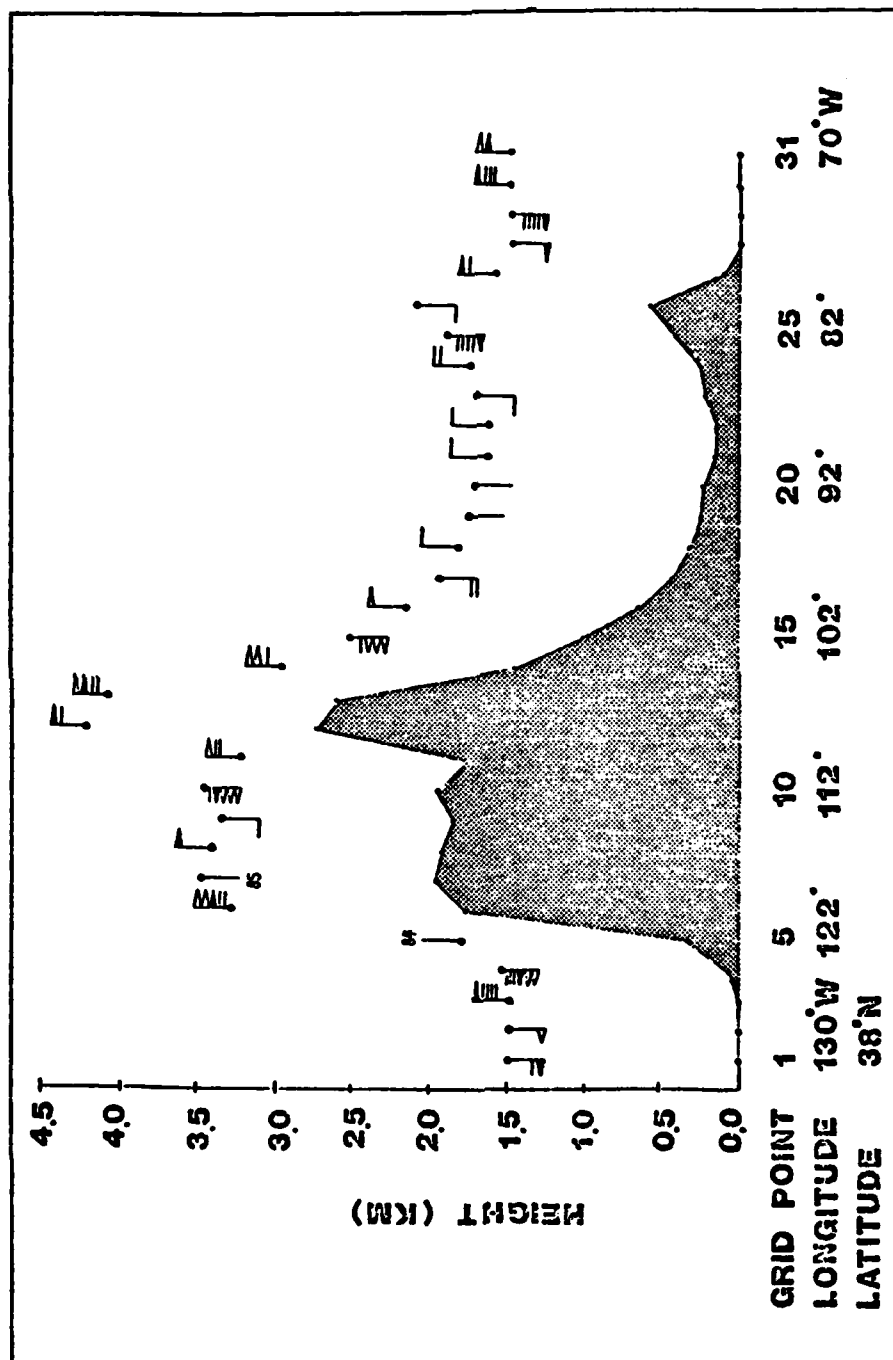


Figure 45. Vertical velocity at the top of the model after eight hours with the standard terrain following coordinate system, Condition C. See Figure 36 for plotting convention.

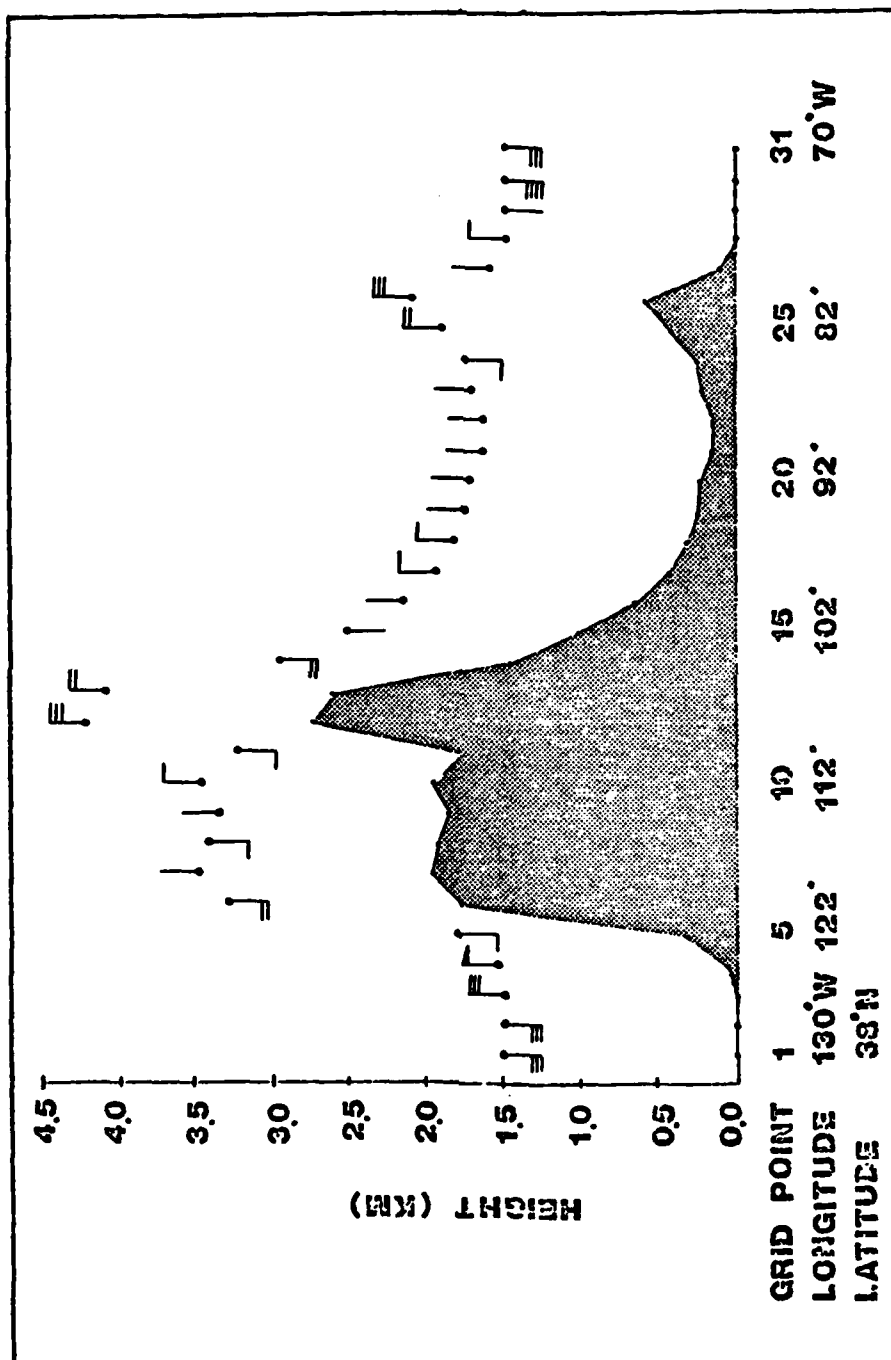


Figure 46. Vertical velocity at the top of the model after 18 hours with the local terrain following coordinate system, Condition C. See Figure 36 for plotting convention.

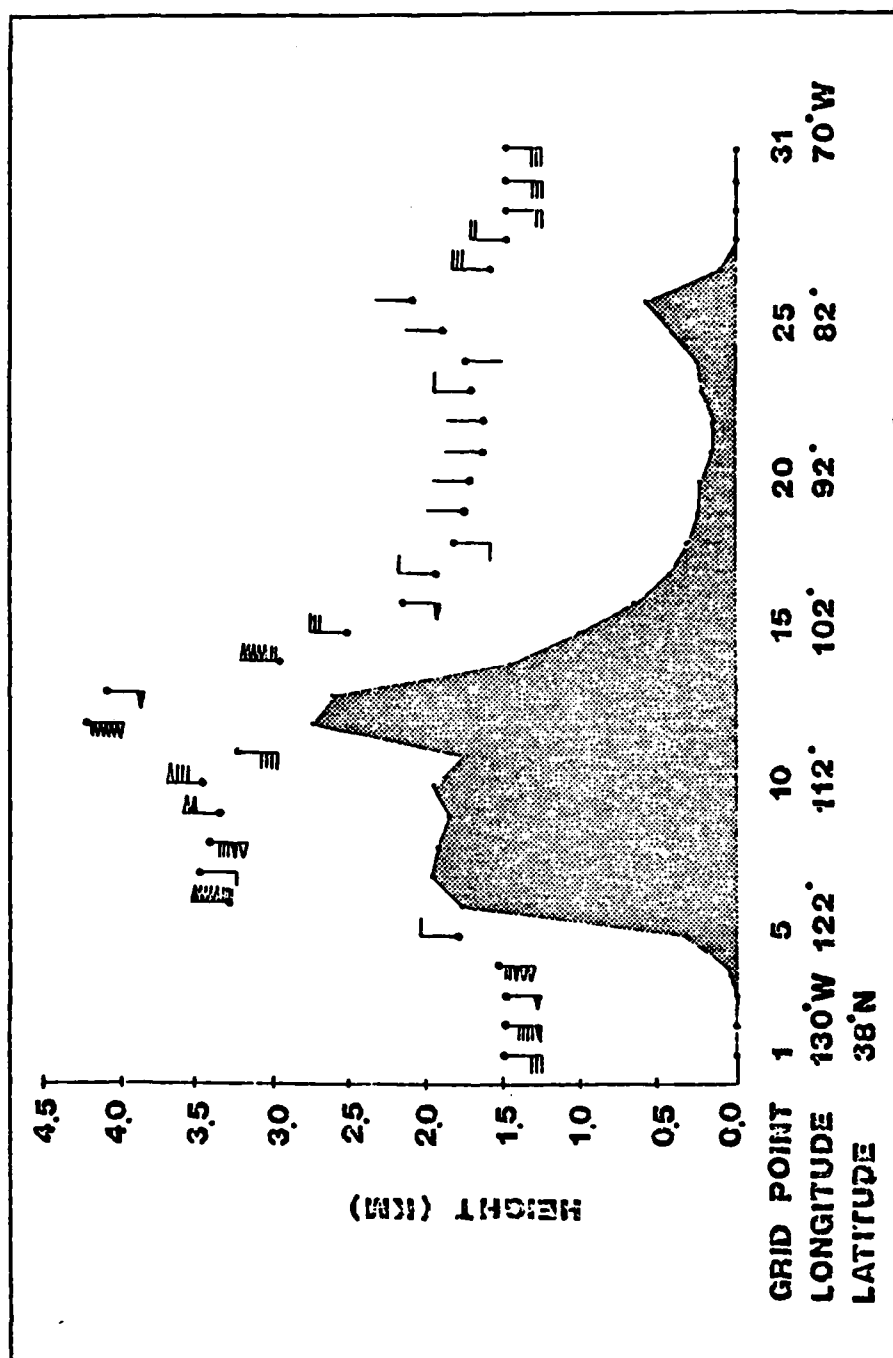


Figure 47. Vertical velocity at the top of the model after 18 hours with the standard terrain following coordinate system, Condition C. See Figure 36 for plotting convention.

low level jets and boundary layer convergence. The period of this oscillation is a function of latitude through the coriolis parameter.

$$\text{Period} = 2\pi/f \quad \text{where } f = \text{Coriolis parameter}$$

$$f = 2\Omega \sin\phi \quad \text{where } \Omega = \text{earth's angular velocity}$$

$$\phi = \text{latitude}$$

The lower the latitude, the longer the period; therefore, boundary layer convergence fields formed by the above type of forcing, would tend to occur later in the day at lower latitudes due to the longer period of the natural oscillation. It should also be mentioned that the diurnal forcing may be in resonance with the natural period of oscillation at certain latitudes, thereby affecting the amplitude of the winds and possibly the boundary layer convergence.




It would therefore be of interest to examine the amplitude and phasing of the vertical motion fields forecast by the boundary layer model for different latitudes.

Latitudes 38° ($f = .0000898$), 30° ($f = .00007292$), and 22° ($f = .00005463$) were selected for the tests. The initial atmosphere for the model contained moisture and a southerly geostrophic wind of 10m/sec. The U and W components of momentum were zero. The V component increased logarithmically from zero at the roughness height to 10m/sec at 50m and was then constant with height to the top of the model. The complete treatments for radiation and friction were used in these tests. The boundary layer model was executed for a 60 hour forecast period at latitudes 38° , 30° , and 22° .

7.2.3 Results

The amplitude and phase of the maximum vertical motion during the

forecast period above each grid point is depicted in Figures 48 through 50. The plotting convention is as follows:

A vector directed from the north denotes a midnight maximum, while one directed from the east denotes a 6 A.M. (local time) maximum, etc. Each barb () denotes 1mm/sec; each full barb () denotes 5mm/sec. Example: . The amplitude and phasing for the example is 1800 local time and 6mm/sec, respectively.

Changes in phase and amplitude are noted at many grid points. A closer examination is made of five grid points; the results, of which, are shown in Figures 51 through 55. These figures contain two parts. The upper part is a dial which depicts the phase and amplitude of W_{\max} for each latitude. The position of the latitude around the dial denotes the time of the maximum W for that latitude while the distance from the center of the dial denotes the amplitude. The amplitudes are plotted in mm/sec with the scale noted on the dial. The scale changes from dial to dial to better depict the particular combination of values to be plotted. The lower part of the figure shows the relative position of the grid point in question.

Figures 51 through 55 show a change of phase of approximately six hours between latitudes 22° and 38° . The time of the maximum increases toward lower latitudes, which is in agreement with the above argument and Paegle's (1978) linearized solutions. There appears to be no significant change in amplitude between latitudes.

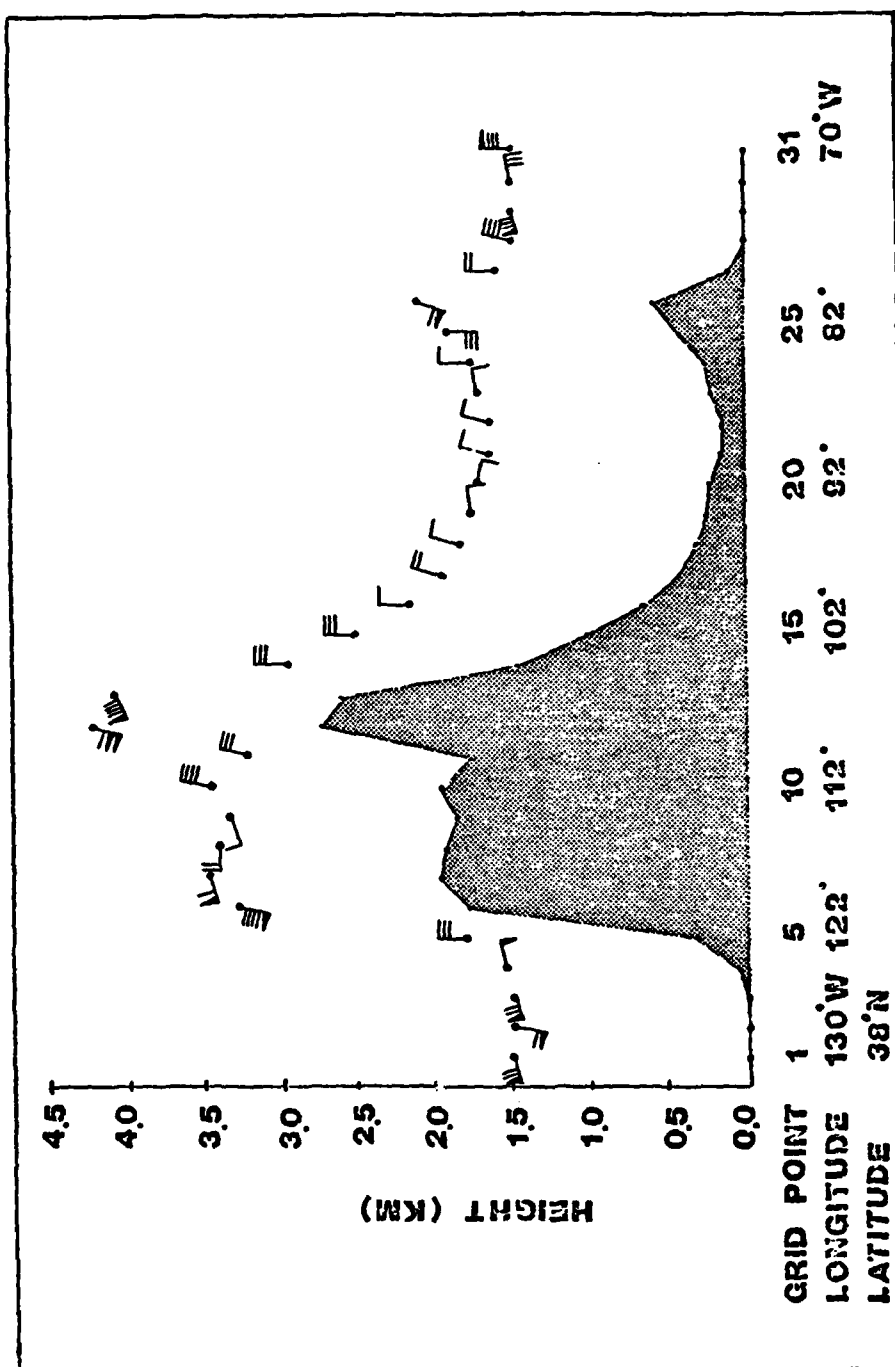


Figure 48. Amplitude and phase of the maximum vertical velocity forecast for 38° latitude. The plotting convention is as follows: A vector directed from the north denotes a midnight maximum, while one directed from the east denotes a 6 A.M. (local time) maximum, etc. 1mm/sec and 1° = 5mm/sec.

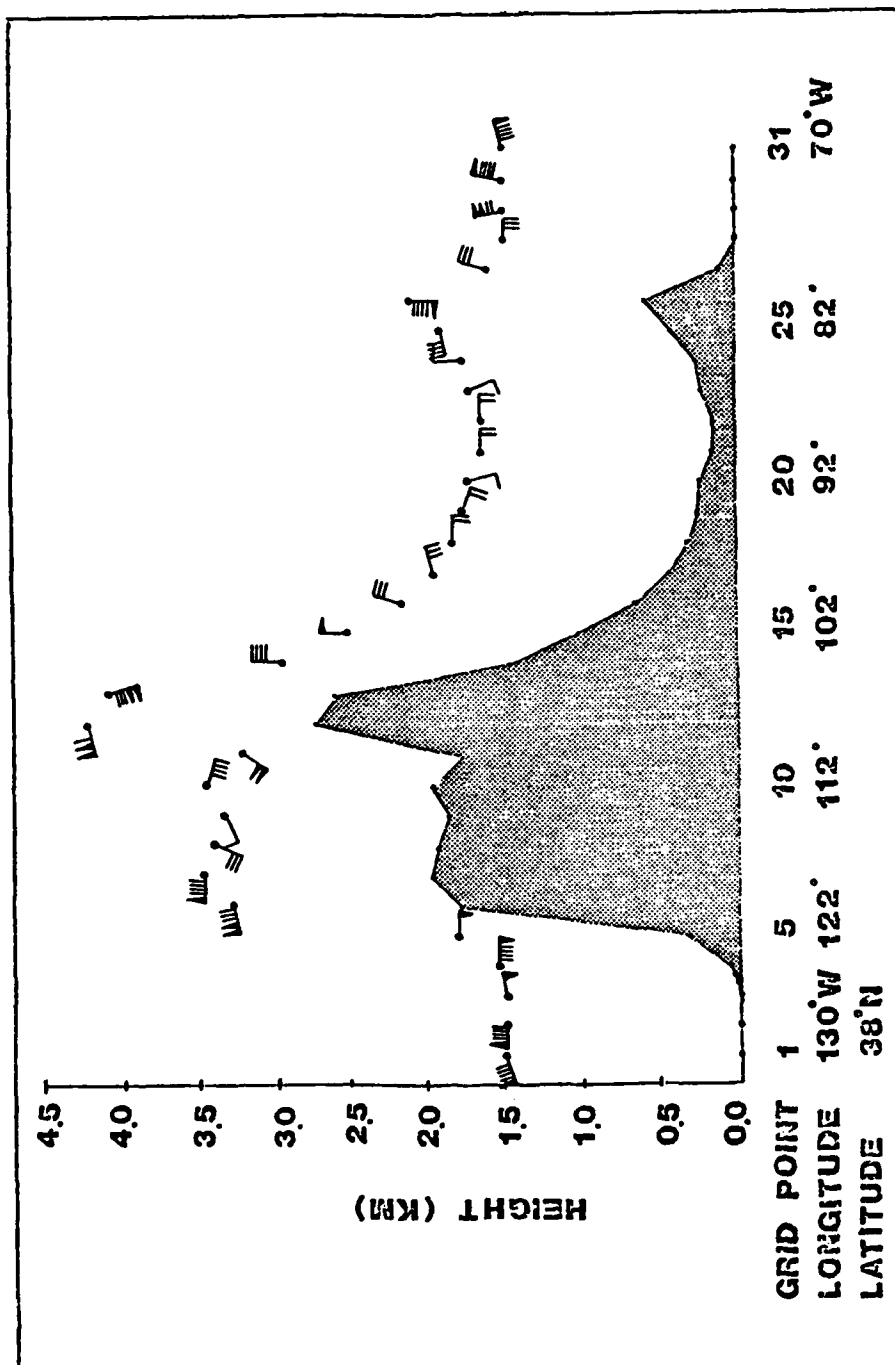


Figure 49. Amplitude and phase of the maximum vertical velocity forecast for 30° latitude. See Figure 48 for plotting convention.

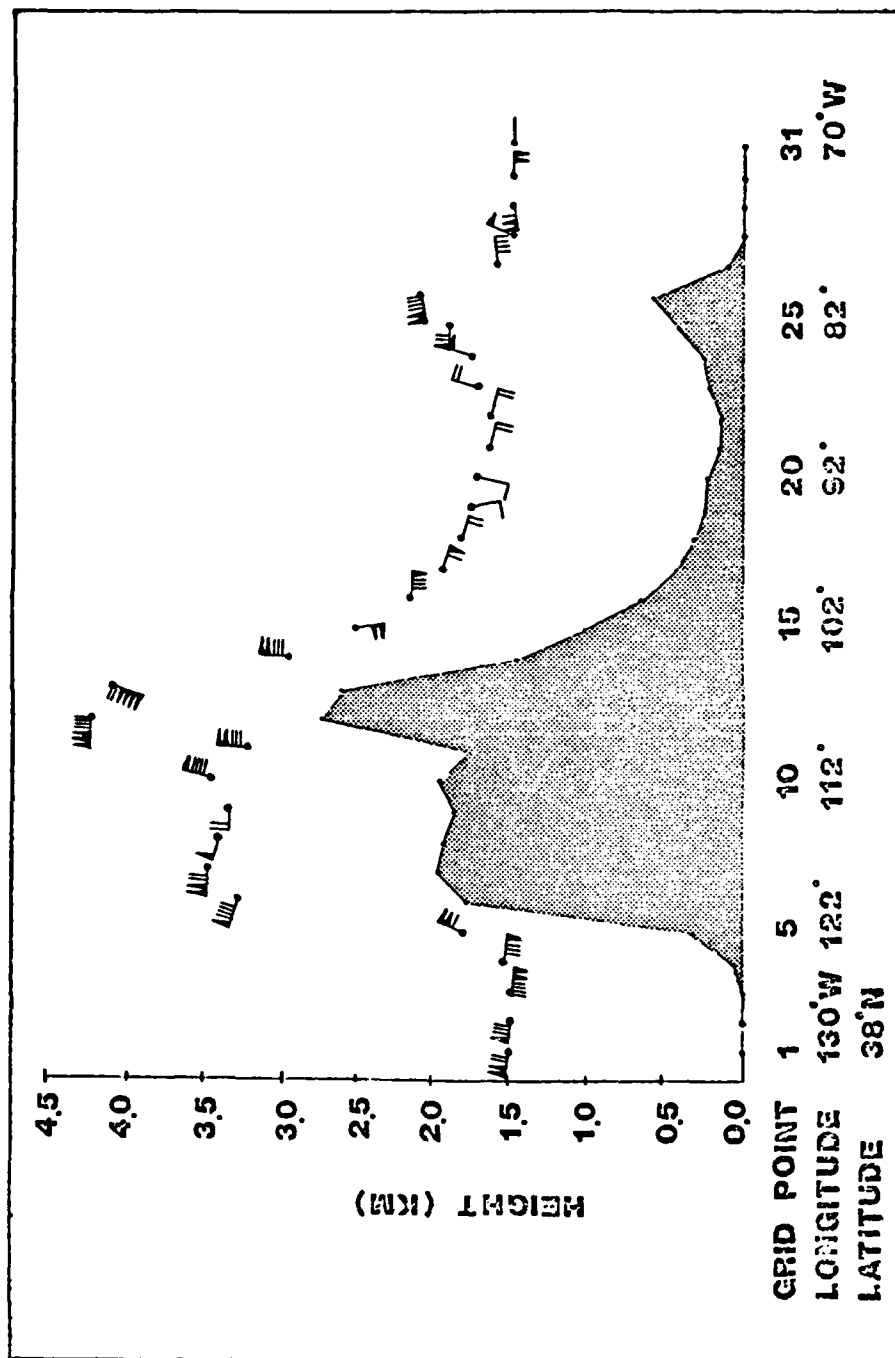


Figure 50. Amplitude and phase of the maximum vertical velocity forecast for 22° latitude. See Figure 48 for plotting convention.

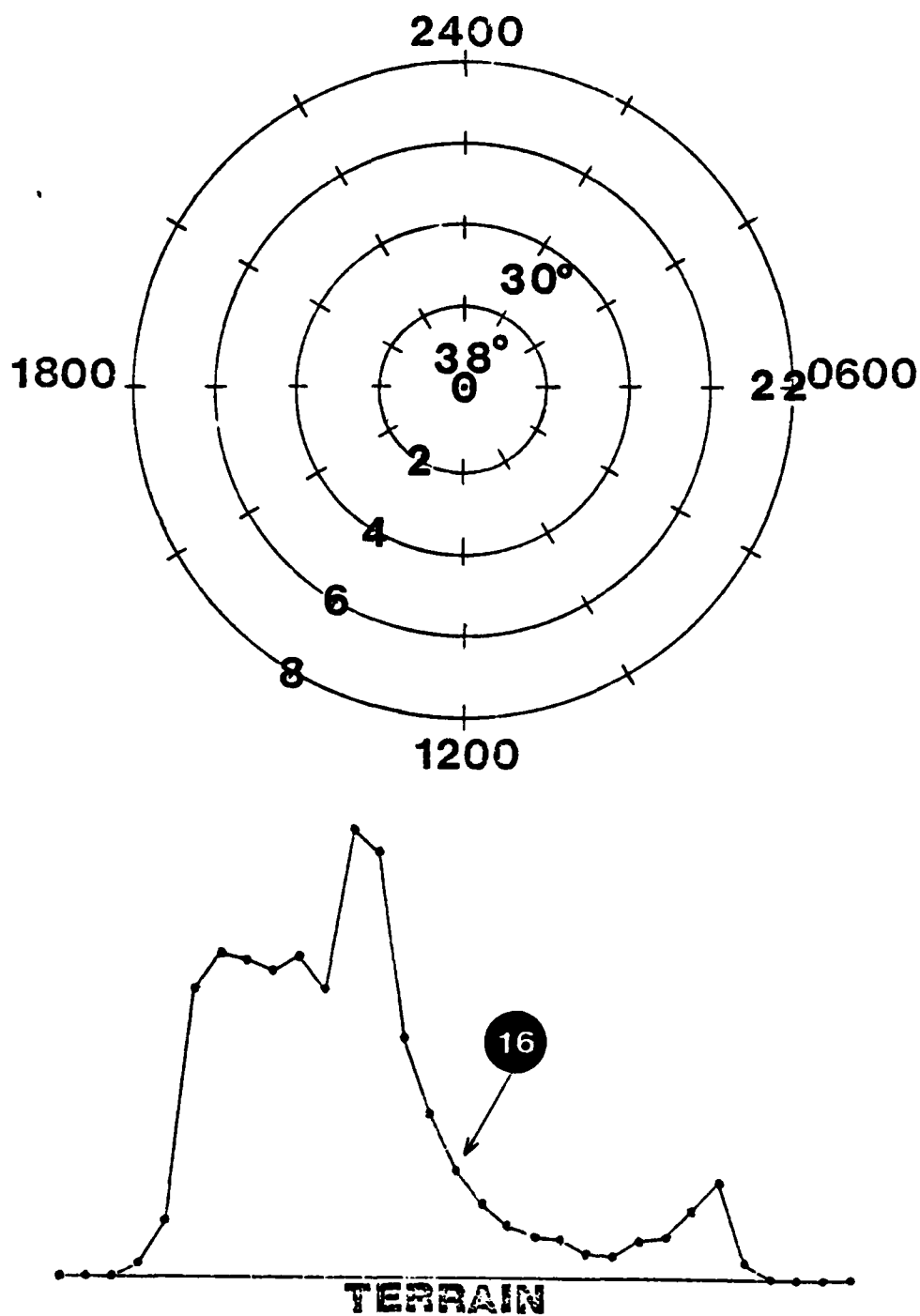


Figure 51. Amplitude and phase of the maximum vertical velocity forecast at grid point 16 for 22°, 30°, and 38° latitude. The position of the latitude around the dial denotes the time of the max W for that latitude while the distance from the center of the dial denotes the amplitude in mm/sec.

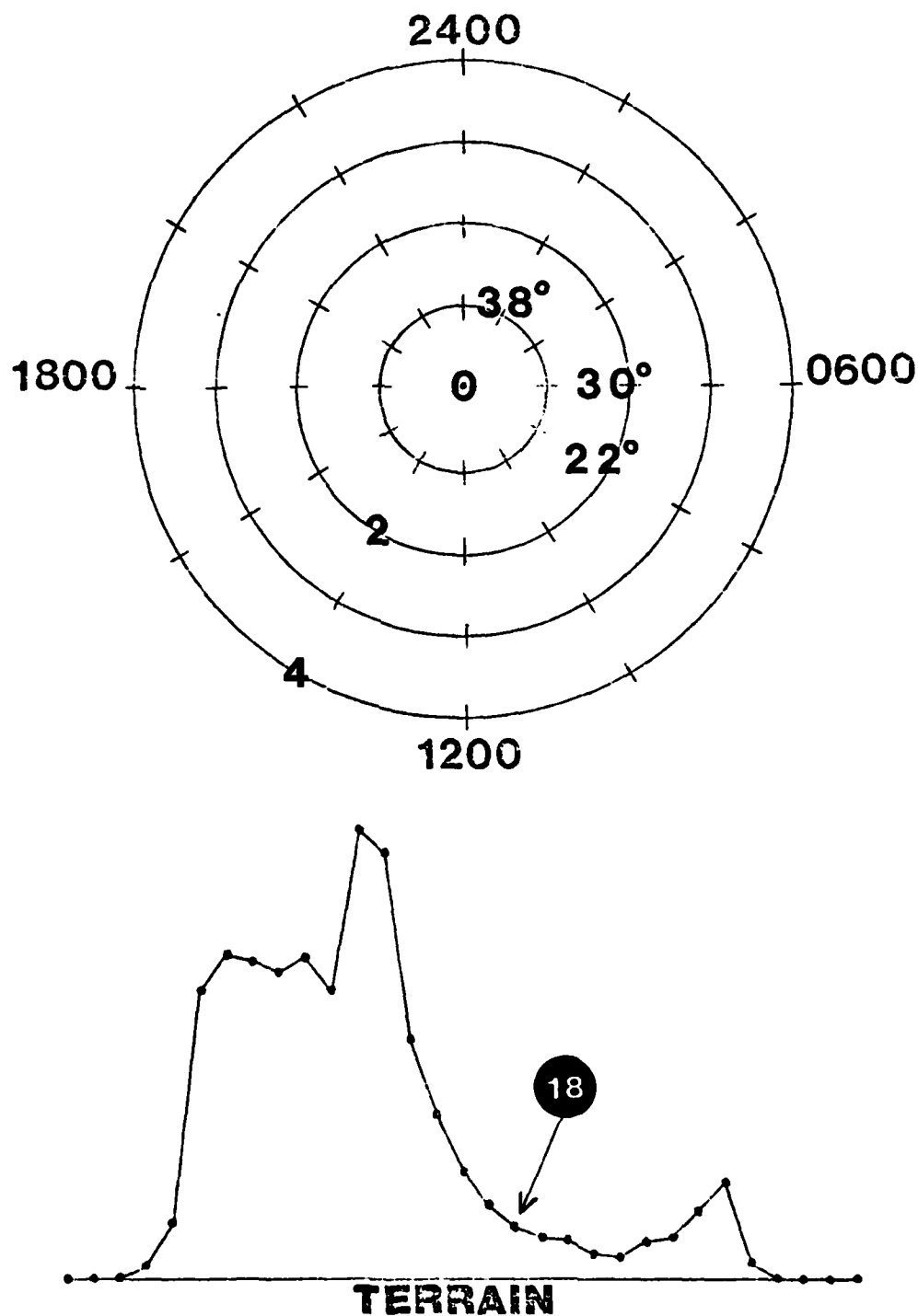


Figure 52. Amplitude and phase of the maximum vertical velocity forecast at grid point 18 for 22°, 30°, and 38° latitude. See Figure 51 for plotting convention.

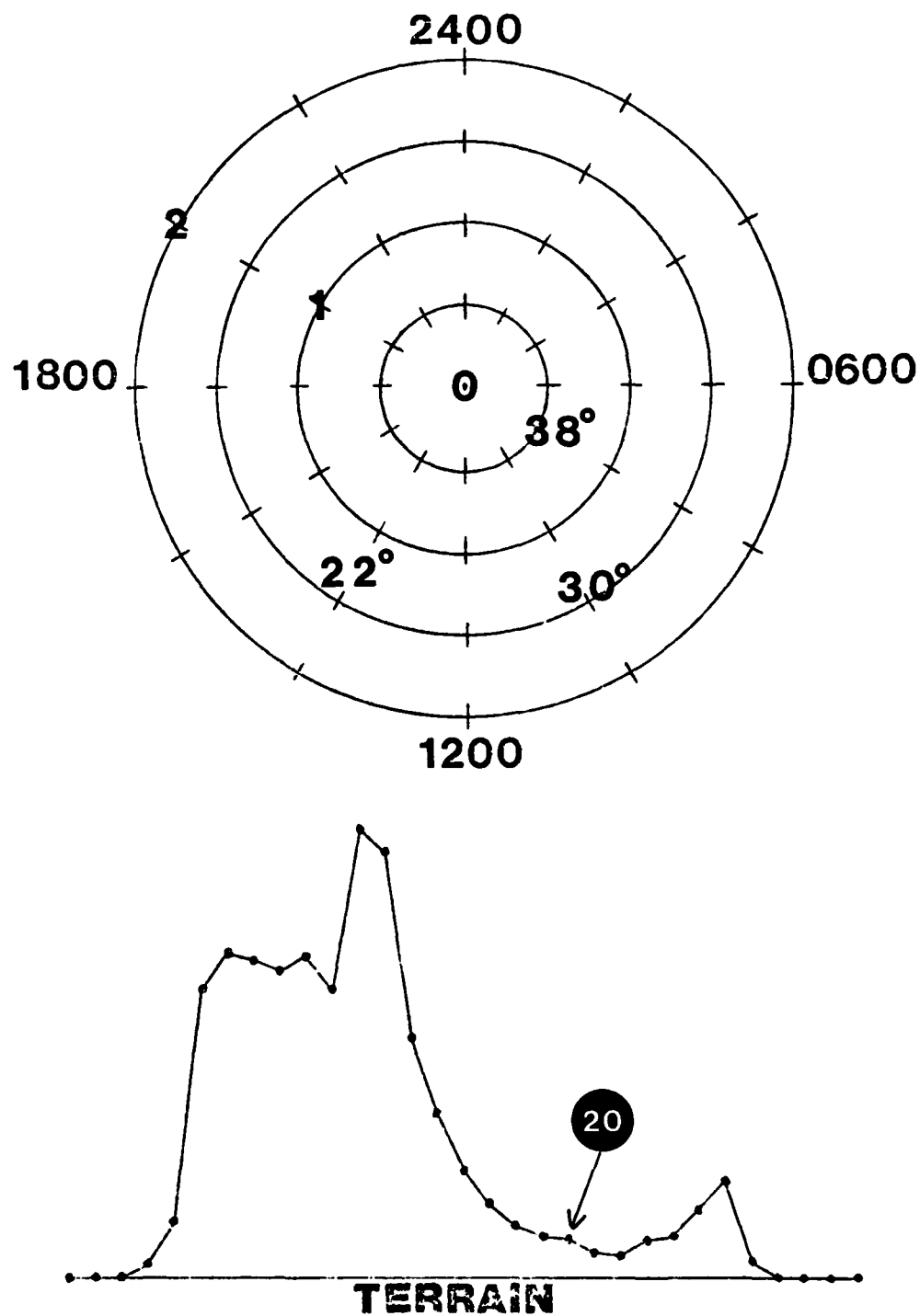


Figure 53. Amplitude and phase of the maximum vertical velocity forecast at grid point 20 for 22°, 30°, and 38° latitude. See Figure 51 for plotting convention.

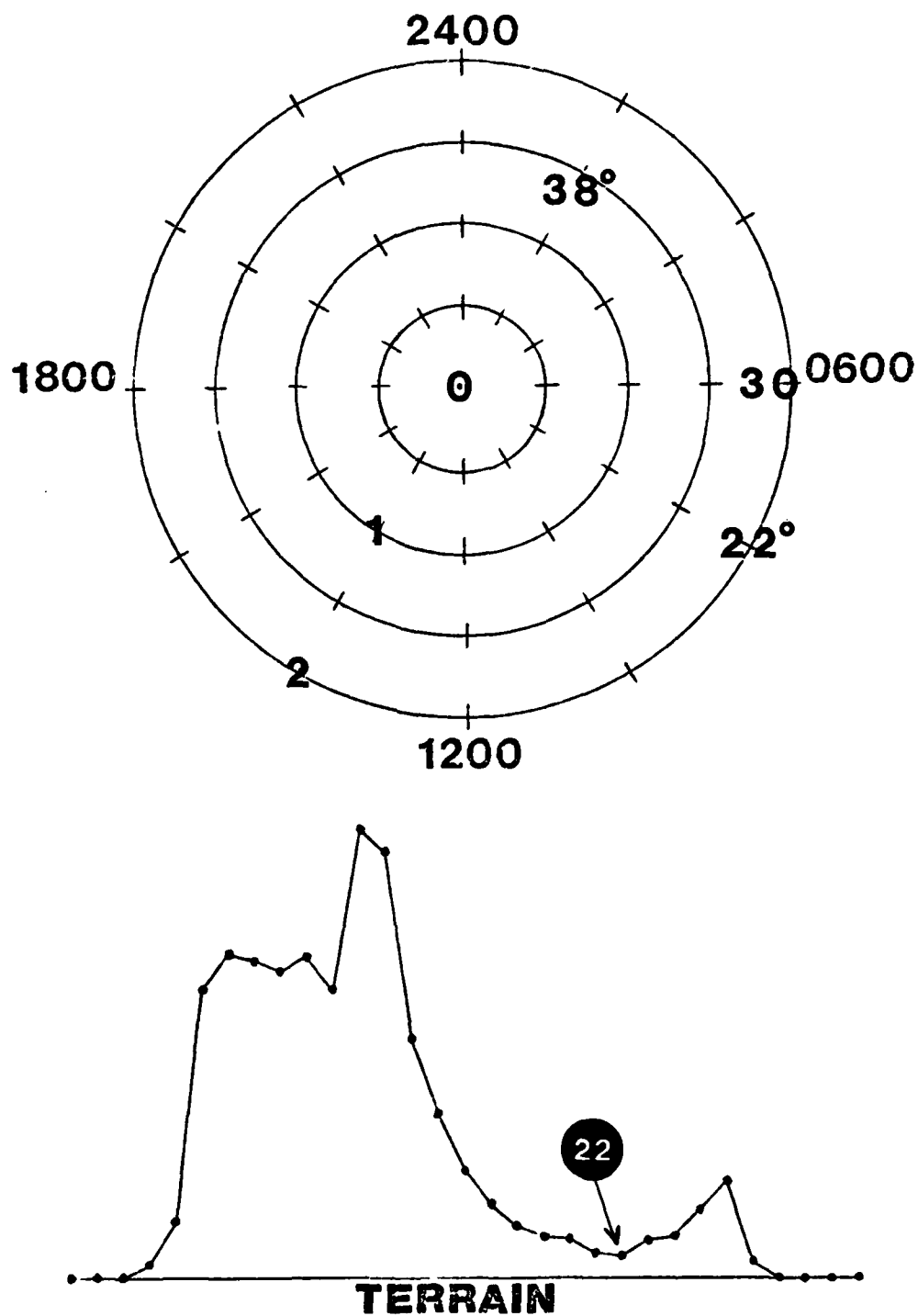


Figure 54. Amplitude and phase of the maximum vertical velocity forecast at grid point 22 for 22°, 30°, and 38° latitude. See Figure 51 for plotting convention.

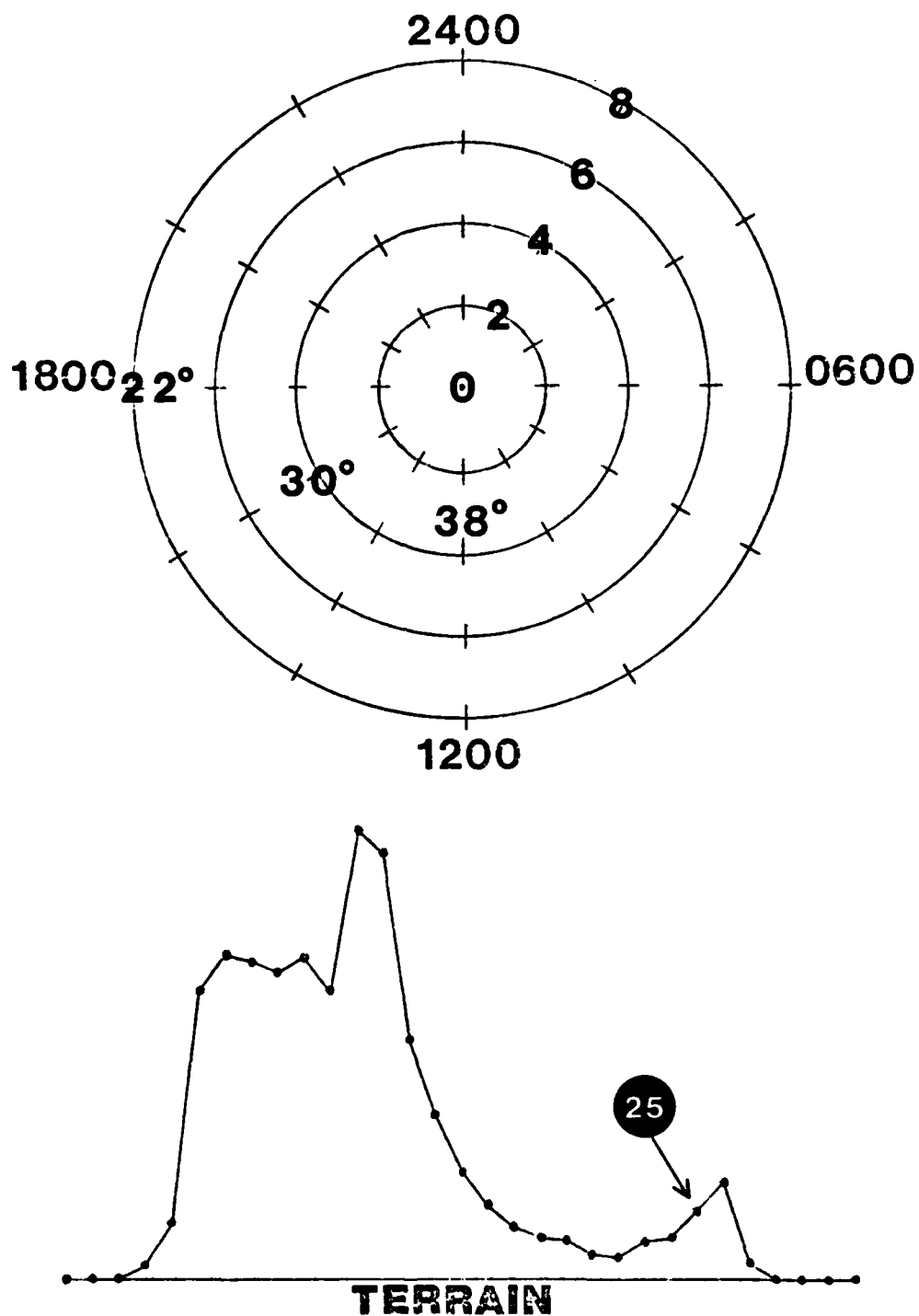


Figure 55. Amplitude and phase of the maximum vertical velocity forecast at grid point 25 for 22°, 30°, and 38° latitude. See Figure 51 for plotting convention.

7.3 Radiation

7.3.1 Purpose

The purpose of the radiation tests is to determine an efficient and economical method of computing the radiation fields.

7.3.2 Test Description

Approximately 30 minutes of Univac 1108 CPU time is required for the complete boundary layer model to produce a four hour forecast for only seven grid points. Radiation calculations were completed each time step and accounted for much of the CPU time. In order to reduce the computer time to an acceptable level without adversely affecting the accuracy of the model, numerous test were conducted. These tests were to check the effect of reducing the depth of the radiational model as well as the frequency with which the radiation calculations are performed.

7.3.3 Results

The top of the radiational model was lowered from nine to six kilometers. This change resulted in the elimination of over 30 computational levels. The vertical grid spacing was changed from 100m to 86m in order to make the radiational and boundary layer models more compatible. Table 6 shows the effect these modifications had on the values of some of the more important radiational parameters.

The next step was to test the sensitivity to the frequency with which the radiation calculations were performed. Numerous tests were conducted in which the radiation calculations were done as frequently as every time step and as infrequently as every four hours. A test was also conducted in which the flux divergence was held constant.

The tests in which the radiation is calculated every two, three, and four hours used the complete boundary layer model as described in

Table 6. Comparison of parameter values computed from radiational models of different depths and vertical grid spacing (McClatchey mid-latitude summer data was used for the calculations).

Vertical Grid Separation (m)	100			86
Model Depth (km)	9	5	3	5
U_1 (cm)	2.424	2.395	2.309	2.395
$F(0)$ ($\text{cal m}^{-2}\text{sec}^{-1}$)	31.61	31.68	31.98	31.69
G ($\text{cal m}^{-2}\text{sec}^{-1}$)	196.1	196.2	196.4	196.2
$(G-F)$ ($\text{cal m}^{-2}\text{sec}^{-1}$)	164.49	164.52	164.42	164.51
<u>Heating ($^{\circ}\text{C}/\text{day}$)</u>				
.01 m	-3.53	-3.57	-3.59	-3.55
49.00 m	-3.07	-3.08	-3.13	-3.08
306.00 m	-2.45	-2.46	-2.52	-2.46
653.00 m	-2.36	-2.37	-2.46	-2.37
1000.00 m	-2.34	-2.37	-2.46	-2.37

Section 7.2 over a 60 hour forecast period. The constant flux test was also conducted using this model with the following specifications: (1) global radiation updated every two hours, (2) $Q=0$, (3) $U_1 = 3.4$, and (4) $F=0$. This test was also conducted over a 60 hour forecast period. The effect of these tests upon the amplitude and phase of the vertical motion and subsidence fields is shown in Figures 56 through 63. The plotting convention is described in Section 7.2. Differences in phase and amplitude are found between all tests with the greatest similarity between the subsidence fields of the tests where radiative fluxes were calculated every three hours and every four hours.

The thermal structure was closely examined through an analysis of the diurnal temperature variations at grid points 15, 18, and 22 (see Figure 64). Temperatures at the roughness height, 49m, 133m, and 480m were plotted over a 48 hour period as forecast in the two, three, and four hour radiational tests (Figures 65 through 76). The plotting convention is as follows:

- + Radiation update at two hour intervals
- O Radiation update at three hour intervals
- Δ Radiation update at four hour intervals

Temperature curves from the above radiational tests are similar at each level.

The tests described in this section did not point to a "best" frequency for the radiational calculations; therefore a two hour frequency was selected since this was the highest frequency considered economically feasible. This frequency adequately resolves temperature oscillations with periods greater than four hours. Based on extensive

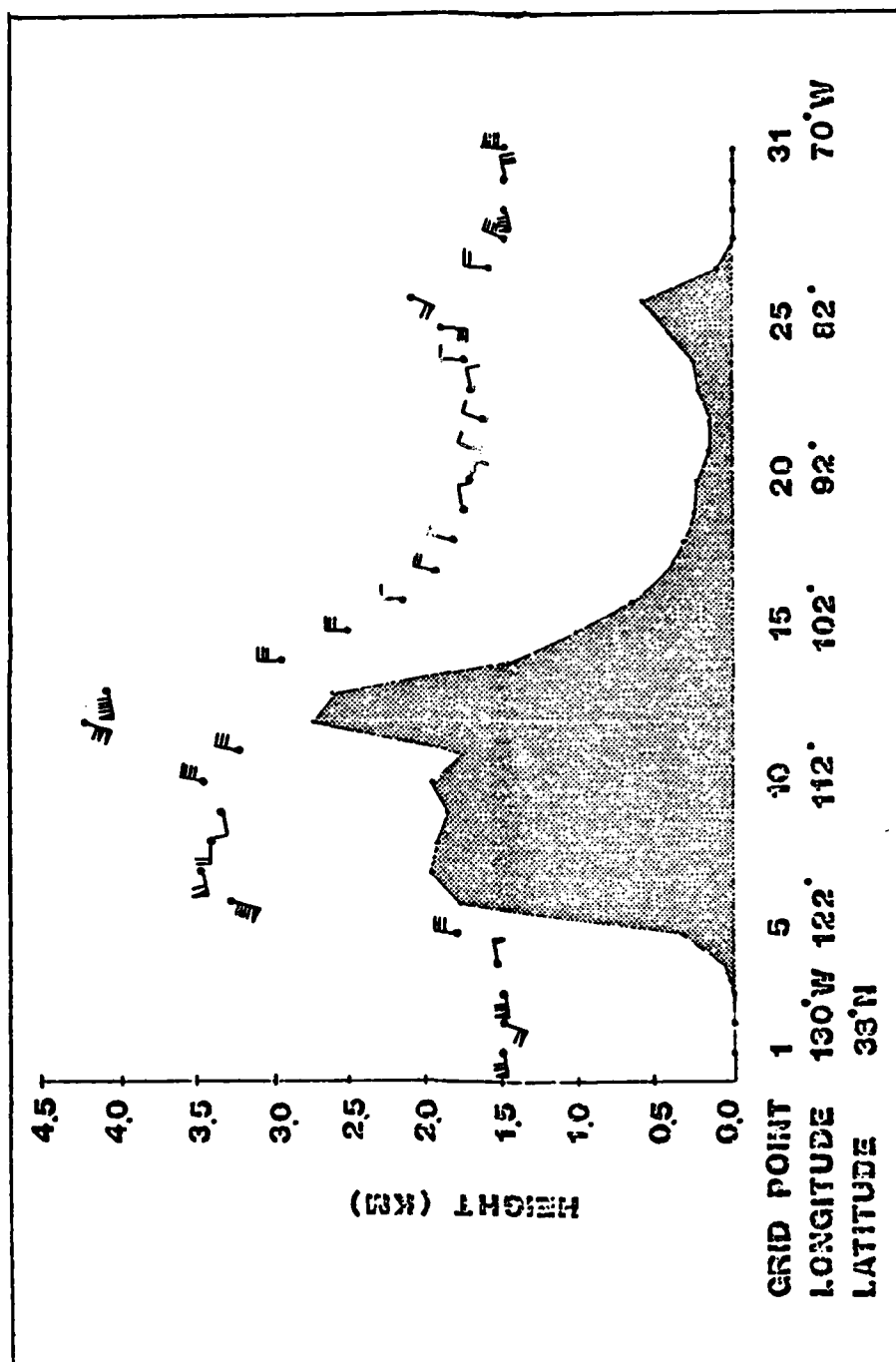


Figure 56. Amplitude and phase of the maximum vertical velocity with radiation fields updated every two hours. See Figure 48 for plotting convention.

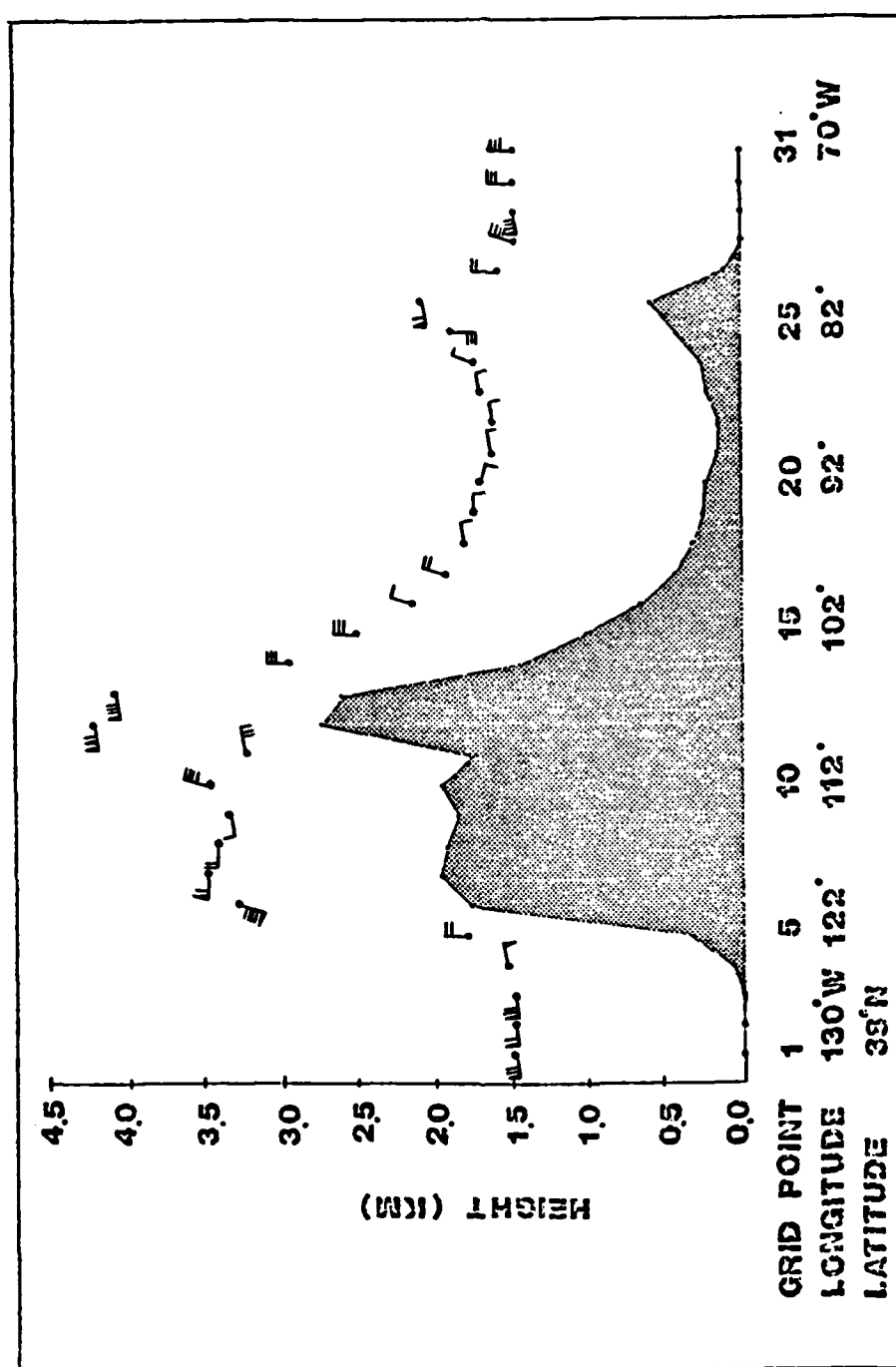


Figure 57. Amplitude and phase of the maximum vertical velocity with radiation fields updated every three hours. See Figure 48 for plotting convention.

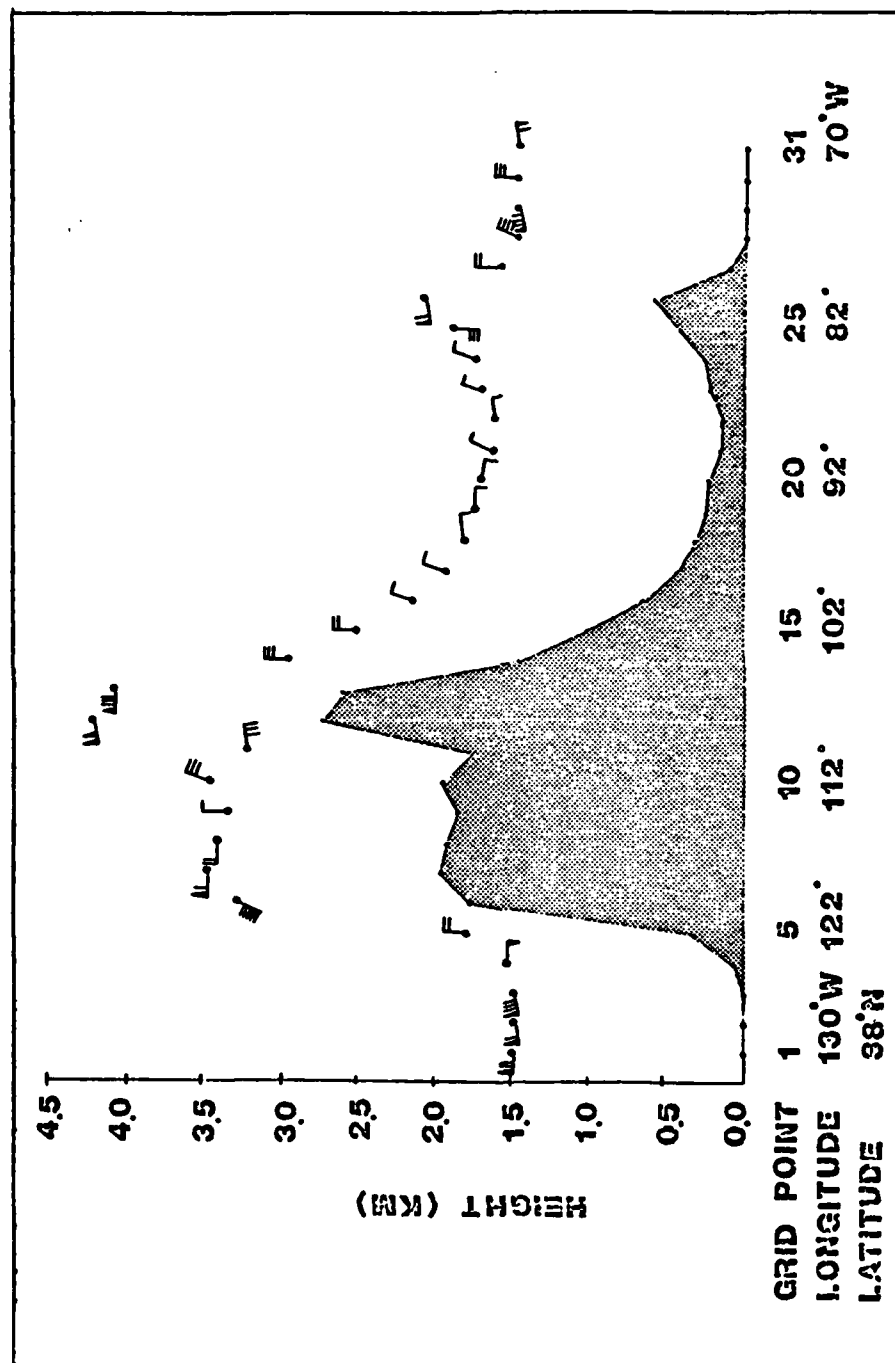


Figure 58. Amplitude and phase of the maximum vertical velocity with radiation fields updated every four hours. See Figure 48 for plotting convention.

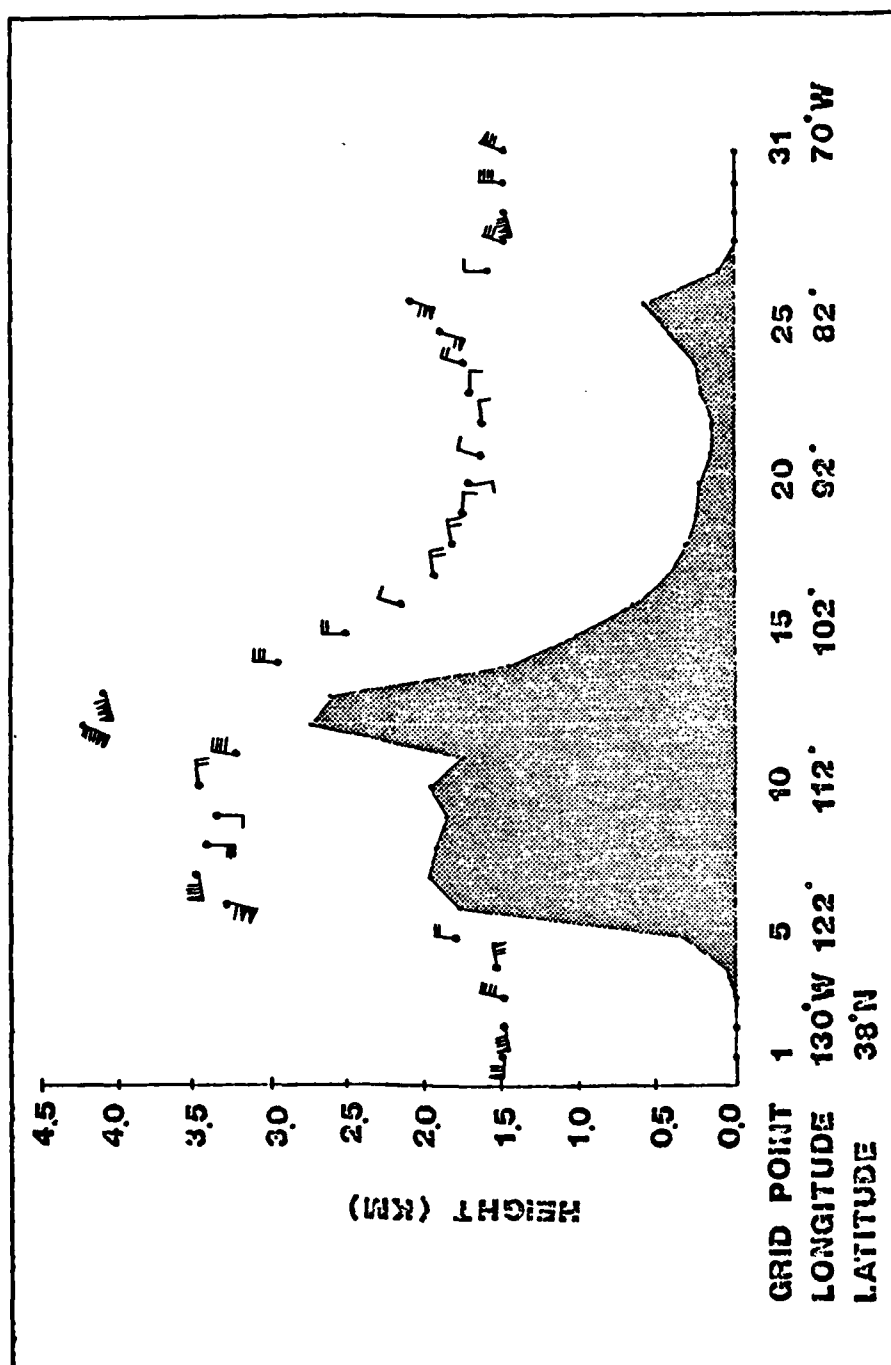


Figure 59. Amplitude and phase of the maximum vertical velocity with infrared radiation a constant. See Figure 48 for plotting convention.

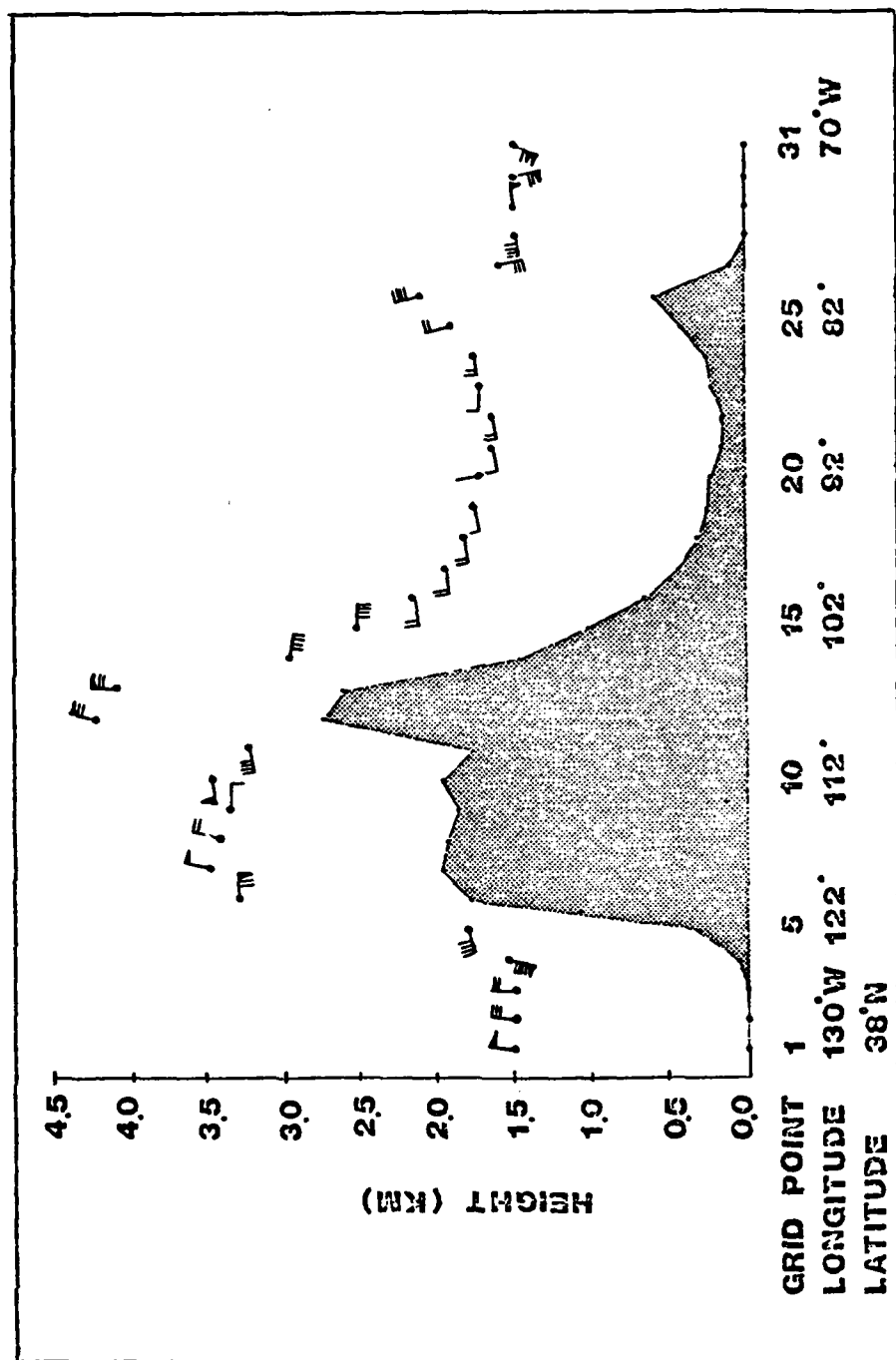


Figure 60. Amplitude and phase of the maximum subsidence with radiational fields updated every two hours. See Figure 48 for plotting convention.

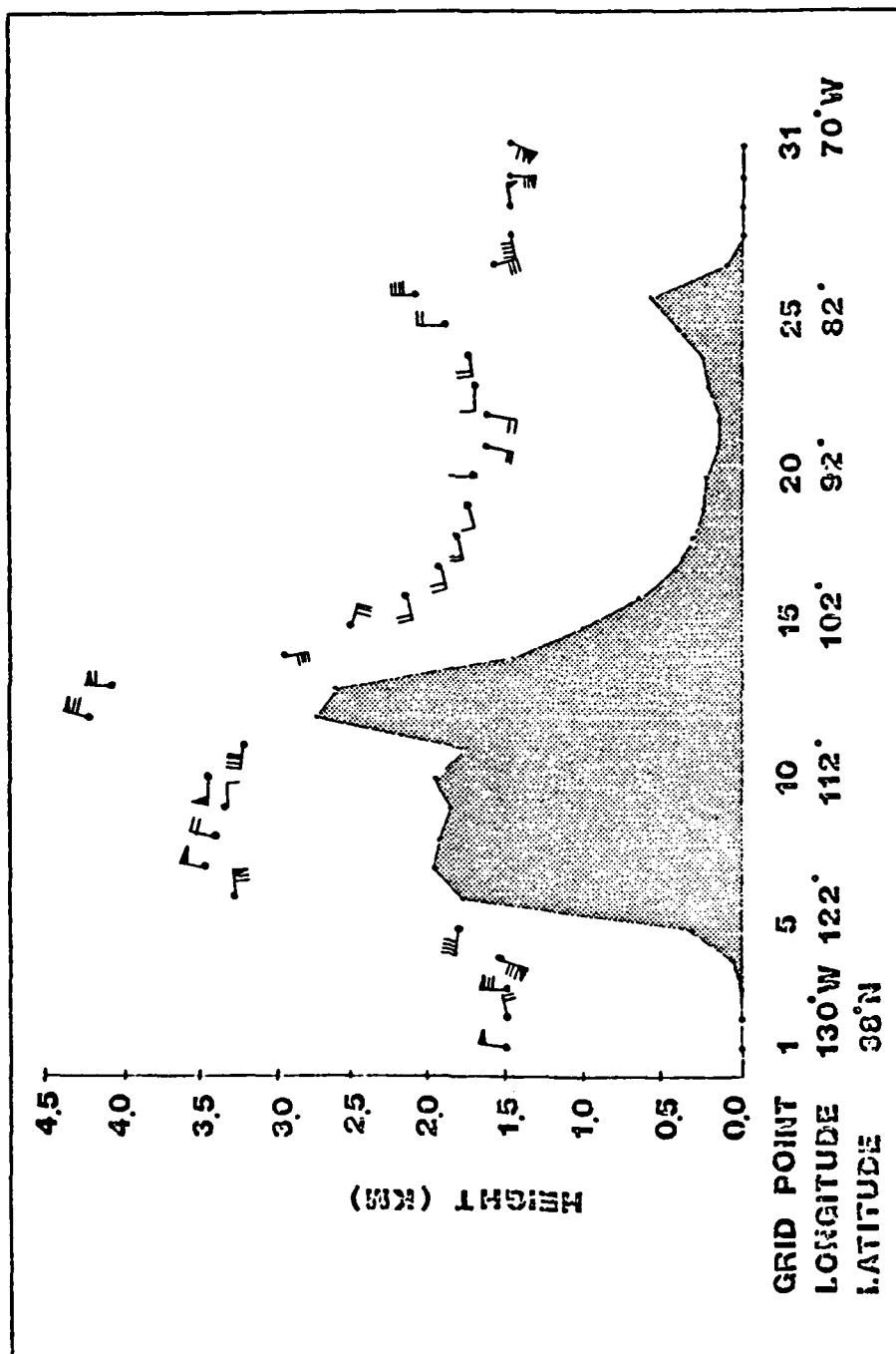


Figure 61. Amplitude and phase of the maximum subsidence with radiational fields updated every three hours. See Figure 48 for plotting convention.

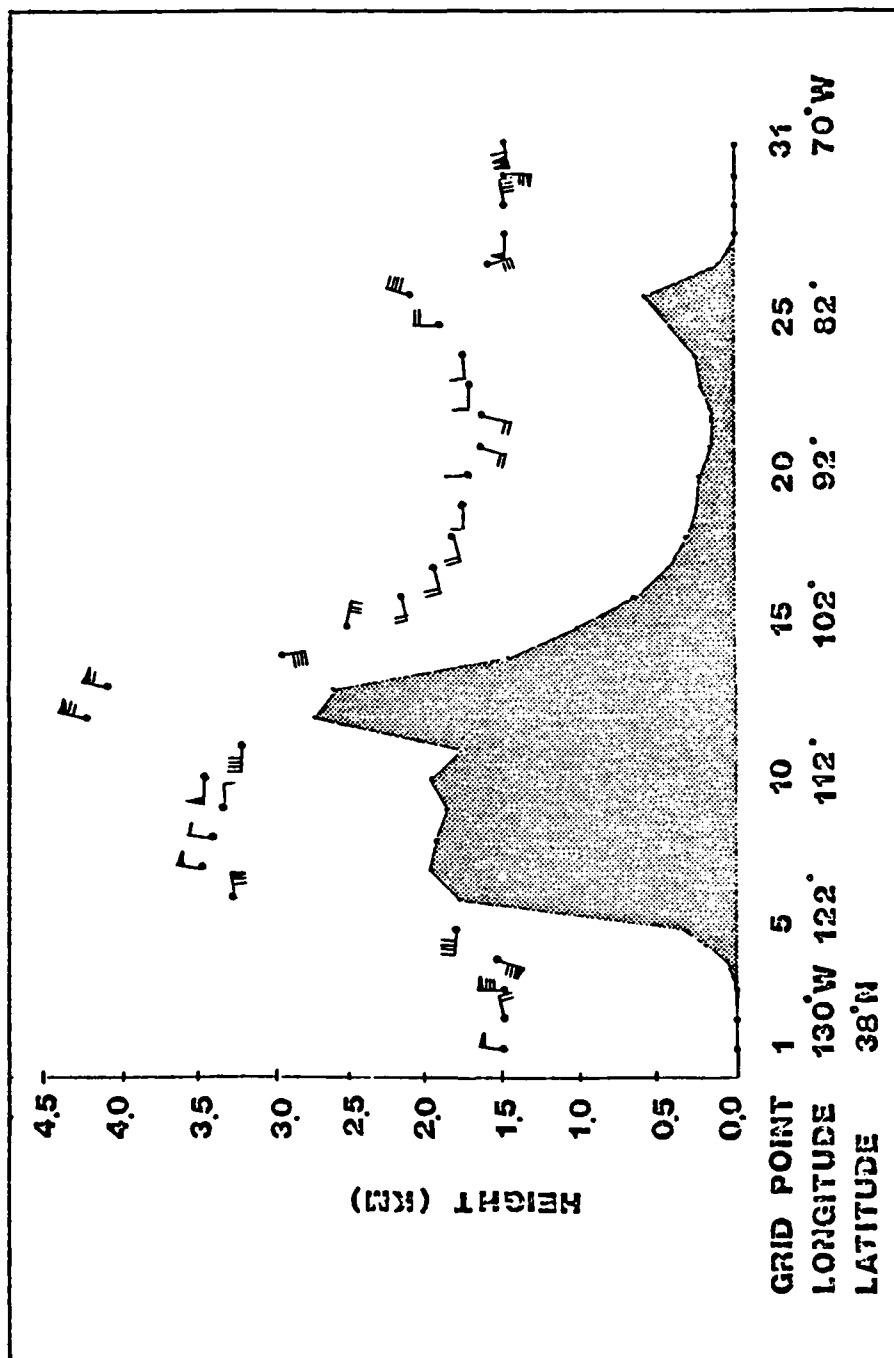


Figure 62. Amplitude and phase of the maximum subsidence with radiation fields updated every four hours. See Figure 48 for plotting convention.

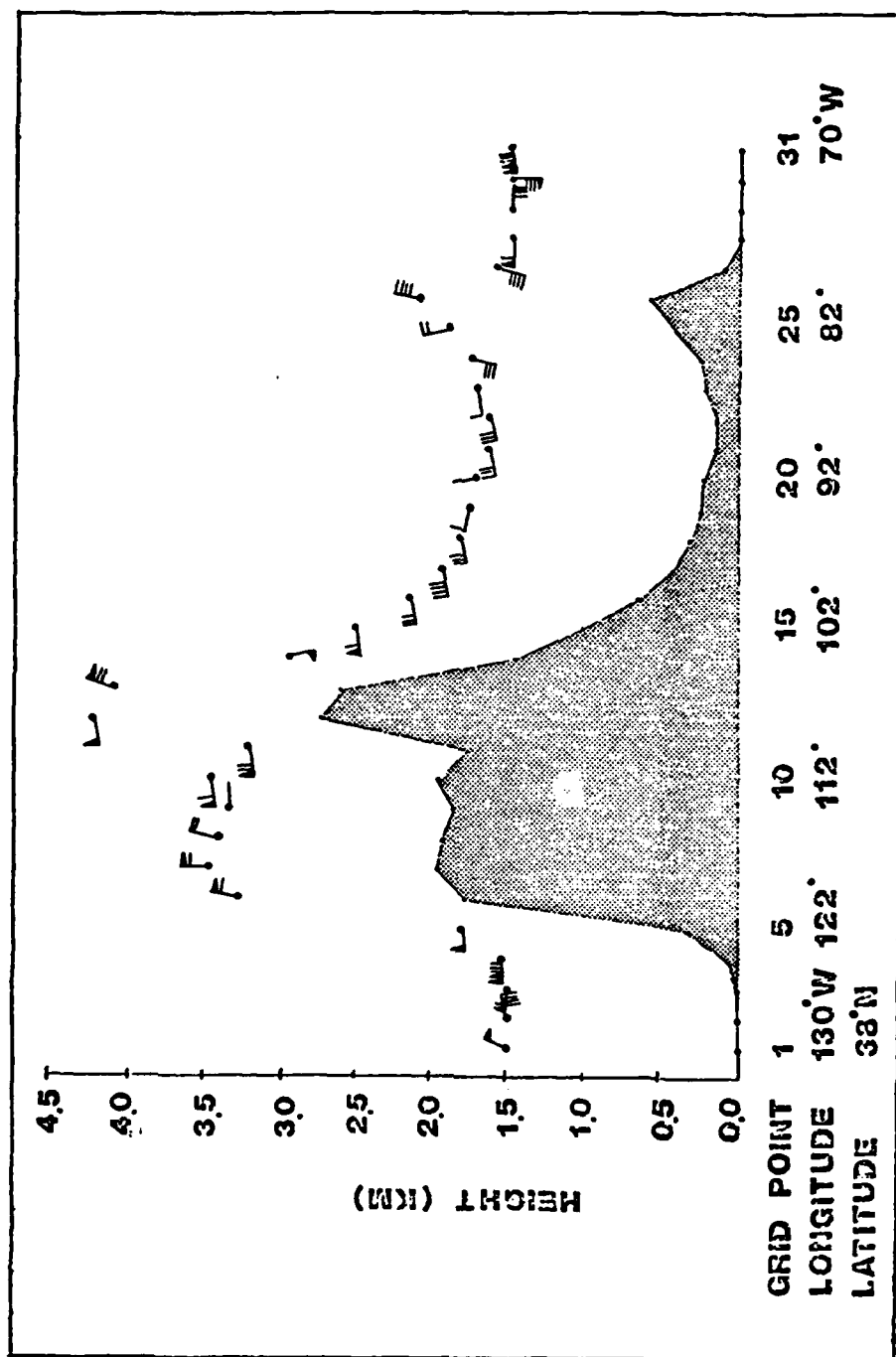


Figure 63. Amplitude and phase of the maximum subsidence with infrared radiation a constant. See Figure 48 for plotting convention.

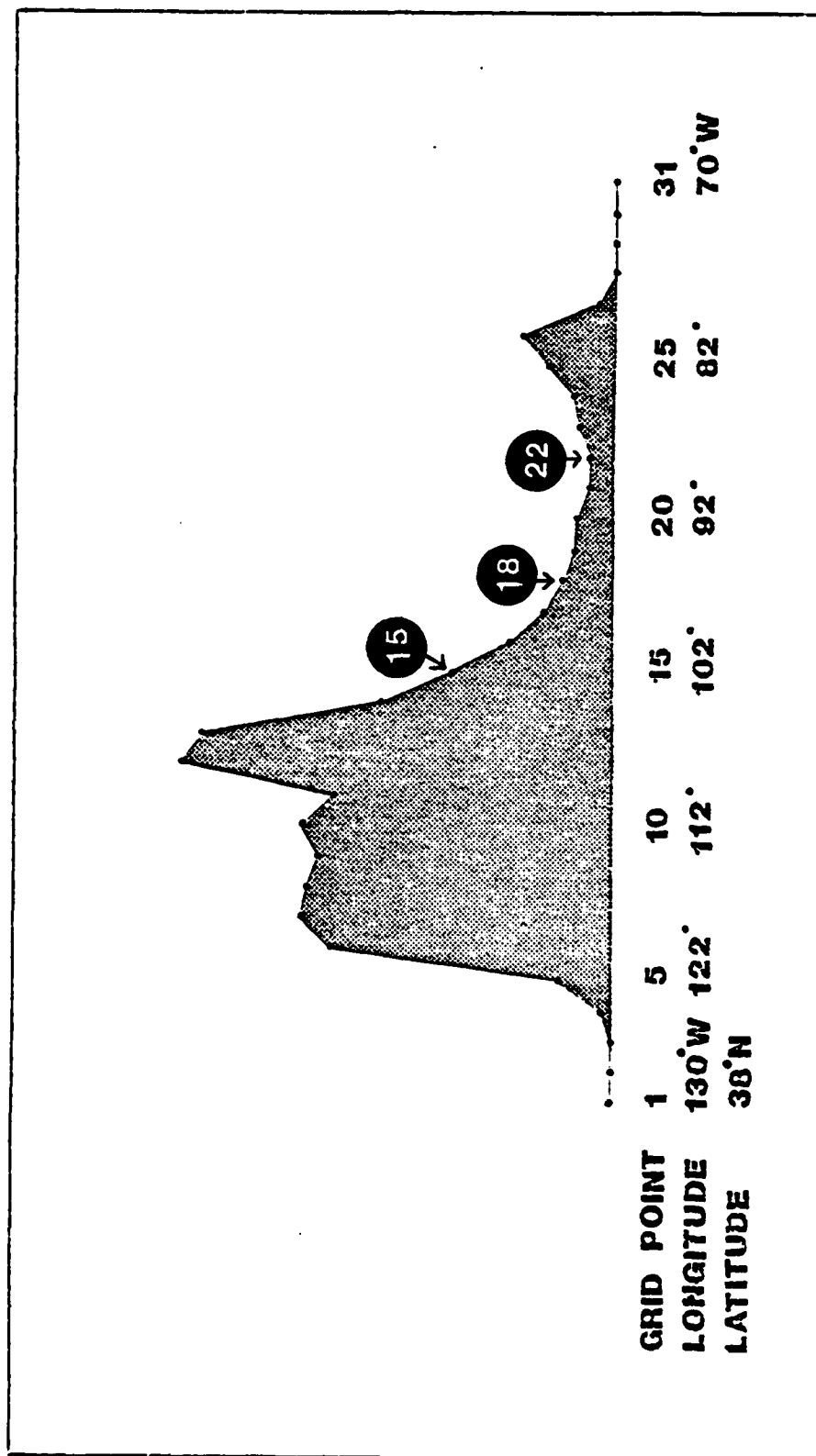


Figure 64. Grid points selected for a study of the radiational effects on the thermal structure.

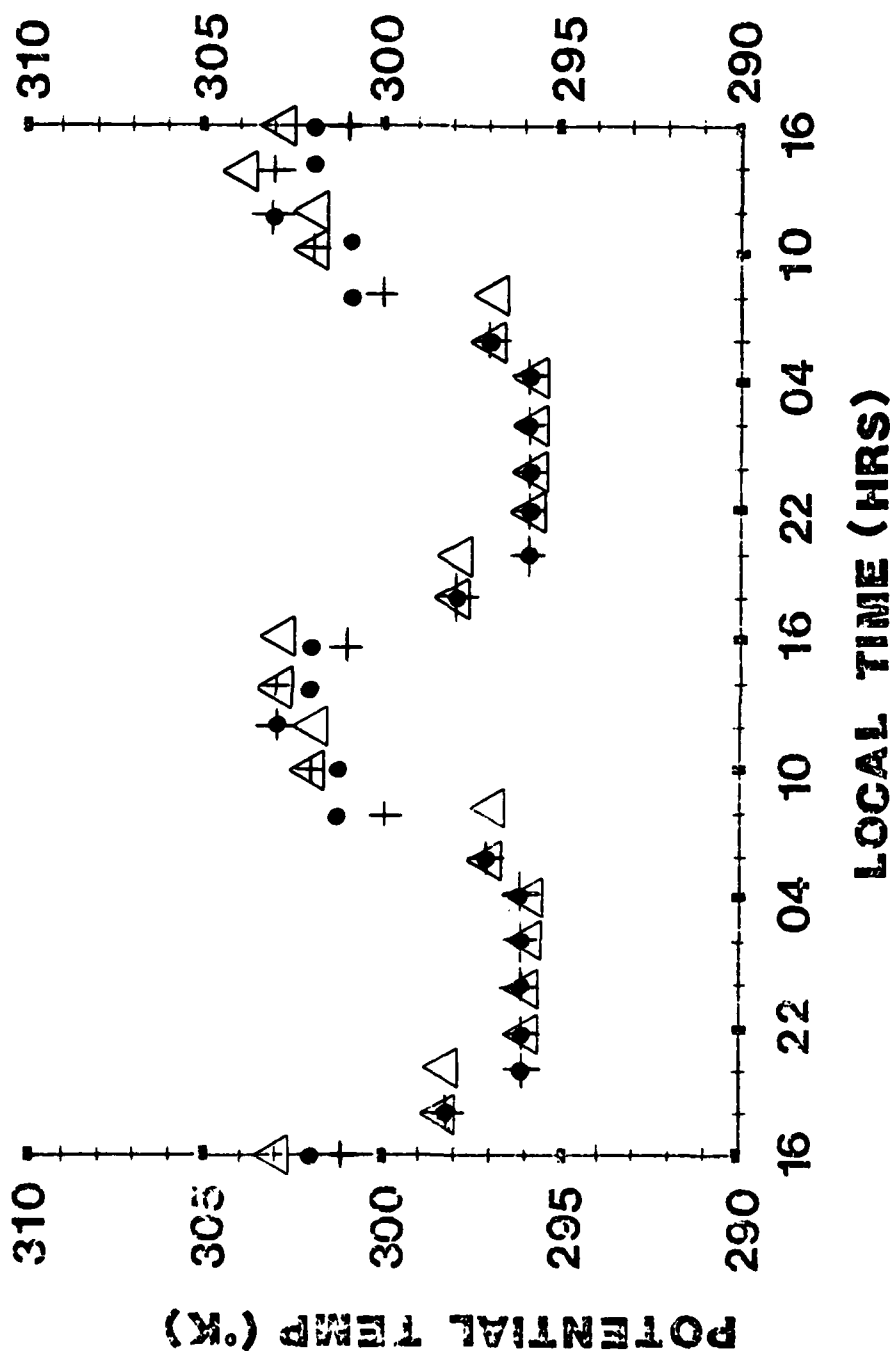


Figure 65. Diurnal temperature curves from grid point 15. Height is .01m. + = radiation update at two hour intervals, \bullet = radiation update at three hour intervals and Δ = radiation update at four hour intervals.

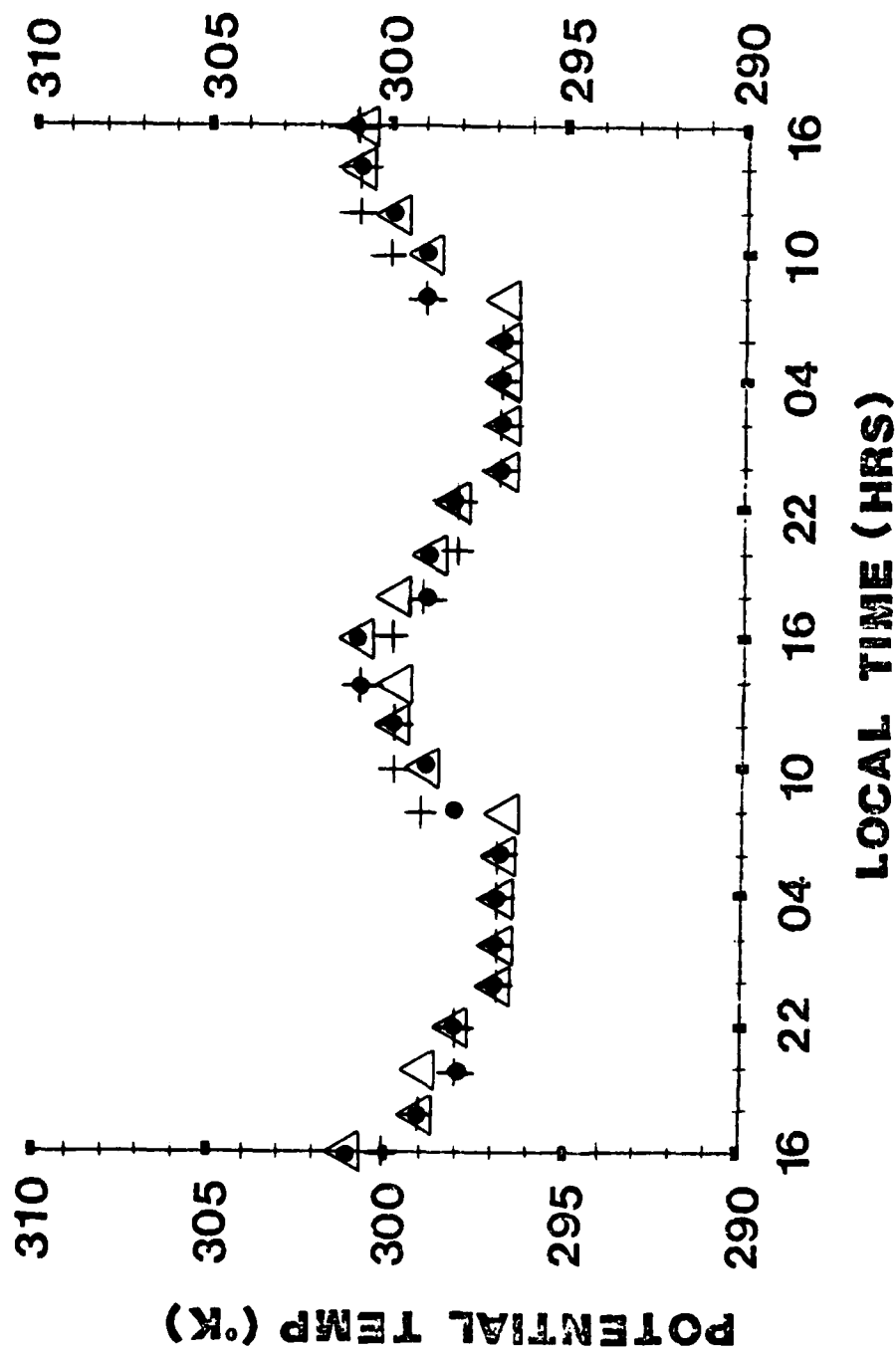


Figure 66. Diurnal temperature curves from grid point 15. Height is 49m. See Figure 65 for plotting convention.

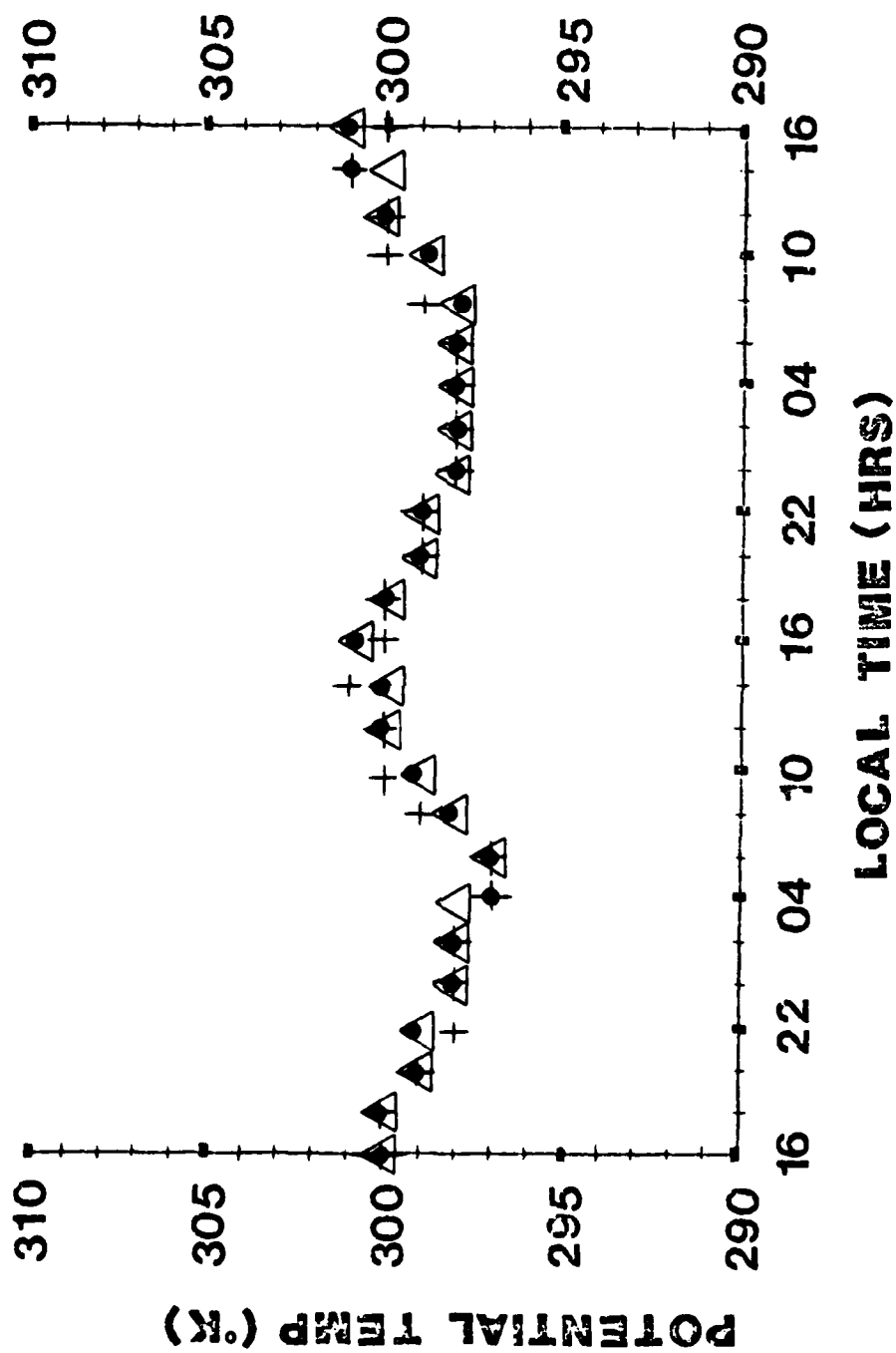


Figure 67. Diurnal temperature curves from grid point 15. Height is 133m. See Figure 65 for plotting convention.

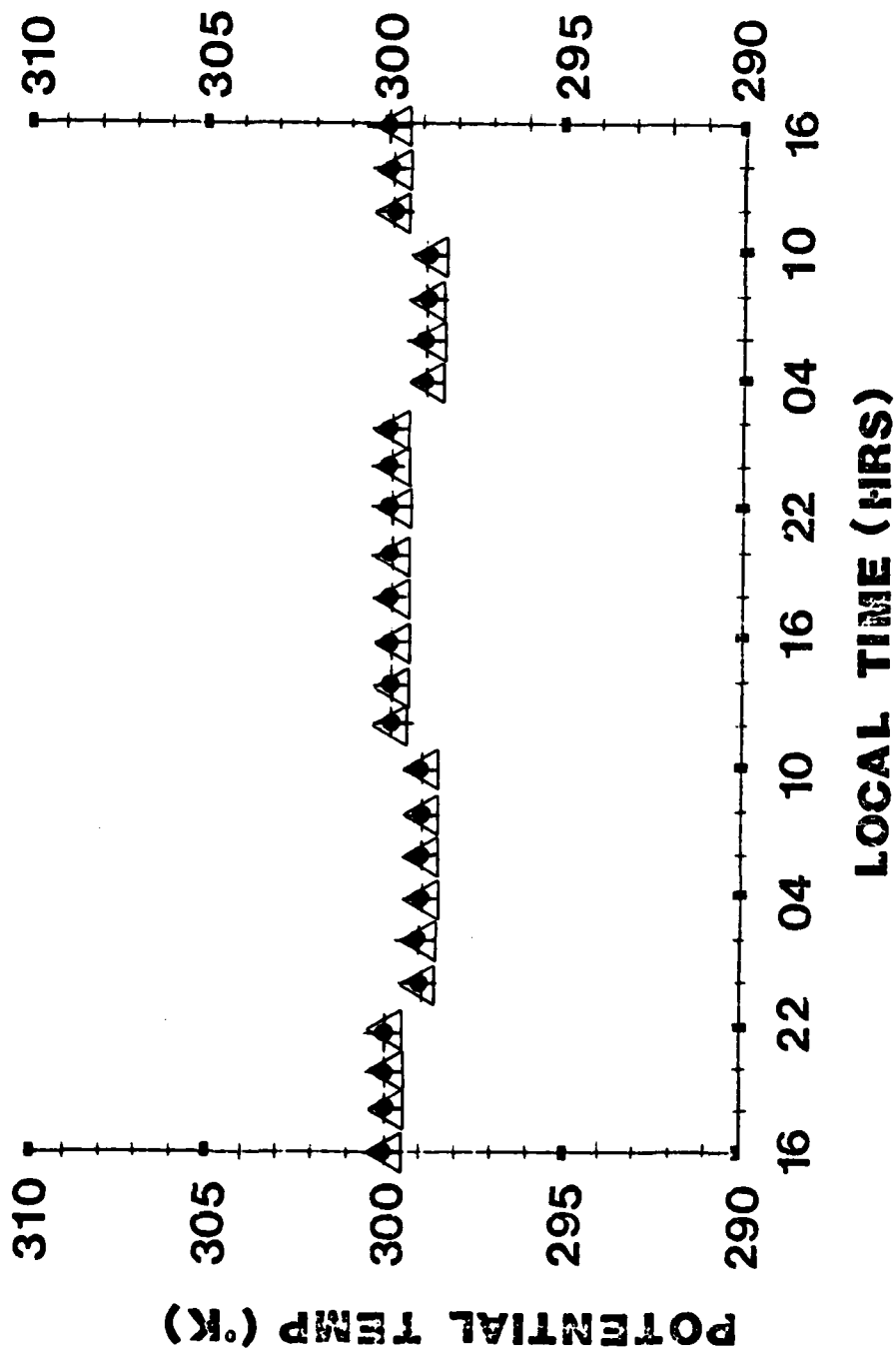


Figure 68. Diurnal temperature curves from grid point 15. Height is 480m. See Figure 65 for plotting convention.

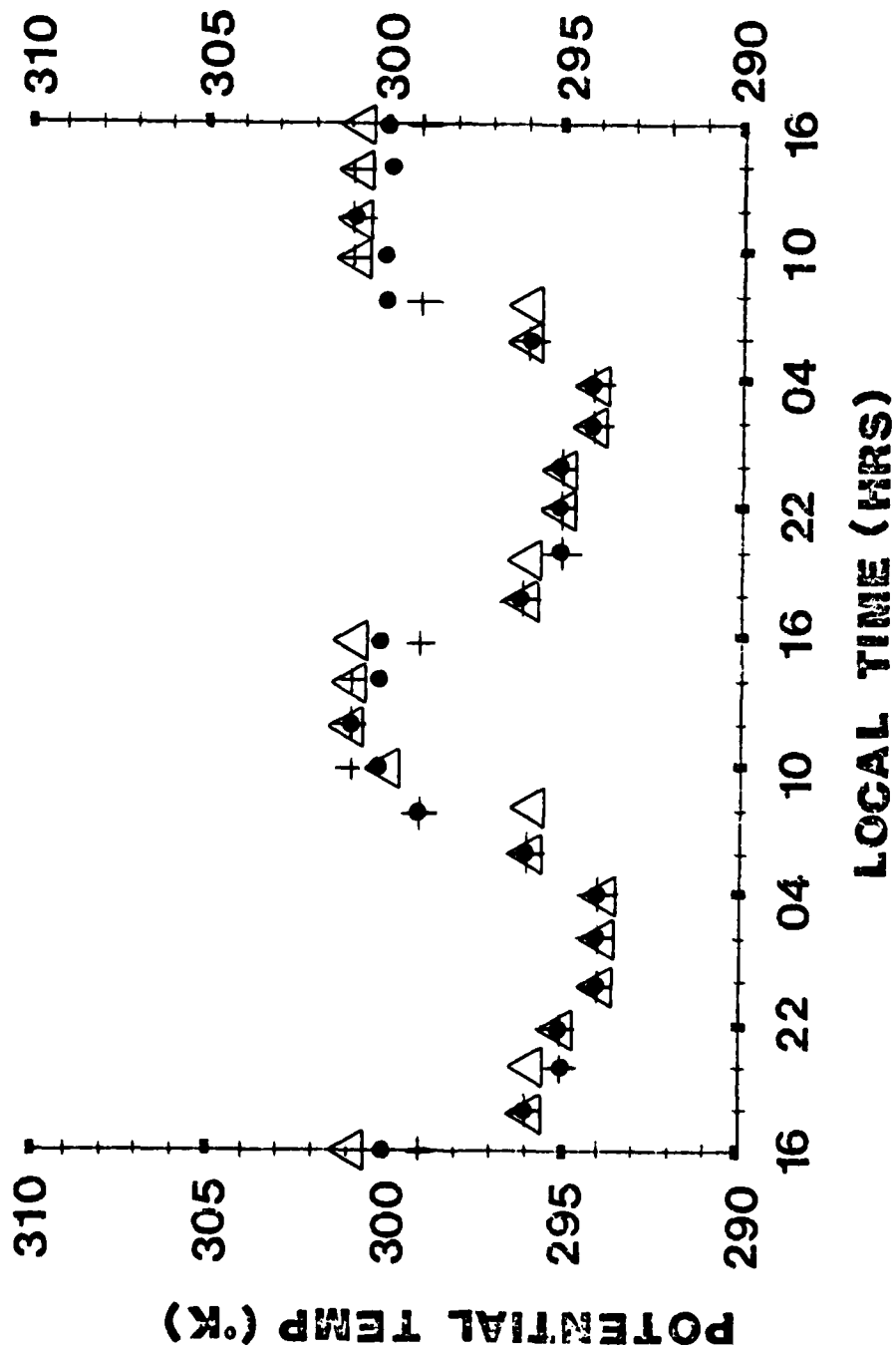


Figure 69. Diurnal temperature curves from grid point 18. Height is .01m. See Figure 65 for plotting convention.

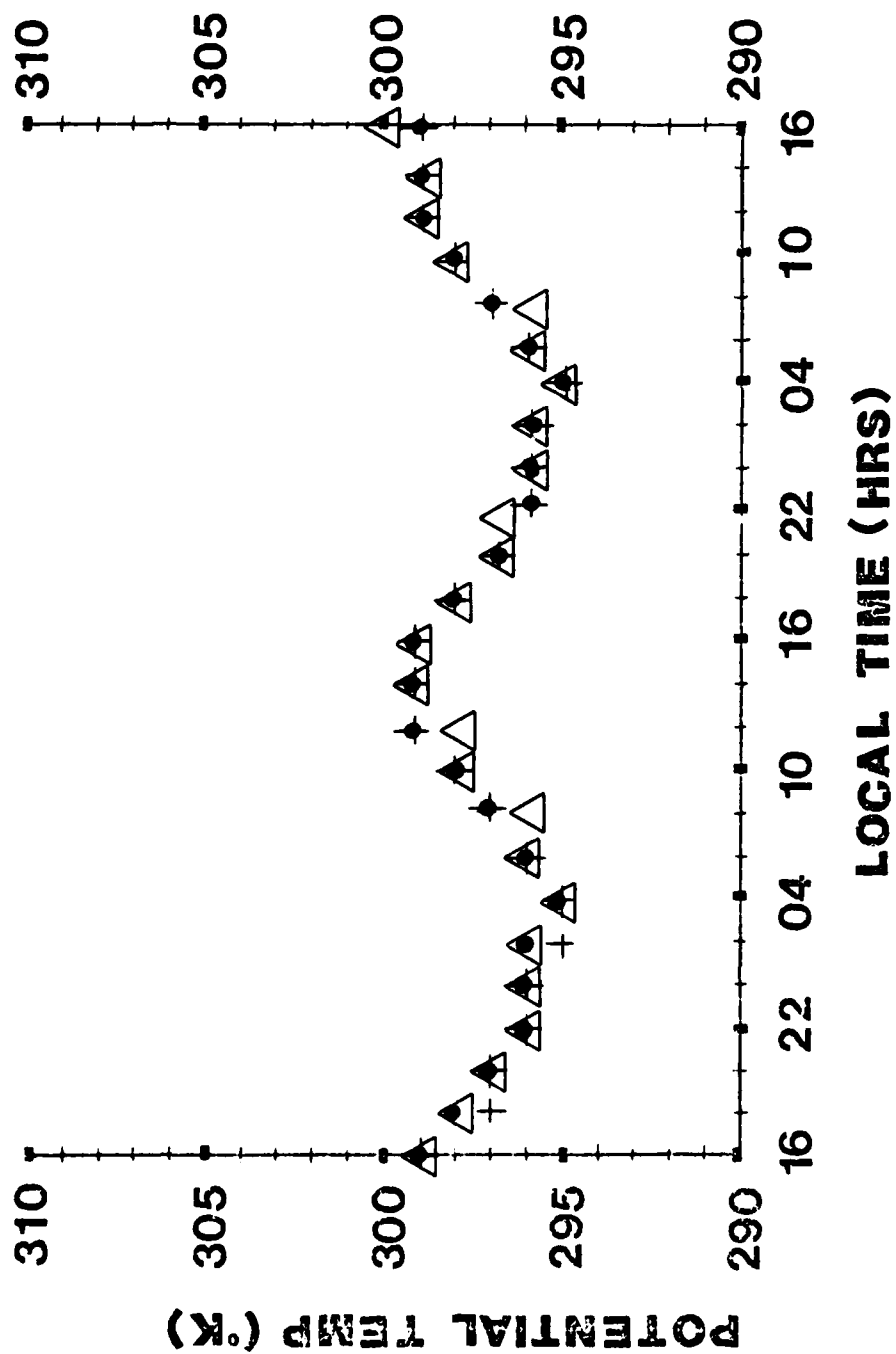


Figure 70. Diurnal temperature curves from grid point 18. Height is 49m. See Figure 65 for plotting convention.

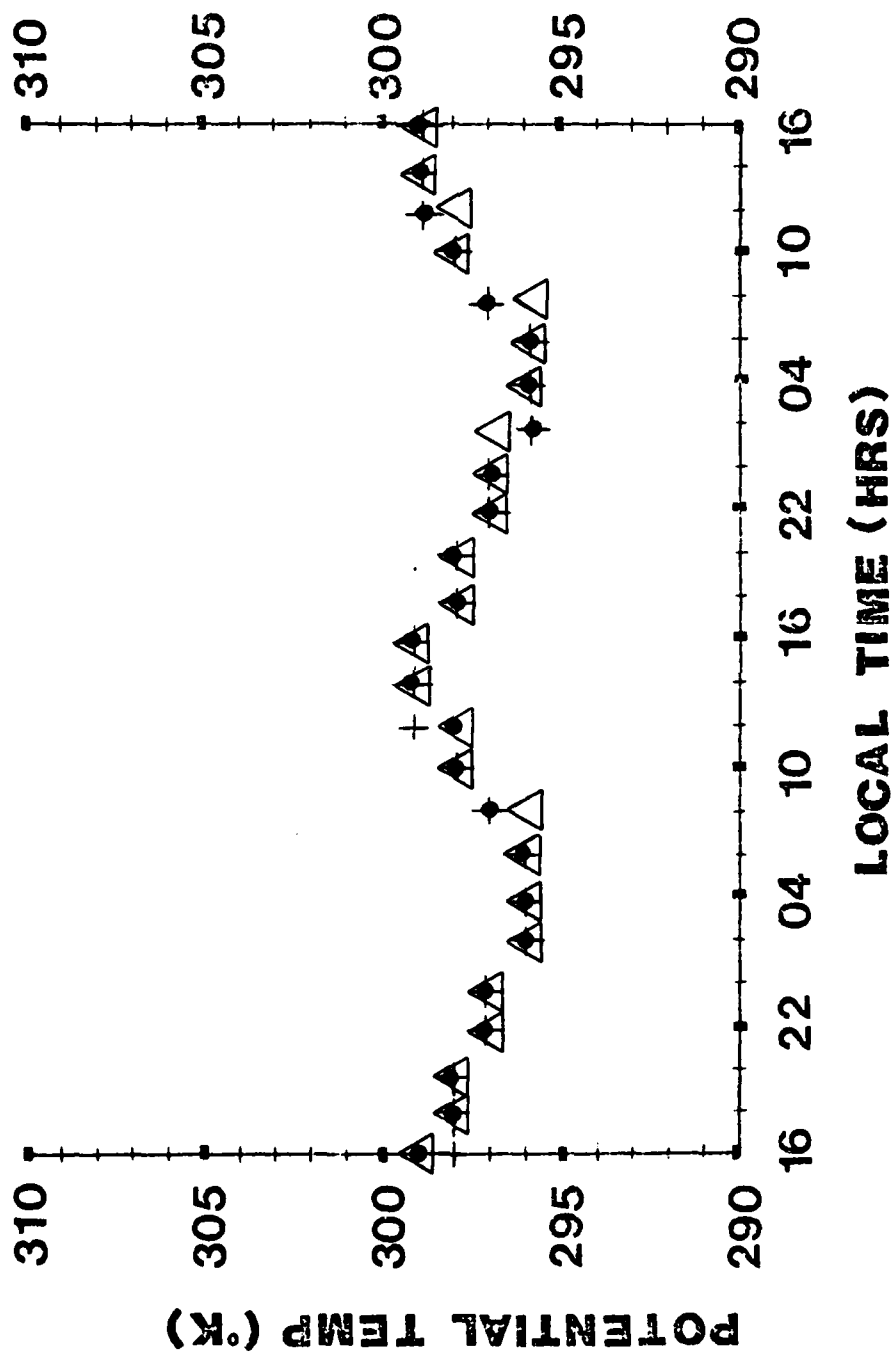


Figure 71. Diurnal temperature curves from grid point 18. Height is 133m. See Figure 65 for plotting convention.

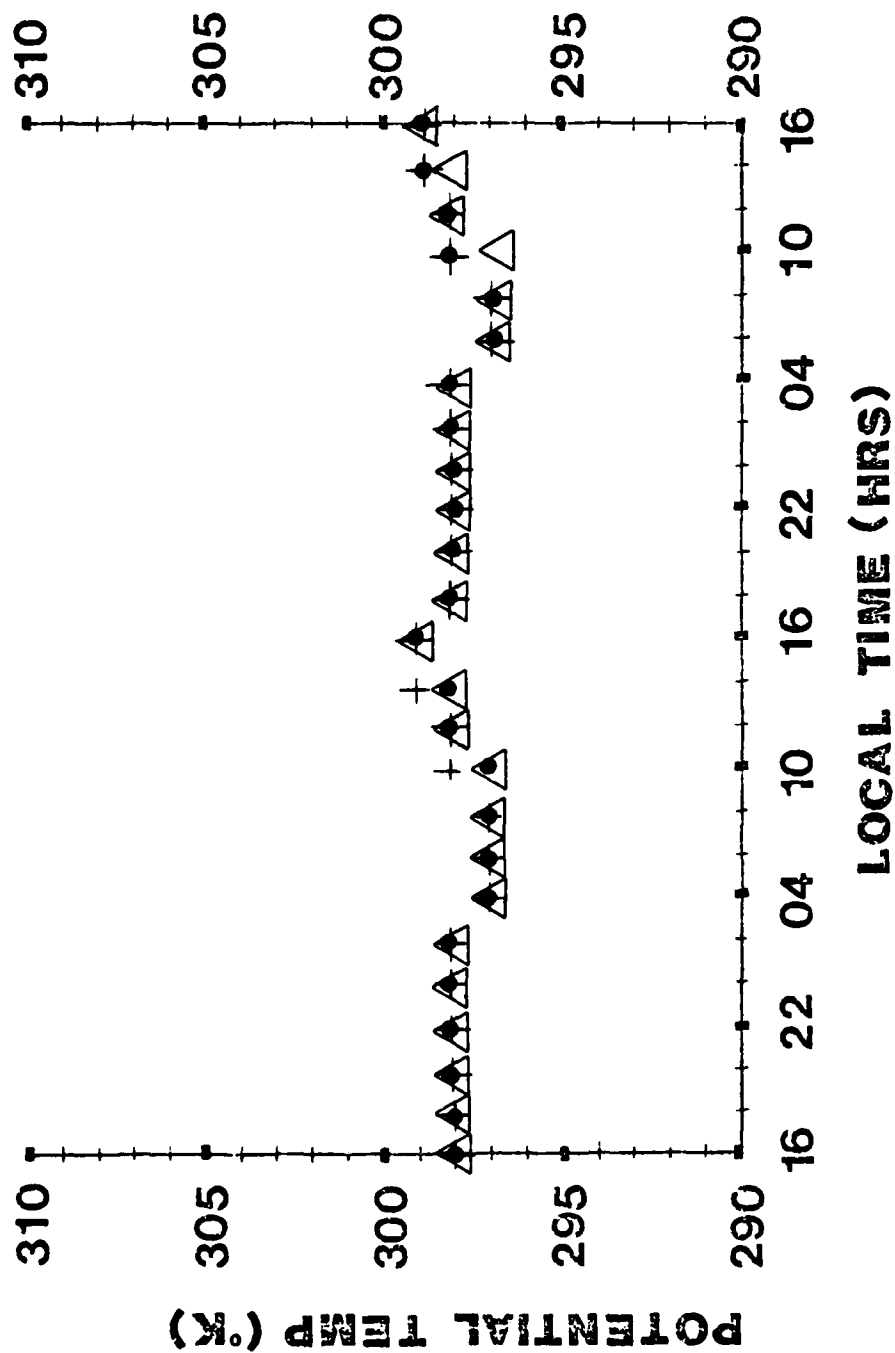


Figure 72. Diurnal temperature curves from grid point 18. Height is 480m. See Figure 65 for plotting convention.

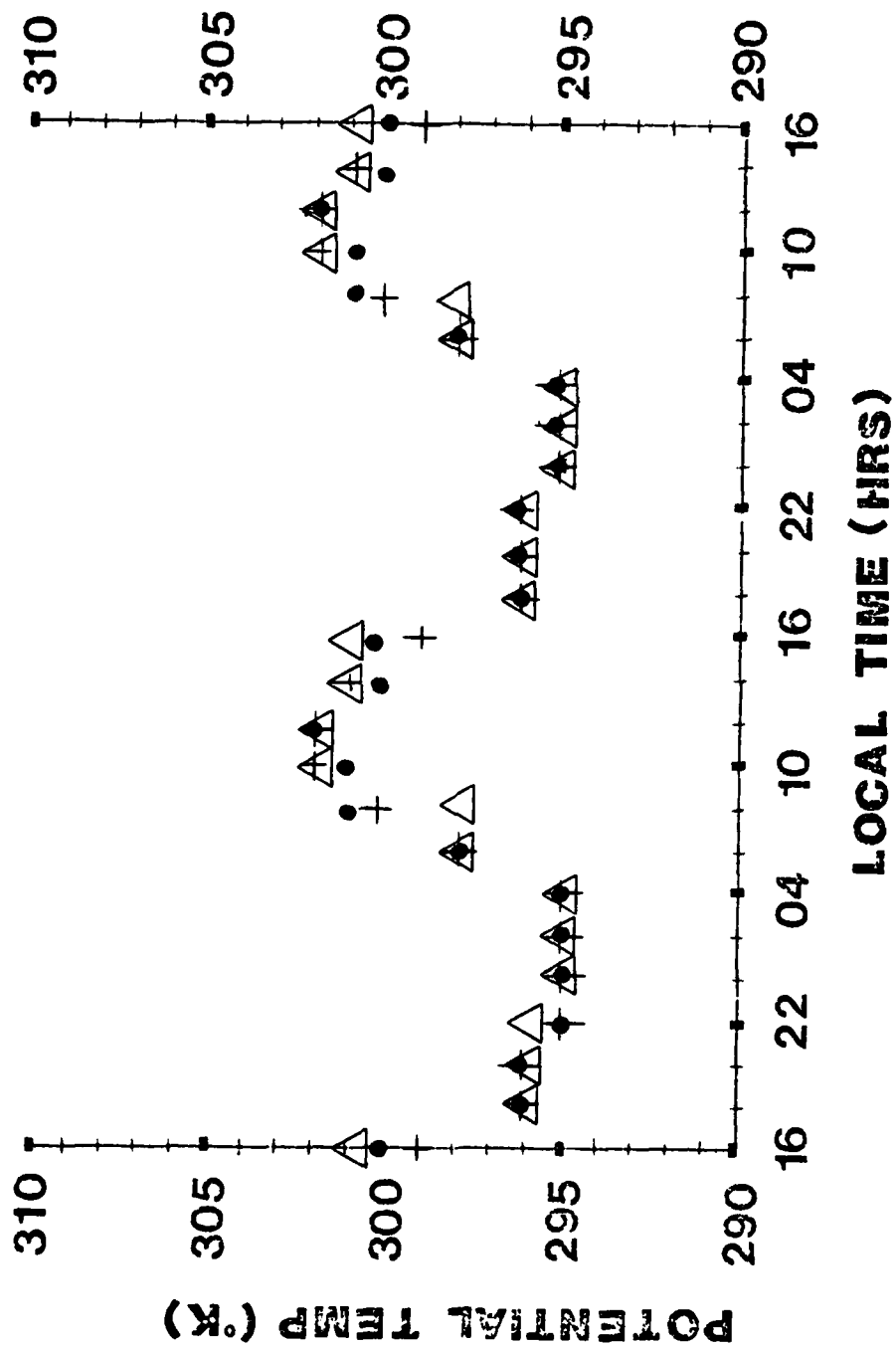


Figure 73. Diurnal temperature curves from grid point 22. Height is .01m. See Figure 65 for plotting convention.

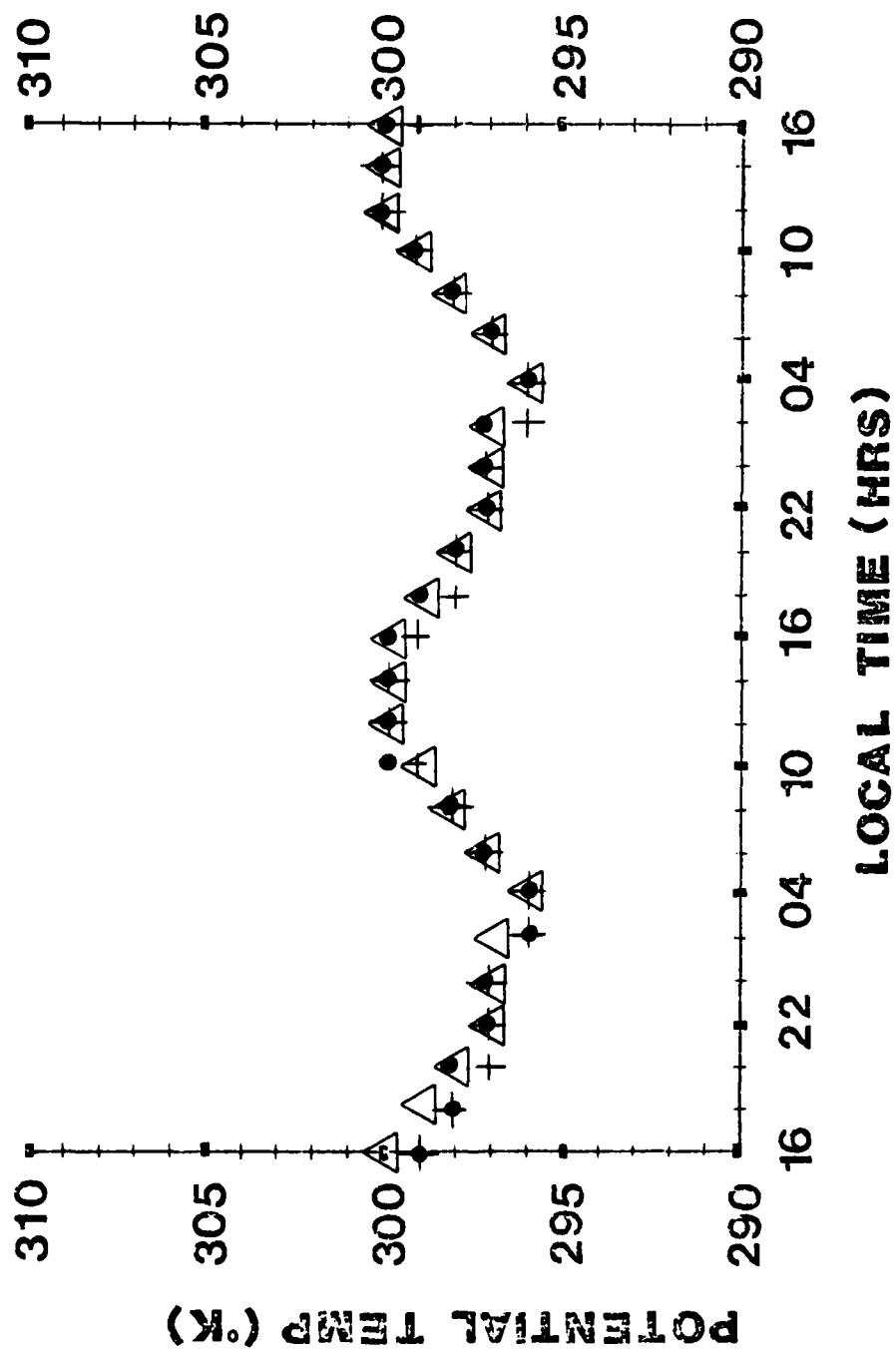


Figure 74. Diurnal temperature curves from grid point 22. Height is 49m. See Figure 65 for plotting convention.

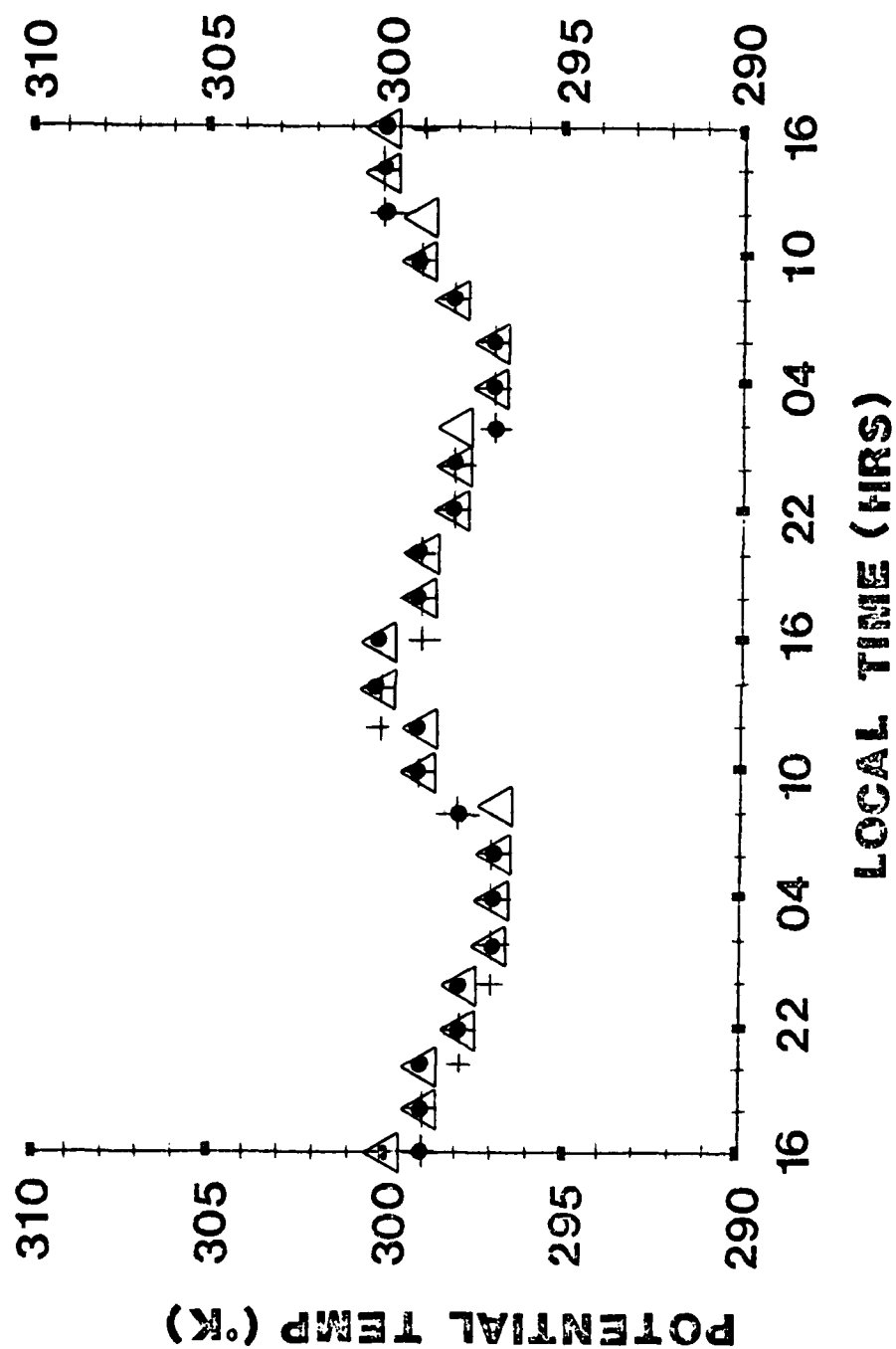


Figure 75. Diurnal temperature curve from grid point 22. Height is 133m. See Figure 65 for plotting convention.

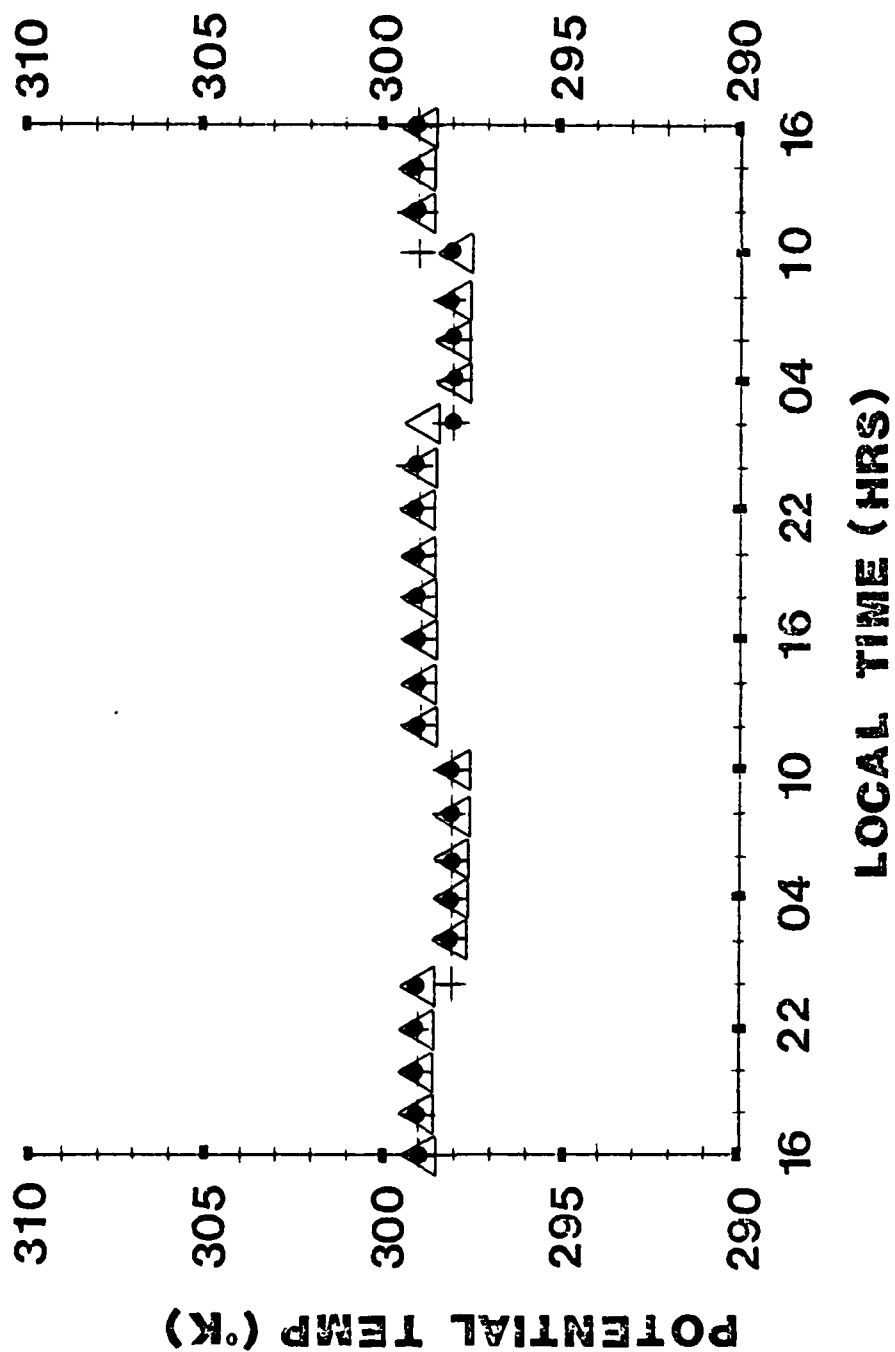


Figure 76. Diurnal temperature curves from grid point 22. Height is 480m. See Figure 65 for plotting convention.

radiational tests with the model, it is felt that this limitation is not an area of concern.

7.4 Soil Type

7.4.1 Purpose

The purpose of this test is to determine the sensitivity of the boundary layer vertical motion field to soil type.

7.4.2 Test Description

Linearized results of Paegle (1978) indicated a sensitivity of the boundary layer convergence fields to the evolution of the low-level temperature field. The question arises as to the effect of soil type on the interacting low-level temperature field and momentum boundary layer.

Three very different soil types were tested using the complete boundary layer model as described in Section 7.2. The amplitude and phase of the vertical motion field as well as the diurnal temperature patterns from several grid points were analysed.

7.4.3 Results

The soils were classified by conductive capacity which is $\rho_s c_s \sqrt{K_s}$. This term is a measure of the soil's efficiency in diffusing heat away from the surface and retaining it, (the larger the capacity, the more efficient the soil). The three soils tested and their identifying parameters are listed in Table 7.

The amplitude and phase of the vertical velocity fields as a function of the soil parameters are shown in Figures 77, 78, and 79. A summary of this data is contained in Table 8. Column A of Table 8 lists the soil types that are being changed; Column B, the average

Table 7. Parameters for the three soils tested.

Soil Type	$\rho_s c_s (\text{cal m}^{-3} \text{ } ^\circ\text{K})$	$K_s (\text{m}^2 \text{sec}^{-1})$	Conductive Capacity
Dry Sand	3.0×10^5	1.3×10^{-7}	108
Clayland	5.6×10^5	1.2×10^{-7}	194
Sandy Clay	5.9×10^5	3.7×10^{-7}	357

Table 8. Effects of altering soil type on amplitude and phase of boundary layer vertical velocity fields

Change in Soil Type	Average Difference In Phase(hrs)/Number of Grid Points	Average Difference In Amplitude(mm/sec)/Number of Grid Points
CP to DS	3/28 -9/3	8/30 -3/1
SC to CP	4/15 -7/7	6/31 ---
SC to DS	6/21 -7/6	14/31 ---
DS = Dry Sand, CP = Clayland Pasture; SC = Sandy Clay		

increase and decrease in the phase of the maximum vertical velocity and the grid points involved as a result of the soil change; and Column C, the same as Column B except this data pertains to the amplitude of the maximum vertical velocity.

A comparison of the amplitudes and phases of the maximum vertical velocity fields for different soil types is made at selected grid points (Figures 80 through 87). The plotting convention is explained

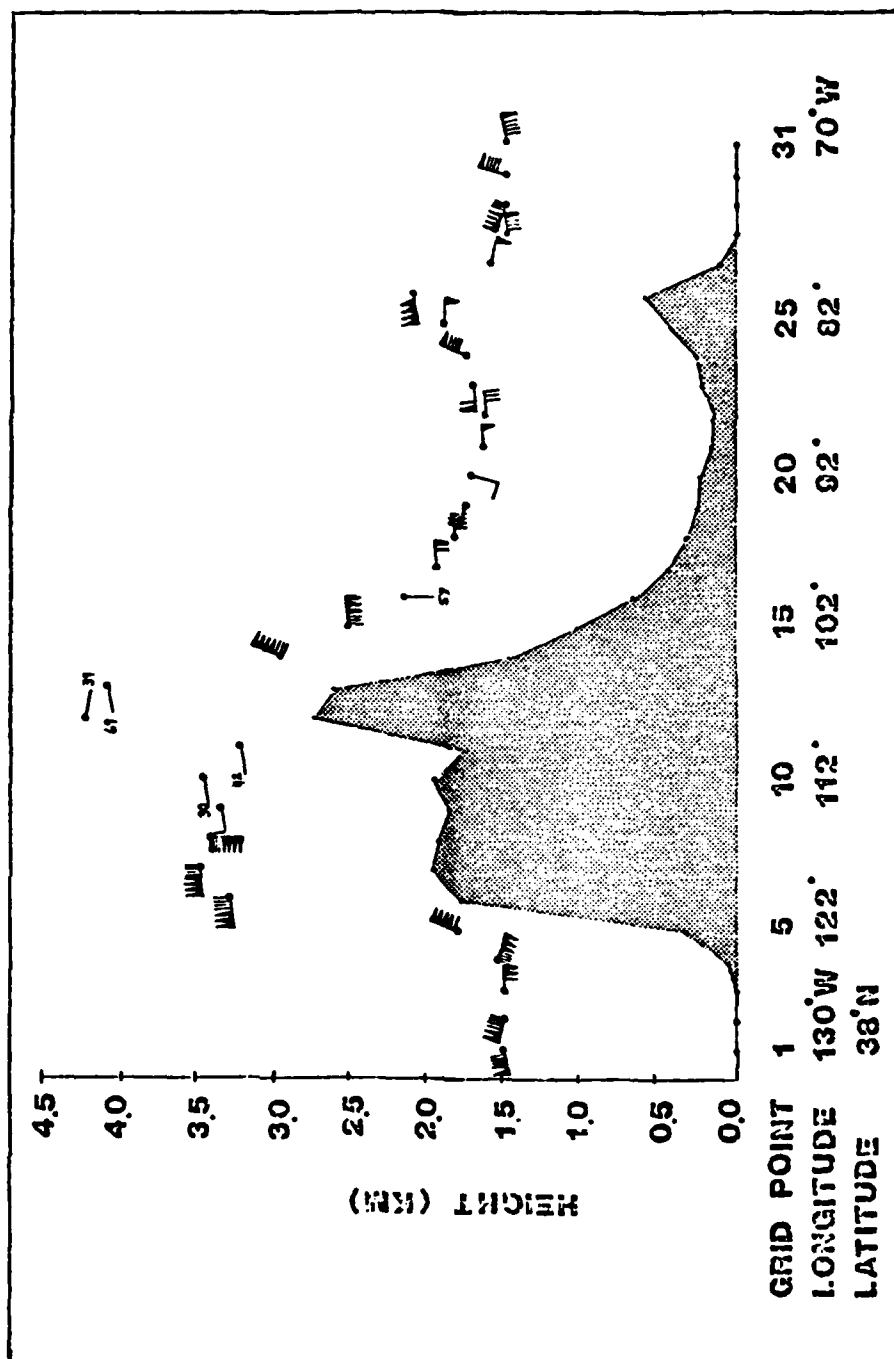


Figure 77. Amplitude and phase of maximum vertical velocity with dry sand soil (conductive capacity = 108). See Figure 48 for plotting convention.

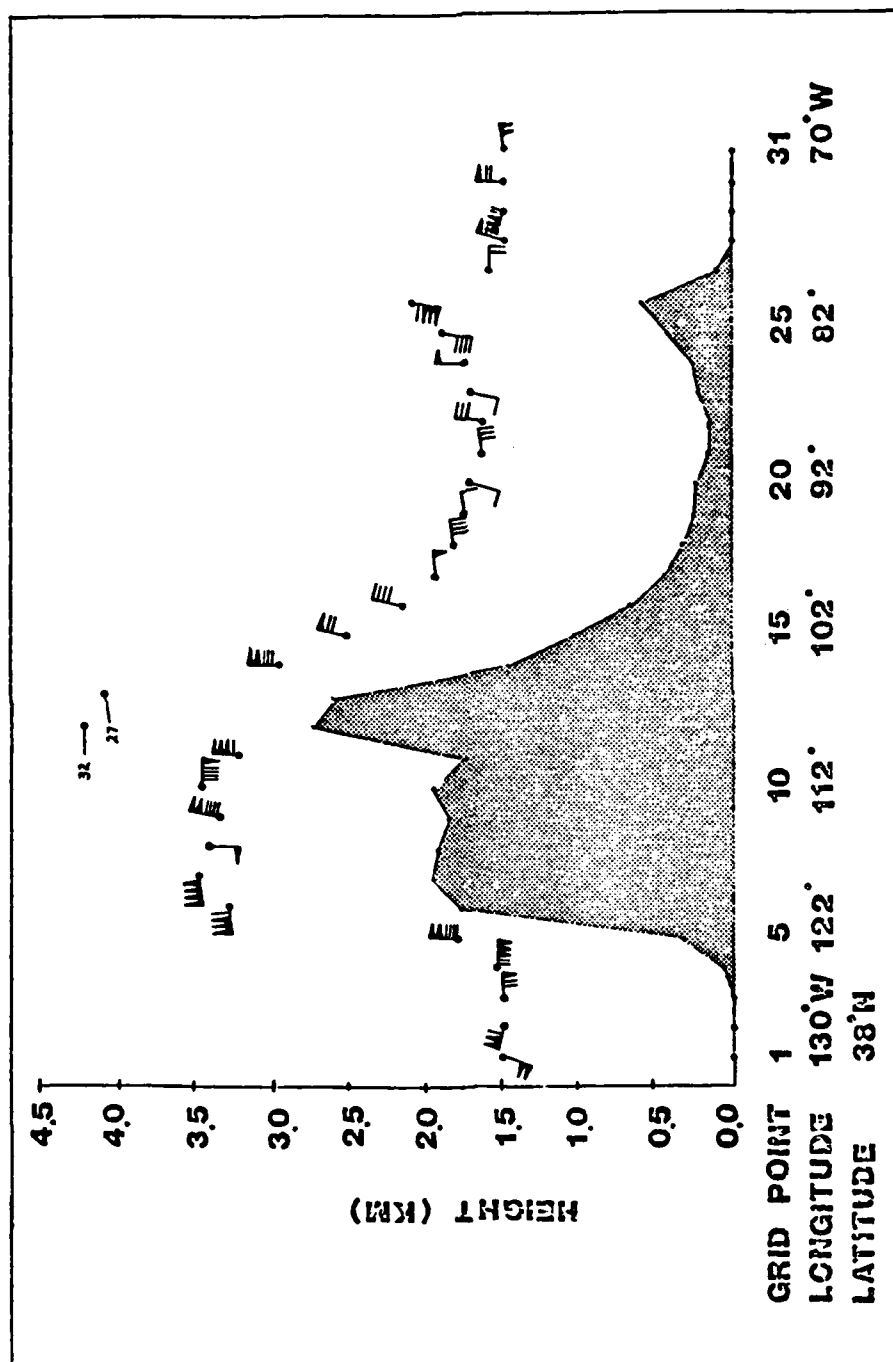


Figure 78. Amplitude and phase of maximum vertical velocity with clayland pasture (conductive capacity = 194). See Figure 48 for plotting convention.

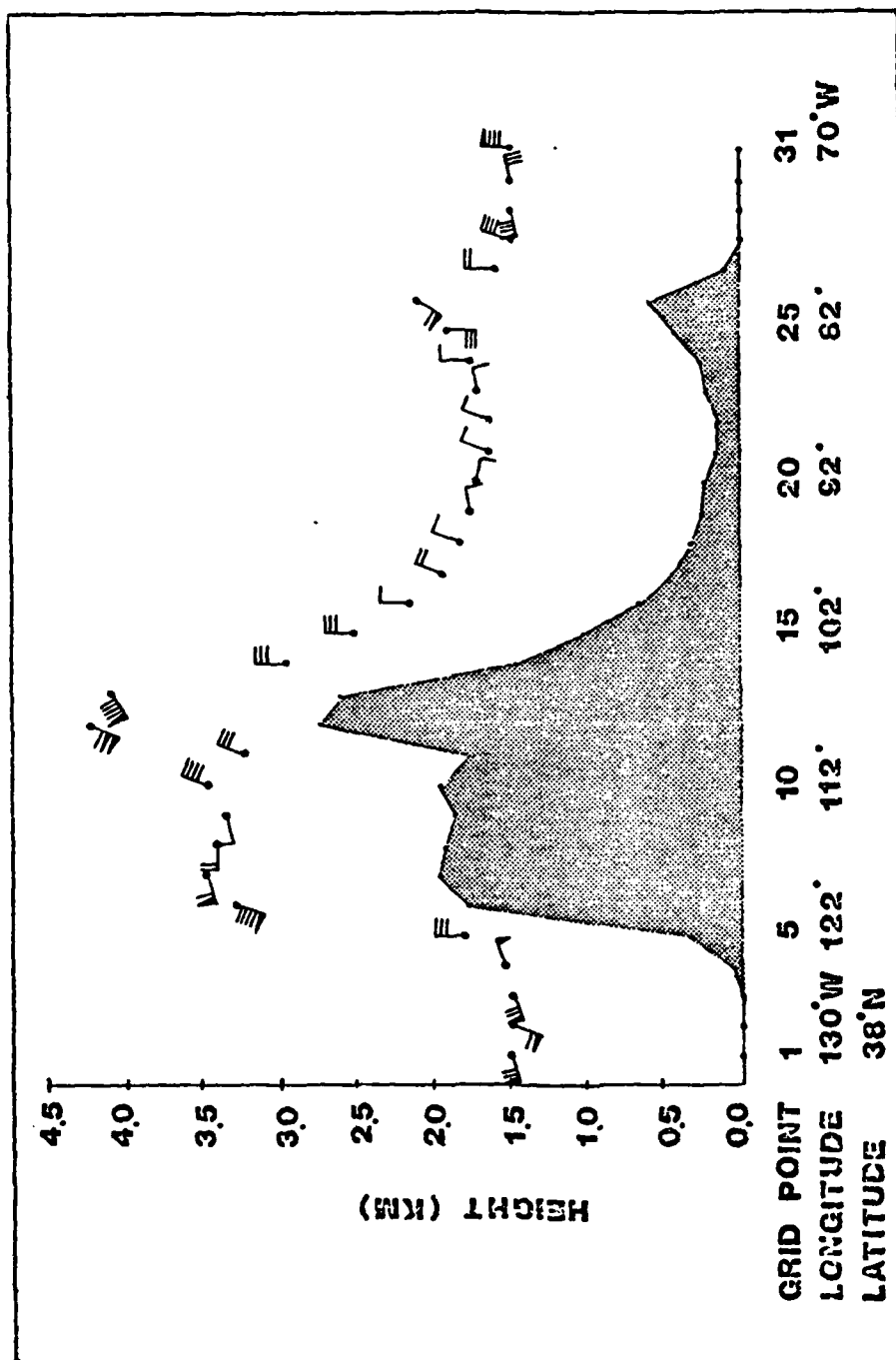


Figure 79. Amplitude and phase of maximum vertical velocity with sandy clay (conductive capacity = 357). See Figure 48 for plotting convention.

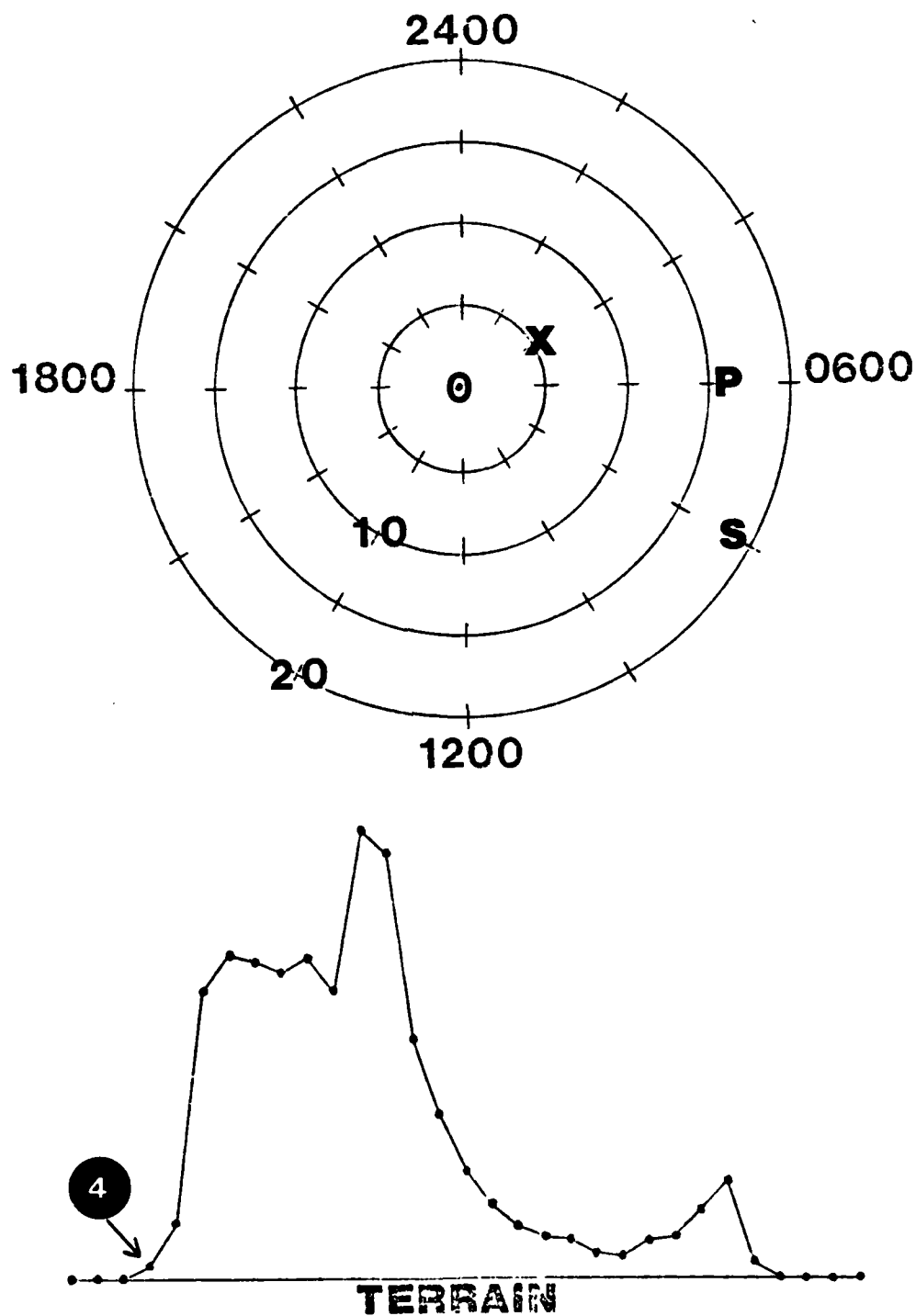


Figure 80. Amplitude and phase of maximum vertical velocity for sandy clay (X), clayland pasture (P), and dry sand (S) for grid point 4. See Figure 51 for plotting convention.

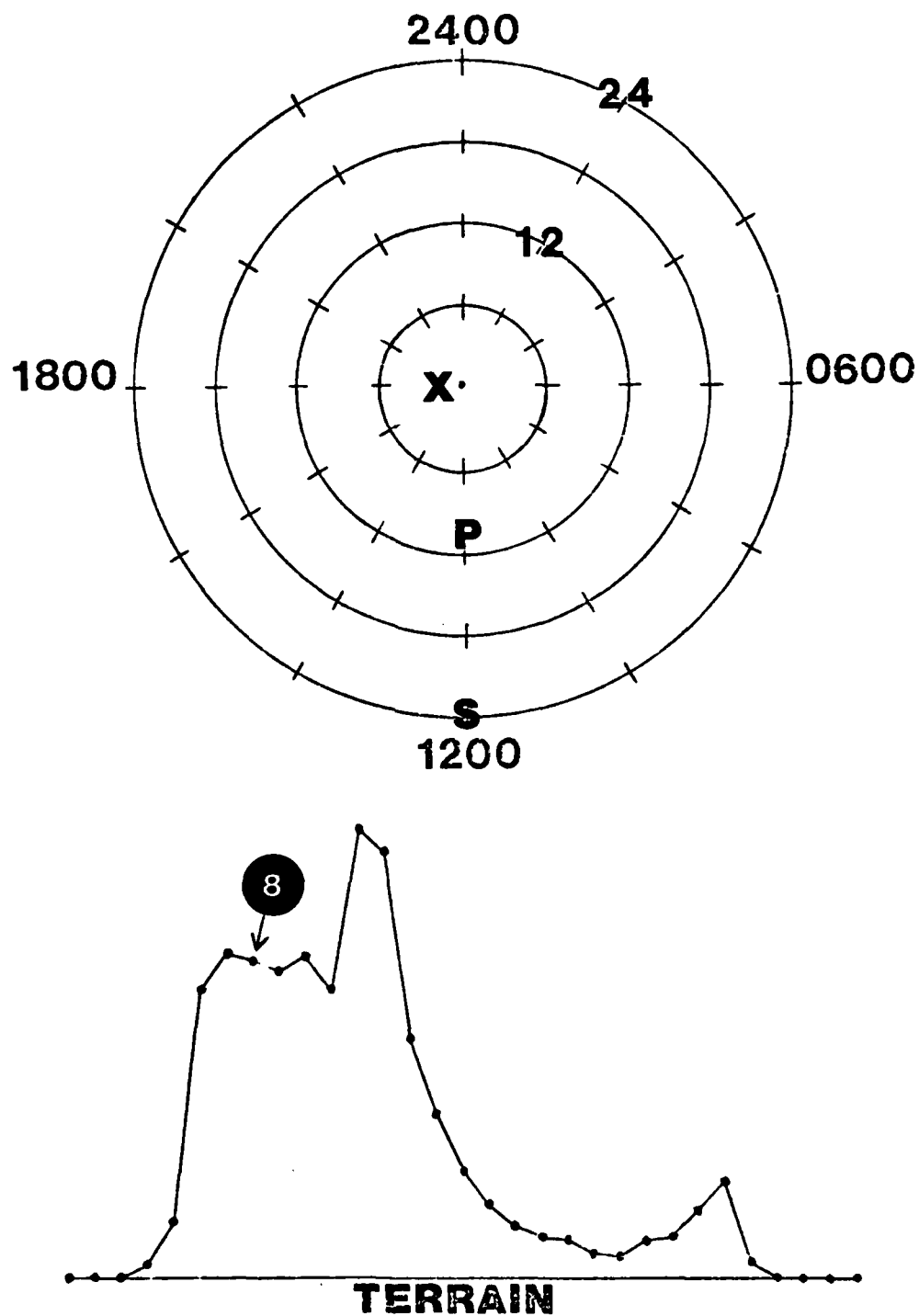


Figure 81. Amplitude and phase of maximum vertical velocity for sandy clay (X), clayland pasture (P), and dry sand (S) for grid point 8. See Figure 51 for plotting convention.

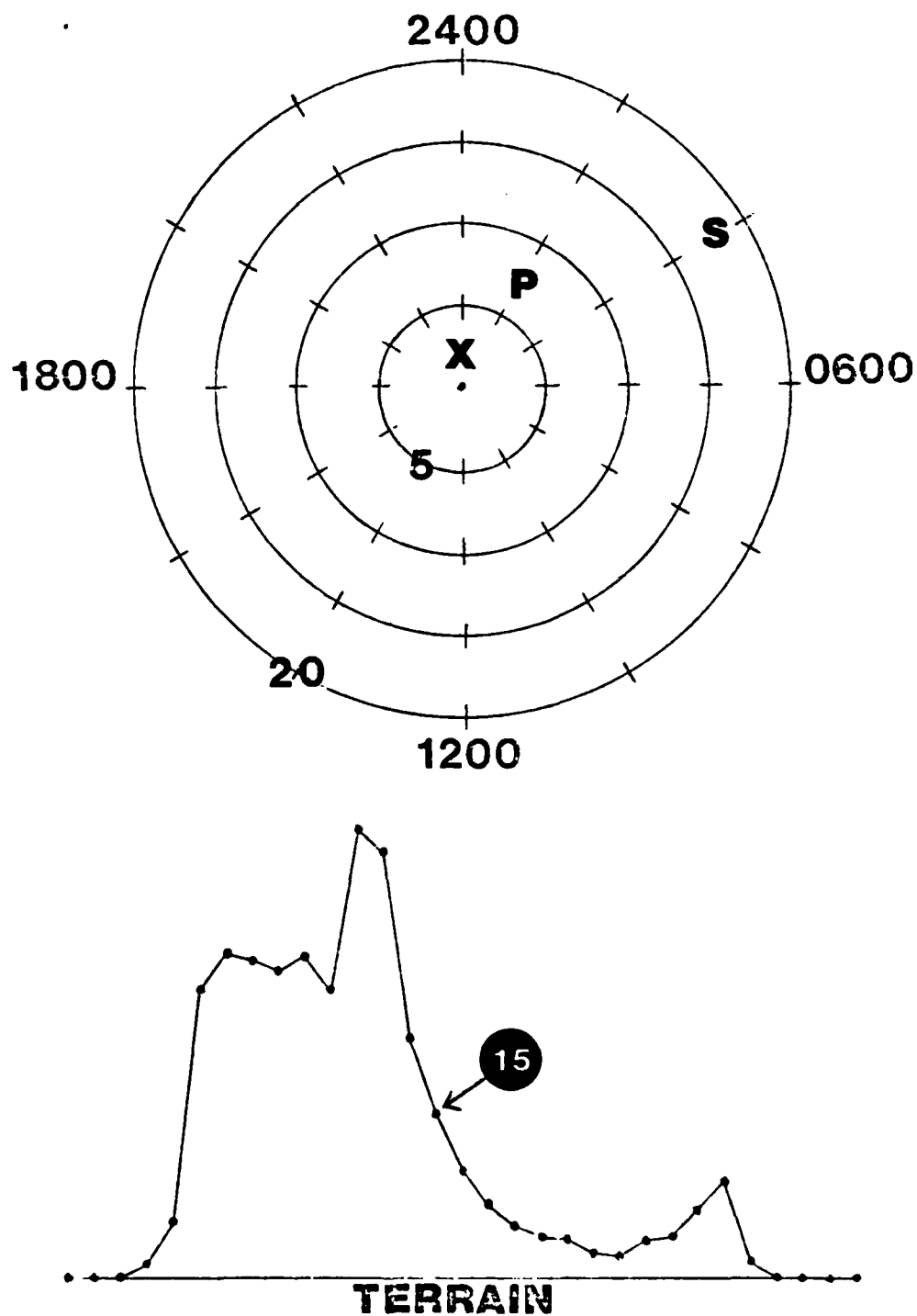


Figure 82. Amplitude and phase of maximum vertical velocity for sandy clay (X), clayland pasture (P), and dry sand (S) for grid point 15. See Figure 51 for plotting convention.

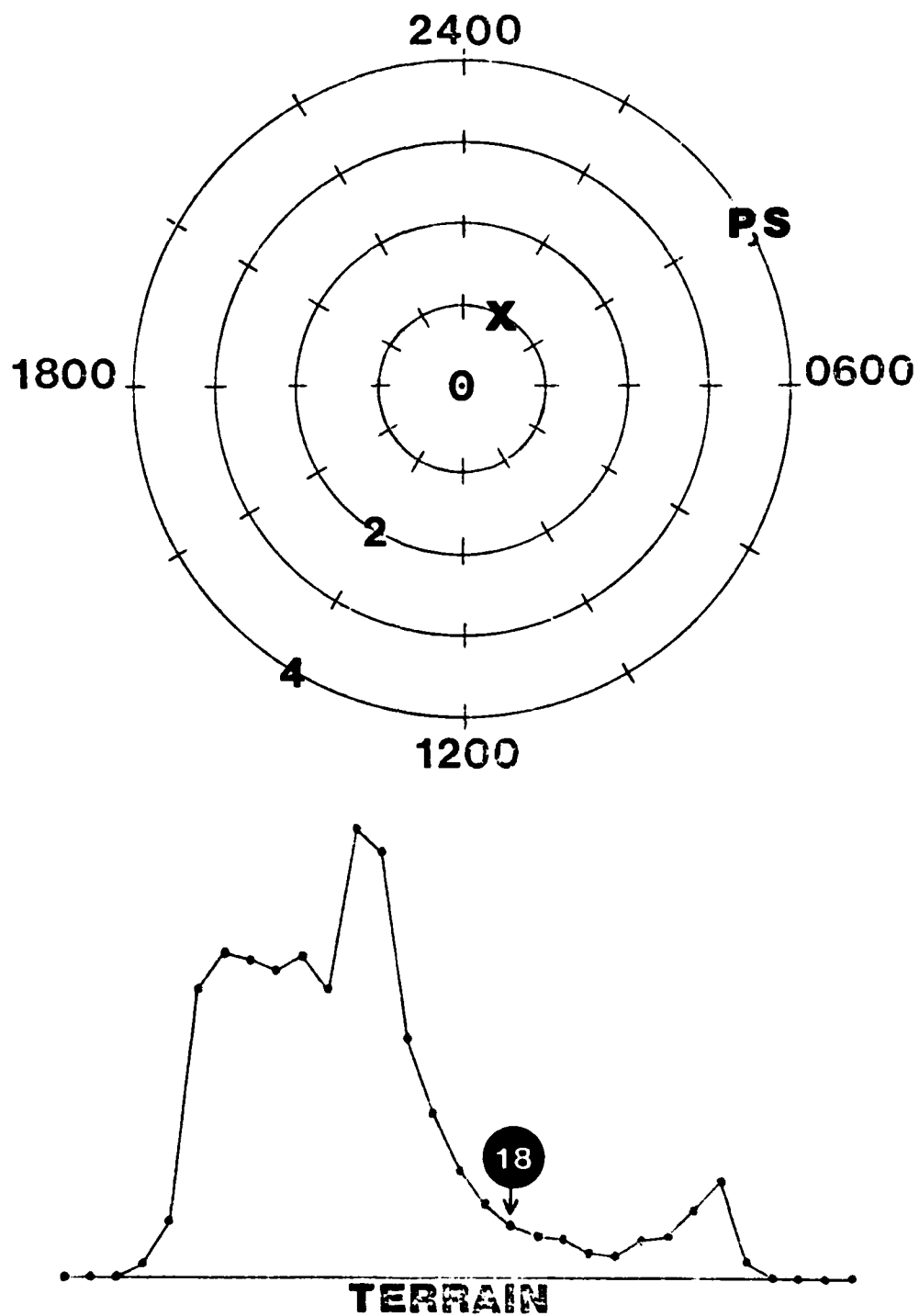


Figure 83. Amplitude and phase of maximum vertical velocity for sandy clay (X), clayland pasture (P), and dry sand (S) for grid point 18. See Figure 51 for plotting convention.

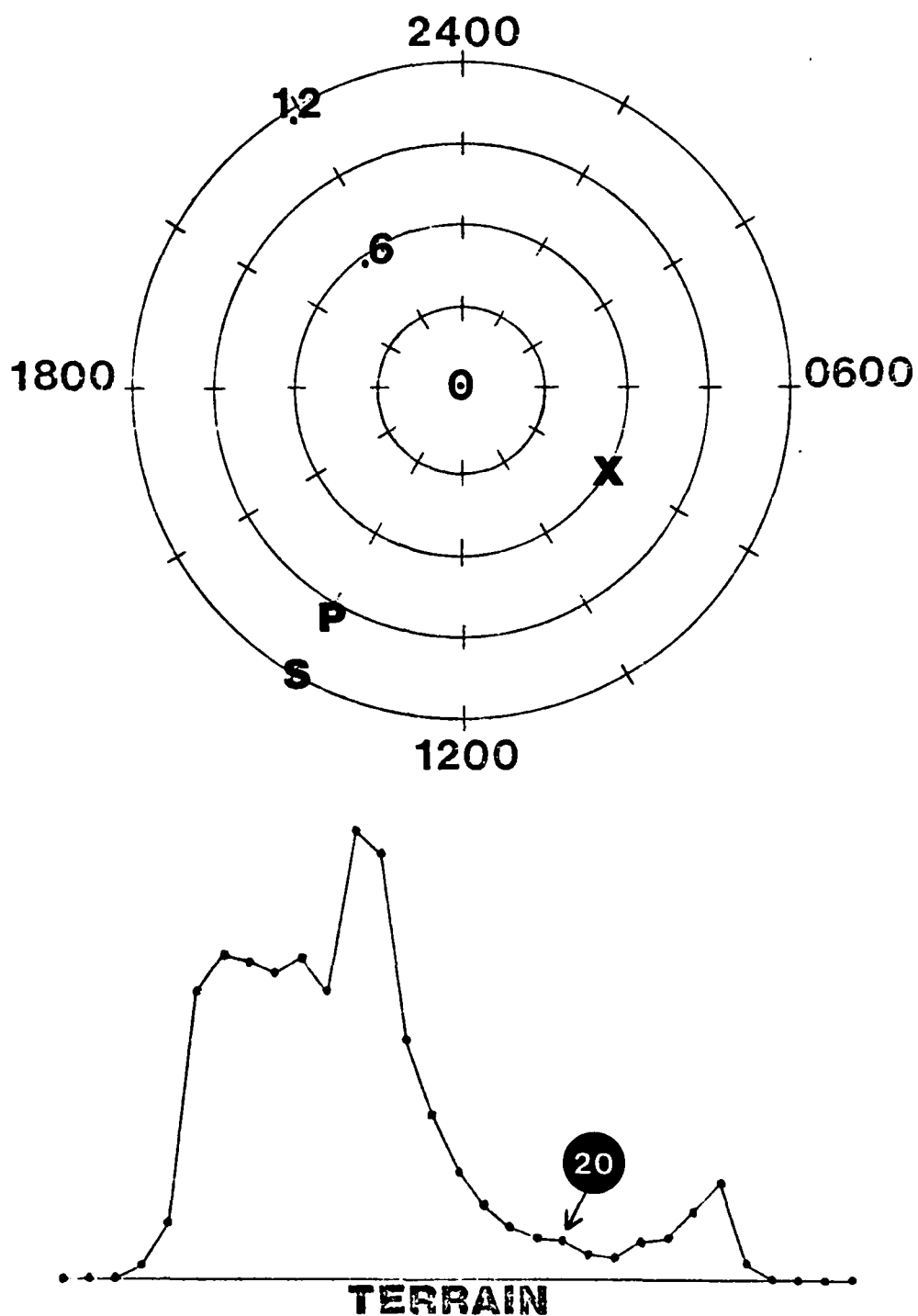


Figure 84. Amplitude and phase of maximum vertical velocity for sand clay (X), clayland pasture (P), and dry sand (S) for grid point 20. See Figure 51 for plotting convention.

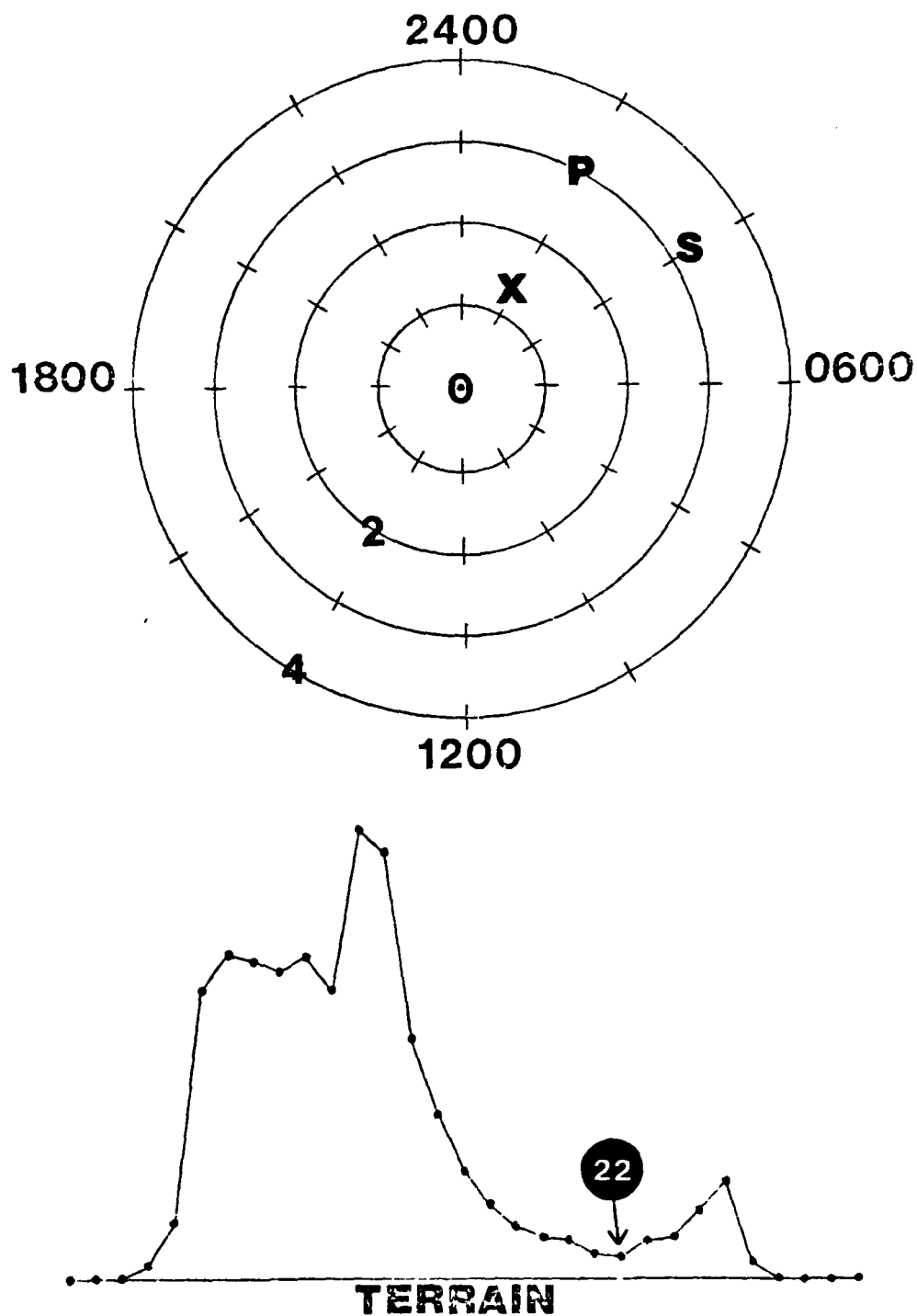


Figure 85. Amplitude and phase of maximum vertical velocity for sandy clay (X), clayland pasture (P), and dry sand (S) for grid point 22. See Figure 51 for plotting convention.

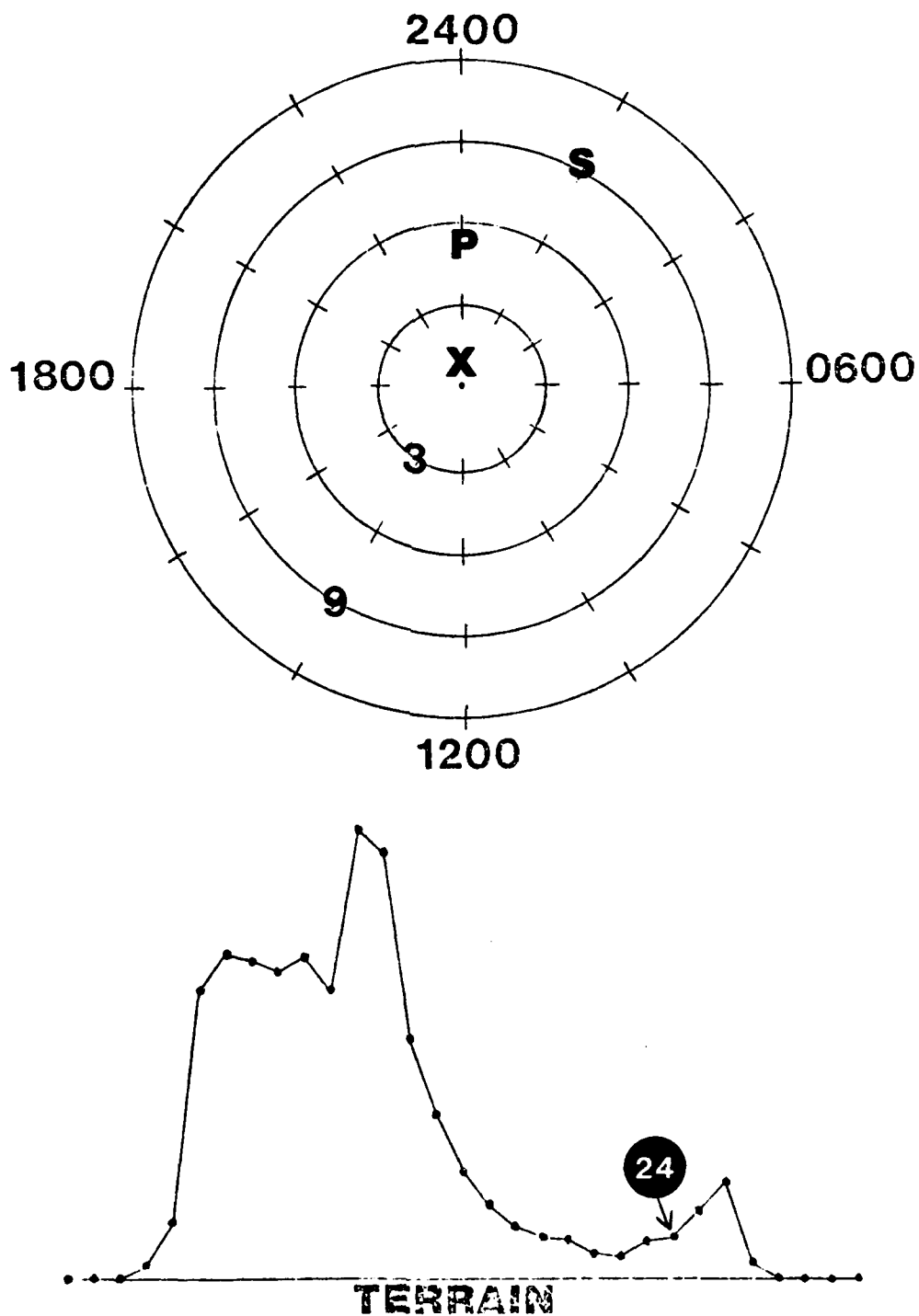


Figure 86. Amplitude and phase of maximum vertical velocity for sandy clay (X), clayland pasture (P), and dry sand (S) for grid point 24. See Figure 51 for plotting convention.

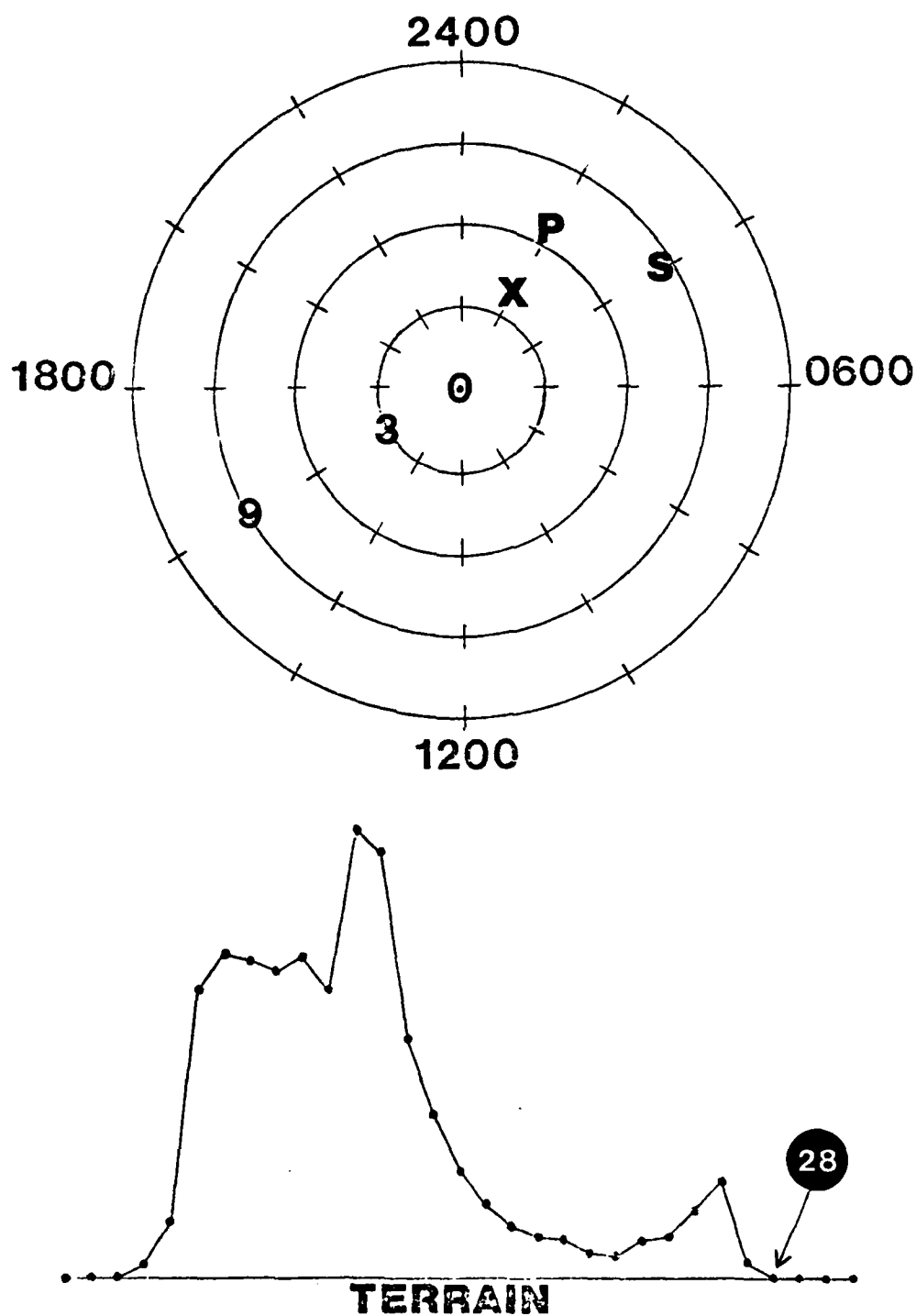


Figure 87. Amplitude and phase of maximum vertical velocity for sandy clay (X), clayland pasture (P), and dry sand (S) for grid point 28. See Figure 51 for plotting convention.

in Section 7.2. These figures and Table 8 clearly indicate that a change in soil type, such that the conductive capacity is altered, may result in a substantial change in the amplitude and phase of the maximum vertical velocity. In the extreme case of changing from a sandy clay to a dry sand soil, the maximum amplitude occurred an average of six hours later for 21 of the 31 grid points and the amplitude increased an average of 14mm/sec at each grid point.

Figures 88 through 99 show the relationship between soil type and diurnal temperature pattern. The following plot convention was used: (1) · clayland pasture, (2) + dry sand, and (3) Δ sandy clay. The larger the conductive capacity of the soil the less variation in the temperature field. These figures also indicate that a change in soil type does not only affect the very low levels of the boundary layer but also at least above 500m where a four to five degree temperature difference is noted between soil types.

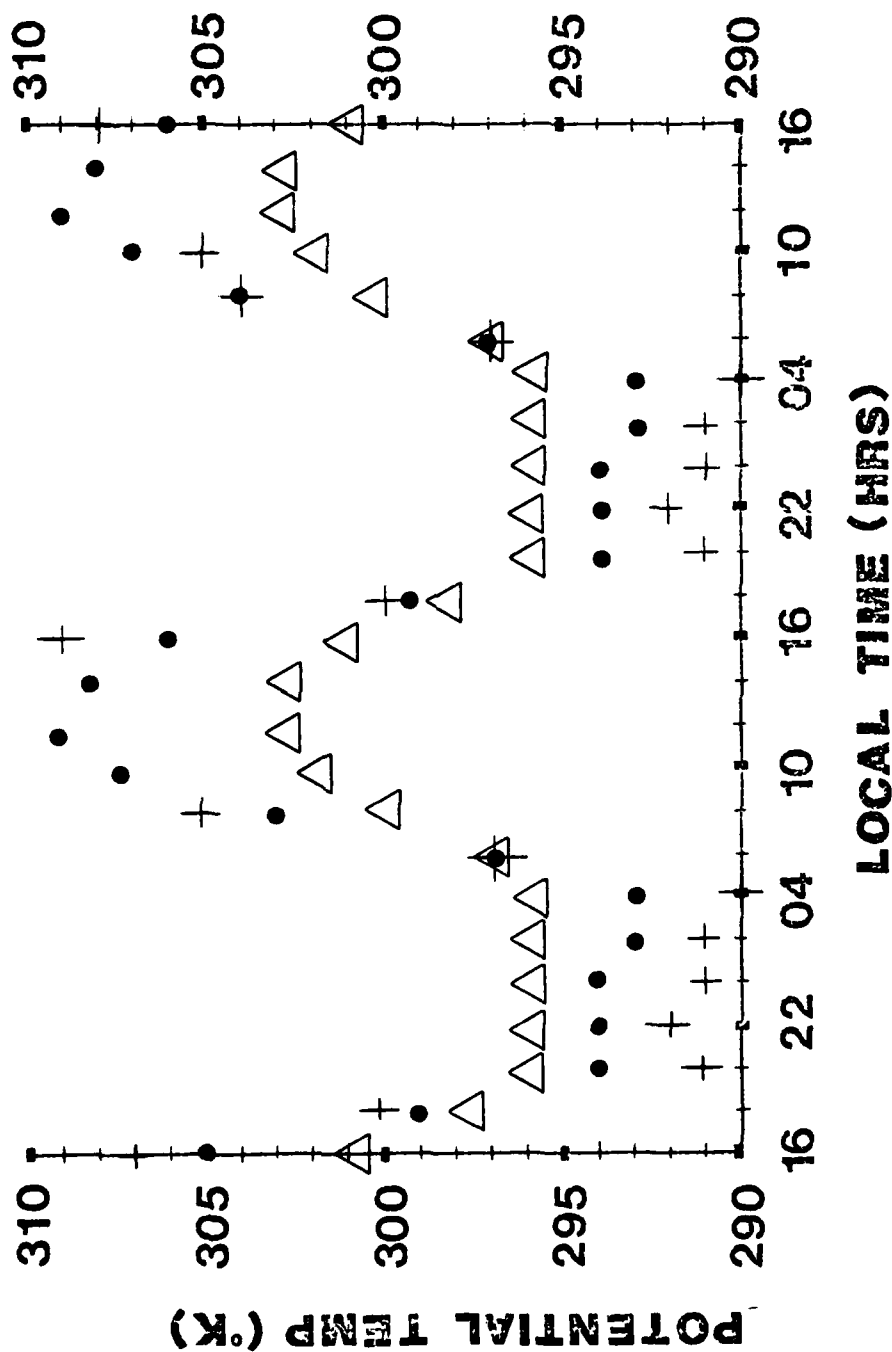


Figure 88. Diurnal temperature curves for grid point 15. Height is Z_0 .
See Figure 65 for plotting convention.

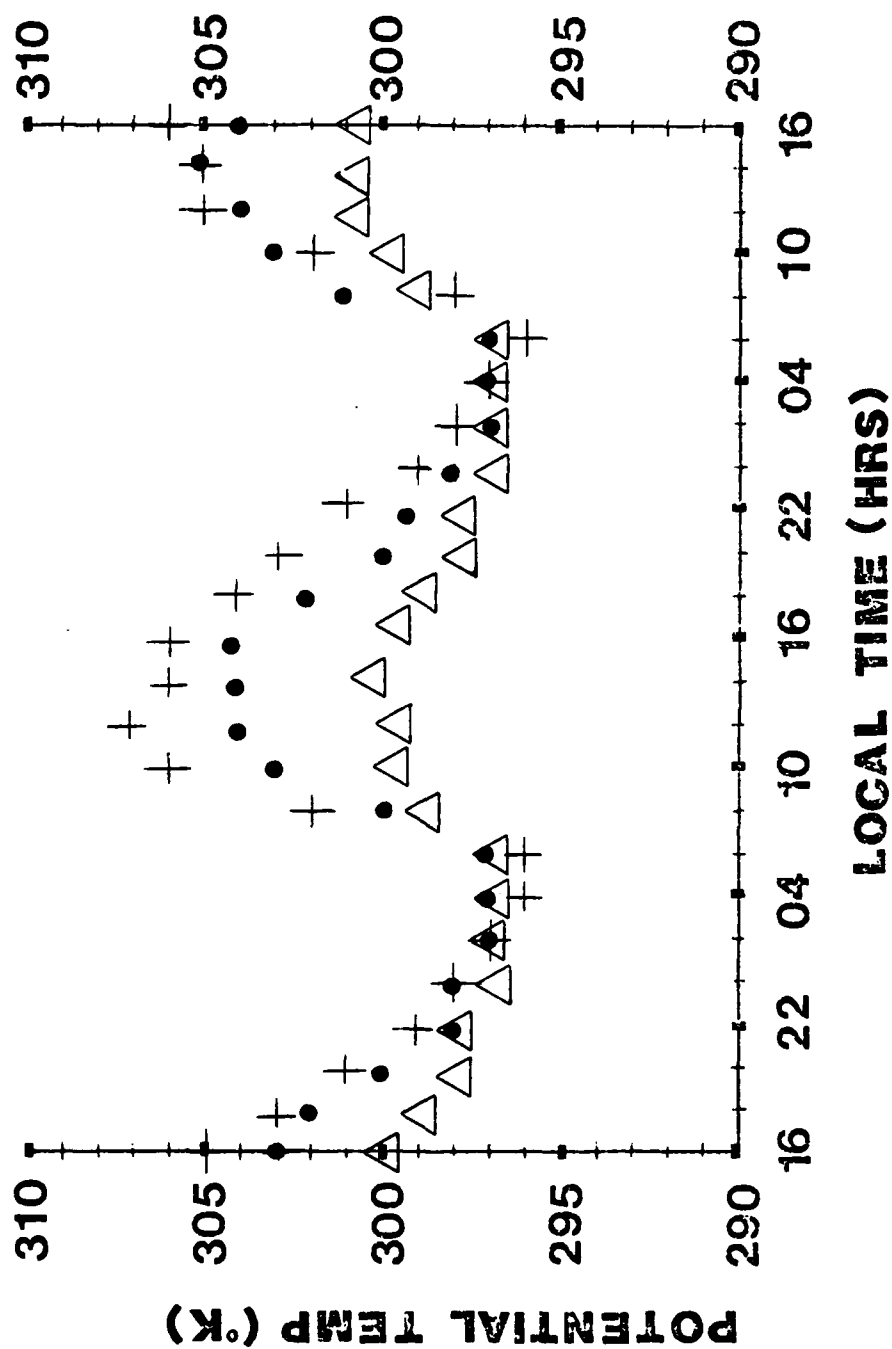


Figure 89. Diurnal temperature curves for grid point 15. Height is 49m.
See Figure 65 for plotting convention.

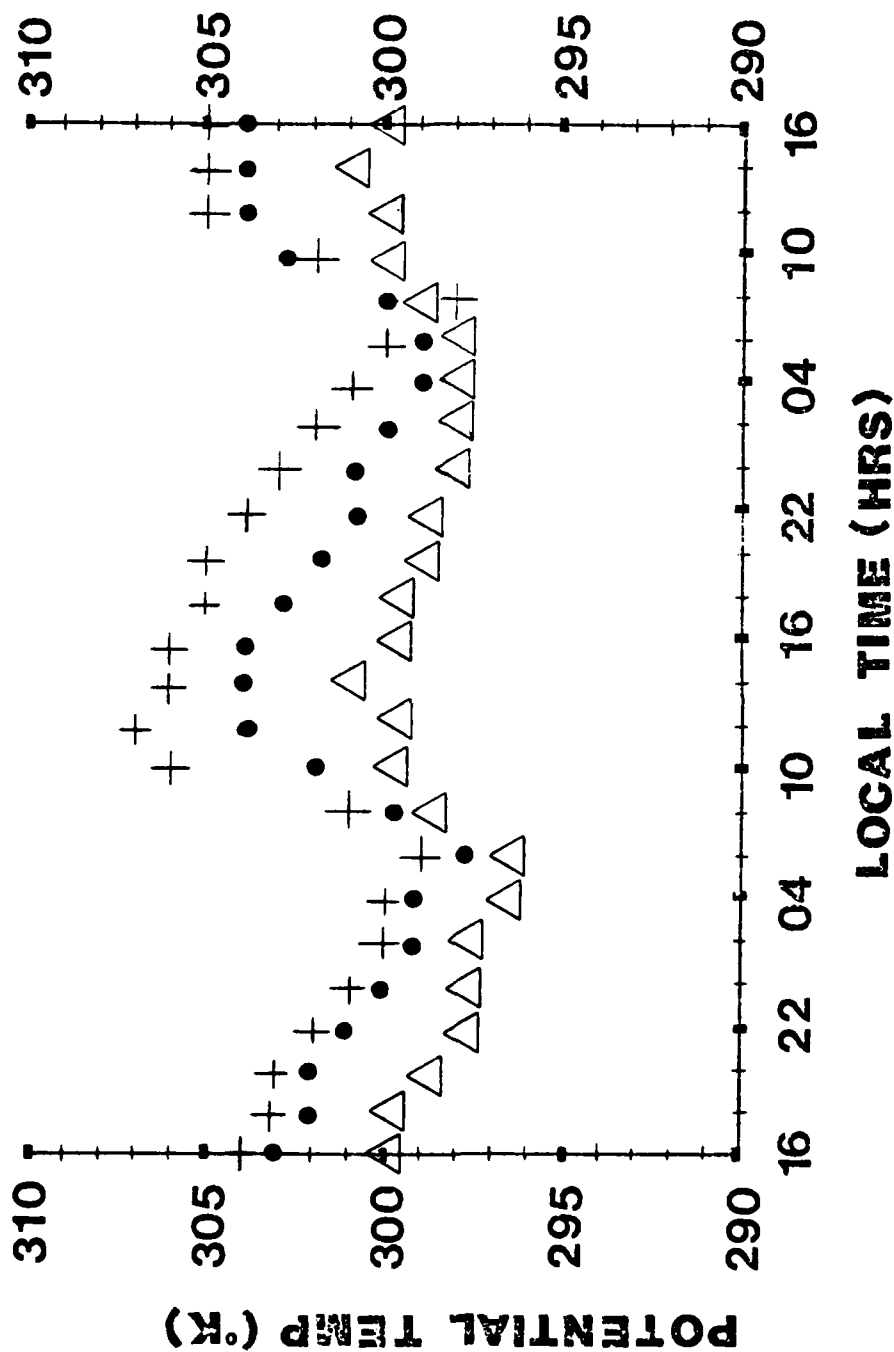


Figure 90. Diurnal temperature curves for grid point 15. Height is 133m.
See Figure 65 for plotting convention.

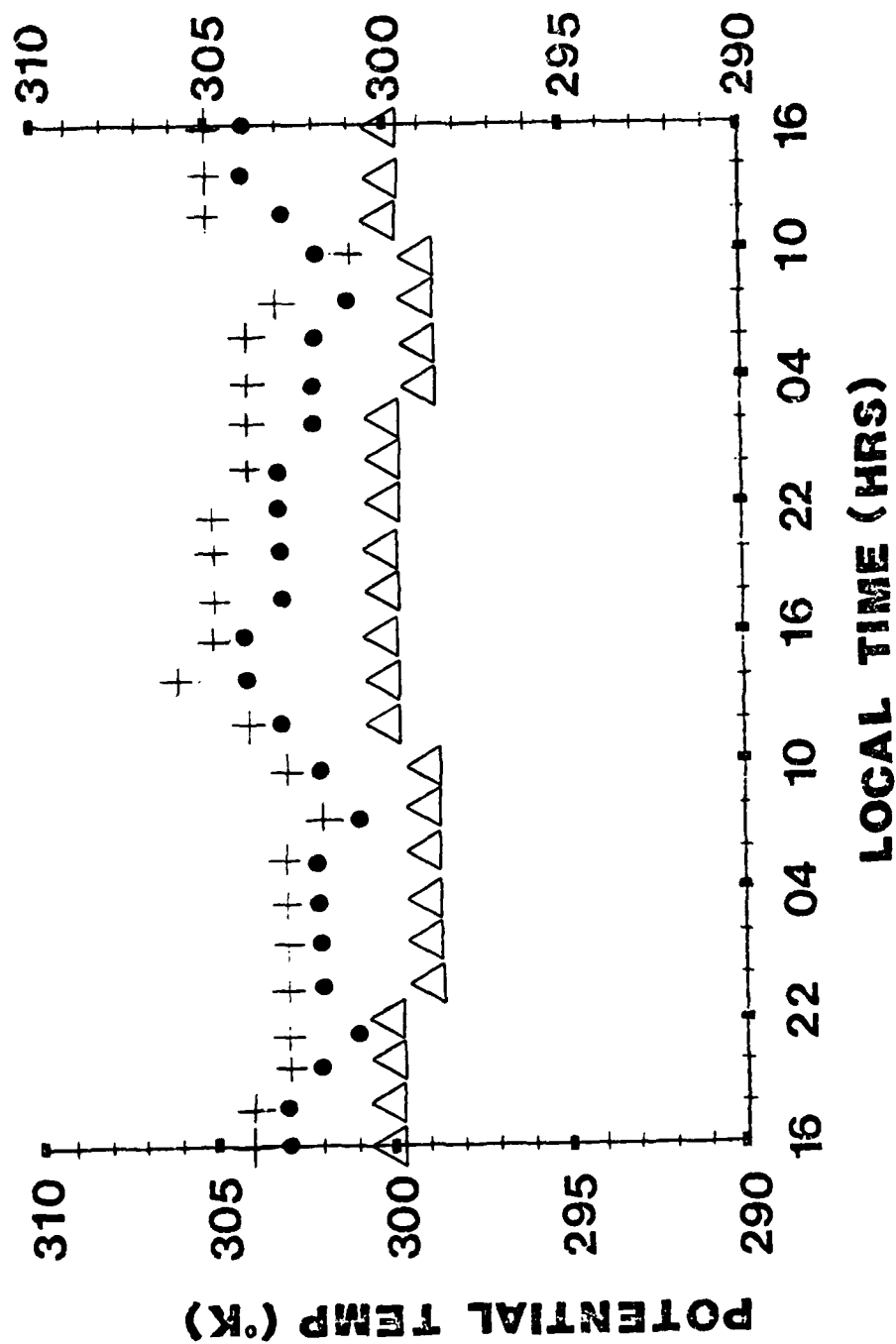


Figure 91. Diurnal temperature curves for grid point 15. Height is 480m.
See Figure 65 for plotting convention.

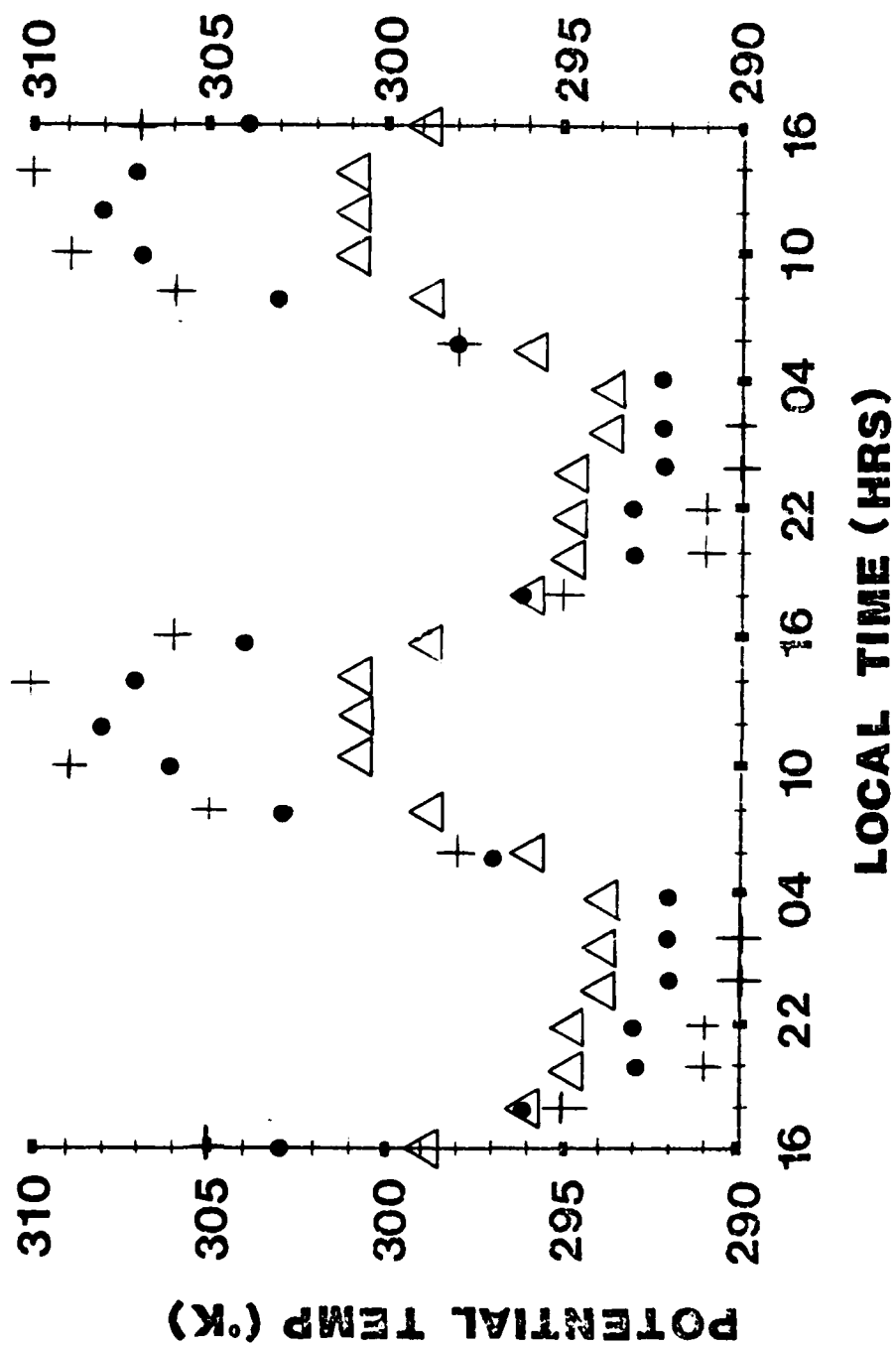


Figure 92. Diurnal temperature curves for grid point 18. Height is Z_0 .
See Figure 65 for plotting convention.

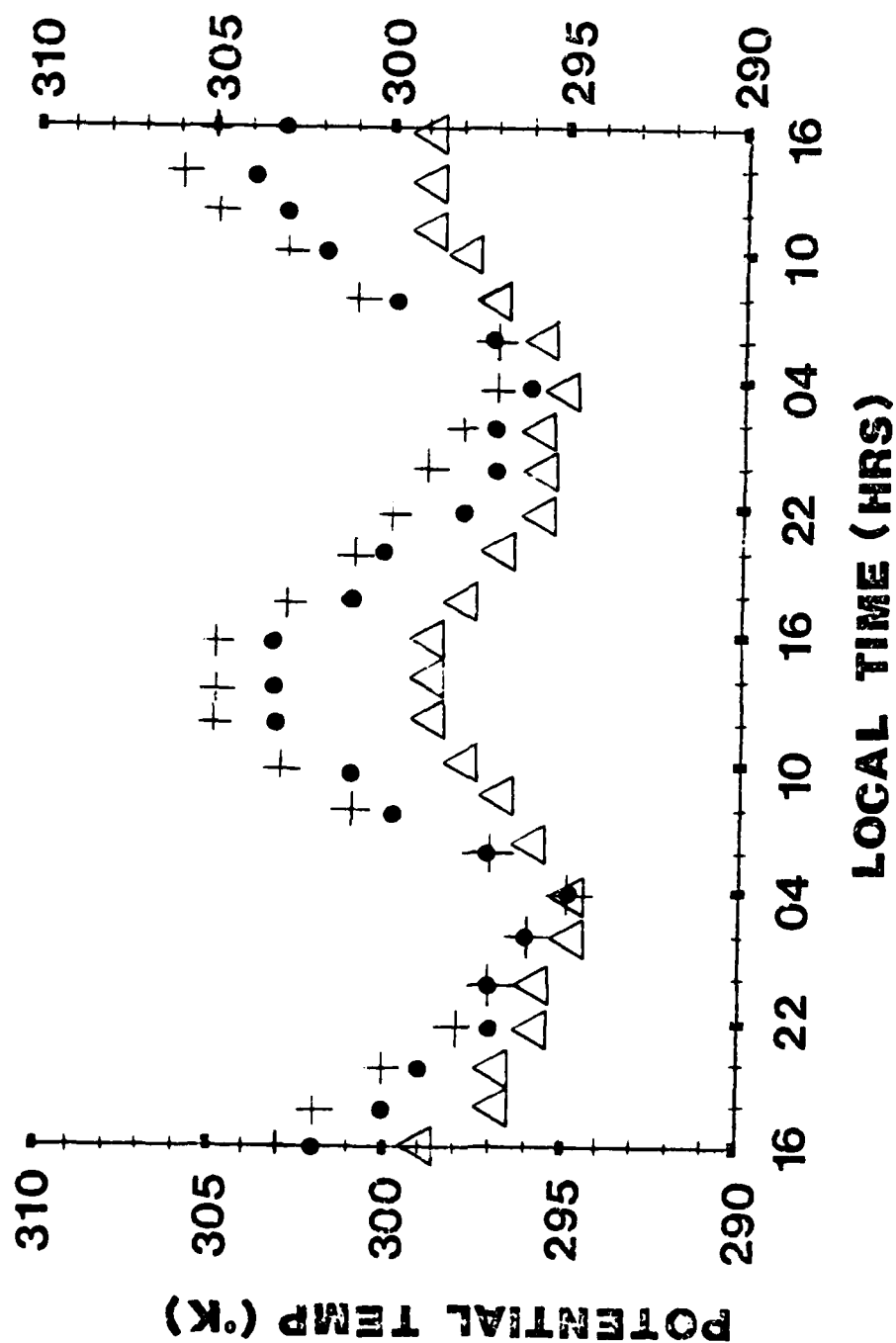


Figure 93. Diurnal temperature curves for grid point 18. Height is 49m. See Figure 65 for plotting convention.

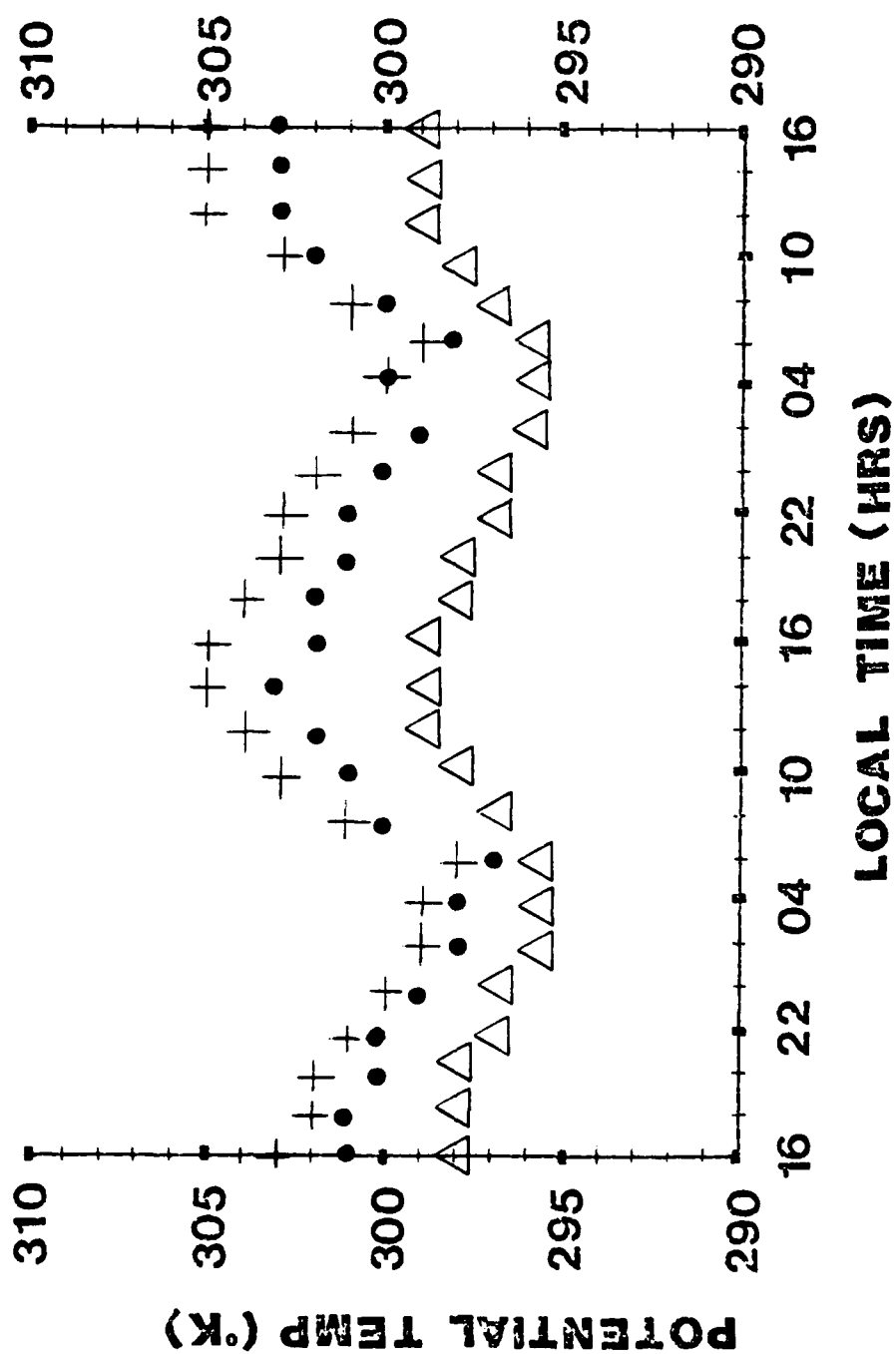


Figure 94. Diurnal temperature curves for grid point 18. Height is 133m.
See Figure 65 for plotting convention.

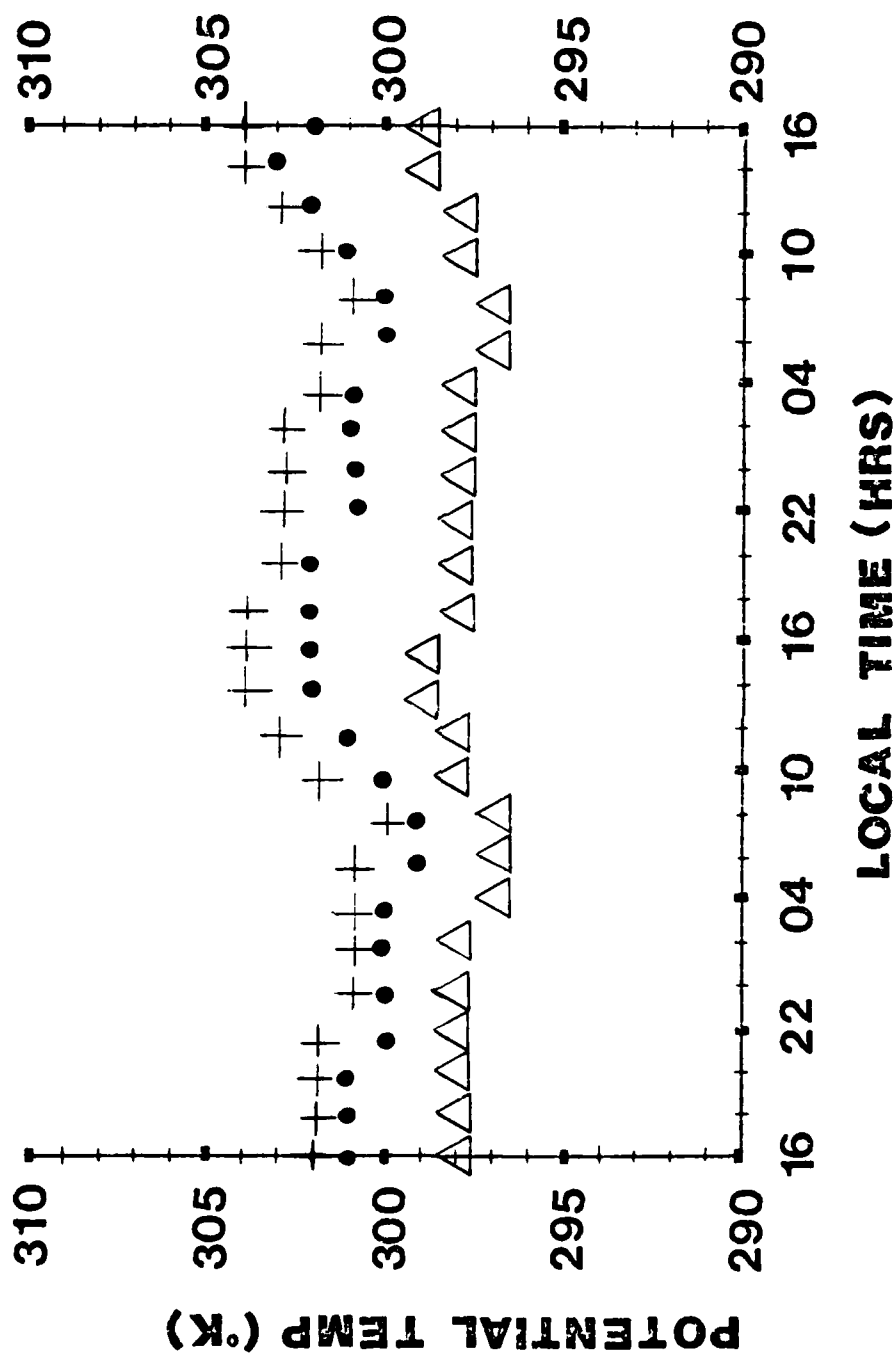


Figure 95. Diurnal temperature curves for grid point 18. Height is 480m.
See Figure 65 for plotting convention.

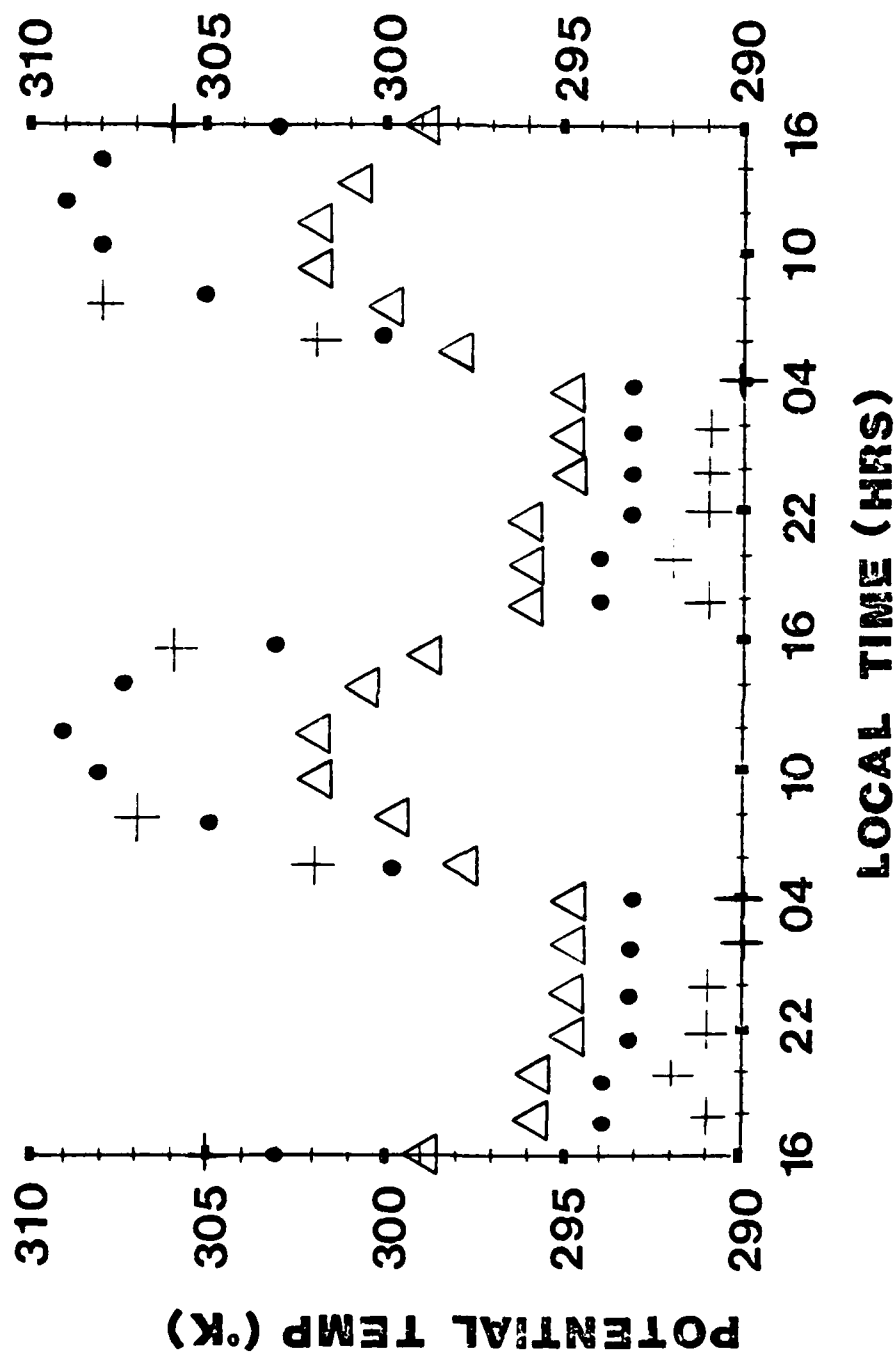


Figure 96. Diurnal temperature curves for grid point 22. Height is Z_0 .
See Figure 65 for plotting convention.

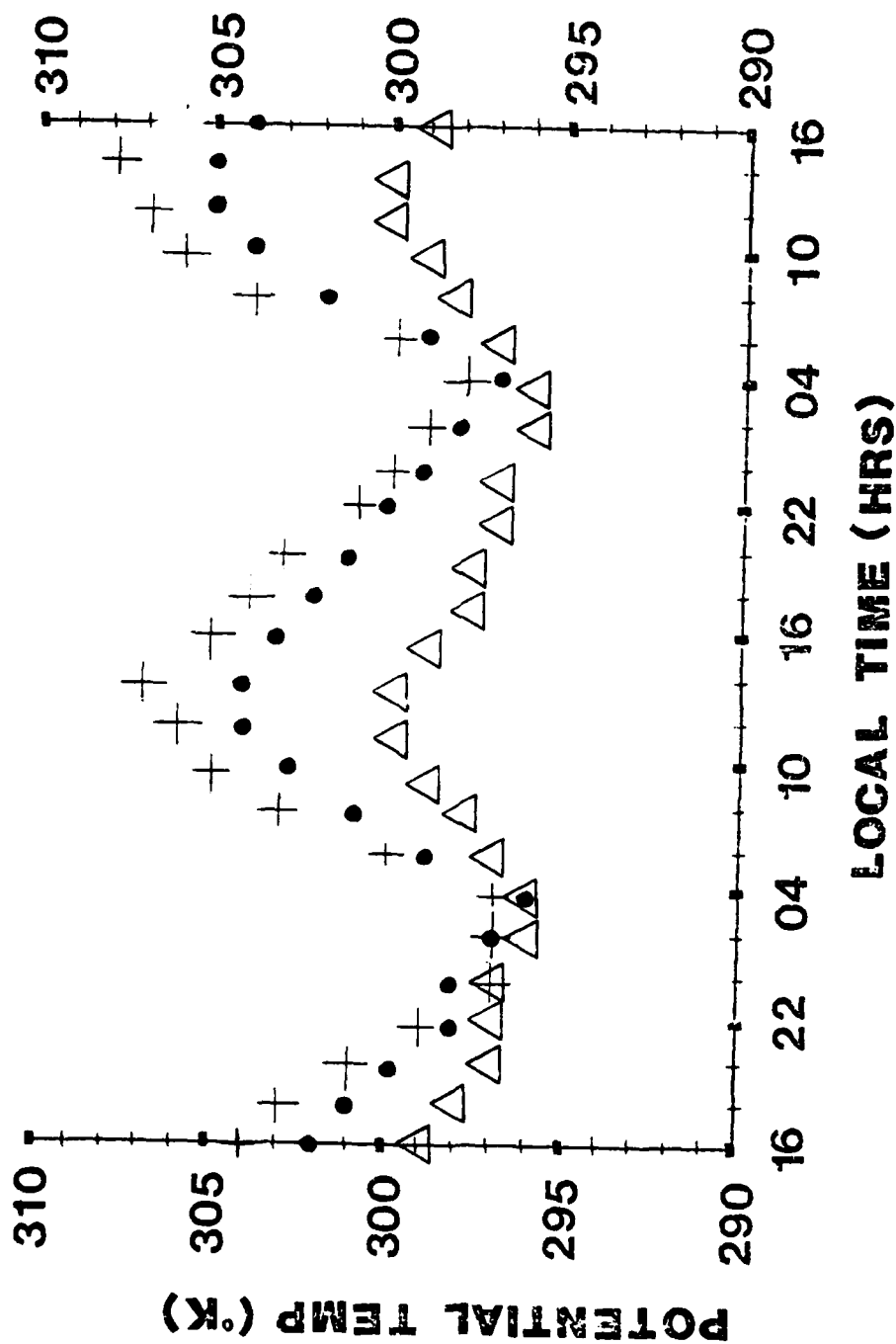


Figure 97. Diurnal temperature curves for grid point 22. Height is 49m.
See Figure 65 for plotting convention.

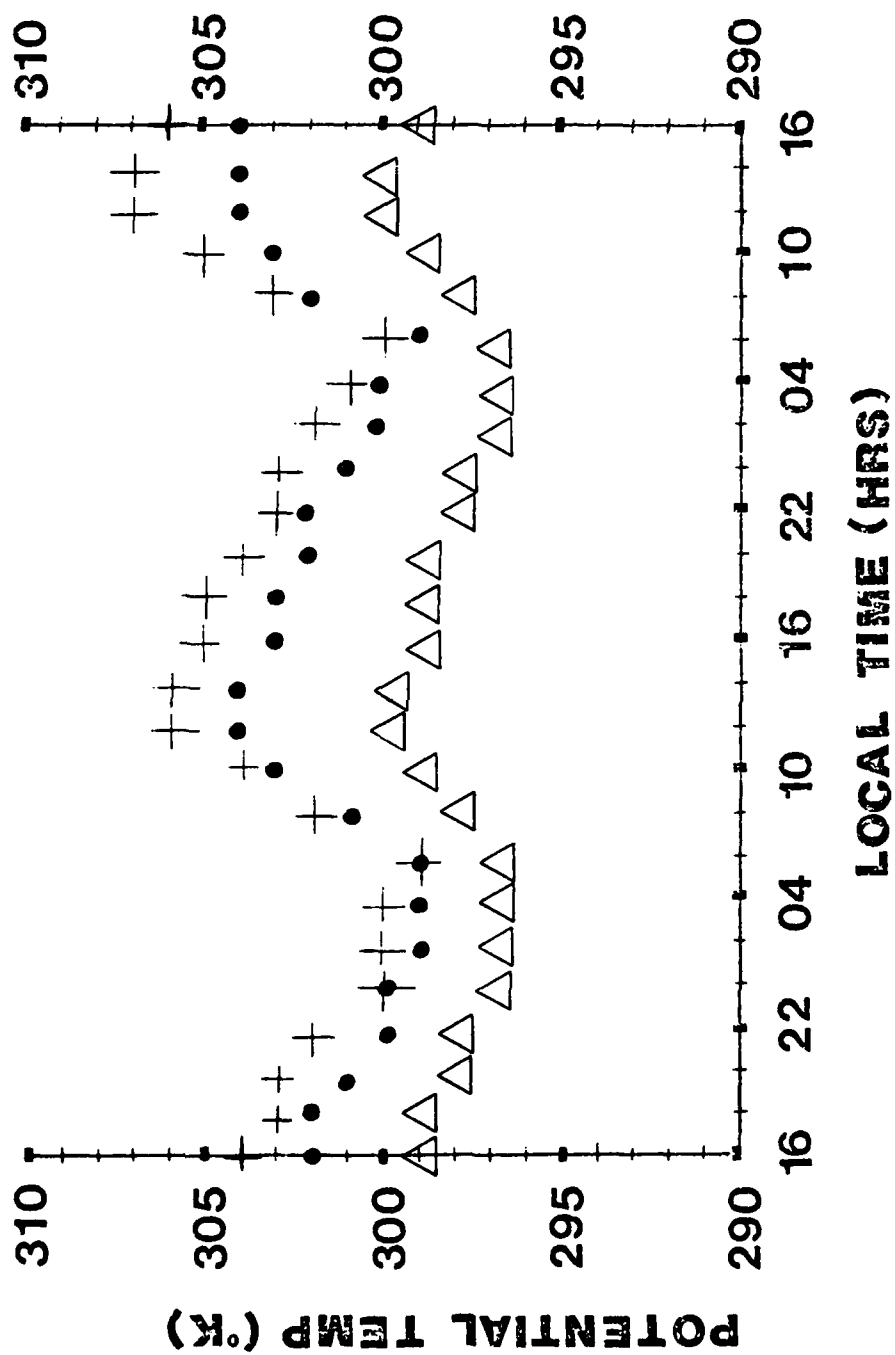


Figure 98. Diurnal temperature curves for grid point 22. Height is 133m.
See Figure 65 for plotting convention.

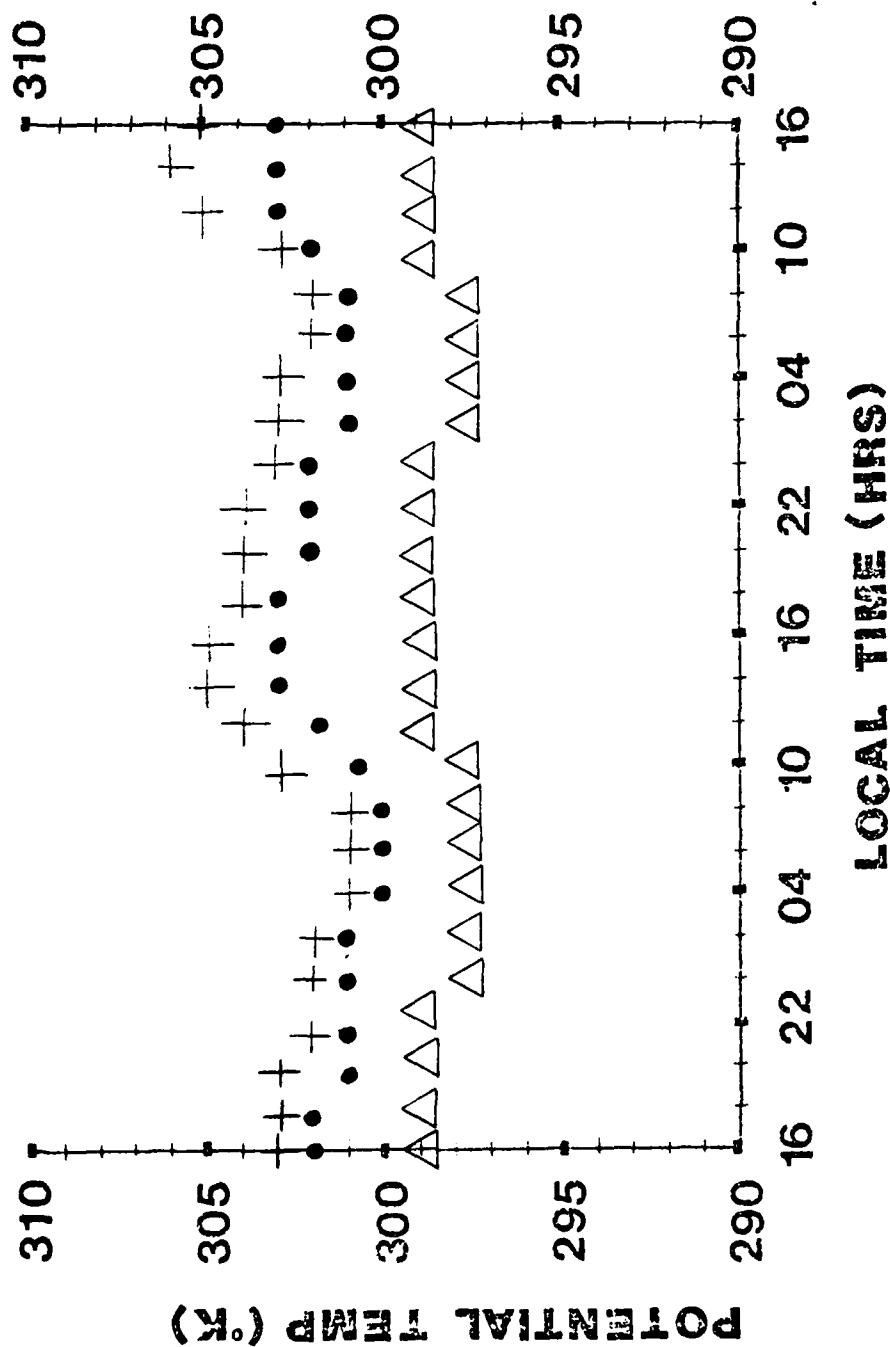


Figure 99. Diurnal temperature curves for grid point 22. Height is 480m.
See Figure 65 for plotting convention.

CHAPTER 8

CONCLUSIONS

The intent of this research has been to develop a boundary layer model with sufficient resolution and physics to define the interacting thermal and momentum boundary layers on diurnal time scales above synoptic scale sloping terrain and thermally inhomogeneous surfaces. It is felt that this model will add understanding to the physical processes and simulation requirements of diurnal boundary layer motions.

Proper resolution of the terrain configuration is essential in models of this type since the terrain slope is one of the primary forcing mechanisms for the diurnal boundary layer motions. This research made significant progress in that area. A local terrain following coordinate system was developed which has characteristics superior to the terrain following coordinate systems commonly used. The local coordinate system produces truncation errors which are significantly less than those produced by the standard systems.

Variations in the flow field due to physical forcing are discernable from those variations due to truncation error in the local coordinate system. This is not always the case with the standard coordinate systems. In the latter, it is not always possible to determine that variations in the flow field are caused by physical forcing or truncation error. The local coordinate system enjoys an additional advantage over the standard systems in that it can apparently resolve a coarser terrain configuration and still provide stable solutions.

The sensitivity of the complete model was tested against parameters which had shown a certain amount of sensitivity in earlier, less complete models. The phenomena believed responsible for boundary layer convergence are the diurnal oscillations of eddy stresses and buoyancy forces above sloping terrain. The argument can be made that if boundary layer convergence fields are formed by the above type of forcing, their formation should occur later in the day at lower latitudes. Also the diurnal forcing may be in resonance with the natural period of oscillation at certain latitudes, thereby affecting the amplitude of the winds and possibly the boundary layer convergence. Forecasts by the complete model did reveal a sensitivity to latitude. The phase of the maximum vertical motion occurred six hours later between 38°N and 22°N . These results are in agreement with Paegle's (1978) linearized solutions. The model did not indicate a significant change in amplitude between latitudes.

Radiation calculations in the complete model were very time consuming. Many sensitivity tests were conducted to find ways to reduce this time. These tests revealed that a radiational model 5 KM thick was as effective in calculating boundary layer global radiation and flux divergence as a model 9 KM thick.

The boundary layer model is apparently not very sensitive to flux divergence calculations; in fact, tests conducted to determine the best frequency for radiation calculations did not show significant differences between every two, three, and four hours. A two hour frequency was selected since it was the highest frequency considered economically feasible. This frequency adequately resolves temperature oscillations with periods greater than four hours and is therefore not a serious

limitation for the model. Caution should be expressed when the sensitivity of the boundary layer model to flux divergence is considered. Approximations in the radiational model and emissivity values resulted in cooling rates which were less than those calculated in more complete radiational models.

Little has been reported in the literature on the relationship between soil type and boundary layer convergence. Sensitivity tests of the complete model with three very different soil types shows a definite connection between the amplitude and phase of the maximum vertical velocity and soil type. In the extreme case of changing from a sandy clay to a dry sand soil, the phase occurs six hours later and the amplitude increases 14 mm/sec. It is apparent from these results that future boundary layer models should seriously consider the inclusion of soil type.

The present results tends to support the viewpoint that the pronounced diurnal control upon air mass thunderstorms over the United States resides in boundary layer processes. This control is not simply in reponse to diurnal low level stability changes, but rather through the boundary layer convergence field which is significantly determined by terrain slopes and curvatures as gentle as $1/500$ and $2/10^6 \text{ km}^{-1}$, respectively. Such terrains are found over the central plains of the United States. Here, the response of W on the order of 1 mm/sec to 10 mm/sec at 1 KM corresponds to layer average divergences of order 10^{-6} sec^{-1} to 10^{-5} sec^{-1} . These magnitudes are similar to those associated with synoptic scale weather systems and suggest that precise timing of thunderstorm activity may be predicted only with a coupled boundary layer-free tropospheric model.

In the past, major problems in the execution of such a model have involved excessive numerical truncation error in the vicinity of sloping terrain and uncertainty with respect to the most relevant boundary layer processes. Both of these problems have been addressed in this research with some success. It appears that the next major obstacle is the availability of a sufficiently powerful computer to process a fully three dimensional coupled model. Based on the computer requirements of the present two dimensional model, this may be technologically feasible on the current largest computers. However, it appears that the most profitable approach to explore the scientific questions and to develop the numerical techniques is with a two dimensional version as done here.

APPENDIX A

DERIVATION OF TERRAIN FOLLOWING COORDINATE SYSTEM

In order to derive the equations it is necessary to connect the coordinates of one point in two Cartesian reference frames possessing the same origin. The equations are developed for the general case in which both systems are oblique and then for the special case in which one system is oblique and the other, orthogonal.

The systems used are $O\text{-}XYZ\text{-}\alpha\beta\gamma$ and $O\text{-}X_1Y_1Z_1\text{-}\alpha_1\beta_1\gamma_1$ with the units the same in each system as shown in Figure 100. The cosines of the angles formed by the axes of these systems are indicated in Table 9.

Table 9. Table of Cosines

O	X	Y	Z
X_1	ℓ_1	m_1	n_1
Y_1	ℓ_2	m_2	n_2
Z_1	ℓ_3	m_3	n_3
Example: $\cos \angle YOZ_1 = m_3$			

Consider a closed broken line which leads from O to P along the edges OP_X , $P_X P_{XY}$, and $P_{XY} P$ of the system $O\text{-}XYZ$ and which returns from P to O along the edges $PP_{X_1Y_1}$, $P_{X_1Y_1} P_{X_1}$, $P_{X_1} O$ of the system $O\text{-}X_1Y_1Z_1$ as

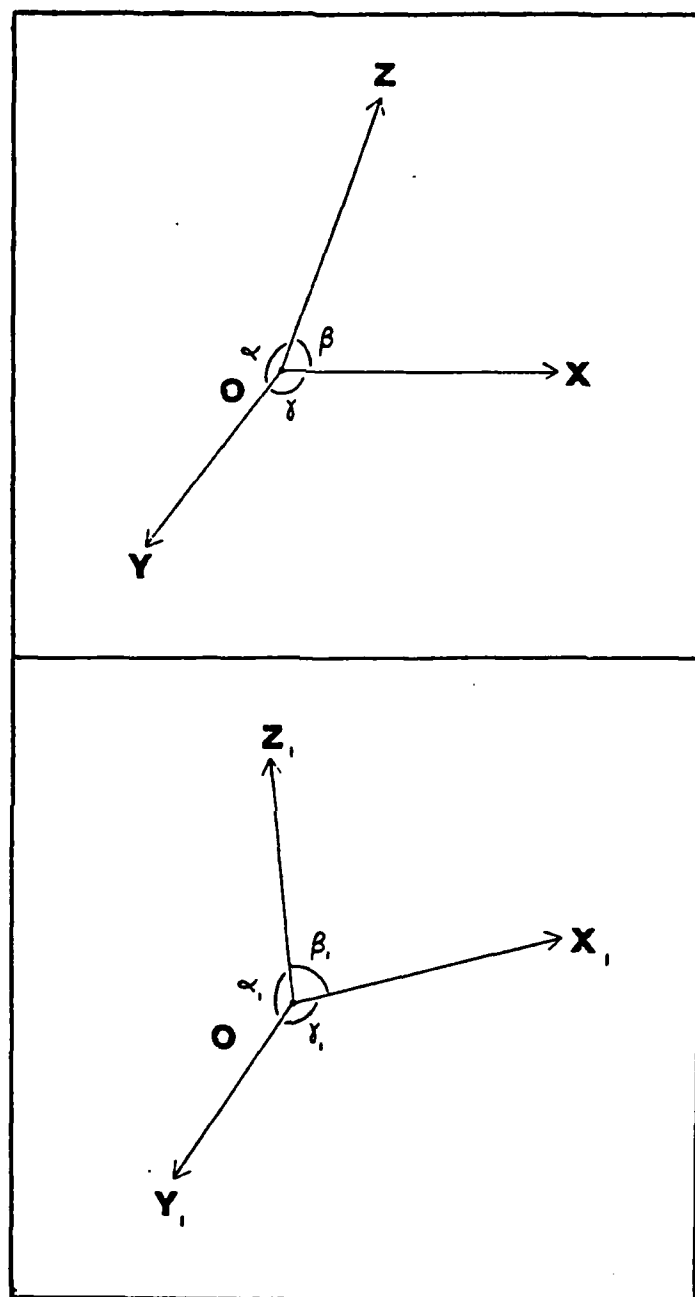


Figure 100. Coordinate systems $O-XYZ-\alpha\beta\gamma$ (top) and $O-X_1Y_1Z_1-\alpha_1\beta_1\gamma_1$ (bottom).

shown in Figure 101. The closed broken line is projected, in turn, on the axes OX , OY , OZ and then on the axes OX_1 , OY_1 , OZ_1 . The following theorems are useful:

Theorem 1. The projection of a segment, AB , of a directed line, ℓ , upon a directed line, m , is equal to the product of AB by the cosine of the angle between the two directed lines.

Theorem 2. The sum of the projections upon a directed line, m , of the segments of a closed broken line in space is equal to zero. Projecting the closed broken line onto OX , OY , and OZ yields the following system:

$$X + Y \cos \gamma + Z \cos \beta - X_1 \ell_1 - Y_1 \ell_2 - Z_1 \ell_3 = 0$$

$$X \cos \gamma + Y + Z \cos \alpha - X_1 m_1 - Y_1 m_2 - Z_1 m_3 = 0$$

$$X \cos \beta + Y \cos \alpha + Z - X_1 n_1 - Y_1 n_2 - Z_1 n_3 = 0$$

Projecting the closed broken line onto OX_1 , OY_1 , and OZ_1 , yields the following system:

$$X \ell_1 + Y m_1 + Z n_1 - X_1 - Y_1 \cos \gamma_1 - Z_1 \cos \beta_1 = 0$$

$$X \ell_2 + Y m_2 + Z n_2 - X_1 \cos \gamma_1 - Y_1 - Z_1 \cos \alpha_1 = 0$$

$$X \ell_3 + Y m_3 + Z n_3 - X_1 \cos \beta_1 - Y_1 \cos \alpha_1 - Z_1 = 0$$

The first system has a unique solution for X, Y, Z in terms of X_1, Y_1, Z_1 while the second system has a unique solution for X_1, Y_1, Z_1 in terms of X, Y, Z . Both systems are solved using Cramer's rule.

The derivation up to this point follows Dresden (1930). A departure from his derivation is taken when the following specifications are made:

- a. Let the system $O-X_1Y_1Z_1-\alpha_1\beta_1\gamma_1$ be orthogonal; therefore $\alpha_1, \beta_1, \gamma_1$ are right angles.

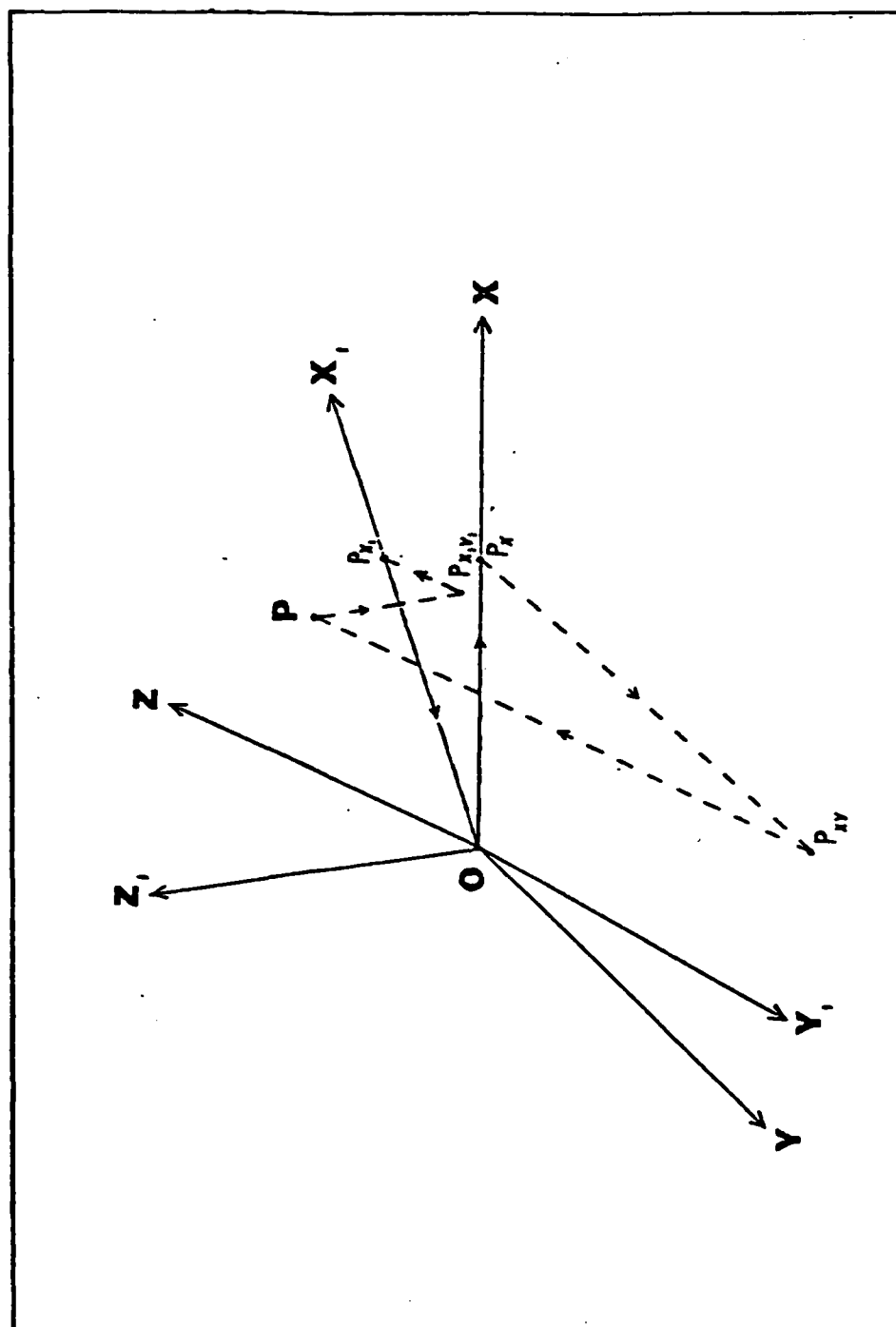


Figure 101. Closed broken line which goes from O to P using the system $O-X_1Y_1Z_1$ and returns from P to O by way of the system $O-X_1Y_1Z_1$.

b. Let the system $O\text{-}XYZ\text{-}\alpha\beta\gamma$ be our "terrain following system" where α and β are right angles. OX rotates in the X_1Z_1 plane and is perpendicular to OY_1 . OY rotates in the Y_1Z_1 plane and is perpendicular to OX_1 as seen in Figure 102. After making these specifications, $\cos\alpha_1 = \cos\beta_1 = \cos\gamma_1 = \cos\beta = \cos\alpha = 0$. Our new table of cosines appears in Table 10.

Table 10. Table of Cosines

O	X	Y	Z
X_1	ℓ_1	$m_1=0$	n_1
Y_1	$\ell_2=0$	m_2	n_2
Z_1	ℓ_3	m_3	n_3

The two systems of equations are:

$$X_1 = \ell_1 X + n_1 Z$$

$$Y_1 = m_2 Y + n_2 Z$$

$$Z_1 = \ell_3 X + m_3 Y + n_3 Z$$

$$X = \left(\frac{\ell_1}{1-\cos^2\gamma}\right)X_1 - \left(\frac{m_2 \cos\gamma}{1-\cos^2\gamma}\right)Y_1 + \left(\frac{\ell_3 - m_3 \cos\gamma}{1-\cos^2\gamma}\right)Z_1$$

$$Y = \left(\frac{-\ell_1 \cos\gamma}{1-\cos^2\gamma}\right)X_1 + \left(\frac{m_2}{1-\cos^2\gamma}\right)Y_1 + \left(\frac{m_3 - \ell_3 \cos\gamma}{1-\cos^2\gamma}\right)Z_1$$

$$Z = n_1 X_1 + n_2 Y_1 + n_3 Z_1$$

The following definitions are made (refer to Figure 103 for clarity):

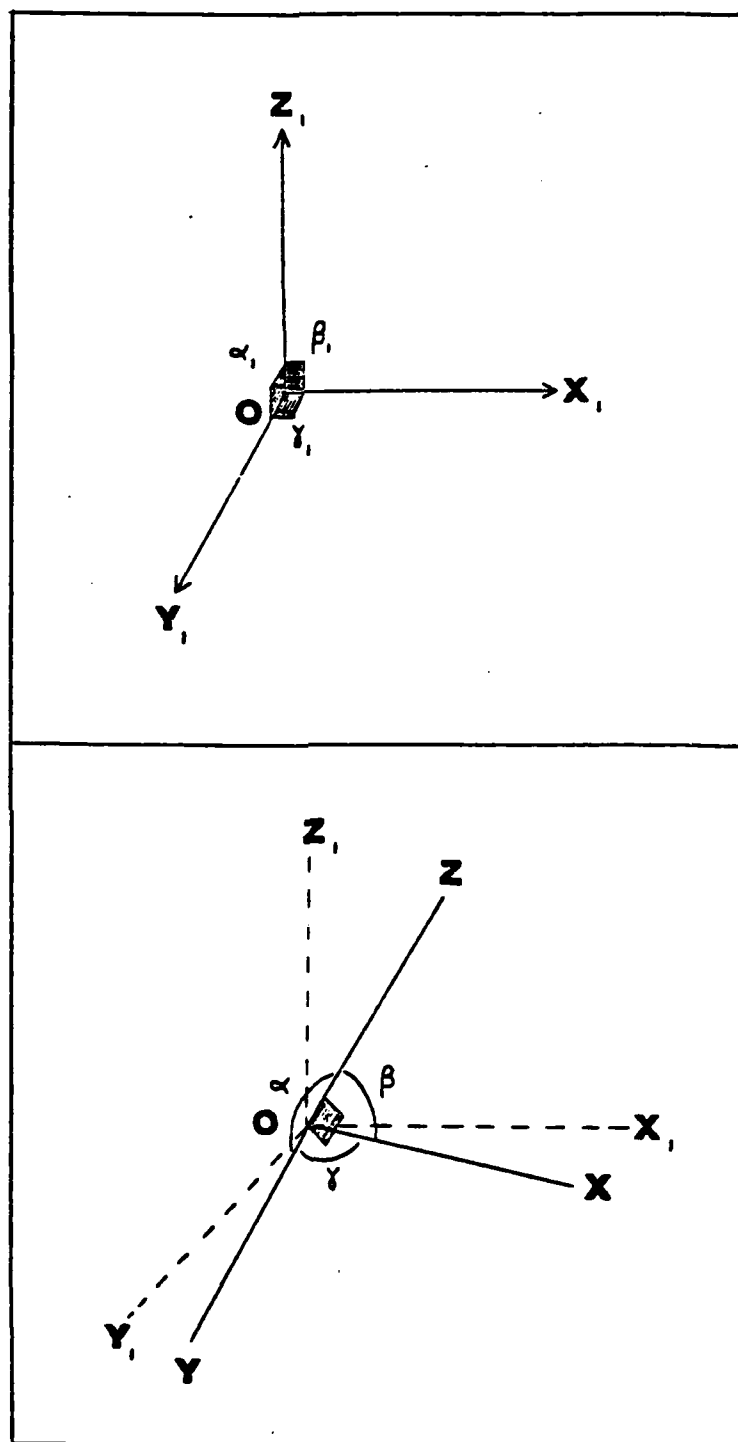


Figure 102. Orthogonal system $O-X_1Y_1Z_1-\alpha_1\beta_1\gamma_1$ (top) and terrain following system $O-XYZ-\alpha\beta\gamma$ (bottom).

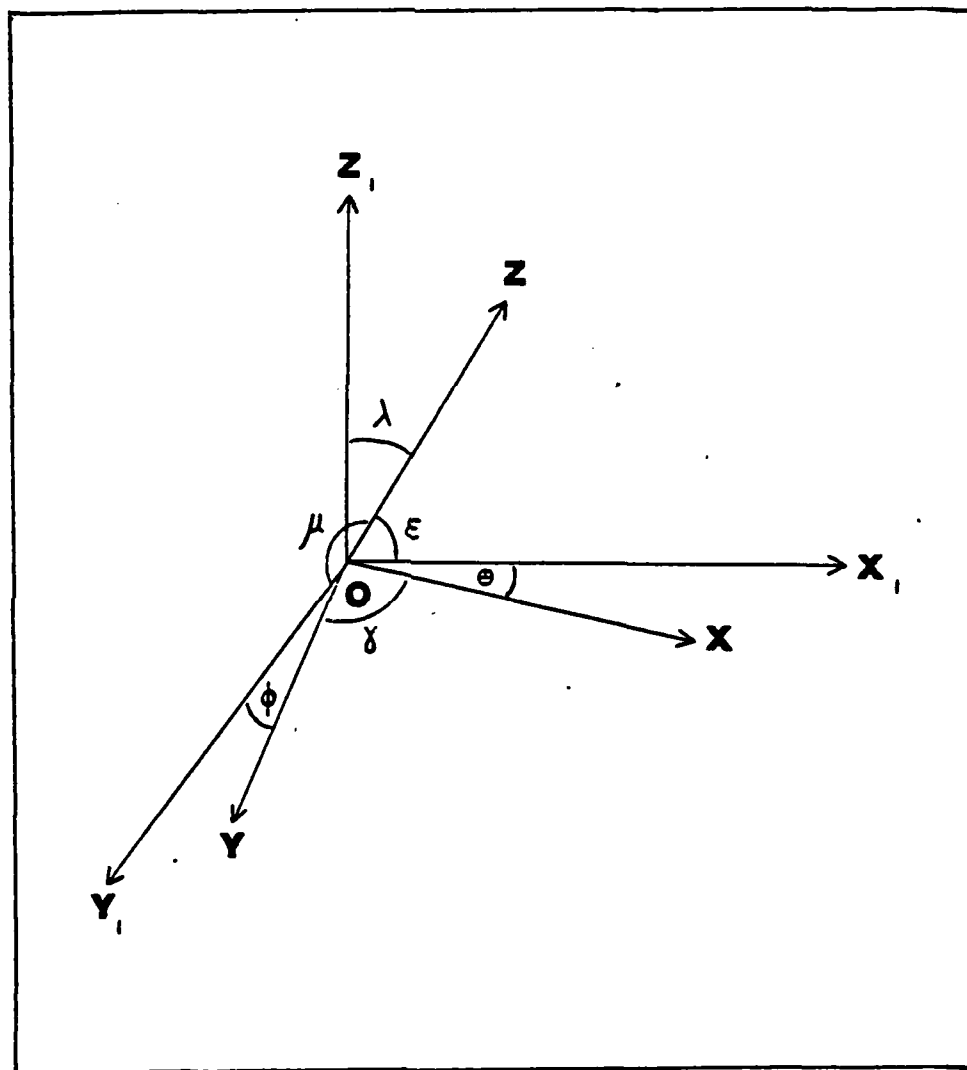


Figure 103. Graphical representation of angles $\hat{\epsilon}$, ϕ , λ , μ , ϵ , and γ .

$$l_1 = \cos < XOX_1 \equiv \cos \theta$$

$$l_3 = \cos < XOZ_1 \equiv \sin \theta$$

$$n_1 = \cos < ZOZ_1 \equiv \cos \epsilon$$

$$m_3 = \cos < YOZ_1 \equiv \sin \phi$$

$$m_2 = \cos < YOY_1 \equiv \cos \phi$$

$$n_3 = \cos < ZOZ_1 \equiv \cos \lambda$$

$$n_2 = \cos < ZOY_1 \equiv \cos \mu$$

It is necessary to express γ , λ , ϵ , and μ in terms of θ and ϕ .

The following relations can be established (e.g. Snyder, 1914):

$$\cos \gamma = \sin \theta \sin \phi$$

$$\cos \lambda = \frac{1}{\sqrt{\tan^2 \theta + \sec^2 \phi}} \quad \cos \mu = \frac{-\tan \phi}{\sqrt{\tan^2 \theta + \sec^2 \phi}}$$

$$\cos \epsilon = \frac{-\tan \theta}{\sqrt{\tan^2 \theta + \sec^2 \phi}}$$

The two systems of equations written in terms of only θ and ϕ are now:

$$X_1 = \cos \theta X - \frac{\tan \theta}{\sqrt{\tan^2 \theta + \sec^2 \phi}} Z$$

$$Y_1 = \cos \phi Y - \frac{\tan \phi}{\sqrt{\tan^2 \theta + \sec^2 \phi}} Z$$

$$Z_1 = \sin \theta X + \sin \phi Y + \frac{1}{\sqrt{\tan^2 \theta + \sec^2 \phi}} Z$$

$$X = \left[\frac{\cos \theta}{1 - \sin^2 \theta \sin^2 \phi} \right] X_1 - \left[\frac{\cos \phi \sin \theta \sin \phi}{1 - \sin^2 \theta \sin^2 \phi} \right] Y_1 + \left[\frac{\sin \theta (1 - \sin^2 \phi)}{1 - \sin^2 \theta \sin^2 \phi} \right] Z_1$$

$$Y = \left[\frac{-\cos \theta \sin \theta \sin \phi}{1 - \sin^2 \theta \sin^2 \phi} \right] X_1 + \left[\frac{\cos \phi}{1 - \sin^2 \theta \sin^2 \phi} \right] Y_1 + \left[\frac{\sin \phi (1 - \sin^2 \theta)}{1 - \sin^2 \theta \sin^2 \phi} \right] Z_1$$

$$Z = \left[\frac{-\tan \theta}{\sqrt{\tan^2 \theta + \sec^2 \phi}} \right] X_1 - \left[\frac{\tan \phi}{\sqrt{\tan^2 \theta + \sec^2 \phi}} \right] Y_1 + \left[\frac{1}{\sqrt{\tan^2 \theta + \sec^2 \phi}} \right] Z_1$$

Using the chain rule:

$$\frac{\partial(\quad)}{\partial X_1} = \frac{\partial(\quad)}{\partial X} \left[\frac{\cos \theta}{1 - \sin^2 \theta \sin^2 \phi} \right] - \frac{\partial(\quad)}{\partial Z} \left[\frac{\tan \theta}{\sqrt{\tan^2 \theta + \sec^2 \phi}} \right]$$

$$\frac{\partial(\quad)}{\partial Y_1} = \frac{\partial(\quad)}{\partial Y} \left[\frac{\cos \phi}{1 - \sin^2 \theta \sin^2 \phi} \right] - \frac{\partial(\quad)}{\partial Z} \left[\frac{\tan \phi}{\sqrt{\tan^2 \theta + \sec^2 \phi}} \right]$$

$$\frac{\partial(\quad)}{\partial Z_1} = \frac{\partial(\quad)}{\partial X} \left[\frac{\sin \theta (1 - \sin^2 \phi)}{1 - \sin^2 \theta \sin^2 \phi} \right] + \frac{\partial(\quad)}{\partial Y} \left[\frac{\sin \phi (1 - \sin^2 \theta)}{1 - \sin^2 \theta \sin^2 \phi} \right] + \frac{\partial(\quad)}{\partial Z} \left[\frac{1}{\sqrt{\tan^2 \theta + \sec^2 \phi}} \right]$$

$$\frac{\partial(\quad)}{\partial X} = \frac{\partial(\quad)}{\partial X_1} \cos \theta + \frac{\partial(\quad)}{\partial Z_1} \sin \theta$$

$$\frac{\partial(\quad)}{\partial Y} = \frac{\partial(\quad)}{\partial Y_1} \cos \phi + \frac{\partial(\quad)}{\partial Z_1} \sin \phi$$

$$\frac{\partial(\quad)}{\partial Z} = \frac{\partial(\quad)}{\partial X_1} \left[\frac{\tan \theta}{\sqrt{\tan^2 \theta + \sec^2 \phi}} \right] - \frac{\partial(\quad)}{\partial Y_1} \left[\frac{\tan \phi}{\sqrt{\tan^2 \theta + \sec^2 \phi}} \right] + \frac{\partial(\quad)}{\partial Z_1} \left[\frac{1}{\sqrt{\tan^2 \theta + \sec^2 \phi}} \right]$$

The formulation of expressions for U_1 , V_1 , and W_1 where

$$U_1 = \frac{dX_1}{dt}, \quad V_1 = \frac{dY_1}{dt}, \quad \text{and} \quad W_1 = \frac{dZ_1}{dt}$$

requires much manipulation which is omitted here for brevity. The results are:

$$U_1 = \cos \theta U - \frac{\tan \theta}{\sqrt{\tan^2 \theta + \sec^2 \phi}} W - \left(\sin \theta X + \frac{\sec^2 \theta \sec^2 \phi}{(\tan^2 \theta + \sec^2 \phi)^{3/2}} Z \right) \frac{d\theta}{dt}$$

$$+ \left(\frac{\tan \theta \tan \phi \sec^2 \phi}{(\tan^2 \theta + \sec^2 \phi)^{3/2}} Z \right) \frac{d\phi}{dt}$$

$$V_1 = \cos \phi V - \frac{\tan \phi}{\sqrt{\tan^2 \theta + \sec^2 \phi}} W - \left(\sin \phi Y + \frac{\sec^2 \phi \sec^2 \theta}{(\tan^2 \theta + \sec^2 \phi)^{3/2}} Z \right) \frac{d\phi}{dt}$$

$$+ \left(\frac{\tan \phi \tan \theta \sec^2 \theta}{(\tan^2 \theta + \sec^2 \phi)^{3/2}} Z \right) \frac{d\theta}{dt}$$

$$\begin{aligned}
W_1 = & \sin\theta U + \sin\phi V + \frac{1}{\sqrt{\tan^2\theta + \sec^2\phi}} W \\
& + \left(\cos\theta X - \frac{\tan\theta \sec^2\theta}{(\tan^2\theta + \sec^2\phi)^{3/2}} Z \right) \frac{d\theta}{dt} \\
& + \left(\cos\phi Y - \frac{\tan\phi \sec^2\phi}{(\tan^2\theta + \sec^2\phi)^{3/2}} Z \right) \frac{d\phi}{dt}
\end{aligned}$$

With the above results the following equations can be written in terms of θ , ϕ , U , V , W , $\bar{\rho}$, ρ' , and P' . The original equations are:

$$\frac{\partial U_1}{\partial t} + U_1 \frac{\partial U_1}{\partial X_1} + V_1 \frac{\partial U_1}{\partial Y_1} + W_1 \frac{\partial U_1}{\partial Z_1} - fV_1 = -\frac{1}{\rho} \frac{\partial P}{\partial X_1} + \frac{\partial}{\partial Z_1} \left(K_M \frac{\partial U_1}{\partial Z_1} \right)$$

$$\frac{\partial V_1}{\partial t} + U_1 \frac{\partial V_1}{\partial X_1} + V_1 \frac{\partial V_1}{\partial Y_1} + W_1 \frac{\partial V_1}{\partial Z_1} + fU_1 = -\frac{1}{\rho} \frac{\partial P}{\partial Y_1} + \frac{\partial}{\partial Z_1} \left(K_M \frac{\partial V_1}{\partial Z_1} \right)$$

$$\frac{\partial q}{\partial t} + U_1 \frac{\partial q}{\partial X_1} + V_1 \frac{\partial q}{\partial Y_1} + W_1 \frac{\partial q}{\partial Z_1} = \frac{\partial}{\partial Z_1} \left(K_\theta \frac{\partial q}{\partial Z_1} \right)$$

$$\frac{\partial \theta}{\partial t} + U_1 \frac{\partial \theta}{\partial X_1} + V_1 \frac{\partial \theta}{\partial Y_1} + W_1 \frac{\partial \theta}{\partial Z_1} = Q + \frac{\partial}{\partial Z_1} \left(K_\theta \frac{\partial \theta}{\partial Z_1} \right)$$

$$\frac{\partial W_1}{\partial Z_1} = - \left(\frac{\partial U_1}{\partial X_1} + \frac{\partial V_1}{\partial Y_1} \right)$$

After much manipulation the equations are formed and then scaled according to the following factors:

a. Time Scale (T) - The diurnal time scale was used; therefore $T \sim O(10^4) = 1/f$ where f was the coriolis parameter.

b. Depth Scale (D) - determined by the physical depth of the model which was 1.5 km $\sim O(10^3)$ meters.

c. Horizontal Wind Speed (V) - $O(10)$ meters per second.

d. Length Scale (L) - determined by 1/4 of the wavelength of the type of motion which could be resolved on the model grid. For a grid spacing of 2° , $L \sim 0(10^5)$ meters.

e. Vertical Scale (W) - $0(10^{-2})$ meters per second.

f. $\frac{\partial \theta}{\partial X}, \frac{\partial \theta}{\partial Y}, \frac{\partial \phi}{\partial X}, \frac{\partial \phi}{\partial Y} < 0(10^{-8})$ This was based on a smoothed terrain.

G. $\theta, \phi = 0(5 \cdot 10^{-3})$

The pressure gradient term requires special attention. Using the U component of the momentum equation as an example, the pressure gradient term is linearized about a basic state in which \bar{P} and $\bar{\rho}$ are constant in X_1 and t . In the terrain following coordinate system we have the following:

$$\begin{aligned} \frac{1}{\rho} \frac{\partial P}{\partial X_1} &= \frac{1}{\rho} \frac{\partial P}{\partial X} \left[\frac{\cos \theta}{1 - \sin^2 \theta \sin^2 \phi} \right] - \frac{1}{\rho} \frac{\partial P}{\partial Z} \left[\frac{\tan \theta}{\sqrt{\tan^2 \theta + \sec^2 \phi}} \right] \\ &\doteq \frac{1}{\bar{\rho}} \frac{\partial P'}{\partial X} \left[\frac{\cos \theta}{1 - \sin^2 \theta \sin^2 \phi} \right] - \frac{1}{\bar{\rho}} \frac{\partial P'}{\partial Z} \left[\frac{\tan \theta}{\sqrt{\tan^2 \theta + \sec^2 \phi}} \right] \end{aligned}$$

$$\text{Note that } \frac{\partial P'}{\partial Z} = -\rho' g \cos \lambda = \frac{\rho' g}{\sqrt{\tan^2 \theta + \sec^2 \phi}}$$

Therefore

$$\frac{1}{\rho} \frac{\partial P}{\partial X_1} \doteq \frac{1}{\bar{\rho}} \frac{\partial P'}{\partial X} \left[\frac{\cos \theta}{1 - \sin^2 \theta \sin^2 \phi} \right] + \frac{\rho'}{\bar{\rho}} g \left[\frac{\tan \theta}{\tan^2 \theta + \sec^2 \phi} \right]$$

The equations can now be written in the local "terrain following coordinates".

$$\frac{\partial U}{\partial t} + \left[\frac{\cos^2 \theta}{1 - \sin^2 \theta \sin^2 \phi} \right] U \frac{\partial U}{\partial X} + \left[\frac{\cos^2 \phi}{1 - \sin^2 \theta \sin^2 \phi} \right] V \frac{\partial U}{\partial Y} + \left[\frac{1}{\tan^2 \theta + \sec^2 \phi} \right] W \frac{\partial U}{\partial Z}$$

$$- \frac{\cos \phi}{\cos \theta} fV = - \left[\frac{1}{1 - \sin^2 \theta \sin^2 \phi} \right] \frac{1}{\rho} \frac{\partial P'}{\partial X} - \left[\frac{\sin \theta}{\cos^2 \theta \tan^2 \phi + 1} \right] \frac{\rho'}{\rho} g$$

$$+ \frac{1}{\cos \theta} \frac{\partial}{\partial Z} (K_M \frac{\partial U}{\partial Z})$$

$$\frac{\partial V}{\partial t} + \left[\frac{\cos^2 \theta}{1 - \sin^2 \theta \sin^2 \phi} \right] U \frac{\partial V}{\partial X} + \left[\frac{\cos^2 \phi}{1 - \sin^2 \theta \sin^2 \phi} \right] V \frac{\partial V}{\partial Y} + \left[\frac{1}{\tan^2 \theta + \sec^2 \phi} \right] W \frac{\partial V}{\partial Z}$$

$$+ \frac{\cos \theta}{\cos \phi} fU = - \left[\frac{1}{1 - \sin^2 \theta \sin^2 \phi} \right] \frac{1}{\rho} \frac{\partial P'}{\partial Y} - \left[\frac{\sin \phi}{\cos^2 \phi \tan^2 \theta + 1} \right] \frac{\rho'}{\rho} g$$

$$+ \frac{1}{\cos \phi} \frac{\partial}{\partial Z} (K_M \frac{\partial V}{\partial Z})$$

$$\frac{\partial q}{\partial t} + \left[\frac{\cos^2 \theta}{1 - \sin^2 \theta \sin^2 \phi} \right] U \frac{\partial q}{\partial X} + \left[\frac{\cos^2 \phi}{1 - \sin^2 \theta \sin^2 \phi} \right] V \frac{\partial q}{\partial Y} + \left[\frac{1}{\tan^2 \theta + \sec^2 \phi} \right] W \frac{\partial q}{\partial Z}$$

$$= \frac{\partial}{\partial Z} (K_\theta \frac{\partial q}{\partial Z})$$

$$\frac{\partial \theta}{\partial t} + \left[\frac{\cos^2 \theta}{1 - \sin^2 \theta \sin^2 \phi} \right] U \frac{\partial \theta}{\partial X} + \left[\frac{\cos^2 \phi}{1 - \sin^2 \theta \sin^2 \phi} \right] V \frac{\partial \theta}{\partial Y} + \left[\frac{1}{\tan^2 \theta + \sec^2 \phi} \right] W \frac{\partial \theta}{\partial Z}$$

$$= Q + \frac{\partial}{\partial Z} (K_\theta \frac{\partial \theta}{\partial Z})$$

$$\left[\frac{1}{\tan^2 \theta + \sec^2 \phi} \right] \frac{\partial W}{\partial Z} = - \left[\frac{\cos^2 \theta}{1 - \sin^2 \theta \sin^2 \phi} \right] \frac{\partial U}{\partial X} - \left[\frac{\cos^2 \phi}{1 - \sin^2 \theta \sin^2 \phi} \right] \frac{\partial V}{\partial Y}$$

The two dimensional simplified version of these equations are used in the model as explained in Chapter 3.

APPENDIX B

CALCULATING SPECIFIC HUMIDITY FROM DEW POINT TEMPERATURE

The derivation begins with the Clausius-Clapeyron equation (Rogers, 1976).

$$\frac{de_s(T)}{dT} = \frac{L_{\ell v}}{T(\alpha_v - \alpha_\ell)}$$

where e_s = saturation vapor pressure

$L_{\ell v}$ = latent heat of vaporization

α_v, α_ℓ = specific volume for vapor and liquid phases of water

Since $\alpha_v \gg \alpha_\ell$ and $e_s \alpha_v = R_v T$, the Clausius-Clapeyron equation can be written in approximate form as

$$\frac{1}{e_s} \frac{de_s}{dT} \approx \frac{L_{\ell v}}{R_v T^2}$$

where R_v = individual gas constant for water vapor.

The above equation is integrated from some reference state (e_0, T_0) to a final state (e_s, T). Over the interval of integration, $L_{\ell v}$ is considered constant ($L_{\ell v} = \bar{L}_{\ell v}$). Integration yields

$$e_s(T) \approx e_0 \exp\left[\frac{\bar{L}_{\ell v}}{R_v} \left(\frac{1}{T_0} - \frac{1}{T}\right)\right]$$

Since saturation occurs at the dew point (T_0), the above equation can be interpreted as

$$e \doteq e_s(T_D) \doteq 6.11 \exp \left[\frac{L_{lv}}{R_v} \left(\frac{1}{273} - \frac{1}{T_D} \right) \right]$$

where the reference state is the triple point. Appropriate values for L_{lv} and R_v are from Rogers (1976) and Dutton (1976)

$$q \doteq .622 \left(\frac{e}{p} \right)$$

Substituting the above expression for e yields the final result.

$$q \doteq .622 \left\{ \frac{6.11}{p} \exp \left[\frac{[597 - .285(T_D - 273)]}{.11} \left(\frac{1}{273} - \frac{1}{T_D} \right) \right] \right\}$$

where P = atmospheric pressure in mb

T_D = dew point temperature in °K.

REFERENCES

- Anthes, R. A., T. T. Warner and A. L. McNab, 1977: Development and testing of a mesoscale primitive equation model at Penn State. Presented at the Third Conference on Numerical Weather Prediction of the A. M. S., Omaha, Nebraska.
- Blackadar, A. K., 1962: Vertical distribution of wind and turbulent exchange in a neutral atmosphere. J. Geophys. Res., 67, 3095-3102.
- Blackadar, A. K., 1957: Boundary layer wind maxima and their significance for the growth of nocturnal inversions. Bull. Amer. Meteor. Soc., 38, 283-290.
- Bleeker, W., and J. Andre, 1951: On the diurnal variation of precipitation, particularly over central U. S. A., and its relation to large-scale orographic circulation systems. Quart. J. Roy. Meteor. Soc., 77, 260-271.
- Bonner, W. D., 1968: Climatology of the low level jet. Mon. Weather Rev., 96, 833-850.
- _____, and Jan Paegle, 1970: Diurnal variations in boundary layer winds over the south-central United States in summer. Mon. Weather Rev., 98, 735-744.
- _____, S. Esbensen and R. Greenberg, 1968: Kinematics of the low-level jet. J. Appl. Meteor., 7, 339-347.
- Buajitti, K. and A. K. Blackadar, 1957: Theoretical studies of diurnal wind-structure variations in the planetary boundary layer. Quart. J. Roy. Meteor. Soc., 83, 486-500.
- Carl, D. M., T. C. Tarbell and H. A. Panofsky, 1973: Profiles of wind and temperature from towers over homogeneous terrain. J. Atmos. Sci., 30, 788-794.
- Curtis, R. C. and H. A. Panofsky, 1958: The relation between large-scale vertical motion and weather in summer. Bull. Amer. Meteor. Soc., 39, 521-531.
- Deardorff, J., 1974: Three-dimensional numerical study of the height and mean structure of a heated planetary boundary layer. Bound. Layer Meteor., 7, 81-106.

- Djolov, G. D., 1973: Modeling of interdependent diurnal variation of meteorological elements in the boundary layer. Ph.D. Thesis, University of Waterloo, Waterloo, Ontario.
- Dresden, A., 1930: Solid Analytical Geometry and Determinants. Chapman and Hall, Limited, London, 118-121.
- Dutton, J. A., 1976: The Ceaseless Wind. McGraw-Hill, 256-274.
- Feussner, K. and P. Dubois, 1930: Trübungs faktor, precipitable water, staub. Gerlands Beitr. Geophys., 27, 132-175.
- Gerrity, J. D., 1976: A physical numerical model for the prediction of synoptic-scale low cloudiness. Mon. Weather Rev., 95, 261-282.
- Hewson, E. W., 1943: The application of wet-bulb potential temperature to air mass analysis. Quart. J. Roy. Meteor. Soc., 63, 323-335.
- Holton, J. R., 1967: The diurnal boundary layer wind oscillation above sloping terrain. Tellus, 19, 199-205.
- Jenne, R. L. and W. Spangler, 1976: USAF average elevation data - one degree and 5 minute (Boulder, Colorado: National Center for Atmospheric Research).
- Kincer, J. B., 1916: Daytime and nighttime precipitation and their economic significance. Mon. Weather Rev., 44, 628-633.
- Lindzen, R. S. and H. L. Kuo, 1969: A reliable method for the numerical integration of a large class of ordinary and partial differential equations. Mon. Weather Rev., 97, 732-734.
- Liou, K. N., 1979: Dept. of Meteor., Univ. of Utah (personal communication).
- Lumley, J. and R. Panofsky, 1964: The Structure of Atmospheric Turbulence. John Wiley and Sons, Inc., New York.
- McClatchey, R. A., R. W. Fenn, J. E. Selby, F. E. Volz and J. S. Garing, 1971: Optical properties of the atmosphere. 3rd ed. AFCRL-72-0497.
- McDonald, J. E., 1960: Direct absorption of solar radiation by atmospheric water vapor. J. Meteor., 17, 319-328.
- Means, L. L., 1952: On thunderstorm forecasting in the central United States. Mon. Weather Rev., 80, 165-189.
- _____, 1944: The nocturnal maximum occurrence of thunderstorms in the midwestern states. Dept. of Meteor., Univ. of Chicago, Misc. Rep. No. 16, 37 pp.

- Monin, A. S. and A. Yaglom, 1971: Statistical Fluid Mechanics; Mechanics of Turbulence. MIT Press, Cambridge, Mass., 373-383.
- Ooyama, Katsuyuki, 1957: A study of diurnal variations of wind caused by periodic variation of eddy viscosity. Final Report, AF 19(604)-1368, College of Engineering, New York University, 80-135.
- Orlanski, I., B. B. Ross and L. J. Polinsky, 1974: Diurnal variation of the planetary boundary layer in a mesoscale model. J. Atmos. Sci., 27, 965-989.
- Paegle, J., 1978: A linearized analysis of diurnal boundary layer convergence over the topography of the United States. Mon. Weather Rev., 106, 492-502.
- _____, and G. E. Rasch, 1973: Three-dimensional characteristics of diurnally varying boundary layer flows. Mon. Weather Rev., 101, 746-756.
- _____, and D. W. McLawhorn, 1973: Correlation of nocturnal thunderstorms and boundary layer convergence. Mon. Weather Rev., 101, 877-883.
- _____, W. G. Zdunkowski and R. M. Welch, 1976: Implicit differencing of predictive equations of the boundary layer. Mon. Weather Rev., 104, 1321-1324.
- Paltridge, G. W. and C. M. R. Platt, 1976: Radiative Processes in Meteorology and Climatology. Elsevier Scientific Publishing Co., New York, 60-66.
- Perkey, D. J. 1977: The effect of geostrophic vs. non-geostrophic initial winds on quantitative precipitation forecasts. Presented at the Third Conference on Numerical Weather Prediction of the A. M. S., Omaha, Nebraska.
- Phillips, H., 1962: Zur theorie des tagesganges der temperatur in der bodennaken atmosphäre und in ihrer unterlage. Z. Meteorol., 16, 5.
- Pielke, R. A. and Y. Mahrer, 1977: Mesoscale model predictions forced by geographic features. Presented at the Third Conference on Numerical Weather Prediction of the A. M. S., Omaha, Nebraska.
- Pitchford, K. L. and J. London, 1962: The low level jet as related to nocturnal thunderstorms over midwest United States. J. Appl. Meteor., 1, 43-47.
- Plate, E. J. 1971: Aerodynamic Characteristics of Atmospheric Boundary Layers. USAEC Division of Technical Information Extension, Oak Ridge, Tennessee.
- Roewe, D. and K. N. Liou, 1978: Influence of cirrus clouds on the infrared cooling rate in the troposphere and lower stratosphere. J. Appl. Meteorol., 17, 92-106.

- Rogers, R. R., 1976: A Short Course In Cloud Physics. Pergamon Press Inc., New York.
- Shuman, F. G., 1957: Numerical methods in weather prediction: II. smoothing and filtering. Mon. Weather Rev., 85, 357-361.
- Snyder, V., 1914: Analytic Geometry of Space. H. Holt and Company, New York.
- Spenser, J. W., 1971: Fourier series representation of the position of the sun. Search, 2, 172.
- Stanley, D. O. and G. M. Jurica, 1970: Flux emissivity tables for water vapor, carbon dioxide and ozone. J. Appl. Meteor., 9, 365-372.
- Wallace, J. M., 1975: Diurnal variations in precipitation and thunderstorm frequency over the conterminous United States. Mon. Weather Rev., 103, 406-419.
- Webb, E. K., 1970: Profile relationships: the log-linear range and extension to strong stability. Quart. J. Roy. Meteor. Soc., 96, 67-90.
- Welch, R. M., J. Paegle and W. G. Zdunkowski, 1978: Two-dimensional numerical simulation of the effect of air pollution upon the urban-rural complex. Tellus, 30, 136-150.
- Wexler, H. 1961: A boundary layer interpretation of the low level jet. Tellus, 13, 368-378.
- Yamada, T. and G. Mellor, 1975: A simulation of the wangan atmospheric boundary layer data. J. Atmos. Sci., 32, 2309-2329.
- Yu, T. W., 1977: Notes on a turbulence parameterization of the atmospheric boundary layer. J. of the Meteor. Soc. of Japan, 55, 617-622.
- Zdunkowski, W. G. R. M. Welch and J. Paegle, 1976: One-dimensional numerical simulation of the effects of air pollution on the planetary boundary layer. J. Atmos. Sci., 33, 2399-2414.
- Zdunkowski, W. G., J. Paegle and J. P. Reilly, 1975: The effect of soil moisture upon the atmospheric and soil temperature near the air-soil interface. Arch. Met. Geoph. Biokl., 24, 245-268.

VITA

NAME	David Wilton McLawhorn
BIRTHPLACE	Ayden, North Carolina
BIRTHDATE	24 February, 1943
HIGH SCHOOL	Winterville High School Winterville, North Carolina
UNIVERSITIES	East Carolina University Greenville, North Carolina 1961-1965 The Pennsylvania State University University Park, Pennsylvania 1965-1966 University of Utah Salt Lake City, Utah 1971-1972 1976-1979
DEGREES	Bachelor of Arts in Mathematics, 1965 East Carolina University Bachelor of Science in Meteorology, 1966 The Pennsylvania State University Master of Science in Meteorology, 1972 University of Utah
PROFESSIONAL AND HONORARY ORGANIZATIONS	Sigma Xi Pi Mu Epsilon Chi Epsilon Pi Phi Kappa Phi
PUBLICATIONS	"The effects of Weather on propaga- tion of electromagnetic energy," Air Defense Command Communication and Electronics Digest, 15-70, 1970.

"Nocturnal Thunderstorms and Boundary Layer Convergence", (Masters thesis, University of Utah, 1972), 147 pages.

"Nocturnal Thunderstorms and Boundary Layer Convergence", 1973, with Jan Paegle. Three Dimensional Characteristics Of Diurnally Varying Boundary Layer Flows (Technical report to the National Science Foundation), 129-275.

"Correlation of Nocturnal Thunderstorms and Boundary-Layer Convergence," 1973, with Jan Paegle. Monthly Weather Review, 101, 877-883.

DATE
ILME